

---

# Partial wave analysis of eta meson photoproduction using fixed-t dispersion relations

---

Dissertation  
zur Erlangung des Grades  
„Doktor der Naturwissenschaften“

am Fachbereich Physik, Mathematik und Informatik  
der Johannes Gutenberg-Universität Mainz



JOHANNES GUTENBERG  
UNIVERSITÄT MAINZ

vorgelegt von

**Kirill Nikonov**

geboren in Leningrad (Russland)

Mainz, 2018



---

# Contents

---

<b>1</b>	<b>Introduction</b>	<b>5</b>
<b>2</b>	<b>Baryon spectroscopy</b>	<b>7</b>
2.1	Quark model . . . . .	7
2.2	Lattice QCD calculations . . . . .	9
<b>3</b>	<b>General formalism of <math>\eta</math> meson photoproduction on proton</b>	<b>11</b>
3.1	Kinematics . . . . .	11
3.2	Cross section and polarization observables . . . . .	14
3.3	Invariant and CGLN amplitudes . . . . .	15
3.4	Nucleon resonances in $\eta$ photoproduction . . . . .	17
<b>4</b>	<b>Partial wave content of polarization observables</b>	<b>21</b>
4.1	Description of the data using Legendre polynomials . . . . .	21
4.2	Differential cross section, $d\sigma/d\Omega$ . . . . .	25
4.2.1	MAMI data . . . . .	25
4.2.2	CB ELSA data . . . . .	30
4.3	Polarization observables $\hat{F}$ , $\hat{T}$ . . . . .	33
4.3.1	$\hat{F}$ . . . . .	34
4.3.2	$\hat{T}$ . . . . .	35
4.4	Polarization observable $\hat{\Sigma}$ . . . . .	37
4.5	Polarization observable $E$ . . . . .	39
4.6	Conclusion . . . . .	39
<b>5</b>	<b>Partial wave analysis</b>	<b>41</b>
5.1	EtaMAID isobar model approach . . . . .	41
5.1.1	Resonance part . . . . .	41
5.1.2	Non-resonant background . . . . .	44
5.2	Other partial wave analysis models . . . . .	50
5.2.1	Bonn-Gatchina approach . . . . .	50
5.2.2	Jülich-Bonn approach . . . . .	51
5.2.3	SAID approach . . . . .	51
<b>6</b>	<b>Fixed-<math>t</math> dispersion relation approach. Previous results</b>	<b>53</b>
6.1	Dispersion relations, mathematical formulation . . . . .	53
6.2	Data analysis using the fixed- $t$ dispersion relations approach . . . . .	54
6.2.1	Data analysis using fixed- $t$ dispersion relations in work of Aznauryan . . . . .	54
6.2.2	Data analysis using fixed- $t$ dispersion relations with EtaMAID . . . . .	56
6.2.3	Restrictions on the $t$ values for dispersion relations . . . . .	59
6.2.4	Comparison of the approaches. . . . .	60

<b>7</b>	<b>Fit results</b>	<b>63</b>
7.1	Starting solution	64
7.2	Solution 1. Fit results with resonances only	65
7.2.1	Description of the $d\sigma/d\Omega$ and the total cross section	65
7.2.2	Description of $T$ and $F$ asymmetries	66
7.2.3	Description of $\Sigma$ and $E$ asymmetries	68
7.2.4	Solution 1 summary	69
7.3	Solution 2. Fit results with resonances and Born terms	70
7.3.1	Description of the $d\sigma/d\Omega$	70
7.3.2	Description of $T$ and $F$ asymmetries	71
7.3.3	Description of $\Sigma$ and $E$ asymmetries	72
7.3.4	Solution 2 summary	72
7.4	Solution 3. Fit results with resonances and Regge contributions ( $s$ )	73
7.4.1	Description of the $d\sigma/d\Omega$	74
7.4.2	Description of $T$ and $F$ asymmetries	74
7.4.3	Description of $\Sigma$ and $E$ asymmetries	75
7.4.4	Description of $d\sigma/dt$ , $\Sigma$ , and $T$ at high energies	76
7.4.5	Regge contributions to the invariant amplitudes at fixed $t$ -values	77
7.4.6	Solution 3 summary	77
7.5	Intermediate conclusion for solutions 1-3	78
7.6	Solution 4. Fit results with resonances $\times e^{i\Phi_j^\alpha}$ for $j : 3/2^-, 3/2^+, 5/2^-$ states, and Born terms	80
7.6.1	Description of the $d\sigma/d\Omega$	80
7.6.2	Description of $T$ and $F$ asymmetries	81
7.6.3	Description of $\Sigma$ and $E$ asymmetries	82
7.6.4	Solution 4 summary	82
7.7	Solution 5. Fit results with resonances $\times e^{i\Phi_j^\alpha}$ for $j : 3/2^-, 3/2^+, 5/2^-$ states, and Regge contributions ( $s$ )	84
7.7.1	Description of the $d\sigma/d\Omega$ and the total cross section	84
7.7.2	Description of $T$ and $F$ asymmetries	85
7.7.3	Description of $\Sigma$ and $E$ asymmetries	86
7.7.4	Description of $d\sigma/dt$ , $\Sigma$ , and $T$ at high energies	87
7.7.5	Solution summary	87
7.8	Solution 6. Fit results with resonances $\times e^{i\Phi_j^\alpha}$ for $j : 3/2^-, 3/2^+, 5/2^-$ states, and Regge contributions ( $\nu$ )	88
7.8.1	Description of the $d\sigma/d\Omega$	89
7.8.2	Description of $T$ and $F$ asymmetries	89
7.8.3	Description of $\Sigma$ and $E$ asymmetries	90
7.8.4	Description of $d\sigma/dt$ , $\Sigma$ , and $T$ at high energies	91
7.8.5	Solution 6 summary	91
7.9	Solution 7. Fit results with resonances $\times e^{i\Phi_j^\alpha}$ for all resonances, and Regge contributions ( $\nu$ )	92
7.9.1	Description of the $d\sigma/d\Omega$	92
7.9.2	Description of $T$ and $F$ asymmetries	93
7.9.3	Description of $\Sigma$ and $E$ asymmetries	94
7.9.4	Description of $d\sigma/dt$ , $\Sigma$ , and $T$ at high energies	95
7.9.5	Regge contributions to the invariant amplitudes at fixed $t$ -values	96
7.9.6	Multipoles	97
7.9.7	Solution 7 summary	98
7.10	Intermediate conclusion for solutions 4-7	98

7.11	Final discussion of the resonance parameters . . . . .	99
7.11.1	Conclusion for the resonance parameters and error discussion . . . . .	109
<b>8</b>	<b>Summary and conclusion</b>	<b>111</b>
<b>A</b>	<b>Formalism</b>	<b>115</b>
A.1	Reduced multipoles in terms of photo decay amplitudes $A_{1/2}$ and $A_{3/2}$ . . . . .	115
A.2	Helicity amplitudes in terms of CGLN amplitudes . . . . .	115
A.3	Expansion of $B_i$ invariant amplitudes in terms of CGLN amplitudes . . . . .	116
A.4	Expansion of CGLN amplitudes in terms of $A_i$ and $B_i$ invariant amplitudes . . . . .	116
A.5	Observables expressed in CGLN amplitudes . . . . .	117
A.6	$T$ asymmetry expressed in terms of multipoles from the set of resonances used in the analysis . . . . .	118
A.7	Projection formulas for multipoles out of CGLN amplitudes . . . . .	118
<b>B</b>	<b>Plots of the fit results</b>	<b>119</b>
B.1	Plots for Solution 1 . . . . .	119
B.2	Plots for Solution 2 . . . . .	122
B.3	Plots for Solution 3 . . . . .	125
B.4	Plots for Solution 4 . . . . .	128
B.5	Plots for Solution 5 . . . . .	131
B.6	Plots for Solution 6 . . . . .	134
B.7	Plots for Solution 7 . . . . .	137
	<b>Bibliography</b>	<b>145</b>



---

# Abstract

---

The photoproduction of  $\eta$  mesons is a powerful source of information about the excitation spectrum of protons and neutrons. There are several methods to extract partial wave or multipole amplitudes from experimentally measured polarized and unpolarized differential cross sections. In so called isobar models the scattering amplitude is parameterized with two parts: resonances and non-resonant background. Such a model, EtaMAID, has been developed in Mainz 15 years ago when first precision data for unpolarized cross sections and beam asymmetries were measured. In the meantime, a significant amount of new data, in particular with polarized beams and targets, are available. Within this thesis, the EtaMaid model was updated and used to fit all available new data.

However, a drawback of all isobar models is the fact that they violate analyticity and crossing symmetry which are important properties of scattering amplitudes. Therefore, in this thesis fixed- $t$  dispersion relations were applied as a constraint to the EtaMAID model in order to obtain solutions which do fulfil analyticity and crossing symmetry. By fitting all modern experimental data resonance parameters are obtained in an improved and less model dependent way. Parameters like masses, widths, branching ratios, and photocouplings for 14 nucleon resonances were determined and are compared to results of the pure isobar model and to existing averages from the PDG.

The thesis is organized as following: After a short introduction, baryon spectroscopy is discussed in Chapter 2 with special focus to quark models and lattice QCD. In Chapter 3 the general formalism of  $\eta$  photoproduction on protons is introduced. In particular, the relations between observables, invariant amplitudes, CGLN amplitudes and multipoles is described. Finally, the connection to the contributing resonances is provided. In Chapter 4 the partial wave content of recently measured polarization observables is studied in terms of a Legendre polynomial expansion. In Chapter 5 different models, in particular the EtaMAID isobar model, are discussed. Fixed- $t$  dispersion relations and their application in  $\eta$  photoproduction are explained in Chapter 6. The results of various fits with different background models are discussed in Chapter 7. The thesis ends with a summary and conclusions.





---

## Zusammenfassung

---

Die Photoproduktion von  $\eta$  Mesonen ist eine wichtige Informationsquelle über das Anregungsspektrum von Protonen und Neutronen. Verschiedene Methoden wurden entwickelt, um Partialwellen oder Multipolamplituden aus gemessenen polarisierten und unpolarisierten differentiellen Wirkungsquerschnitten zu bestimmen. In sog. Isobaren-Modellen wird die Streuamplitude aufgebaut aus der Summe von Resonanzen und nicht-resonantem Untergrund. Ein solches Modell, EtaMAID, wurde vor etwa 15 Jahren in Mainz entwickelt, als erste präzise Daten für Wirkungsquerschnitte und Strahlasymmetrien gemessen wurden. Inzwischen gibt es eine große Menge an neuen Daten, die mit polarisierten Strahlen und Targets gemessen wurden. In dieser Arbeit wurde das EtaMAID Modell aktualisiert und verwendet, um alle neuen Daten zu beschreiben.

Alle Isobaren Modelle haben jedoch das Problem, dass sie mit Analytizität und Crossing-Symmetrie wichtige Eigenschaften von Streuamplituden verletzen. Daher wurden im Rahmen dieser Arbeit fixed-t Dispersionsrelationen als Randbedingung für das EtaMAID Modell verwendet, um Lösungen zu erhalten, die analytisch sind und die Crossing-Symmetrie erfüllen. Durch die Anpassung des Modells an alle moderen Daten wurden Resonanzparameter auf bessere und modelunabhängigere Weise bestimmt. Parameter wie, Massen, Breiten, Verzweigungsverhältnisse und Photo-Kopplungen für 14 Resonanzen wurden bestimmt und mit Ergebnissen des reinen Isobaren Modells sowie mit Mittelwerten der PDG verglichen.

Die Arbeit ist folgendermaßen gegliedert: Nach einer kurzen Einführung wird die Baryonspektroskopie in Kapitel 2 diskutiert. Ein spezieller Fokus liegt dabei auf Quarkmodellen und Gitter-QCD. In Kapitel 3 wird der allgemeine Formalismus der  $\eta$  Photoproduktion erläutert. Insbesondere werden die Zusammenhänge zwischen Observablen, invarianten Amplituden, CGLN Amplituden und Multipolen hergestellt. Abschließend wird die Verbindung zu den Resonanzbeiträgen erläutert. In Kapitel 4 werden kürzlich gemessene Polarisationsobservable hinsichtlich den beitragenden Partialwellen in einer Entwicklung nach Legendre-Polynomen untersucht. In Kapitel 5 werden dann verschiedene Modelle, insbesondere EtaMAID, vorgestellt. Fixed-t Dispersionsanalysen und deren Anwendung in der  $\eta$  Photoproduktion werden in Kapitel 6 erläutert. Die Ergebnisse verschiedener Anpassungen mit unterschiedlichen Ansätzen für den nicht-resonanten Untergrund werden in Kapitel 7 vorgestellt und diskutiert. Die Arbeit endet mit Schlussfolgerungen und einer Zusammenfassung.



# Chapter 1

---

## Introduction

---

At the present time Quantum Chromodynamics (QCD) is the universally recognized theory of strong interactions. According to QCD particles consist of gluons and quarks. Gluons transfer interaction between quarks and quarks carrying non-integer electric charge and do not exist in a free state, this phenomenon called confinement. According to QCD mesons consist of quark-antiquark pairs, baryons consist of three quarks. However some models suppose existence of so-called exotic particles, which consist of other numbers of quarks (4,5,6) [1–3] and also gluons and its mix: hybrids [4] and glueballs ([5] and references therein).

Although the lagrangian of the strong interactions (QCD) is well-known [6, 7], our knowledge about interaction of particles at low and intermediate energies is very limited. This knowledge is crucial because, for example, baryons form most of the known matter and understanding of their structure is a very important task. Due to this problem a number of models were created which explained properties of the ground states and predicted the spectrum of excited baryons. The classical quark model which considered the baryons as bound states of three constituent quarks explained very successfully the spectrum of baryon resonances below 1.7 GeV. However with obtaining of the new data on different reactions it becomes obvious, that such quark model is a too simplified approach for the description of strong interacting particles. For baryons, this model predicts a large number of excited states with masses above 1.7 GeV, but it is not supported by the experimental data. This is the problem of so called *missing states*: number of particles predicted by different models exceeds the number of experimentally found states. The possibly explanation can be that we just did not find new states in the experiment or just do not see them in the data.

However even in the energy region below 1.7 GeV where the number of states is well known the picture is not so clear. For example in case of  $\gamma p \rightarrow \eta p$  the intermediate states (resonances) have sometimes large widths therefore they overlap and it is rather hard to determine their parameters. The procedure of the the analysis of the scattering amplitude is called partial wave analysis (PWA) and can be done in different approaches. There are different groups that are working in this area and using different models. The well known groups are: MAID [8, 9], Bonn-Gatchina (BnGa) [10, 11], Jülich-Bonn (JüBo) [12, 13], SAID [14]. All these groups have their own web-pages [15–18].

The first direct source of information about baryon resonances was pion-nucleon scattering reactions. The corresponding data were collected in a set of laboratories over the world, see SAID web page [18], and a number of new states had been discovered. However a lot of modern data come from different photoproduction reactions, see BnGa web page [16]. This gives us an opportunity to analyze these data in order to determine the parameters of poorly known states or to make the parameters of well known states more accurate.

An approach that is used in Mainz for a data analysis is called isobar model approach. It has been developed more than 15 years ago [8] when first precision data for unpolarized cross sections and beam asymmetries were measured. In so called isobar models the scattering amplitude is parameterized with two parts: resonances and non-resonant background.

However with this procedure we do not take into account very important properties of the scattering amplitude: analyticity and crossing symmetry. In order to fulfill them we introduce

a procedure of fixed- $t$  dispersion relations for invariant amplitudes [19–29]. This procedure allows us to analyze the existing data on  $\eta$  photoproduction with additional constraints and less model dependence. In our analysis we work in the energy region  $W \leq 1863$  MeV, however we are also able to describe the high energy data at small  $t$  values.

The thesis is organized as following: After a short introduction, baryon spectroscopy is discussed in Chapter 2 with special focus to quark models and lattice QCD. In Chapter 3 the general formalism of  $\eta$  photoproduction on protons is introduced. In particular, the relations between observables, invariant amplitudes, CGLN amplitudes and multipoles is described. Finally, the connection to the contributing resonances is provided. In Chapter 4 the partial wave content of recently measured polarization observables is studied in terms of a Legendre polynomial expansion. In Chapter 5 different models, in particular the EtaMAID isobar model, are discussed. Fixed- $t$  dispersion relations and their application in  $\eta$  photoproduction are explained in Chapter 6. The results of various fits with different background models are discussed in Chapter 7. The thesis ends with a summary and conclusions.

## Chapter 2

---

### Baryon spectroscopy

---

It is good to start this chapter with a very interesting question from Nathan Isgur which he asked on  $N * 2000$  workshop [30] "Why  $N^*$ 's?" He gave three answers:

- The first is that nucleons are the stuff of which our world is made. As such they must be at the center of any discussion of why the world we actually experience has the character it does. I am convinced that completing this chapter in the history of science will be one of the most interesting and fruitful areas of physics for at least the next thirty years.
- My second reason is that they are the simplest system in which the quintessentially nonabelian character of QCD is manifest. There are, after all,  $N_c$  quarks in a proton because there are  $N_c$  colors.
- The third reason is that history has taught us that, while relatively simple, baryons are sufficiently complex to reveal physics hidden from us in the mesons. There are many examples of this, but one famous example should suffice: GellMann [6] and Zweig [7] were forced to the quarks by  $3 \otimes 3 \otimes 3$  giving the octet and decuplet, while mesons admitted of many possible solutions.

Thus he predicted that baryon spectroscopy will be one of the most interesting areas for many years.

This chapter is devoted to different approaches which give information about the baryon spectrum. As an example the quark model and the lattice calculations are shown. This short review is mainly based on PDG review [31] and book on mesons and baryons [32].

### 2.1 Quark model

In early sixties with the growth of the experimentally observed particles a question of systematization of them rased up. As a tool for systematization the quark model was developed. It was done in the papers of Gell-Mann [6] and Zweig [7] where it was first shown that known at that time hadrons could be built up of three quarks ( $u, d, s$ ) carrying the non integer charge and obeying the rules of  $SU(3)$  symmetry. Later it became clear that hadrons have to be considered as bound states of quarks (objects which we call now "constituent quarks"). In this picture hadrons consist of quark-anitquark  $M = \bar{q}q$  pairs (mesons), and three quarks  $B = qqq$  (baryons).

In further development of the quark model one was realized that new quantum numbers turned out to be necessary. Thus the picture of colored quarks was formulated by Gell-Mann. In this picture quark possesses a quantum number color, which has three values: red, green and blue. For the two-quark mesons and the three-quark baryons quark wave functions are

$$M = \frac{1}{\sqrt{3}} \sum q_i \bar{q}_i, \quad B = \frac{1}{\sqrt{6}} \sum_{i,k,\ell} \varepsilon_{ik\ell} q_i q_k q_\ell. \quad (2.1)$$

The sum is over the quark colours  $i, k, \ell$  and  $\varepsilon_{ik\ell}$  is the fully antisymmetric unit tensor.

It is known that quarks are strongly interacting fermions with spin 1/2 and, by convention, have positive parity. Antiquarks have therefore negative parity. Quarks have the additive baryon number 1/3, antiquarks  $-1/3$ . Table 2.1 and gives the other additive quantum numbers (flavors) for the three generations of quarks.

Table 2.1: Quarks

	d	u	s	c	b	t
Q - electric charge	$-\frac{1}{3}$	$+\frac{2}{3}$	$-\frac{1}{3}$	$+\frac{2}{3}$	$-\frac{1}{3}$	$+\frac{2}{3}$
I - isospin	$\frac{1}{2}$	$\frac{1}{2}$	0	0	0	0
$I_z$ - isospin z-component	$-\frac{1}{2}$	$+\frac{1}{2}$	0	0	0	0
S - strangeness	0	0	-1	0	0	0
C - charm	0	0	0	+1	0	0
B - bottomness	0	0	0	0	-1	0
T - topness	0	0	0	0	0	+1

The quantum numbers are related to the charge  $Q$  (in units of the elementary charge  $e$  through the generalized Gell-Mann-Nishijima formula:

$$Q = I_z + \frac{\mathcal{B} + S + C + B + T}{2} \quad (2.2)$$

where  $\mathcal{B}$  is the baryon number. The convention is that the flavor of a quark ( $I_z$ , S, C, B, or T) has the same sign as its charge  $Q$ . With this convention, any flavor carried by a charged meson has the same sign as its charge. Antiquarks have the opposite flavor signs. The hypercharge is defined as

$$Y = \mathcal{B} + S - \frac{C+B+T}{3} \quad (2.3)$$

If we consider the baryon spectrum we can see that three quarks  $u, d, s$  form multiplets: the octet with  $J^P = 1/2^+$ :

isospin	strangeness	particles
1/2	0	$p, n$
0	-1	$\Lambda$
1	-1	$\Sigma^+, \Sigma^0, \Sigma^-$
1/2	-2	$\Xi^0, \Xi^-$ ;

(2.4)

and the decuplet with  $J^P = 3/2^+$ :

isospin	strangeness	particles
3/2	0	$\Delta^{++}, \Delta^+, \Delta^0, \Delta^-$
1	-1	$\Sigma^{*+}, \Sigma^{*0}, \Sigma^{*-}$
1/2	-2	$\Xi^{*0}, \Xi^{*-}$
0	-3	$\Omega$ .

(2.5)

With this example we obtain the so called low lying baryons which are well known. Many of their properties, in particular their masses, are in good agreement even with the most basic versions of the quark model.

Low-lying baryons, octets and decuplets may also be described qualitatively in the framework of  $SU(6)$  symmetry.

$$6 \otimes 6 \otimes 6 = 56_S \oplus 70_M \oplus 70_M \oplus 20_A \quad (2.6)$$

Here the subscripts indicate symmetric, mixed-symmetry, or antisymmetric states under interchange of any two quarks. The described above octet and decuplet together form 56-plet in which the angular momenta between the quark pairs are zero. For 70 and 20 we require additional spatial excitation and as a result we get states with non zero orbital angular momenta. As it was said before the spectra of low lying baryons are well known however in case of excitation spectra the situation is different. Quark model predict more states that are really observed. This is so-called *missing states* problem, which appears, for example, also on the lattice QCD calculations which will be described in the next section.

Different models were developed to decrease the number of predicted states. For example, quark-diquark model where two quarks are clustering into a diquark allows to decrease the number of degrees of freedom and therefore number of predicted states. But this number of states is still more than experimentally observed ones.

Most of the information about excited baryons came from  $\pi N$  scattering. But some excited states can be weakly coupled to  $\pi N$  channel. However a lot of new experiments on meson photoproduction was made by many experimental groups over the world. This gives us an opportunity to get information about excited baryons coupled to many different two- and three-body final states. To extract this information is a very important task of partial wave analysis.

## 2.2 Lattice QCD calculations

Theoretical calculations of hadron properties based on QCD principles is a difficult task which includes nonperturbative approaches. Such a method is lattice QCD [33] which needs a big computational power and effective calculation methods.

An example of lattice results is shown on Fig. 2.1 where the resonance spectrum of nucleons and Deltas is presented. with  $m_\pi = 396$  MeV.

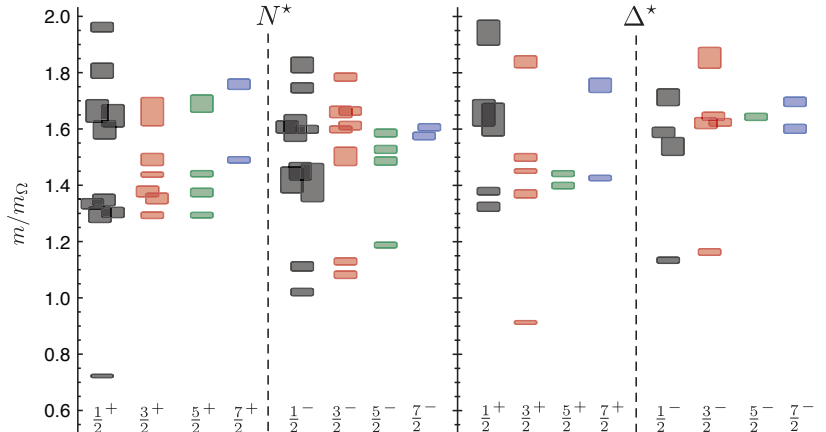


Figure 2.1: The nucleon excitation spectrum from lattice gauge calculations [34].  $J^P$  notation is used for identifying excitation states.

One can see how good  $\Delta(1232) 3/2^+$  is reproduced. However not all states presented here were found in PWA. This is the already introduced problem of *missing states*. Which can be solved by analyzing the photoproduction spectrum. One can then decide whether the resonances couple weakly to  $\pi N$  or if the lattice calculations, when using large masses, do not pick up the correct degrees of freedom adapted to baryon resonances.





## Chapter 3

---

# General formalism of $\eta$ meson photoproduction on proton

---

In this chapter the formalism of  $\eta$  meson photoproduction is presented. The following quantities are introduced: Mandelstam variables, invariant amplitudes, CGLN amplitudes and multipoles. The notation for resonances and their relation with multipoles will be explained. Differential cross section and polarization observables are discussed. The part on the observables is based on the common work of our group and colleagues from Tuzla and Zagreb, see [35].

The notations for the variables introduced here will be kept and used in further chapters.

### 3.1 Kinematics

Let us first define the kinematics of a process, consider the reaction:

$$\gamma(k^\mu) + p(p_i^\mu) \rightarrow \eta(q^\mu) + p(p_f^\mu), \quad (3.1)$$

variables in brackets denote the 4-momenta of the participating particles. The 4-momentum of the photon is denoted as  $p_\gamma^\mu = k^\mu = (E_\gamma, \mathbf{k})$ . The 4-momenta of target and recoil protons are denoted as  $p_i^\mu = (E_i, \mathbf{p}_i)$  and  $p_f^\mu = (E_f, \mathbf{p}_f)$  respectively. The subscripts  $i$  and  $f$  stays for initial and final states. The 4-momentum of the  $\eta$  meson is denoted as  $p_\eta^\mu = q^\mu = (\omega, \mathbf{q})$ . The 4-momentum conservation holds for the reaction

$$k^\mu + p_i^\mu = q^\mu + p_f^\mu. \quad (3.2)$$

The reaction can be described by the three Mandelstam variables [36]  $s$ ,  $t$  and  $u$ . They are:

$$s = (p_i^\mu + k^\mu)^2 = (q^\mu + p_f^\mu)^2, \quad t = (q^\mu - k^\mu)^2 = (p_f^\mu - p_i^\mu)^2, \quad u = (p_i^\mu - q^\mu)^2 = (p_i^\mu - p_f^\mu)^2, \quad (3.3)$$

the sum of them is equal to the sum of squares of the external masses

$$s + t + u = 2m_p^2 + m_\eta^2. \quad (3.4)$$

Up to now the described physical quantities are independent from the reference frame. In order to describe the scattering process explicitly two reference frames are used. The laboratory (*lab*) frame, where the target nucleon is initially at rest, and the center of mass frame (*c.m.*). Both *lab* and *c.m.* coordinates can be transformed in each other by use of Lorentz transformations.

Below the graphical representation of these two frames is shown:

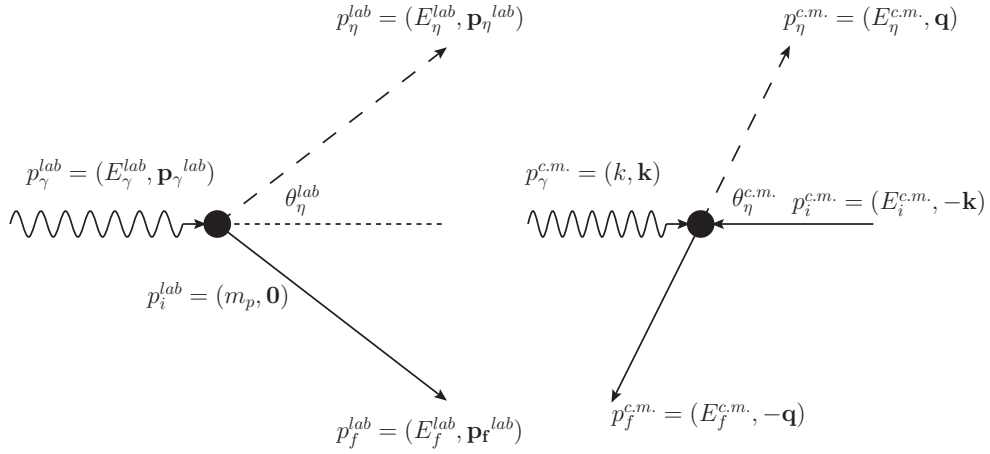


Figure 3.1: Kinematics of  $\eta$  photoproduction in both laboratory and center of mass frames.

Kinematical quantities can be written in both frames, for example the total energy written in terms photon *lab* energy looks like

$$W = \sqrt{s} = \sqrt{m_p(m_p + 2E_\gamma^{lab})}. \quad (3.5)$$

The photon laboratory energy therefore

$$E_\gamma^{lab} = \frac{W^2 - m_p^2}{2m_p}. \quad (3.6)$$

Now, let us go into the *c.m.* frame. Thus one gets the following quantities for the 4-momenta of participating particles

$$\begin{aligned} p_i^\mu &= (E_i, -\mathbf{k}), & p_f^\mu &= (E_f, -\mathbf{q}), \\ k^\mu &= (k, \mathbf{k}), & q^\mu &= (\omega, \mathbf{q}), \end{aligned} \quad (3.7)$$

note that the subscript *c.m.* is now dropped.

$$\begin{aligned} k &= |\mathbf{k}| = \frac{W^2 - m_p^2}{2W}, & \omega &= \frac{W^2 + m_\eta^2 - m_p^2}{2W}, \\ q &= |\mathbf{q}| = \left[ \left( \frac{W^2 + m_\eta^2 - m_p^2}{2W} \right)^2 - m_\eta^2 \right]^{1/2}, \\ E_i &= W - k = \frac{W^2 + m_p^2}{2W}, \\ E_f &= W - \omega = \frac{W^2 + m_p^2 - m_\eta^2}{2W}, \end{aligned} \quad (3.8)$$

The formula below gives the relation for the cosine of the scattering angle in *c.m.* frame

$$\cos \theta = \frac{t - m_\eta^2 + 2k\omega}{2kq}. \quad (3.9)$$

The face-space-factor is given by

$$\rho = \frac{q}{k}. \quad (3.10)$$

In order to determine the kinematical limits of our reaction the Mandelstam plane [37] as a function of 2 variables  $\nu$ , and  $t$  can be drawn. Where  $\nu$  is so-called crossing symmetrical variable  $\nu$  which is expressed by

$$\nu = \frac{s - u}{4m_p}, \quad (3.11)$$

$$\nu = E_\gamma^{lab} + \frac{t - m_\eta}{4m_p}. \quad (3.12)$$

Now using  $t$  and  $\nu$  we draw the Mandelstam plane [37] that shows the physical region for our reaction and three production thresholds:

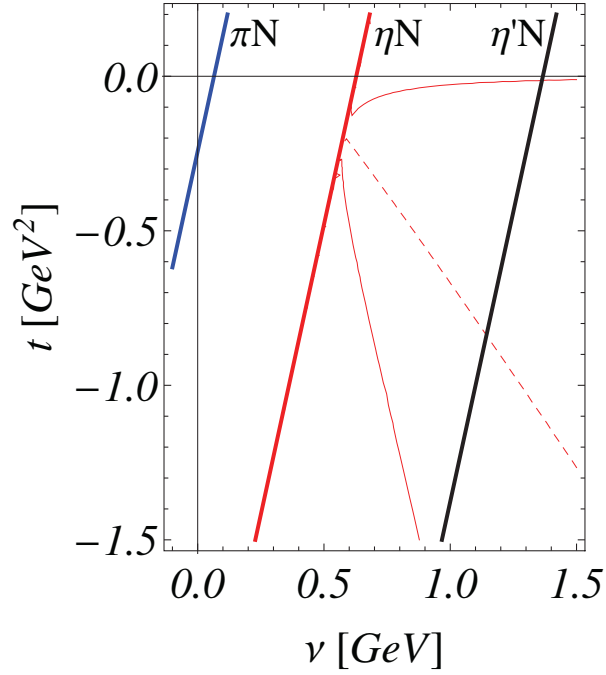


Figure 3.2: The Mandelstam plane for  $\gamma p \rightarrow \eta p$ . The red solid curves are the boundaries of the physical region from  $\theta = 0$  to  $\theta = 180^\circ$ . The red dashed line shows  $\theta = 90^\circ$ . The inclined vertical lines from left to right denote the thresholds for  $\pi N$ ,  $\eta N$ ,  $\eta' N$  production respectively.

### 3.2 Cross section and polarization observables

Experiments with three types of polarization can be performed in  $\eta$  photoproduction: photon beam polarization, polarization of the target nucleon and polarization of the recoil nucleon. Target polarization will be described in the frame  $\{x, y, z\}$  in Fig. 3.3, with the  $z$ -axis pointing into the direction of the photon momentum  $\hat{\mathbf{k}}$ , the  $y$ -axis perpendicular to the reaction plane,  $\hat{\mathbf{y}} = \hat{\mathbf{k}} \times \hat{\mathbf{q}} / \sin \theta$ , and the  $x$ -axis given by  $\hat{\mathbf{x}} = \hat{\mathbf{y}} \times \hat{\mathbf{z}}$ . For recoil polarization the frame  $\{x', y', z'\}$  is used, with the  $z'$ -axis defined by the momentum vector of the outgoing meson  $\hat{\mathbf{q}}$ , the  $y'$ -axis as for target polarization and the  $x'$ -axis given by  $\hat{\mathbf{x}}' = \hat{\mathbf{y}}' \times \hat{\mathbf{z}}'$ .

The photon polarization can be linear or circular. For a linear photon polarization ( $P_T = 1$ ) in the reaction plane  $\hat{\mathbf{x}}$  we get  $\varphi = 0$  and perpendicular, in direction  $\hat{\mathbf{y}}$ , the polarization angle is  $\varphi = \pi/2$ . For right-handed circular polarization  $P_\odot = +1$ .

Here the hat notation is used to define the unit vector.

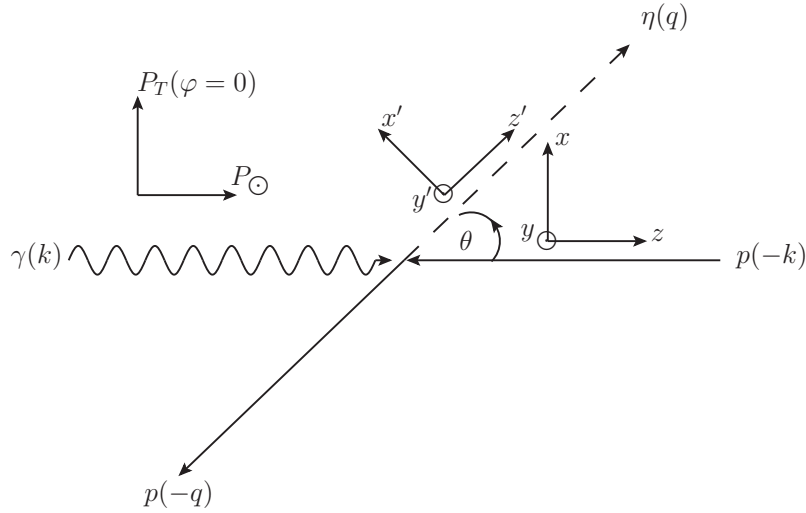


Figure 3.3: Kinematics of photoproduction and frames for polarization. The frame  $\{x, y, z\}$  is used for target polarization  $\{P_x, P_y, P_z\}$ , whereas the recoil polarization  $\{P_{x'}, P_{y'}, P_{z'}\}$  is defined in the frame  $\{x', y', z'\}$ , which is rotated around  $y' = y$  by the polar angle  $\theta$ .  $\varphi$  is the azimuthal angle of the photon polarization vector in respect to the reaction plane  $\{x, y\}$  and is zero in the projection shown in the figure.

One can classify the differential cross sections by the three classes of double polarization experiments and one class of triple polarization experiments:

- polarized photons (linearly or circularly) and polarized target (transverse or longitudinally)

$$\begin{aligned}
 \frac{d\sigma}{d\Omega}(E_\gamma, \theta) = & \sigma_0 \{1 - P_T \Sigma(E_\gamma, \theta) \cos 2\varphi \\
 & + P_x (-P_T H(E_\gamma, \theta) \sin 2\varphi + P_\odot F(E_\gamma, \theta)) \\
 & + P_y (T(E_\gamma, \theta) - P_T P(E_\gamma, \theta) \cos 2\varphi) \\
 & + P_z (P_T G(E_\gamma, \theta) \sin 2\varphi - P_\odot E(E_\gamma, \theta))\} , \quad (3.13)
 \end{aligned}$$

- polarized photons (linearly or circularly) and recoil polarization

$$\begin{aligned}
 \frac{d\sigma}{d\Omega}(E_\gamma, \theta) = & \sigma_0 \{1 - P_T \Sigma(E_\gamma, \theta) \cos 2\varphi \\
 & + P_{x'} (-P_T O_{x'}(E_\gamma, \theta) \sin 2\varphi - P_\odot C_{x'}(E_\gamma, \theta)) \\
 & + P_{y'} (P(E_\gamma, \theta) - P_T T(E_\gamma, \theta) \cos 2\varphi) \\
 & + P_{z'} (-P_T O_{z'}(E_\gamma, \theta) \sin 2\varphi - P_\odot C_{z'}(E_\gamma, \theta))\} , \quad (3.14)
 \end{aligned}$$

- polarized target (transverse or longitudinally) and recoil polarization

$$\begin{aligned}
 \frac{d\sigma}{d\Omega}(E_\gamma, \theta) = & \sigma_0 \{1 + P_y T(E_\gamma, \theta) + P_{y'} P(E_\gamma, \theta) + P_{x'} (P_x T_{x'}(E_\gamma, \theta) - P_z L_{x'}(E_\gamma, \theta)) \\
 & + P_{y'} P_y \Sigma(E_\gamma, \theta) + P_{z'} (P_x T_{z'}(E_\gamma, \theta) + P_z L_{z'}(E_\gamma, \theta))\} . \quad (3.15)
 \end{aligned}$$

In these equations  $\sigma_0$  denotes the unpolarized differential cross section. The transverse degree of photon polarization is denoted by  $P_T$ . The right-handed circular photon polarization is denoted as  $P_\odot$ .

### 3.3 Invariant and CGLN amplitudes

According to the paper of Berends [38] the most general Lorentz covariant pseudo-four-vector for the nucleon electromagnetic current can be expressed in terms of the eight matrix elements.

By having two photon polarization states, two initial proton target spin states and finally two proton recoil spin states we obtain eight matrix elements of the electromagnetic current and thus eight invariant amplitudes.

In the case of  $\eta$  photoproduction the set of eight amplitudes is reduced to the set of four amplitudes by applying the parity conservation. Thus the electromagnetic current takes the form [39]:

$$J_{\eta p}^\mu = \sum_{i=1}^4 A_i(\nu, t) M_i^\mu . \quad (3.16)$$

The complex functions

$$A_1(\nu, t), A_2(\nu, t), A_3(\nu, t), A_4(\nu, t), \quad (3.17)$$

are called invariant photoproduction amplitudes and carry kinematical dependencies.

Invariant amplitudes have definite crossing symmetry. For  $\eta$  photoproduction, the amplitudes  $A_{1,2,4}(\nu, t)$  are crossing even, i.e.  $A_{1,2,4}(-\nu, t) = A_{1,2,4}^*(\nu, t)$ . The amplitude  $A_3(\nu, t)$  is crossing odd, i.e.  $A_3(-\nu, t) = -A_3^*(\nu, t)$ .

The operators  $M_i$  are gauge-invariant four-vectors and were written by Chew, Goldberger, Low and Nambu (CGLN) [39]. They have the following form:

$$\begin{aligned}
 M_1^\mu &= -\frac{1}{2} i \gamma_5 (\gamma^\mu \not{k} - \not{k} \gamma^\mu) , \\
 M_2^\mu &= 2i \gamma_5 \left( P^\mu k \cdot (q - \frac{1}{2} k) - (q - \frac{1}{2} k)^\mu k \cdot P \right) , \\
 M_3^\mu &= -i \gamma_5 (\gamma^\mu k \cdot q - \not{k} q^\mu) , \\
 M_4^\mu &= -2i \gamma_5 (\gamma^\mu k \cdot P - \not{k} P^\mu) - 2M_N M_1^\mu , \quad (3.18)
 \end{aligned}$$

here  $\not{k} = k_\mu \gamma^\mu$ , for  $P^\mu$  the following convention is used  $P^\mu = (p_i^\mu + p_f^\mu)/2$  and the gamma matrices are defined as in Ref. [40].

The transition matrix element of the electromagnetic current has the form:

$$\epsilon_\mu J_{\eta p}^\mu = \bar{u}(p_f) \sum_{i=1}^4 A_i \epsilon_\mu M_i^\mu u(p_i) = -\frac{4\pi W}{m_p} \chi_f^\dagger \mathcal{F} \chi_i, \quad (3.19)$$

here  $u(p)$  is the Dirac spinor of the proton carrying information of the spin states of the baryon,  $\bar{u}(p)u(p) = 2m_p$ , and  $\chi$  the Pauli spinor of the nucleon.

The operator  $\mathcal{F}$  can be decomposed in *c.m.* frame into four complex variables  $F_i$  which are called CGLN amplitudes,

$$\begin{aligned} \mathcal{F} &= -\epsilon_\mu J_{\eta p}^\mu \\ &= i(\vec{\sigma} \cdot \hat{\epsilon}) F_1 + (\vec{\sigma} \cdot \hat{q})(\vec{\sigma} \times \hat{k}) \cdot \hat{\epsilon} F_2 + i(\hat{\epsilon} \cdot \hat{q})(\vec{\sigma} \cdot \hat{k}) F_3 + i(\hat{\epsilon} \cdot \hat{q})(\vec{\sigma} \cdot \hat{q}) F_4, \end{aligned} \quad (3.20)$$

where  $\epsilon^\mu = (\epsilon_0, \vec{\epsilon})$  and  $\vec{\epsilon} \cdot \vec{k} = 0$ . and  $\vec{\sigma}$  is the Pauli spin operator which has the following matrix form:

$$\sigma_1 = \begin{pmatrix} 0 & 1 \\ 1 & 0 \end{pmatrix}, \quad \sigma_2 = \begin{pmatrix} 0 & -i \\ i & 0 \end{pmatrix}, \quad \sigma_3 = \begin{pmatrix} 1 & 0 \\ 0 & -1 \end{pmatrix}. \quad (3.21)$$

These amplitudes have energy and angular dependence:

$$F_1(W, x), \quad F_2(W, x), \quad F_3(W, x), \quad F_4(W, x), \quad (3.22)$$

where  $W$  is the total energy and  $x = \cos \theta$ . As we can see from Eq. (3.19) CGLN and invariant amplitudes are related to each other by a linear transformation.

CGLN amplitudes can be decomposed in terms of partial waves (multipoles) and Legendre polynomials and their derivatives [41], the relations between them we show below.

$$\begin{aligned} F_1(W, x) &= \sum_{\ell=0}^{\infty} [(\ell M_{\ell+} + E_{\ell+}) P'_{\ell+1}(x) + ((\ell+1) M_{\ell-} + E_{\ell-}) P'_{\ell-1}(x)], \\ F_2(W, x) &= \sum_{\ell=1}^{\infty} [(\ell+1) M_{\ell+} + \ell M_{\ell-}] P'_\ell(x), \\ F_3(W, x) &= \sum_{\ell=1}^{\infty} [(E_{\ell+} - M_{\ell+}) P''_{\ell+1}(x) + (E_{\ell-} + M_{\ell-}) P''_{\ell-1}(x)], \\ F_4(W, x) &= \sum_{\ell=2}^{\infty} [M_{\ell+} - E_{\ell+} - M_{\ell-} - E_{\ell-}] P''_\ell(x). \end{aligned} \quad (3.23)$$

where  $x = \cos \theta$  is the already introduced cosine of the scattering angle,  $\ell$  is an orbital angular momentum of the  $\eta N$  system,  $P_\ell(x)$  and  $P'_\ell(x)$ ,  $P''_\ell(x)$  are Legendre polynomials and their derivatives.

Factors  $E_{\ell\pm}(W)$  and  $M_{\ell\pm}(W)$  in the expansion are complex numbers and are called multipoles. Multipoles are energy dependent functions that can be of two types: electric ( $E$ ) and magnetic ( $M$ ). A certain terminology has been adopted for distinguishing of these types. A photon having total angular momentum  $J_\gamma$  and parity  $P_\gamma = (-1)^{J_\gamma}$  is called electric dipole photon or  $Ej$  photon, a photon having parity  $P_\gamma = (-1)^{J_\gamma+1}$  is called magnetic dipole or  $Mj$  photon [42]. The labels  $+$  or  $-$  on multipoles denote the angular momentum addition.

Another important conserved quantity that has not been discussed up to now is an isospin ( $I$ ). Isospin is an internal quantum number which determines the number of charge states of hadrons. Isospin is conserved in strong interactions and is not conserved in weak and electromagnetic interactions.

### 3.4 Nucleon resonances in $\eta$ photoproduction

The multipoles  $E_{\ell\pm}(W)$  and  $M_{\ell\pm}(W)$  that were discussed in the previous section are partial wave amplitudes of photoproduction and contain contributions from  $s$ -,  $t$ - and  $u$ -channel processes. The biggest contributions in the low energy region come from the  $s$ -channel exchanges (resonances). In PDG [31] one can find the discussion about resonance spectrum of photoproduction on proton. The notation scheme is also given there. Here we will discuss some important aspects from the review and show connection between resonances and multipoles.

In the  $s$ -channel we can observe different types of baryons, e.g.  $N$  baryons,  $\Delta$  baryons,  $\Lambda$  baryons etc. These types are related to the different quantum numbers of the intermediate states: isospin ( $I$ ) and strangeness ( $S$ ). For example in photoproduction reactions on a proton, which has an  $I = 1/2$ , one can only have  $N$  (nucleon) resonances with  $I = 1/2$  or  $\Delta$  resonances with  $I = 3/2$ . Then in order to distinguish between the resonances of the same type a notation  $J^P$  is used, where  $J$  is the total angular momentum and  $P$  is parity.

In our case of  $\gamma p \rightarrow \eta p$  reaction we observe only nucleon resonances in the  $s$ -channel, because  $\eta$  meson has an isospin  $I = 0$ . The next step is to define the possible values of  $J$  for resonances. The produced  $\eta$  meson is a pseudoscalar therefore it is  $IJ^P = 00^-$ , the recoil proton is  $IJ^P = \frac{1}{2}\frac{1}{2}^+$ . Eta-meson and a proton can have an orbital angular momentum  $\ell$ , thus the total angular momentum  $J$  can have values  $J = \ell \pm 1/2$  and parity  $P = P_\eta P_p (-1)^\ell = -(-1)^\ell$ . Below a diagram that describes the  $s$ -channel process is drawn:

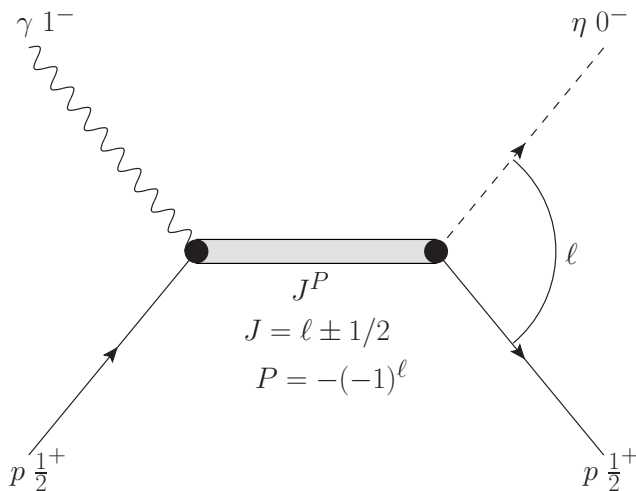


Figure 3.4: A schematic description of the  $s$ -channel process. Here the notation  $J^P$  for the participating particles is used.  $J$  is the total angular momentum,  $P$  is a parity.  $\ell$  denotes the orbital angular momentum of the  $\eta N$  system. Double line indicates  $s$ -channel intermediate state (resonance).  $I$  isospin quantum number are omitted on this picture.

The general rules for quantum numbers of a  $2 \rightarrow 2$  processes are given below.

$$I_1^{G_1} J_1^{P_1 C_1} + I_2^{G_2} J_2^{P_2 C_2} \rightarrow I^G J^{PC} \rightarrow I_1'^{G_1'} J_1'^{P_1' C_1'} + I_2'^{G_2'} J_2'^{P_2' C_2'}. \quad (3.24)$$

$$\begin{aligned}
 G &= G_1 G_2 & G &= G'_1 G'_2 \\
 P &= P_1 P_2 (-1)^\ell & P &= P'_1 P'_2 (-1)^{\ell'} \\
 |I_1 - I_2| &< I < I_1 + I_2 & |I'_1 - I'_2| &< I < I'_1 + I'_2 \\
 |J_1 - J_2| &< S < J_1 + J_2 & |J'_1 - J'_2| &< S' < J'_1 + J'_2 \\
 |S - \ell| &< J < S + \ell & |S' - \ell'| &< J < S' + \ell'
 \end{aligned} \tag{3.25}$$

where  $I$  is an isospin,  $G$  denotes  $G$ -parity,  $J$  is the total angular momentum,  $P$  is parity,  $C$  is  $C$ -parity,  $S$  is a spin of a particle.

Let us now consider the resonance spectrum of nucleon resonances. Below the table, taken from PDG, shows the resonances and their PDG rating that were used in the present data analysis:

Table 3.1: Resonances used in the data analysis shown along with the PDG star rating.

Resonance	Overall rating	$N\gamma$ rating	$N\eta$ rating
$N(1440) 1/2^+$	****	****	
$N(1520) 3/2^-$	****	****	***
$N(1535) 1/2^-$	****	****	****
$N(1650) 1/2^-$	****	****	***
$N(1675) 5/2^-$	****	****	*
$N(1680) 5/2^+$	****	****	*
$N(1700) 3/2^-$	***	***	*
$N(1710) 1/2^+$	****	****	***
$N(1720) 3/2^+$	****	****	***
$N(1860) 5/2^+$	**		
$N(1875) 3/2^-$	***	***	
$N(1880) 1/2^+$	**	*	
$N(1895) 1/2^-$	**	*	**
$N(1900) 3/2^+$	***	**	**

\*\*\*\* Existence is certain, and properties are at least fairly well explored

\*\*\* Existence is very likely but further confirmation of decay modes is required.

\*\* Evidence of existence is only fair.

\* Evidence of existence is poor.



The presented above resonances are related to the multipoles that were discussed in the previous section. In the Tab. 3.2 we show these resonances along with their quantum numbers and the related multipoles.

Table 3.2: Resonances in used in the analysis and related multipoles.

Resonance	$\ell$	$J$	$P$	Multipole
$N(1535) 1/2^-$	0	1/2	-	$E_{0+}$
$N(1650) 1/2^-$	0	1/2	-	$E_{0+}$
$N(1895) 1/2^-$	0	1/2	-	$E_{0+}$
$N(1440) 1/2^+$	1	1/2	+	$M_{1-}$
$N(1710) 1/2^+$	1	1/2	+	$M_{1-}$
$N(1880) 1/2^+$	1	1/2	+	$M_{1-}$
$N(1720) 3/2^+$	1	3/2	+	$E_{1+}, M_{1+}$
$N(1900) 3/2^+$	1	3/2	+	$E_{1+}, M_{1+}$
$N(1520) 3/2^-$	2	3/2	-	$E_{2-}, M_{2-}$
$N(1700) 3/2^-$	2	3/2	-	$E_{2-}, M_{2-}$
$N(1875) 3/2^-$	2	3/2	-	$E_{2-}, M_{2-}$
$N(1675) 5/2^-$	2	5/2	-	$E_{2+}, M_{2+}$
$N(1680) 5/2^+$	3	5/2	+	$E_{3-}, M_{3-}$
$N(1860) 5/2^+$	3	5/2	+	$E_{3-}, M_{3-}$

Let us discuss the relations between the notations of the multipoles and resonances. We consider the  $N(1535) 1/2^-$  resonance and the related  $E_{0+}$  multipole as an example.

First let us describe the subscript  $0+$ . This resonance appears is the  $S$ -wave of the  $\eta N$  system, therefore it has orbital angular momentum  $\ell = 0$ . Then according to the quantum mechanical rules the total orbital angular momentum is obtained  $J = 0 + 1/2$ . By putting these two things together we get the subscript  $0+$ .

The explanation why this resonance has only electric multipole is a bit more complicated. As it was written before there are two types of multipoles: electric and magnetic. In order to distinguish between them we can use parity conservation arguments and write down the selection rules [41]:

$$Ej : (-1)^{J_\gamma} = P = (-1)^{\ell+1} \Rightarrow |J_\gamma - \ell| = 1, \quad (3.26)$$

$$Mj : (-1)^{J_\gamma+1} = P = (-1)^{\ell+1} \Rightarrow J_\gamma = 1. \quad (3.27)$$

Now let us have a look on  $\gamma p \rightarrow N(1535) 1/2^-$  process under a different angle. Suppose that we have  $\gamma \rightarrow p + N(1535) 1/2^-$ . Photon has an total angular momentum and parity  $J_\gamma^-$  that we can get as a sum of  $J_{Res} = 1/2^-$  and  $J_p = 1/2^+$ , following the quantum mechanical rules we get  $J_\gamma = 1^-$ . We also know that photon has a spin  $S = 1$  therefore  $S = J_\gamma \pm L_\gamma$ . In order to obtain this value and to conserve the parity the orbital angular momentum of the photon must be  $L_\gamma = 0$ . Taking into account Eq. (3.27) we get  $L_\gamma = J_\gamma - 1$  which means that the multipole is electric.

The same procedure we can apply for other resonances and one can see that for  $1/2^+$  intermediate states only  $M_{1+}$  multipole is physical. For states with higher total angular momentum  $J$  both multipoles are present.



## Chapter 4

---

### Partial wave content of polarization observables

---

Before we perform a partial wave analysis, the sensitivity of experimental data to high partial waves can be discussed. The so-called partial wave content of polarization observables can be investigated. In this chapter such a procedure is done for the data on the  $\gamma p \rightarrow \eta p$  reaction. The errors of the data are discussed as well. The analysis of the data is performed using the Legendre expansion of polarization observables which provides qualitative results on their partial wave content.

#### 4.1 Description of the data using Legendre polynomials

Legendre polynomials are an orthogonal set of functions in the range  $[-1,1]$ . Below the formalism is briefly shown and an example is given.

Table 4.1 shows all available data, the energy and angular coverage, the number of angular bins of fitted observables and whether the data are used in the partial wave analysis.

Table 4.1: Observables in  $\eta$  photoproduction

$\gamma p \rightarrow \eta p$	Observable	Energy range (MeV)	$\cos(\theta)$	Number of angles	Used in the analysis
[43] MAMI-C	$d\sigma/d\Omega$	1488-1870	[-0.958,0.958]	24	—
[44] MAMI	$d\sigma/d\Omega$	1488-1956	[-0.958,0.958]	24	+
[45] CBELSA/TAPS	$d\sigma/d\Omega$	1588-2370	[-0.95,0.95]	20	—
[46] CLAS	$d\sigma/d\Omega$	1685-2895	[-0.85,0.85]	18	—
[47] GRAAL	$\Sigma$	1490-1910	[-0.95,0.84]	10	+
[48] GRAAL	$\Sigma$	1506-1688	[-0.8,-0.8]	9	—
[49] A2 MAMI	$T$	1495-1850	[-0.916,0.916]	12	+
[49] A2 MAMI	$F$	1495-1850	[-0.916,0.916]	12	+
[50] CLAS	$E$	1525-2125	[-0.9,0.7]	8	+

All observables can be expanded in Legendre series. For getting compact formulas, associated Legendre polynomials  $\{P_\ell^0(x), P_\ell^1(x), P_\ell^2(x)\}$  are used. They have the form:

$$\begin{aligned}
 P_\ell^0(x) &= P_\ell(x), \\
 P_\ell^1(x) &= -\sqrt{1-x^2} P_\ell'(x), \\
 P_\ell^2(x) &= (1-x^2) P_\ell''(x),
 \end{aligned}
 \tag{4.1}$$

where  $P_\ell'(x)$ ,  $P_\ell''(x)$  are first and second derivatives of Legendre polynomials over  $x$ . Using

these notations one can rewrite expressions for the observables in the following form

$$\begin{aligned}
 O_i(W, x) &= \sum_{k=0}^{2\ell_{max}} A_k^i(W) P_k^0(x), \text{ for } O_i = \{d\sigma/d\Omega, \hat{E}\}, \\
 O_i(W, x) &= \sum_{k=1}^{2\ell_{max}} A_k^i(W) P_k^1(x), \text{ for } O_i = \{\hat{T}, \hat{P}, \hat{F}, \hat{H}\}, \\
 O_i(W, x) &= \sum_{k=2}^{2\ell_{max}} A_k^i(W) P_k^2(x), \text{ for } O_i = \{\hat{\Sigma}, \hat{G}\},
 \end{aligned} \tag{4.2}$$

here  $O_i(W, x)$  is the general notation for an observable.  $W$  is the total energy,  $\ell_{max}$  is the highest angular momentum up to which the series is truncated.

For all double polarization observables that include recoil polarization, the summation runs up to  $2\ell_{max} + 1$ , one term higher than for the other observables

$$\begin{aligned}
 O_i(W, \theta) &= \sum_{k=0}^{2\ell_{max}+1} A_k^i(W) P_k^0(\cos\theta), \text{ for } O_i = \{\hat{C}_{z'}, \hat{L}_{z'}\}, \\
 O_i(W, \theta) &= \sum_{k=1}^{2\ell_{max}+1} A_k^i(W) P_k^1(\cos\theta), \text{ for } O_i = \{\hat{C}_{x'}, \hat{O}_{x'}, \hat{L}_{x'}, \hat{T}_{z'}\}, \\
 O_i(W, \theta) &= \sum_{k=2}^{2\ell_{max}+1} A_k^i(W) P_k^2(\cos\theta), \text{ for } O_i = \{\hat{O}_{z'}, \hat{T}_{x'}\}.
 \end{aligned} \tag{4.3}$$

It was shown that CGLN amplitudes can be expressed as infinite series in terms of multipoles, Legendre polynomials and their derivatives Eq. (3.23). In the Legendre analysis one has to truncate the series at some  $\ell_{max}$  which gives information about the highest orbital angular momentum. For the CGLN amplitudes  $F_i(W, x)$  we therefore obtain the following set of equations

$$\begin{aligned}
 F_1(W, x) &= \sum_{\ell=0}^{\ell_{max}} [(\ell M_{\ell+} + E_{\ell+}) P'_{\ell+1}(x) + ((\ell + 1) M_{\ell-} + E_{\ell-}) P'_{\ell-1}(x)], \\
 F_2(W, x) &= \sum_{\ell=1}^{\ell_{max}} [(\ell + 1) M_{\ell+} + \ell M_{\ell-}] P'_\ell(x), \\
 F_3(W, x) &= \sum_{\ell=1}^{\ell_{max}} [(E_{\ell+} - M_{\ell+}) P''_{\ell+1}(x) + (E_{\ell-} + M_{\ell-}) P''_{\ell-1}(x)], \\
 F_4(W, x) &= \sum_{\ell=2}^{\ell_{max}} [M_{\ell+} - E_{\ell+} - M_{\ell-} - E_{\ell-}] P''_\ell(x).
 \end{aligned} \tag{4.4}$$

In the work of Fasano and Tabakin [41] it was shown that the experimental observables can be expressed in terms of CGLN amplitudes. Let us consider examples of the differential cross section and target asymmetry and determine the partial wave content of them.

Assuming the highest orbital angular momentum  $\ell_{max} = 1$  for the differential cross section ( $d\sigma/d\Omega$ ) the expression has the following form

$$d\sigma/d\Omega = \text{Re} \{ F_1^* F_1 + F_2^* F_2 + (1 - x^2) (F_3^* F_3/2 + F_2^* F_3) - 2x F_1^* F_2 \}. \tag{4.5}$$

Substituting the expansion from Eq. (4.4) one gets the result:

$$\begin{aligned}
 d\sigma/d\Omega &= \operatorname{Re} \left\{ |E_{0+}|^2 + \frac{9}{2}|E_{1+}|^2 + |M_{1-}|^2 + \frac{5}{2}|M_{1+}|^2 + M_{1-}^*(3E_{1+} + M_{1+}) \right. \\
 &\quad \left. - 3E_{1+}^*M_{1+} + x[2E_{0+}^*(3E_{1+} + M_{1+}) - 2E_{0+}^*M_{1-}] \right. \\
 &\quad \left. + x^2 \left[ \frac{9}{2}|E_{1+}|^2 - \frac{3}{2}|M_{1+}|^2 - 3M_{1-}^*(3E_{1+} + M_{1+}) + 9E_{1+}^*M_{1+} \right] \right\}. \quad (4.6)
 \end{aligned}$$

Using the expansion for observables Eq. (4.2) one can write the following expression

$$d\sigma/d\Omega = \sum_{k=0}^2 A_k^{\sigma_0}(W) P_k^0(x), \quad (4.7)$$

where

$$\begin{aligned}
 A_0^{d\sigma/d\Omega}(W) &= \operatorname{Re} \left\{ |E_{0+}|^2 + \frac{9}{2}|E_{1+}|^2 + |M_{1-}|^2 + \frac{5}{2}|M_{1+}|^2 + M_{1-}^*(3E_{1+} + M_{1+}) - 3E_{1+}^*M_{1+} \right\}, \\
 A_1^{d\sigma/d\Omega}(W) &= \operatorname{Im} \left\{ 2E_{0+}^*(3E_{1+} + M_{1+}) - 2E_{0+}^*M_{1-} \right\}, \\
 A_2^{d\sigma/d\Omega}(W) &= \operatorname{Im} \left\{ \frac{9}{2}|E_{1+}|^2 - \frac{3}{2}|M_{1+}|^2 - 3M_{1-}^*(3E_{1+} + M_{1+}) + 9E_{1+}^*M_{1+} \right\}, \quad (4.8)
 \end{aligned}$$

are Legendre coefficients containing the information about the partial wave content of the  $d\sigma/d\Omega$ .

Thus the lowest partial wave contribution to  $A_0^{d\sigma/d\Omega}$  comes from the modulus of  $S$ -waves  $|E_{0+}|^2$ , in  $A_1^{d\sigma/d\Omega}$  it comes from the interference of  $S$  and  $P$  waves  $2E_{0+}^*(3E_{1+} + M_{1+}) - 2E_{0+}^*M_{1-}$ , and for  $A_2^{d\sigma/d\Omega}$  it comes from the modulus of  $P$  waves:  $\frac{9}{2}|E_{1+}|^2$ .

For the target asymmetry  $\hat{T}$  one gets the following:

$$\hat{T} = \sqrt{1-x^2} \operatorname{Im} \{ F_1^* F_3 - x F_2^* F_3 \}, \quad (4.9)$$

$$\hat{T} = 3\sqrt{1-x^2} \operatorname{Im} \{ E_{0+}^*(E_{1+} - M_{1+}) - x[M_{1-}^*(E_{1+} - M_{1+}) - 4M_{1+}^*E_{1+}] \}. \quad (4.10)$$

Using the Eq. (4.2) we have

$$\hat{T} = \sum_{k=1}^2 A_k^{\hat{T}} P_k^1(x), \quad (4.11)$$

where Legendere coefficients have the following form

$$A_1^{\hat{T}} = 3\operatorname{Im} \{ E_{0+}^*(E_{1+} - M_{1+}) \}, \quad (4.12)$$

$$A_2^{\hat{T}} = 3\operatorname{Im} \{ M_{1-}^*(E_{1+} - M_{1+}) - 4M_{1+}^*E_{1+} \}. \quad (4.13)$$

Thus we get the interference of  $S$  and  $P$ -waves  $E_{0+}^*(E_{1+} - M_{1+})$  as the lowest partial wave contribution to  $A_1^{\hat{T}}$ . The lowest partial wave contribution to  $A_2^{\hat{T}}$  comes from the interference of  $P$ -waves:  $M_{1-}^*(E_{1+} - M_{1+}) - 4M_{1+}^*E_{1+}$ .

If we assume that partial waves with orbital angular momentum higher than  $\ell = 3$  do not appear in the reaction. One can write partial wave content of the Legendre coefficients in a more schematic way. The coefficients  $A_k^{d\sigma/d\Omega}(W)$  of Eq. 4.2 for the differential cross section have the following combinations of partial waves with different  $\ell = 0, 1, 2, 3$ , or in notations  $S, P, D, F$ :

$$\begin{aligned}
 A_0^{d\sigma/d\Omega} &= SS + PP + SD + DD + PF + FF \\
 A_1^{d\sigma/d\Omega} &= SP + PD + SF + DF \\
 A_2^{d\sigma/d\Omega} &= PP + SD + DD + PF + FF \\
 A_3^{d\sigma/d\Omega} &= PD + SF + DF \\
 A_4^{d\sigma/d\Omega} &= DD + PF + FF \\
 A_5^{d\sigma/d\Omega} &= DF \\
 A_6^{d\sigma/d\Omega} &= FF
 \end{aligned}$$

The first summand shows the lowest partial wave contribution which can be seen in the coefficient. For example  $A_0^{d\sigma/d\Omega}$  contains squares of all partial waves and the lowest combination of partial waves that could be observed is the modulus of  $S$ -waves, whereas  $A_6^{d\sigma/d\Omega}$  contains only modulus of  $F$ -waves.

## 4.2 Differential cross section, $d\sigma/d\Omega$

In this section, results of the analysis of Legendre coefficients on differential cross section data from MAMI [44] and CBELSA [45] are presented.

### 4.2.1 MAMI data

For these data two combined data sets are analyzed. The first data set (Run II) has 24 narrow angular bins for each of 113 energy bins in the range from  $W = 1488$  up to  $W = 1891$  MeV. The second one (Run III) has the same angular coverage and 12 energy bins which cover an energy range from  $W = 1887$  MeV up to  $W = 1956$  MeV. Such quality of the data allows us to obtain the information about partial wave content with good accuracy.

There is also another data set from MAMI [43] (Run I) which is not analyzed in present work because the analysis of this run was repeated in Run II [44] with an improved cluster algorithm that better separates electromagnetic showers which are partly overlapping in the calorimeters, and with finer angular binning which provides better sensitivity to higher order partial waves.

For the first data set (Run II) only  $\eta \rightarrow 3\pi_0$  decays were used in the analysis of  $\eta$  photoproduction. Therefore cross sections were obtained by identifying the  $\eta$  meson via its  $3\pi_0$  mode. For the second data set (Run III) both neutral decay modes ( $\eta \rightarrow \gamma\gamma$  and  $\eta \rightarrow 3\pi_0$ ) were analyzed.

The statistical uncertainties come from the number of events in  $(E_\gamma, \cos\theta)$ . The overall systematic uncertainty due to the calculation of the detection efficiency and the photon-beam flux was estimated as 4% and 5% for Run II and III respectively. An additional angular-dependent systematic uncertainty is calculated as well. It includes a combined effect caused by the angular resolution, background subtraction, and uncertainties in the angular dependence of the reconstruction efficiency. For the first data set this kind of additional systematic uncertainty was evaluated as 3%, and 5 % for the second one.

The angular-dependent systematic uncertainties were added in quadrature with the statistical uncertainties in order to combine the results obtained from the different decay modes.

In the Legendre analysis the systematic uncertainties are not taken into account.

Fits with  $\ell_{max} = 1, 2, 3, 4$  were done in order to test the sensitivity of data to  $P$ ,  $D$ ,  $F$  and  $G$  waves. Below the comparison of  $\chi^2$  distributions and data description are shown.

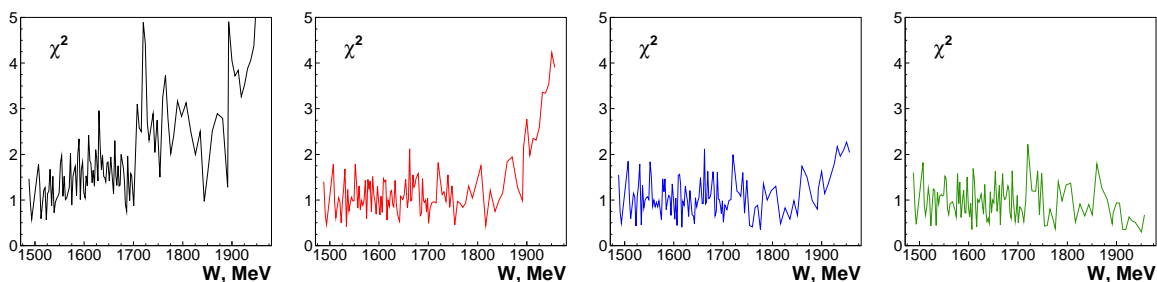


Figure 4.1:  $\chi^2$  distributions for the description of the differential cross section by the series of Legendre polynomials with the maximum  $\ell = 1$  (black),  $\ell = 2$  (red),  $\ell = 3$  (blue) and  $\ell = 4$  (green).

From the  $\chi^2$  plots it is clearly seen that the fit with  $\ell_{max} = 1$  poorly describes the data with the exception of energies below  $W = 1500$  MeV, where the differential cross section is almost flat, see Fig. 4.2.  $\chi^2$  distributions for  $\ell_{max} = 2, 3$  optically look almost identical at energies

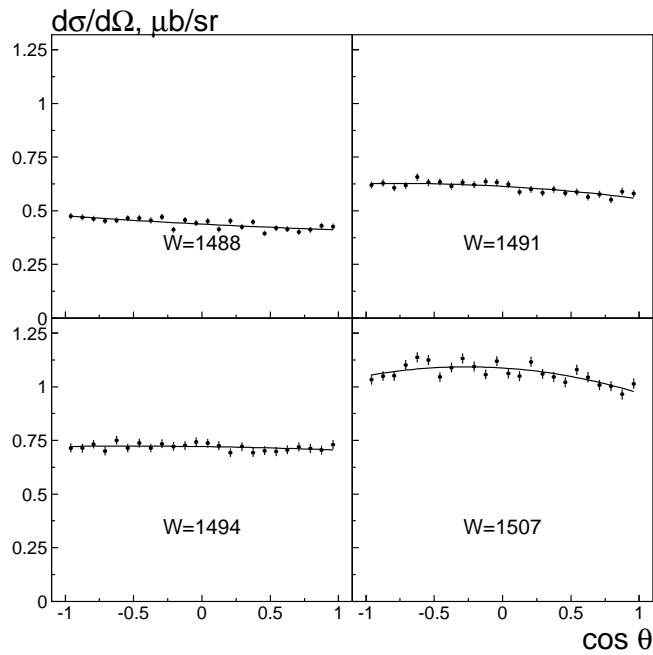


Figure 4.2: Description of the differential cross section by the series of Legendre polynomials with the maximum  $\ell = 1$  (black).

between  $W = 1500$  and  $W = 1800$  MeV, and the only difference which can be seen is at energies higher than  $W = 1800$  MeV.

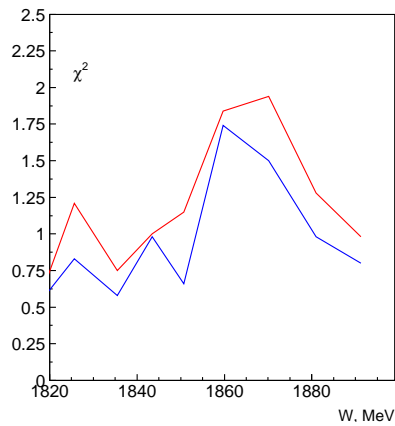


Figure 4.3:  $\chi^2$  distributions for the description of the differential cross section at high energies by the series of Legendre polynomials with the maximum  $\ell = 2$  (red) and  $\ell = 3$  (blue).

Which means that  $F$  waves start to contribute. To check this assumption one can see how the fits with  $\ell_{max} = 2, 3$  describe these data.



On the plot the hint is seen in the higher energy bins: the forward data point comes down together with the blue curve. Also this forward point cannot be explained as a statistical deviation. Further at higher energies one can observe the same behavior at forward angles.

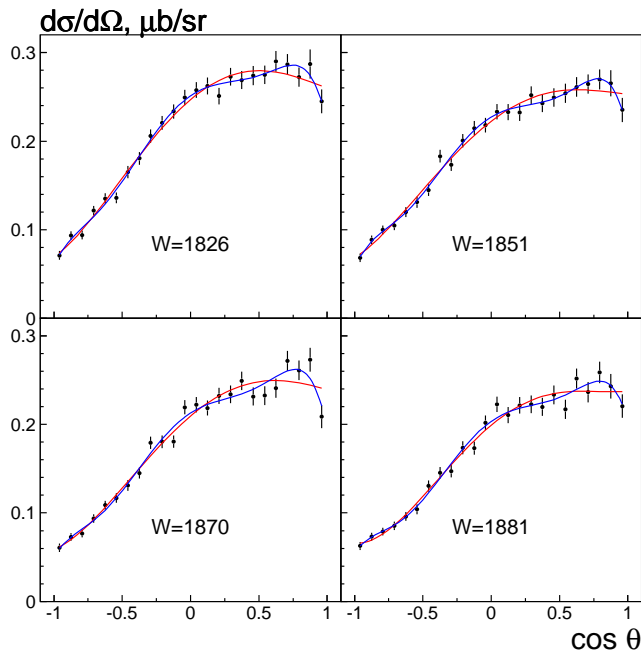


Figure 4.4: Description of the differential cross section by the series of Legendre polynomials with the maximum  $\ell = 2$  (red) and  $\ell = 3$  (blue).

From such a comparison it is seen that the fit with  $\ell_{max} = 3$  gives a better result, although the change in  $\chi^2$  is very small. To better solve this puzzle one needs to treat the data at higher energies and to make such an expansion for polarization observables, where the interference of higher waves is more important in comparison with the differential cross section and, finally, perform the partial wave analysis.

However despite the very good quality of the data, the low and the middle energy regions are not sensitive to  $\ell_{max} = 3$ . Either the quality of the data is still not enough to provide information about higher partial waves or, which is more likely, due to the fact that in contributions from higher partial waves are suppressed by the  $N(1535) 1/2^-$  and  $N(1650) 1/2^-$  resonances  $\eta$  photoproduction in these energy regions. Therefore the influence of higher partial waves cannot be seen in such type of an analysis.

The most significant difference is seen at energies above  $W = 1900$  MeV, which corresponds to the second data set. There the inclusion of  $G$  waves certainly improves the  $\chi^2$  significantly. By having a closer look at the  $\chi^2$  distributions one can see how significant the change is.

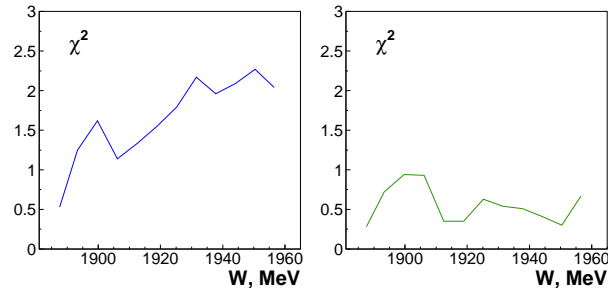


Figure 4.5:  $\chi^2$  distributions for the description of the differential cross section by the series of Legendre polynomials with the maximum  $\ell = 3$  (blue),  $\ell = 4$  (green).

Indeed the indication of the presence of  $F$  and  $G$  waves is seen on the Fig. 4.6. The case with  $\ell_{max} = 3$  (blue curves) does not describe the shape of the data above  $W = 1900$  MeV. Curves with  $\ell_{max} = 4$  describes the data well.

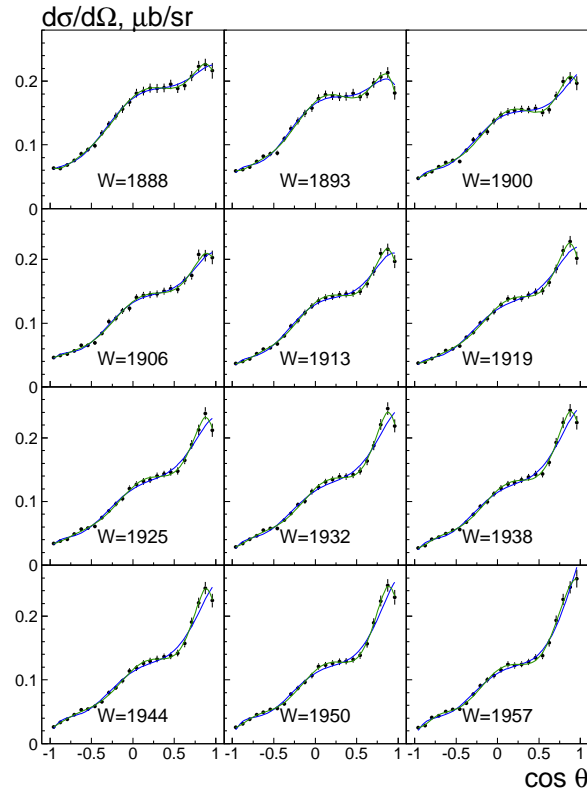


Figure 4.6: Description of the differential cross section by the series of Legendre polynomials with the maximum  $\ell = 3$  (blue) and  $\ell = 4$  (green).

Taking into account the discussed results in this section we choose the  $\ell_{max} = 4$ . Figure 4.7 shows the corresponding Legendre coefficients along with the model predictions from BnGa, MAID07, and SAID models.

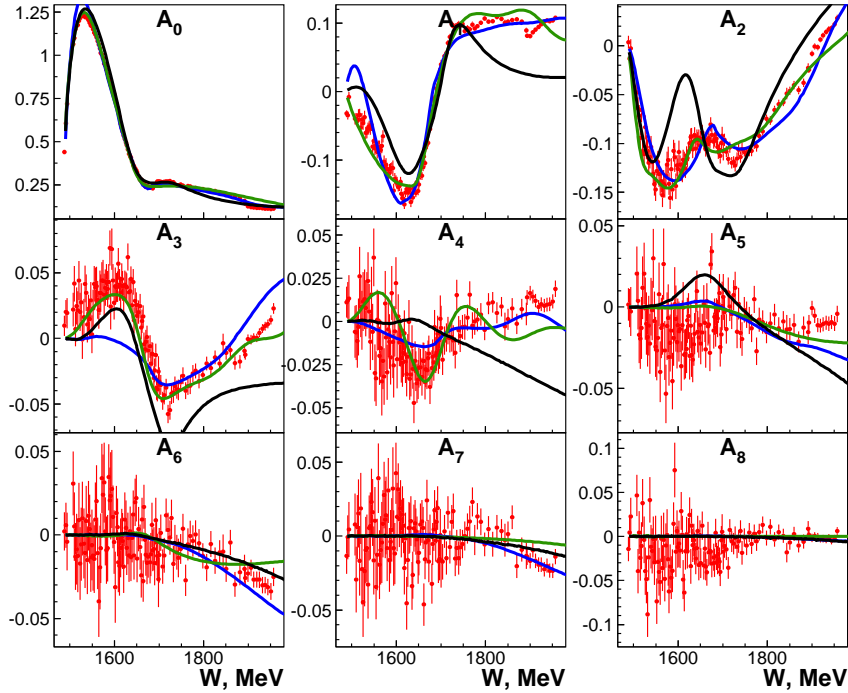


Figure 4.7: Legendre coefficients from the fit with  $\ell_{max} = 4$  for  $\frac{d\sigma}{d\Omega}$ . Compared with models MAID07 (black), BnGa (blue), SAID (green)

As seen from predictions  $A_0^{d\sigma/d\Omega}$  is described almost identical with all of the models. SAID and BnGa solutions show close results in all other coefficients. Except energies below  $W = 1700$  MeV where SAID gives better description. Also MAID07 solution generally does not provide proper quality of the fit.

By looking on Legendre coefficients one can see the resonance structures in coefficients up to  $A_4^{d\sigma/d\Omega}$  in the regions below  $W = 1800$  MeV. Which can be produced by the following well known resonances:  $N(1535) 1/2^-$ ,  $N(1440) 1/2^+$ ,  $N(1710) 1/2^+$ ,  $N(1720) 3/2^+$ ,  $N(1520) 3/2^-$ ,  $N(1700) 3/2^-$ . Which means that data allows to determine modulus of  $D$  waves as the lowest contribution in this coefficient. However the influence of  $F$  and higher waves, in particular:  $N(1680) 5/2^+$ ,  $N(1860) 5/2^+$ ,  $N(1990) 7/2^+$  and  $G$ -waves due to large errors is not observed in the coefficients.

### 4.2.2 CB ELSA data

CBELSA/TAPS collaboration has published data on the differential cross section [45] which cover a wide energy range from  $W = 1588$  to  $W = 2370$  MeV with a good angular coverage. The cross sections were measured by identifying the  $\eta$  meson via:  $\eta \rightarrow 2\gamma$  and  $\eta \rightarrow 3\pi^0 \rightarrow 6\gamma$  detection modes. Statistical errors are determined from the number of events in each  $(E_\gamma, \cos\theta)$  and are bigger than in MAMI [44] data. In addition to the statistical uncertainties the systematic ones are also present.

According to the [45] the systematic errors come from the uncertainties in the positioning of the liquid hydrogen target and from the offset of the photon beam. Using kinematical fit and Monte Carlo simulations the position of the target cell was found to be shifted upstream by 0.65 cm. Which led us to the angular dependent errors which are 2-3 % on the average and  $\leq 5$  % at most around  $\cos\theta = 0$ .

In addition the photon beam was assumed to be shifted by less than 2 mm off axis at the target position. The uncertainty of the proton trigger has been determined from the small disagreement of the differential  $\eta$  cross sections for energies  $E_\gamma < 1$  GeV and cosine values  $\cos\theta < 0$  using two different decay channels.

In addition an overall  $\pm 5.7$  % error is assigned to the reconstruction efficiency. And also 3 % systematic error accounts for the slightly different effects of confidence level cuts on data and Monte-Carlo events.

Since this data set covers the energy range of MAMI EPT data [44] It is interesting to take closer look and make a Legendre polynomials expansion for energies above the highest MAMI EPT limit. Nevertheless the low energy limit is also described. Therefore fits with  $\ell_{max} = 3, 4$  were applied to the whole energy range.

Fig. 4.8 shows the  $\chi^2$  distributions. From these plots fits give adequate description of the data. The energies below  $W = 1900$  MeV are described much lower  $\chi^2$  in comparison with MAMI data [44] which is due to the large errors of the data.

For the energies above  $W = 1900$  MeV both fits provide similar description of the data.

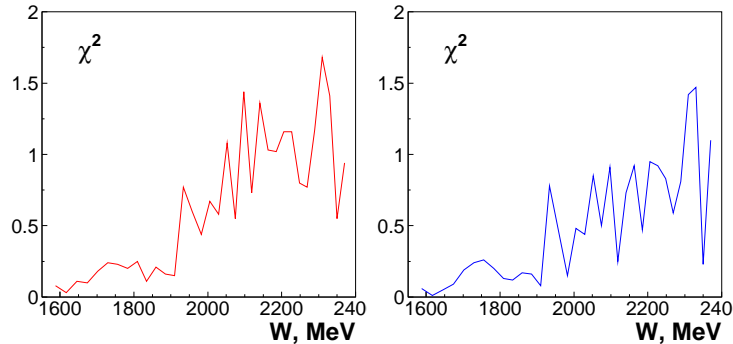


Figure 4.8:  $\chi^2$  distributions for the description of the differential cross section by the series of Legendre polynomials with the maximum  $\ell = 3$  (red) and  $\ell = 4$  (blue).

In close comparison of  $\chi^2$  distributions in the high energy region one can see that fit with  $\ell_{max} = 4$  gives slightly better results.

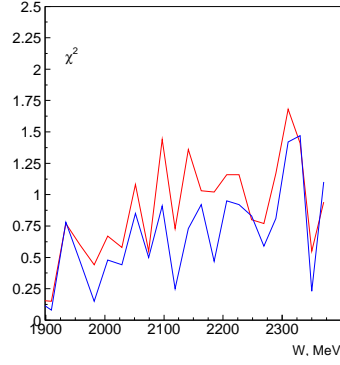


Figure 4.9:  $\chi^2$  distributions for the description of the differential cross section at high energies by the series of Legendre polynomials with the maximum  $\ell = 3$  (red) and  $\ell = 4$  (blue).

As one can see from the Fig. 4.10, blue curves give a better description in the forward region, following the shape of data, where the very forward point comes down. The same behavior was also observed in MAMI EPT data, see Fig. 4.6.

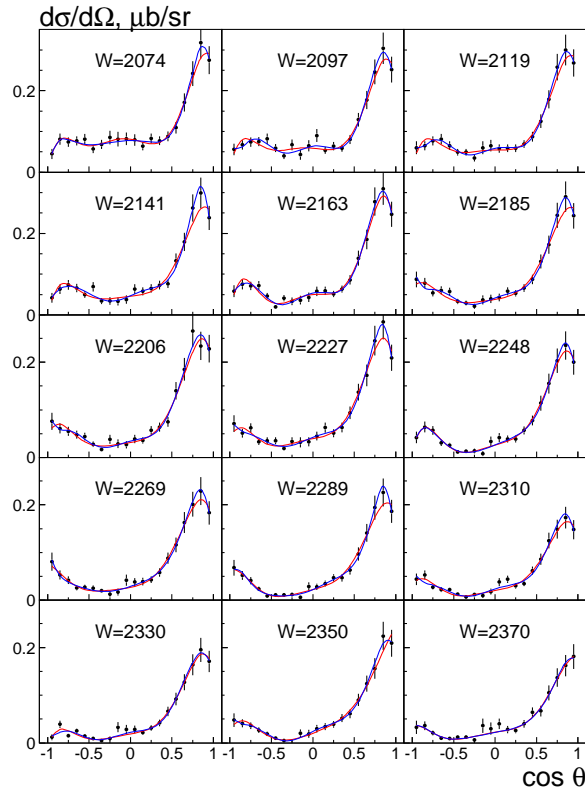


Figure 4.10: Description of the differential cross section by the series of Legendre polynomials with the maximum  $\ell = 3$  (red) and  $\ell = 4$  (blue).

Despite the fact that data from CB ELSA have a larger energy range, and the description with  $\ell_{max} = 4$  shows similar behaviour at forward angles, the data does not have the proper quality to allow us to check the sensitivity to  $G$ -waves in the high energy region. Therefore it

is useful to stop the fitting procedure at  $\ell_{max} = 3$ .

Fig. 4.11 shows the Legendre coefficients for the best fit with  $\ell_{max} = 3$ .

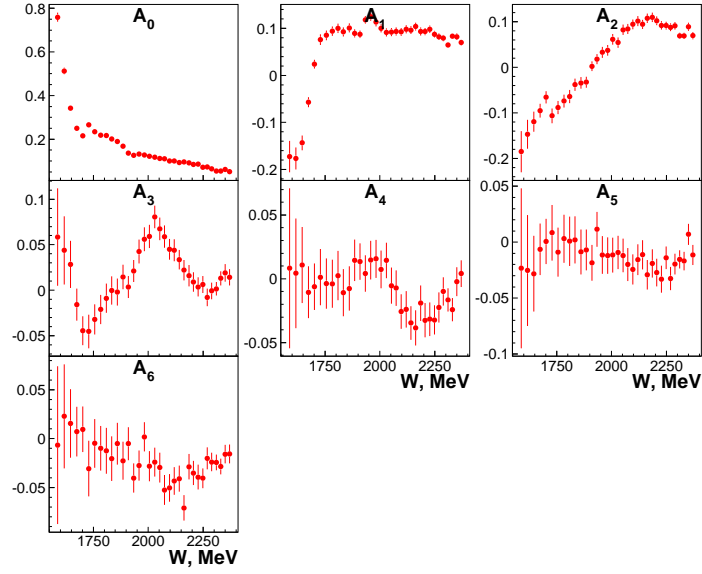


Figure 4.11: Legendre coefficients from the fit with  $\ell_{max} = 3$  for  $d\sigma/d\Omega$ .

Below the comparison with MAMI cross section is shown.

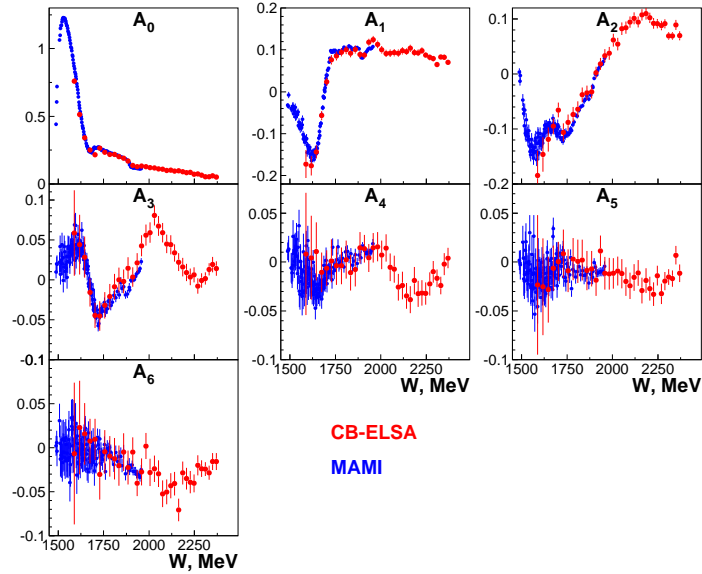


Figure 4.12: Comparison of Legendre coefficients from the fit with  $\ell_{max} = 3$  for MAMI (blue) and CB-ELSA (red) data for  $d\sigma/d\Omega$ .

As seen from the plot there is a good agreement with both data sets in the overlapping energy region. MAMI [44] provides the description of the  $\eta$  threshold region, CB-ELSA [45] provides information above  $\eta'$  threshold.

From the Fig. 4.12 one can conclude that the structure in  $A_{d\sigma/d\Omega}^4$  Legendre coefficient at energies above  $W = 1900$  MeV is produced by the modulus of  $D$ -waves, by the interference of  $D$  and  $F$  waves and by the modulus of  $F$ -waves. Higher coefficients could be considered as 0. Nevertheless using  $\ell_{max} = 4$  in the fit slightly smoothen the behavior of higher coefficients

basically  $A_{d\sigma/d\Omega}^5$  and  $A_{d\sigma/d\Omega}^6$ .

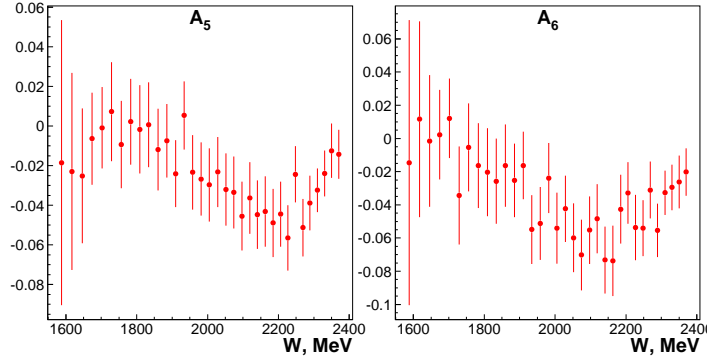


Figure 4.13:  $A_{d\sigma/d\Omega}^5$  and  $A_{d\sigma/d\Omega}^6$  from the fit with  $\ell_{max} = 4$  for  $d\sigma/d\Omega$ .

This happens because of better fitting of the forward angles, but such change can not be considered as a purpose to use  $\ell_{max} = 4$  for truncation.

### 4.3 Polarization observables $\hat{F}$ , $\hat{T}$

This section will be devoted to the description of  $T$  and  $F$  polarization observables [49]. These two data sets were obtained with the Crystal-Ball/TAPS detector setup at the Glasgow tagged photon facility of the Mainz Microtron MAMI. The mesons were identified via  $\eta \rightarrow 2\gamma$  or  $\eta \rightarrow 3\pi^0 \rightarrow 6\gamma$  decay modes.

In order to apply Legendre expansion Eq. (4.2) one has to multiply the measured observable with the differential cross section. For such a procedure the energy and the angular rebinning procedure was applied to the [44] cross sections data. Uncertainties of the cross sections and asymmetries were summed quadratically.

The asymmetries  $T$  and  $F$  are determined in each energy and angular bin as count rate asymmetries from the number  $N^\pm$  of reconstructed  $\gamma p \rightarrow \eta p$  events with different orientations of target and spin beam helicity

$$\begin{aligned} T &= \frac{1}{P_T |\sin \varphi|} \frac{N^{\pi=+1} - N^{\pi=-1}}{N^{\pi=+1} + N^{\pi=-1}} \\ F &= \frac{1}{P_T |\cos \varphi|} \frac{1}{P_\odot} \frac{N^{\sigma=+1} - N^{\sigma=-1}}{N^{\sigma=+1} + N^{\sigma=-1}} \end{aligned} \quad (4.14)$$

Here  $P_\odot$  and  $P_T$  denote the degree of circular beam and transverse target polarization  $\varphi$  is the azimuthal angle of the target polarization vector in a coordinate frame fixed to the reaction plane with  $\hat{z} = \vec{p}_\gamma / |\vec{p}_\gamma|$ ,  $\hat{y} = \vec{p}_\gamma \times \vec{p}_\eta / |\vec{p}_\gamma \times \vec{p}_\eta|$ ,  $\hat{x} = \hat{y} \times \hat{z}$ ,  $\pi = \vec{P}_T \cdot \hat{y} / |\vec{P}_T \cdot \hat{y}| = \pm 1$  denotes the orientation of the target polarized vector  $\vec{P}_T$  to the normal of the production plane and, in the case of the  $F$  asymmetry  $\sigma = h \vec{P}_T \cdot \hat{x} / |\vec{P}_T \cdot \hat{x}| = \pm 1$  is given by the product of the beam helicity  $h$  and the orientation of  $\vec{P}_T$  relative to the  $\hat{x}$  axis.

The systematic uncertainty is dominated by the determination of the degree of photon polarization (4%), the degree of photon beam polarization (2%) and the background subtraction procedure (3-4%). By adding all contributions quadratically a total systematic uncertainty of less than 6% is obtained.

First the data of the  $\hat{F}$  asymmetry is described then the data of the  $\hat{T}$  asymmetry.

### 4.3.1 $\hat{F}$

In order to check the sensitivity of data to  $D$ ,  $F$  and  $G$  waves fits with  $\ell_{max} = 2, 3, 4$  were done.

Fig. 4.14 shows the comparison of 3 different  $\chi^2$  distributions.

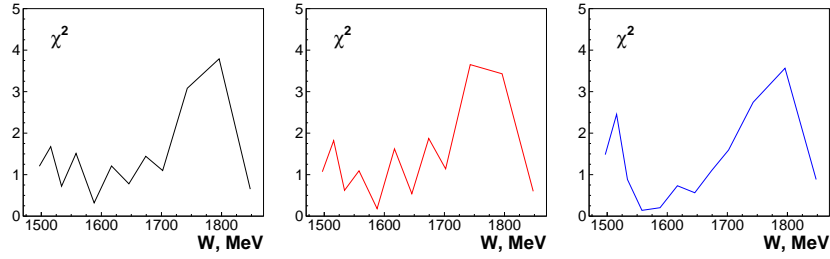


Figure 4.14:  $\chi^2$  distributions for the description of the differential cross section by the series of Legendre polynomials with the maximum  $\ell = 2$  (black)  $\ell = 3$  (red) and  $\ell = 4$  (blue).

As seen from the plots fits with  $\ell_{max} = 2, 3$  give almost identical results. Fit with  $\ell_{max} = 4$  gives much better description in the middle energy range which can be explained as overfitting the data. Indeed on Fig. 4.15 which shows description of the data using Eq. (4.2) one can see how the blue curve is describing each single wiggle in the data.

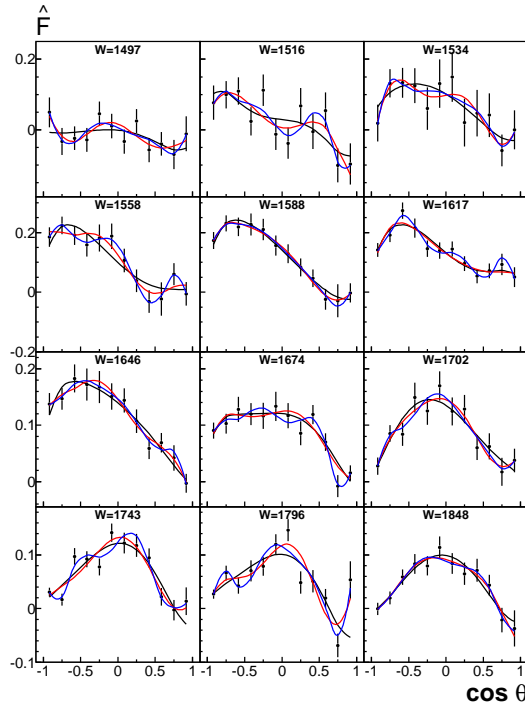


Figure 4.15: Description of the differential cross section by the series of Legendre polynomials with the maximum  $\ell = 2$  (black),  $\ell = 3$  (red) and  $\ell = 4$  (blue).



Due to the identity of  $\chi^2$  distributions for  $\ell_{max} = 2, 3$  and by looking on the data description, shown Fig. 4.15 one can conclude that there is no physical reason to use  $\ell_{max} = 3$  for the best fit parameter. Therefore we choose the value  $\ell_{max} = 2$ .

Below the Legendre coefficients for the best fit and also the model descriptions are shown. As one can see the only model which describes the coefficients is BnGa.

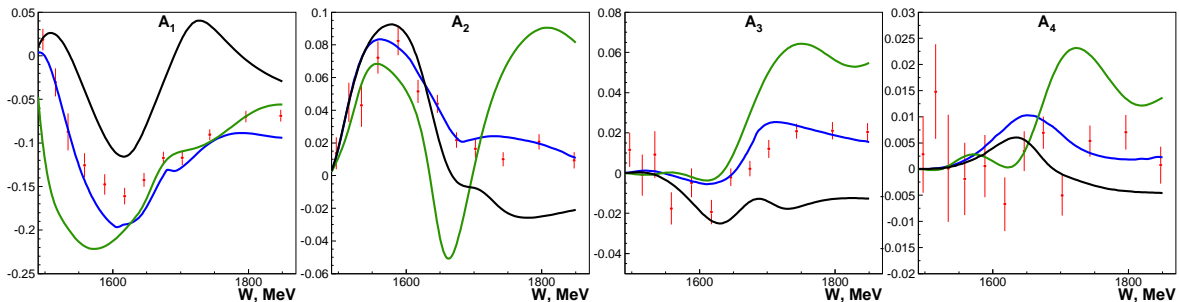


Figure 4.16: Legendre coefficients for the fit with  $\ell_{max} = 2$  for the  $\hat{F}$ . Compared with models MAID07 (black), BnGa (blue), SAID (green)

By looking on Legendre coefficients one can see that the last coefficient which provides reasonable information is  $A_3^{\hat{F}}$ . The structure of this coefficient gives the knowledge that interference of  $P$  and  $D$  waves creates such a structure.  $A_4^{\hat{F}}$  is noise, which means modulus of  $D$  waves cannot be seen in such an analysis.

### 4.3.2 $\hat{T}$

The same procedure as for  $\hat{F}$  was applied for  $\hat{T}$ . In order to check the sensitivity of data to  $D$ ,  $F$  and  $G$  waves fits with  $\ell_{max} = 2, 3, 4$  were done.

Fig. 4.17 shows the comparison of 3 different  $\chi^2$  distributions.

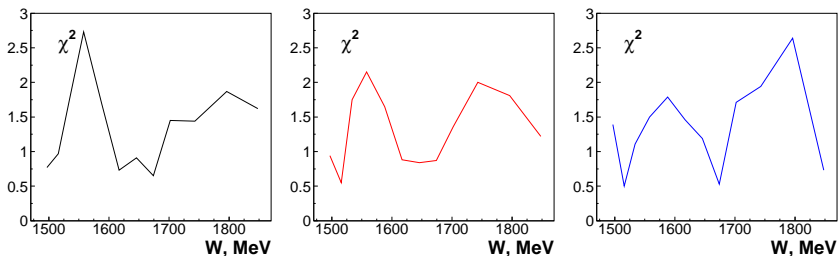


Figure 4.17:  $\chi^2$  distributions for the description of the differential cross section by the series of Legendre polynomials with the maximum  $\ell = 2$  (black)  $\ell = 3$  (red) and  $\ell = 4$  (blue).

As seen from the plots all fits with give very close results. Fit with  $\ell_{max} = 4$  may be neglected due to the same reason as for  $\hat{F}$ : the data points are scattered therefore the blue line tries to describe every single wiggle in the data points which has no physical sense. Due to the close results of  $\chi^2$  distributions for first two  $\ell_{max}$  and by looking on the data description, see Fig. 4.18 there is no physical reason to use  $\ell_{max} = 3$  as a fit parameter. Data is not sensitive to the modulus of  $D$  waves. Therefore the best fit is the fit with  $\ell_{max} = 2$

Fig.4.18 shows description of the data using Eq. (4.2)

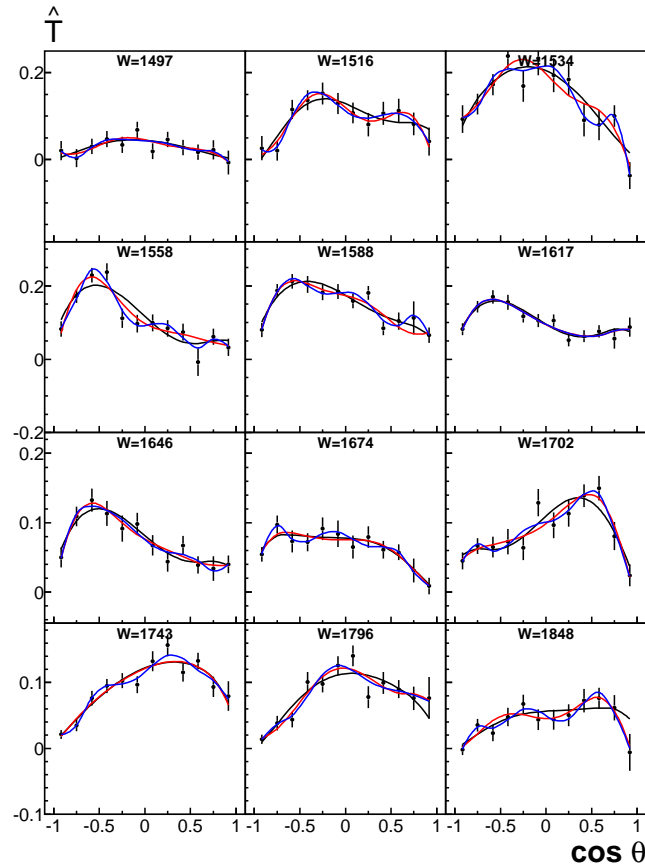


Figure 4.18: Description of the differential cross section by the series of Legendre polynomials with the maximum  $\ell = 2$  (black),  $\ell = 3$  (red) and  $\ell = 4$  (blue).

Below the Legendre coefficients for the best fit and also the model descriptions are shown. As one can see again, that the only model which describes the coefficients is BnGa.

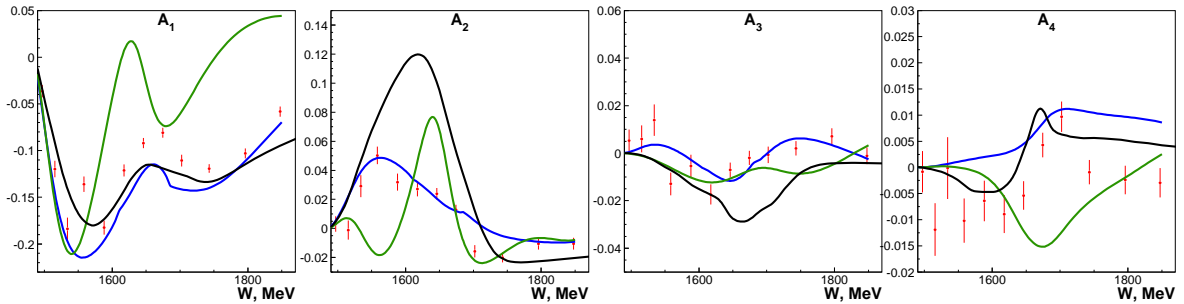


Figure 4.19: Legendre coefficients for the fit with  $\ell_{max} = 2$  for the  $\hat{F}$  compared with models MAID07 (black), BnGa (blue), SAID (green)

By looking on Legendre coefficients for certain one can see that the last coefficient which provides reasonable information is  $A_3^{\hat{T}}$ . The structure of this coefficient gives the information that interference of  $P$  and  $D$  waves creates it.  $A_4^{\hat{T}}$  has no structure, which means that modulus of  $D$  waves cannot be seen in such analysis.

## 4.4 Polarization observable $\hat{\Sigma}$

This section is devoted to fit of the experimental data on beam asymmetry [47]. This data set was obtained by GRAAL collaboration and published in 2007. It has 66 energy bins with the coverage from  $W = 1490$  up to  $W = 1850$  MeV. Each energy bin contains 10 angular bins with non-constant range. In general it covers  $\theta$  angles from  $\approx 33$  up to  $\approx 160$  degrees, or  $\cos\theta \in [-0.95, 0.84]$ .

The beam asymmetry was determined from the standard expression:

$$\frac{\bar{N}_V(\varphi) - \bar{N}_H(\varphi)}{\bar{N}_V(\varphi) + \bar{N}_H(\varphi)} = P_\gamma \Sigma \cos(2\varphi) \quad (4.15)$$

Where  $\bar{N}_V(\varphi)$  and  $\bar{N}_H(\varphi)$  are the azimuthal yields normalized by the integrated flux for the vertical and horizontal polarization states, respectively.  $P_\gamma$  is the degree of linear polarization of the beam and  $\varphi$  the azimuthal angle of the reaction plane. For a given bin in energy  $E_\gamma$  and  $\theta$ , the beam asymmetry  $\Sigma$  was extracted from the fit of the normalized ratio Eq. (4.15) by the function  $P_\gamma \Sigma \cos(2\varphi)$ , using the known energy dependence of  $P_\gamma$ . The measured asymmetries were corrected for the finite  $\varphi$  binning  $\Sigma_{true} = \Sigma_{meas}(1 + R_\varphi)$  with  $R_\varphi = 0.026$  for 16 bins.

Two source of systematic uncertainties were considered: the uncertainty to the beam polarization (2%) and the uncertainty from the background contamination. For the second one, two main contributions were identified: other photoproduction (hadronic) reactions and target wall events. The uncertainty due to hadronic contamination was estimated from the variation of the extracted asymmetries when opening cuts from  $\pm 3\sigma$  to  $\pm 4\sigma$ . The resulting errors range from  $\delta\Sigma = 0.003$  to  $0.035$ . The rate of target wall events was measured via empty target runs and found to be less than 1%. The corresponding error was neglected.

Fits with  $\ell_{max} = 2, 3, 4$  were done. Below the  $\chi^2$  distribution plots are shown.

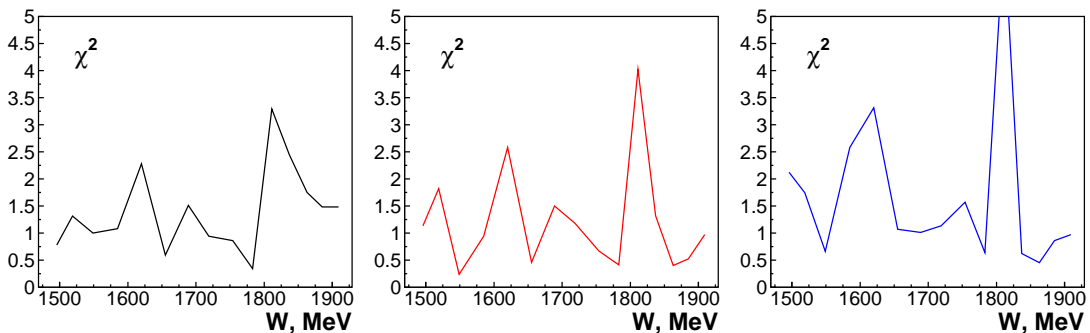


Figure 4.20:  $\chi^2$  distributions for  $\hat{\Sigma}$  by the series of Legendre polynomials with the maximum  $\ell = 2$  (black)  $\ell = 3$  (red) and  $\ell = 4$  (blue).

It is seen from the plot that the data only sensitive to fits with  $\ell_{max} = 2, 3$ . Both fits give close results, despite forward angles at energies higher than  $W = 1800$  MeV, where inclusion of  $F$  waves in the fit improves the description, see Fig. 4.21. This figure shows the description of the data using Eq. (4.2).

Fit with  $\ell_{max} = 4$  does not produce good description. Therefore it is necessary to stop at  $\ell_{max} = 2$ , keeping in mind that in further partial wave analysis one has to take into account that  $F$  waves ( $\ell_{max} = 3$ ) could be considered at high energies.

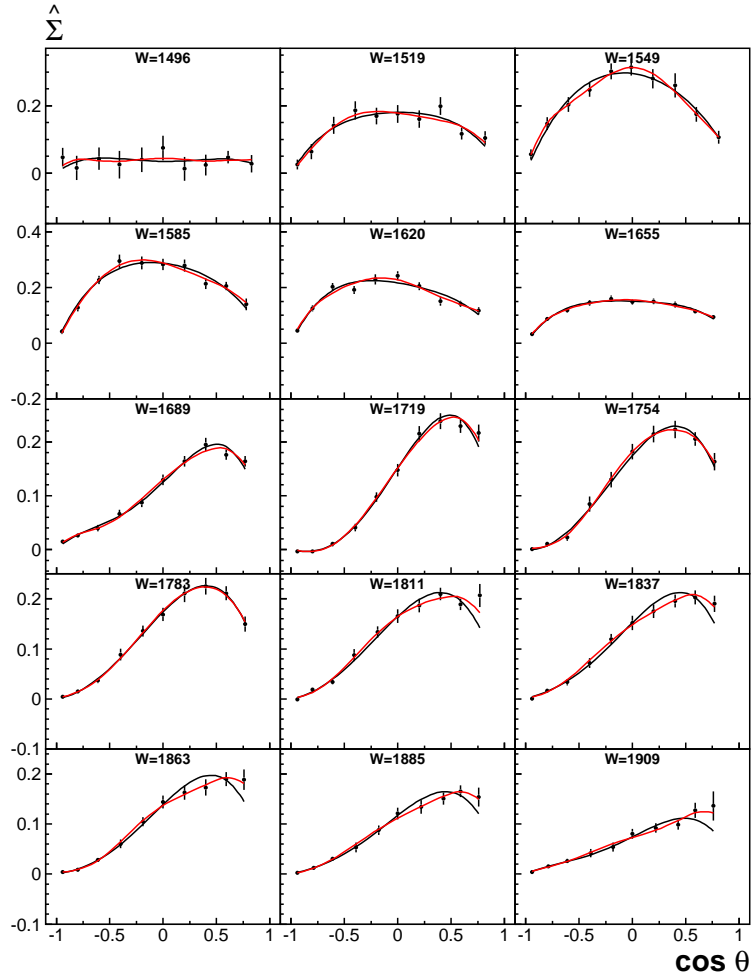


Figure 4.21: Description of  $\hat{\Sigma}$  by the series of Legendre polynomials with the maximum  $\ell = 2$  (black) and  $\ell = 3$  (red).

Below the Legendre coefficients along with the models for the best fit is shown. It is seen that almost all models describe the coefficients with a good agreement. Despite  $A_4^{\hat{\Sigma}}$  where only Bonn-Gatchina model give adequate description.

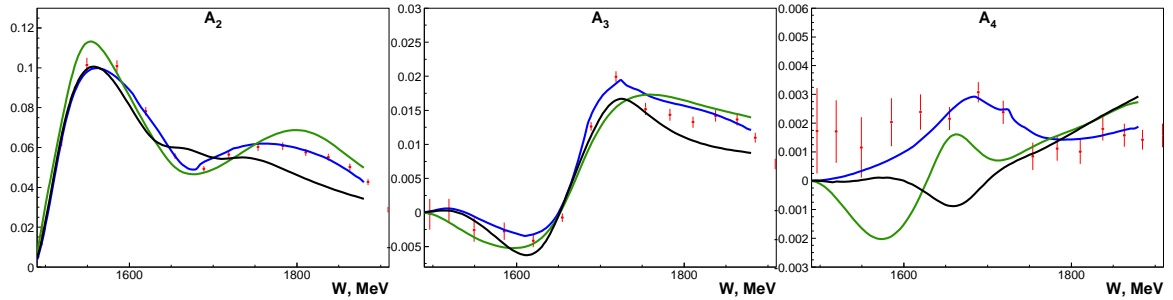


Figure 4.22: Legendre coefficients for the fit with  $\ell_{max} = 2$  for  $\hat{\Sigma}$  compared with models MAID07 (black), BnGa (blue), SAID (green)

It is clearly seen that the lowest contribution to the Legendre coefficients comes from the modulus of  $P$  waves and from interference of  $P$  and  $D$  waves.

## 4.5 Polarization observable $E$

These data were obtained in 2015 by CLAS collaboration [50]. However due to a small impact to the overall  $\chi^2$  and having a small number of data points it plays minor role in the analysis. Nevertheless one should give a short overview of this observable.

In order to determine the helicity asymmetry  $E$  in a discrete event counting experiment, the following equation is used to form the asymmetry

$$E = -\frac{1}{|P_z^T||P_\odot^\gamma|} \left( \frac{N_+ - N_-}{N_+ + N_-} \right), \quad (4.16)$$

where  $N_+$  and  $N_-$  which are the number of  $\eta$  mesons counted in beam-target helicity aligned and anti-aligned settings, respectively.

The measurements were done on a frozen butanol target ( $C_4H_9OH$ ), the final state particles photoproduction were detected using CLAS, which is a set of six identical detectors and  $\eta$  meson was identified via charge mode  $\eta \rightarrow \pi^+\pi^-\pi^0$ .

Statistical uncertainties dominated the systematic uncertainties in all analyzed bins. The systematic uncertainties include the target polarization  $P_z^T$  uncertainty (6.1%) and photon beam polarization  $P_\odot^\gamma$  uncertainty (3.1%).

## 4.6 Conclusion

In this section a short conclusion on the fit results of the used data is presented.

### $d\sigma/d\Omega$ from MAMI

These data have narrow energy and angular binning and small errors. Fit with  $\ell_{max} = 4$  was done for a combined data set. Structures for energies below  $W = 1600$  MeV up to  $A_4^{\sigma_0}$  are observed. Modulus of  $D$  waves is the lowest contribution in this coefficient. Contributions of higher partial waves are suppressed by the  $N(1535) 1/2^-$  and cannot be observed in this type of analysis.

### $d\sigma/d\Omega$ from CBELSA

In comparison with [44] this data has larger angular and energy bins as well as the errors. But it has larger energy coverage. Threshold region of  $\eta$  meson is not covered. At energies above  $W = 1900$  MeV the resonance structure in  $A_4^{d\sigma/d\Omega}$  is observed. The modulus of  $D$  and  $F$  waves and also the interference of them produces it.

### Polarization observables $T$ and $F$

Truncation was done at  $\ell_{max} = 2$ . The resonance structure is observed in the coefficients up to  $A_3^{\hat{T}, \hat{F}}$  which means that the interference of  $P$  and  $D$  produces it.

### Polarization observable $\Sigma$

Fit with  $\ell_{max} = 2$  was done. The structure is observed up to  $A_3^{\hat{\Sigma}}$  which means that the modulus of  $P$  waves and also the interference of  $P$  and  $D$  waves produces it.



# Chapter 5

---

## Partial wave analysis

---

In this chapter we discuss different partial wave analysis procedures. The main part is devoted to the description of the procedure that was used in our analysis. After that we give a short overview of other approaches.

### 5.1 EtaMAID isobar model approach

The approach which we used for the data analysis and which is historically used in Mainz is an isobar model approach. Speaking of it an abbreviation MAID is generally used. MAID was first developed for pion photo- and electroproduction [8], later it was extended to the  $\eta$  photo- and electroproduction [9]. This model is usually called EtaMAID and also has a reggeized version [51].

The ansatz is basically simple.

$$t_{\gamma,\eta}(W) = t_{\gamma,\eta}^{bg}(W) + t_{\gamma,\eta}^{Res}(W) \quad (5.1)$$

The scattering amplitude  $t_{\gamma,\eta}(W)$  is decomposed into two parts. The first part is the non-resonant background  $t_{\gamma,\eta}^{bg}(W)$  which consists of Born terms (nucleon exchanges in the  $s$ - and  $u$ -channels) and the  $t$ -channel vector meson exchanges. The second part is the resonance amplitude  $t_{\gamma,\eta}^{Res}(W)$  that contains nucleon resonance excitations in the  $s$ -channel parameterized with the Breit-Wigner ansatz.

In addition to the  $s$ -channel resonances the  $u$ -channel resonances should be included as well in order to fulfill the crossing symmetry. However this does not work in practice because the energy dependent width in the  $s$ -channel is finite and in the  $u$ -channel it is off shell and therefore it disappears. Therefore conceptually these channels in an isobar model are always different and do not fulfill the crossing symmetry. In our approach we treat effectively  $u$ -channel exchanges within a background and fulfill the crossing symmetry with the fixed- $t$  dispersion relations.

#### 5.1.1 Resonance part

We parameterize the resonance part as a sum of Breit-Wigner resonance functions with a unitary phase  $\Phi_j^\alpha$  for each resonance

$$t_{\gamma,\eta}^{\alpha,Res}(W) = \sum_{j=1}^{N_\alpha} t_{\gamma,\eta}^{\alpha,BW,j}(W) e^{i\Phi_j^\alpha}, \quad (5.2)$$

where  $N_\alpha$  is the number of resonances for each partial wave.

Resonances are related to the multipoles ( $\mathcal{M}_{\ell\pm}$ ), see Eq. (3.23). We parameterize them with the following ansatz:

$$\mathcal{M}_{\ell\pm}(W) = \bar{\mathcal{M}}_{\ell\pm} f_{\eta N}(W) \frac{M_R \Gamma_{\text{tot}}(W)}{M_R^2 - W^2 - i M_R \Gamma_{\text{tot}}(W)} f_{\eta N}(W) C_{\eta N}, \quad (5.3)$$

where  $f_{\eta N}(W)$  is the usual Breit-Wigner factor describing the  $\eta N$  decay of the  $N^*$  resonance with total energy dependent width  $\Gamma_{\text{tot}}(W)$ ,  $C_{\eta N}$  is an isospin factor, which is  $-1$  for  $\eta N$  final

states. The co-called reduced multipoles are denoted as  $\bar{\mathcal{M}}_{\ell\pm}$  and related to the photon decay amplitudes  $A_{1/2}$  and  $A_{3/2}$ . The reduced multipoles  $\bar{\mathcal{M}}_{\ell\pm}$  in terms of an  $A_{1/2}$  and  $A_{3/2}$  can be found in Appendix Eq. (A.4) and Tab. A.1

The Breit-Wigner factor  $f_{\eta N}(W)$  and the photon vertex  $f_{\gamma N}(W)$  are described by:

$$f_{\eta N}(W) = \zeta_{\eta N} \left[ \frac{1}{(2J+1)\pi} \frac{m_p k(W)}{M_R q(W)} \frac{\Gamma_{\eta N}(W)}{\Gamma_{\text{tot}}(W)^2} \right]^{1/2}, \quad (5.4)$$

$$f_{\gamma N}(W) = \left( \frac{k(W)}{k_R} \right)^2 \left( \frac{X_\gamma^2 + k_R^2}{X_\gamma^2 + k^2(W)} \right)^2, \quad (5.5)$$

with  $k(W)$  and  $q(W)$  the photon and the  $\eta$  meson momenta given in set of Eqs. (3.8). Factor  $\zeta_{\eta N} = \pm 1$  is a relative sign between the  $N^* \rightarrow \eta N$  and  $N^* \rightarrow \pi N$  couplings,  $X$  and  $X_\gamma$  are phenomenological damping parameters. All momenta taken at the resonance position  $M_R$  are denoted with an additional index  $R$ .

In our approach we assume that all resonances decay at least into 3 channels:  $\pi N$ ,  $\eta N$  and  $\pi\pi N$ . The traditional MAID parametrization of the energy dependent partial width is following:

$$\begin{aligned} \Gamma_{\pi N}(W) &= \beta_{\pi N} \Gamma_R \left( \frac{q_\pi(W)}{q_{\pi,R}} \right)^{2\ell+1} \left( \frac{X^2 + q_{\pi,R}^2}{X^2 + q_\pi^2(W)} \right)^\ell, \\ \Gamma_{\eta N}(W) &= \beta_{\eta N} \Gamma_R \left( \frac{q(W)}{q_R} \right)^{2\ell+1} \left( \frac{X^2 + q_R^2}{X^2 + q(W)^2} \right)^\ell, \\ \Gamma_{\pi\pi N}(W) &= \beta_{\pi\pi N} \Gamma_R \left( \frac{q_{2\pi}(W)}{q_{2\pi,R}} \right)^{2\ell+4} \left( \frac{X^2 + q_{2\pi,R}^2}{X^2 + q_{2\pi}^2(W)} \right)^{\ell+2}. \end{aligned} \quad (5.6)$$

with the *c.m.* momenta of pion denoted by  $q_\pi(W)$ . For the effective  $2\pi$  channel we use a mass of  $2m_\pi$ . Constants  $\beta_{\pi N}$ ,  $\beta_{\eta N}$  are branching ratios of the resonances into respective channels.

However this parametrization fails when a resonance has a mass  $M_R$  that is lower than production threshold. In this case the momentum  $q_R$  as well as the branching ratio  $\beta_{\eta N}$  become complex. The best example is  $N(1440) 1/2^+$  which mass lies below  $\eta N$  threshold but this resonance contributes to the  $\eta N$  production mechanism. For this case we use different parametrization which takes correctly into account the excitation of the resonances below threshold.

In this parametrization we set  $\beta_{\alpha N} = 0$  below  $\alpha N$  production threshold and  $q^2(W) < 0$ . After that we calculate the energy dependent width as shown below:

$$\Gamma_{\alpha N}(W) = g_{\alpha N}^2 \sqrt{|q_\alpha^2(W)|} \left( \frac{|q_\alpha^2(W)|}{X^2 + |q_\alpha^2(W)|} \right)^\ell, \quad (5.7)$$

where now  $|q_\alpha^2(W)|$  is well defined and always positive function, thus one can take  $\sqrt{q_\alpha^2(W)}$ . Parameter  $g_{\alpha N}$  is called coupling constant which plays a role of a branching ratio. We use this constant in the analysis as a fitting parameter.

However our parametrization is not unique and there are other parameterizations which take care of the sub-threshold resonances, for example Flatté parametrization, which can as well be alternatively used.

It is also possible and convenient to use our parametrization of the energy dependent width above threshold. For this we write the following relations between  $g_{\alpha N}^2$  and  $\beta_{\alpha N}$ :

$$g_{\alpha N}^2 = \frac{\beta_{\alpha N} \Gamma_R}{q_{\alpha,R}} \left( 1 + \frac{X^2}{q_{\alpha,R}^2} \right)^\ell, \quad (5.8)$$



$$\beta_{\alpha N} = \frac{g_{\alpha N}^2 q_{\alpha, R}}{\Gamma_R (1 + X^2/q_{\alpha, R}^2)^\ell}, \quad (5.9)$$

with the  $\Gamma_R$  as a width of a resonance.

For the 3-body  $2\pi$  channel we also make a small adjustment:

$$\Gamma_{\pi\pi N}(W) = g_{\pi\pi}^2 q_{\pi\pi}(W) \left( \frac{|q_{\pi\pi}^2(W)|}{X^2 + q_{\pi\pi}^2(W)} \right)^{\ell+2}. \quad (5.10)$$

In our analysis we take into account 7 different production thresholds, thus the total width is calculated as shown below

$$\Gamma_{tot} = \Gamma_{\pi N} + \Gamma_{\pi\pi N} + \Gamma_{\eta N} + \Gamma_{K\Lambda} + \Gamma_{K\Sigma} + \Gamma_{\omega N} + \Gamma_{\eta' N}, \quad (5.11)$$

and the threshold values for the described above decays are mentioned in the Table 5.1

Table 5.1: Threshold values in  $W$  (MeV) of various  $N^*$  decay channels

$\pi N$	$\pi\pi N$	$\eta N$	$K\Lambda$	$K\Sigma$	$\omega N$	$\eta' N$
1077.84	1217.41	1486.13	1609.36	1686.32	1720.92	1896.05

Now let us make final remarks of the Breit-Wigner parametrization. First, one should note that the total width in the numerator of Eq. (5.3) is canceled by the total width in  $f_{\eta N}(W)$ . The complex quantity in the partial width  $\Gamma_{\eta N}$  is canceled by the momentum in the denominator in Eq. (5.4). Therefore it may be better to write the multipole parametrization in the following way:

$$\mathcal{M}_{\ell\pm}(W) = \bar{\mathcal{M}}_{\ell\pm} f_{\gamma N}(W) \frac{M_R \tilde{f}_{\eta N}(W)}{M_R^2 - W^2 - iM_R \Gamma_{tot}(W)} C_{\eta N}, \quad (5.12)$$

where now the Breit-Wigner factor  $\tilde{f}_{\eta N}(W)$  is described by:

$$\tilde{f}_{\eta N}(W) = g_{\eta N} \left[ \frac{k}{(2J+1)\pi} \frac{m_p}{M_R} \left( \frac{|q(W)^2|}{X^2 + |q(W)^2|} \right)^\ell \right]^{1/2}, \quad (5.13)$$

where the coupling constant  $g_{\eta N}$  now carries the sign of  $\zeta_{\eta N}$ .

Second, let us talk about the unitarity resonance phase  $\Phi_j^\alpha$ . If we consider the MAID analysis of pion production [8], then  $\Phi_j^\alpha$  is an energy dependent function and is used, in accordance with the Fermi-Watson theorem, to adjust the phase of the total multipole (background plus resonance) to the corresponding pion-nucleon scattering phase  $\delta_{\pi N}$  or to the experimentally observed one.

However, in case of  $\eta$  production we do not have any theoretical approach for it. Also phase was not used in the previous data analysis [9, 52, 53]. Therefore we decided to set it to a constant.

In recent analysis which is as well combined with the fixed- $t$  dispersion relations approach we found this modification very productive as it significantly improves the results for the analysis with the fixed- $t$  dispersion relations constrains.

However, such parametrization is not an optimal one, as it produces problems, i.e phase is not vanishing at threshold. But on the other hand more sophisticated parametrization introduces a lot of new fitting parameters, which in our case we do not have.

### 5.1.2 Non-resonant background

The non-resonant background in EtaMAID consists of two parts: Born terms and  $t$ -channel exchanges.

$$t_{\gamma,\eta}^{bg}(W) = t_{\gamma,\eta}^{Born}(W) + t_{\gamma,\eta}^{t-channel}(W) \quad (5.14)$$

Born terms are constructed similarly to the work [9]. For the  $t$ -channel vector meson exchanges we use two Regge parameterizations [54]. In the first one the Regge amplitudes are formulated in terms of Mandelstam variable  $s$ . In the second one, the Mandelstam variable  $s$  is replaced by crossing symmetrical variable  $\nu$ .

#### Born terms

Born terms are obtained by evaluating the Feynman diagrams derived from an effective Lagrangian density.

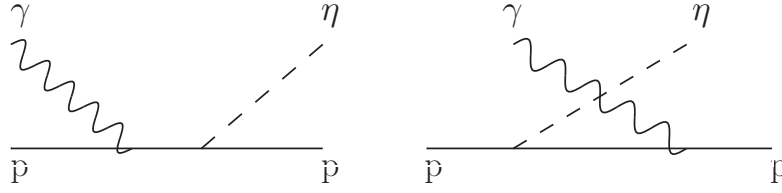


Figure 5.1: Feynman diagram for  $s$  and  $u$  Born terms.

The structure for the electromagnetic  $\gamma NN$  vertex is known:

$$\mathcal{L}_{\gamma NN} = -e \bar{\psi} \left[ \gamma_\mu A^\mu F_1^p(Q^2) + \frac{\sigma_{\mu\nu}}{2m_p} (\partial^\mu A^\nu) F_2^p(Q^2) \right] \psi, \quad (5.15)$$

with  $A^\mu$  the electromagnetic vector potential,  $m_p$  the proton mass and  $\psi$  the nucleon field operators. In Eq. (5.15) ( $F_{1,2}^p(Q^2)$ ) are the proton electromagnetic form factors, with  $Q^2 = 0$ . For real photons the form factors are equal to  $F_1^p(0) = 1$  and  $F_2^p(0) = \kappa_p = 1.79$ .

The  $\eta NN$  hadronic vertex is described with 2 couplings the pseudoscalar (PS)

$$\mathcal{L}_{\eta NN}^{PS} = -i g_{\eta NN} \bar{\psi} \gamma_5 \psi \phi_\eta, \quad (5.16)$$

and the pseudovector (PV)

$$\mathcal{L}_{\eta NN}^{PV} = \frac{g_{\eta NN}}{2m_p} \bar{\psi} \gamma_5 \gamma_\mu \psi \partial^\mu \phi_\eta. \quad (5.17)$$

Using the previous equations (5.15)-(5.17), the usual Born terms are constructed. The contributions from them into invariant amplitudes  $A_i(\nu, t)$  can be expressed in terms of the following variables: the crossing variable  $\nu$  and the variable  $\nu_B(t)$ .

$$A_1^{pole}(\nu, t) = \frac{e g_{\eta NN}}{m_p} \frac{\nu_B}{\nu^2 - \nu_B^2}, \quad (5.18)$$

$$A_2^{pole}(\nu, t) = \frac{-e g_{\eta NN}}{2m_p^2} \frac{1}{\nu^2 - \nu_B^2}, \quad (5.19)$$

$$A_3^{pole}(\nu, t) = -\frac{e g_{\eta NN} \kappa_p}{2m_p^2} \frac{\nu}{\nu^2 - \nu_B^2}. \quad (5.20)$$

$$A_4^{pole}(\nu, t) = -\frac{e g_{\eta NN} \kappa_p}{2m_p^2} \frac{\nu_B}{\nu^2 - \nu_B^2}, \quad (5.21)$$

$$\nu_B = \frac{t - m_\eta^2}{4m_p}, \quad (5.22)$$

where coupling  $g_{\eta NN}^2/4\pi \leq 0.1$  is very small in comparison with for example  $g_{\pi N}^2/4\pi \approx 14$ . This small value for the  $\eta$ -meson coupling was observed after the first measurement of the differential cross section with MAMI in Mainz [55] it was also shown in this work that the coupling must be a pseudo scalar.

In our present analysis we even get smaller results for the  $g_{\eta NN}^2/4\pi$  constant. Therefore we conclude that Born terms play very small role in the data analysis in our energy region and, therefore, may be neglected. Much more important role play  $t$ -channel vector meson exchanges which we will discuss now.

### Contribution from the $t$ -channel vector meson exchanges

Traditional and old MAID approach for the  $t$ -channel vector meson exchanges is described in [8] where contributions from  $\rho$  and  $\omega$  mesons were considered as a single poles. In the current work single poles are replaced with Regge poles [56] and Regge cuts [57–60] and contributions from more mesons are taken into account, we will describe them later in the text.

The parameterizations for the  $t$ -channel exchanges that are used in the model are taken from the work of Kashevarov, Ostrick and Tiator [54]. In this work Regge approach was applied to the description of high energy data on  $\eta$  and  $\pi^0$  photoproduction. By modifying the energy behavior one can apply Regge parametrization to the analysis of the low energy data and describe the high energy data as well. With this modification we also solve the duality problem.

This problem appears when we use at the same time resonances in the  $s$ -channel and Regge exchanges in the  $t$ -channel. Whenever we add an infinite series of the resonances in the  $s$ -channel it is equivalent that we add an infinite series in the  $t$ -channel. By adding these contributions together we have a double counting. In our case we only have a partial double counting since we have only 14 resonances in the  $s$ -channel and infinite series in the  $t$ -channel. Therefore in order to deal with it we decided to apply a damping factor, which we discuss in the end of this section.

The  $t$ -channel contributions can be derived from the Feynman diagrams presented below.

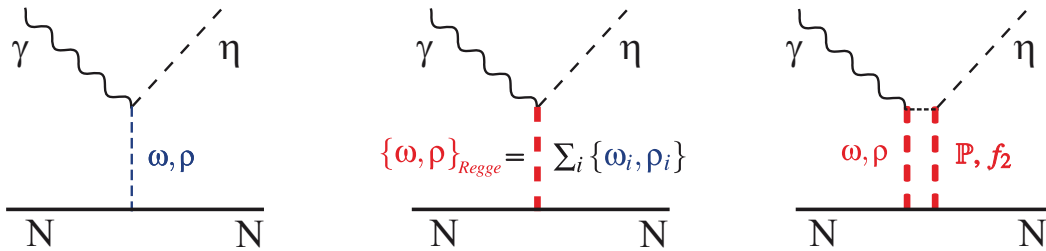


Figure 5.2:  $t$ -channel contributions to  $\eta$  photoproduction from single poles (left figure), Regge poles (middle figure), and Regge cuts (right figure). An example for  $\rho$  and  $\omega$  meson exchange and  $\mathbb{P}$  and  $f_2$  mesons for rescattering of two Reggeons.

If we consider the contributions from vector and axial-vector mesons, parameterized as a single poles, into invariant amplitudes we get the following set of equations:

$$A_1(t) = \frac{e \lambda_V g_V^t}{2m_\eta M_N} \frac{t}{t - M_V^2}, \quad (5.23)$$

$$A_2'(t) = -\frac{e \lambda_A g_A^t}{2m_\eta M_N} \frac{t}{t - M_A^2}, \quad (5.24)$$

$$A_3(t) = \frac{e \lambda_A g_A^v}{m_\eta} \frac{1}{t - M_A^2}, \quad (5.25)$$

$$A_4(t) = \frac{-e \lambda_V g_V^v}{m_\eta} \frac{1}{t - M_V^2}, \quad (5.26)$$

where  $A_2'$  amplitude is calculated using formula below:

$$A_2'(t) = A_1(t) + t A_2(t). \quad (5.27)$$

With this parametrization we separate the vector and tensor contributions from individual mesons. Thus the invariant amplitude  $A_2'$  now has only contributions from the tensor coupling of an axial-vector exchange.

In these formulas  $\lambda_{V(A)}$  denotes the electromagnetic coupling of the vector ( $V$ ) or axial ( $A$ ) vector meson with mass  $M_{V(A)}$ . The constants  $g_{V(A)}^{v(t)}$  denote their vector ( $v$ ) or tensor ( $t$ ) couplings to the nucleon.

In the work [54] couplings  $\lambda_{V(A)}$  were used as a fixed parameters and were determined from the radiative widths  $\Gamma_{V(A)}$  of the decay  $V(A) \rightarrow \eta\gamma$  via formula below

$$\Gamma_{V(A)} = \frac{\alpha(M_{V(A)}^2 - m_\eta^2)^3}{24 M_{V(A)}^3 m_\eta^2} \lambda_{V(A)}^2, \quad (5.28)$$

where  $\alpha$  is a fine-structure constant. Constants  $g_{V(A)}^{v(t)}$  vice versa were used as a fitting parameters.

Table 5.2 and Tab. 5.3 show the quantum numbers of the reggeons and their couplings

Table 5.2: Quantum numbers for pseudoscalar, vector and axial-vector mesons. Isospin  $I$ ,  $G$ -parity, spin  $J$ , parity  $P$ , and charge conjugation  $C$ .

	$\gamma$	$\eta$	$\rho(770)$	$\omega(782)$	$\phi(1020)$	$b_1(1235)$	$h_1(1170)$
$I^G$	0, 1	0 <sup>+</sup>	1 <sup>+</sup>	0 <sup>-</sup>	0 <sup>-</sup>	1 <sup>+</sup>	0 <sup>-</sup>
$J^{PC}$	1 <sup>--</sup>	0 <sup>-+</sup>	1 <sup>--</sup>	1 <sup>--</sup>	1 <sup>--</sup>	1 <sup>+-</sup>	1 <sup>+-</sup>

Table 5.3: Coupling constants for  $\eta$  photoproduction used in the analysis.

Reggeon	$\Gamma_{V(A) \rightarrow \eta\gamma}$ (keV)	$\lambda_{\eta\gamma}$	$g^v$	$g^t$
$\rho$	50.6	0.910	2.7	4.2
$\omega$	3.9	0.246	14.2	0.
$\phi$	55.84	0.38	-4.3	-0.08
$b_1$	-	0.1	0.	-7.6
$h_1$	-	2/3 $b_1$	0.	2/3 $b_1$

Since there are no data for the decay  $b_1 \rightarrow \eta\gamma$ , therefore  $\lambda_{\eta\gamma}$  was arbitrary fixed to  $\lambda_{\eta\gamma} = 0.1$ . The contribution of the  $h_1$  meson is suggested to be a fraction of 2/3 of the  $b_1$  contribution.

An experimental observation is that mesons fall into linear trajectories when their spin is plotted over the squared meson masses (Chew-Frautschi plot) [61,62]. These trajectories are called Regge trajectories and are shown on the Fig. 5.3. In addition to them the so-called Regge cuts trajectories,  $f_2$  and Pomeron trajectories are plotted on the right side of the figure. We will discuss Regge cuts further in the text.

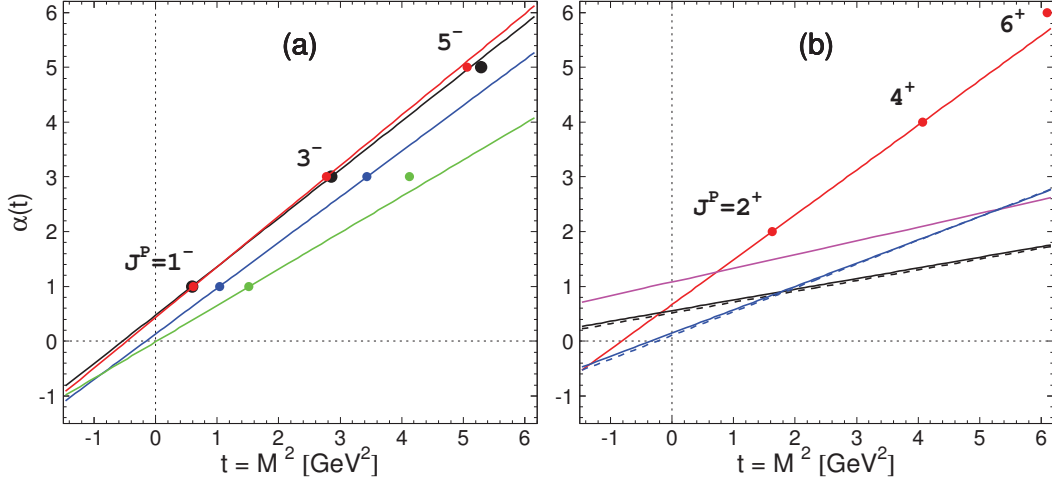


Figure 5.3: Regge trajectories: (a)  $\rho$  black,  $\omega$  red,  $\phi$  blue,  $b_1$  and  $h_1$  green; Regge cuts (b)  $f_2$  red,  $\mathbb{P}$  magenta,  $\rho\mathbb{P}$  black solid,  $\omega f_2$  blue dashed,  $\rho\mathbb{P}$  black solid,  $\omega\mathbb{P}$  black dashed.

For the Regge trajectories the general parametrization [63] is used:

$$\alpha(t) = \alpha_0 + \alpha' t, \quad (5.29)$$

Technically, the  $t$ -channel exchange of Regge trajectories is done by replacing the single meson propagator by the following expression:

$$\frac{1}{t - M_{V(A)}^2} \Rightarrow \left(\frac{s}{s_0}\right)^{\alpha(t)-1} \frac{\pi \alpha'}{\sin[\pi\alpha(t)]} \frac{\mathcal{S} + e^{-i\pi\alpha(t)}}{2} \frac{1}{\Gamma(\alpha(t))}, \quad (5.30)$$

where  $\mathcal{S}$  is the signature of the Regge trajectory,  $s_0$  is a mass scale factor, commonly set to  $1 \text{ GeV}^2$ . The Gamma function  $\Gamma(\alpha(t))$  is introduced to suppress additional poles of the propagator.

The signature  $\mathcal{S}$  is determined as  $\mathcal{S} = (-1)^J$  for bosons and  $\mathcal{S} = (-1)^{J+1/2}$  for fermions. So  $\mathcal{S} = -1$  for the vector and axial-vector mesons, and  $\mathcal{S} = +1$  for tensor mesons.

As Donnachie and Kalashnikova suggested [60], in addition to Regge trajectories, also Regge cuts play an important role and can even dominate, they are also shown on Fig. 5.3. These Regge cuts can be considered as a box diagram, where always two particles are exchanged. In case of  $\eta$  photoproduction  $\rho\mathbb{P}$ ,  $\rho f_2$  and  $\omega\mathbb{P}$ ,  $\omega f_2$  cuts were taken into account. Here  $\mathbb{P}$  is the Pomeron with quantum numbers of the vacuum  $0^+(0^{++})$  and  $f_2$  is a tensor meson with quantum numbers  $0^+(2^{++})$ .

The exchange of two Reggeons with linear trajectories

$$\alpha_i(t) = \alpha_i(0) + \alpha'_i t, \quad i = 1, 2 \quad (5.31)$$

yields a cut with a linear trajectory  $\alpha_c(t)$  [59]

$$\alpha_c(t) = \alpha_c(0) + \alpha'_c t, \quad (5.32)$$

where

$$\begin{aligned}\alpha_c(0) &= \alpha_1(0) + \alpha_2(0) - 1, \\ \alpha'_c &= \frac{\alpha'_1 \alpha'_2}{\alpha'_1 + \alpha'_2}.\end{aligned}\quad (5.33)$$

All four contributions from Regge cuts can be written in the following form:

$$D_{cut} = \left(\frac{s}{s_0}\right)^{\alpha_c(t)-1} e^{-i\pi\alpha_c(t)/2} e^{d_c t}.\quad (5.34)$$

Thus, the vector meson propagators are replaced by:

$$D_V = D_V + c_{V\mathbb{P}} D_{V\mathbb{P}} + c_{Vf} D_{Vf}, \quad V = \rho, \omega, \quad (5.35)$$

the axial vector meson propagators are replaced by:

$$D_A = D_A + \sum_{V=\rho,\omega} (\tilde{c}_{V\mathbb{P}} D_{V\mathbb{P}} + \tilde{c}_{Vf} D_{Vf}), \quad A = b_1, h_1 \quad (5.36)$$

where the coefficients  $c_{V\mathbb{P}}, c_{Vf}$  are for natural parity cuts and  $\tilde{c}_{V\mathbb{P}}, \tilde{c}_{Vf}$  for un-natural parity cuts.

With this addition the invariant amplitudes will be upgraded to the following form:

$$\lambda_\rho g_\rho^{v,t} \frac{1}{t - M_\rho^2} \rightarrow \lambda_\rho g_\rho^{v,t} [D_\rho(s, t) + c_{\rho\mathbb{P}} D_{\rho\mathbb{P}}(s, t) + c_{\rho f} D_{\rho f}(s, t)], \quad (5.37)$$

$$\lambda_\omega g_\omega^{v,t} \frac{1}{t - M_\omega^2} \rightarrow \lambda_\omega g_\omega^{v,t} [D_\omega(s, t) + c_{\omega\mathbb{P}} D_{\omega\mathbb{P}}(s, t) + c_{\omega f} D_{\omega f}(s, t)], \quad (5.38)$$

$$\begin{aligned}\lambda_{b_1} g_{b_1}^t \frac{1}{t - M_{b_1}^2} &\rightarrow \lambda_{b_1} g_{b_1}^t D_{b_1}(s, t) + \lambda_\rho g_\rho^t [\tilde{c}_{\rho\mathbb{P}} D_{\rho\mathbb{P}}(s, t) + \tilde{c}_{\rho f_2} D_{\rho f_2}(s, t)] \\ &\quad + \lambda_\omega g_\omega^t [\tilde{c}_{\omega\mathbb{P}} D_{\omega\mathbb{P}}(s, t) + \tilde{c}_{\omega f_2} D_{\omega f_2}(s, t)].\end{aligned}\quad (5.39)$$

An alternative Regge formalism is discussed in [54] as well. If we consider the Regge propagator from Eq. (5.30) we will see that the energy dependence is proportional to  $s^{\alpha(t)-1}$ , which violates the crossing symmetry. Therefore we cannot predict the behavior of this amplitude under the dispersion integral. Thus the alternative parametrization is given below:

$$D_{V,A} = -\beta_i(t) \frac{e^{-i\pi\alpha_{V,A}(t)} - 1}{\sin[\pi\alpha_{V,A}(t)]} (r_i^{V,A} \nu)^{\alpha_{V,A}(t)-1}. \quad (5.40)$$

Here the Mandelstam variable  $s$  is replaced by the crossing variable  $\nu$  and the Gamma function in the denominator of Eq. (5.30) is replaced by a more general residue  $\beta_i(t)$ , where  $i = 1, 2, 3, 4$  is index of the invariant amplitudes.  $r_i^{V,A}$  are scale parameters of dimension  $\text{GeV}^{-1}$ . Each exchange,  $V$  or  $A$ , has its own scale parameter.

In Ref. [64] the following residues for  $V = \rho, \omega, \phi$  and  $A = b_1, h_1$  are given

$$\beta_1^V(t) = g_1^V t \frac{-\pi\alpha'^V}{2} \frac{1}{\Gamma(\alpha^V(t) + 1)}, \quad (5.41)$$

$$\beta_4^V(t) = g_4^V \frac{-\pi\alpha'^V}{2} \frac{1}{\Gamma(\alpha^V(t))}, \quad (5.42)$$

$$\beta_2^A(t) = g_2^A t \frac{-\pi\alpha'^A}{2} \frac{1}{\Gamma(\alpha^A(t) + 1)}. \quad (5.43)$$

Here the prime in  $\beta'_2$  denotes the fact that this is the  $A'_2$  residue, which explains the factor of  $t$ . The factor  $-\pi\alpha'/2$  ensures the correct on-shell couplings. Both functions  $1/\Gamma(\alpha+1)$  and  $1/\Gamma(\alpha)$  are equal to 1 at the pole  $\alpha=1$ , however they differ in the physical region.

The values for the given trajectories as well as for Regge cuts are shown in Tab. 5.4

Table 5.4: The Reggeon and cut trajectories used in [54] and present work. Solution I (Regge ( $s$ ) in present work)) has contributions from  $\rho$ ,  $\omega$ ,  $b_1$ ,  $h_1$  and  $\rho f_2$ ,  $\omega f_2$ ,  $\rho\mathbb{P}$ ,  $\omega\mathbb{P}$ . Solution IV (Regge ( $\nu$ ) in present work)) has contributions from  $\rho$ ,  $\omega$ ,  $b_1$ ,  $h_1$ ,  $\phi$ .

Reggeon or cut	$\alpha(t)$
$\rho$	$0.477 + 0.885 t$
$\omega$	$0.434 + 0.923 t$
$b_1, h_1$	$-0.013 + 0.664 t$
$f_2$	$0.671 + 0.817 t$
$\mathbb{P}$	$1.08 + 0.25 t$
$\phi$	$0.10 + 0.85 t$
$\rho f_2$	$0.148 + 0.425 t$
$\omega f_2$	$0.106 + 0.436 t$
$\rho\mathbb{P}$	$0.557 + 0.195 t$
$\omega\mathbb{P}$	$0.514 + 0.197 t$

Both these models were used in the present data analysis. In the beginning we did not consider the implementation of the reggeized background into our model, since we are working in the low energy region from  $\eta$  production threshold up to  $W \approx 1850$  MeV. However, as it was written in the beginning, we found a productive method to decrease the impact from such background in the resonance region and perform partial wave analysis.

This method is following. We multiply each Regge amplitude with an energy dependent damping factor that has a form

$$DF(W) = 1 - e^{-\frac{W-W_{thr}}{\Lambda}}, \quad (5.44)$$

for Regge amplitudes written in terms of  $s$ , and

$$DF(\nu) = 1 - e^{-\frac{\nu-\nu_{thr}}{\Lambda}}, \quad (5.45)$$

for Regge amplitudes, written in terms of  $\nu$ . Here  $W_{thr} = m_p + m_\eta$ , and  $\nu_{thr}$  corresponds to the  $\eta N$  production threshold for each  $t$  value on which we perform our integration. Factors  $\Lambda$  were obtained from the fit of the data in the resonance region with an isobar model. We discuss the values for them in Chapter 7.

As a result of this procedure we obtain the following behavior:

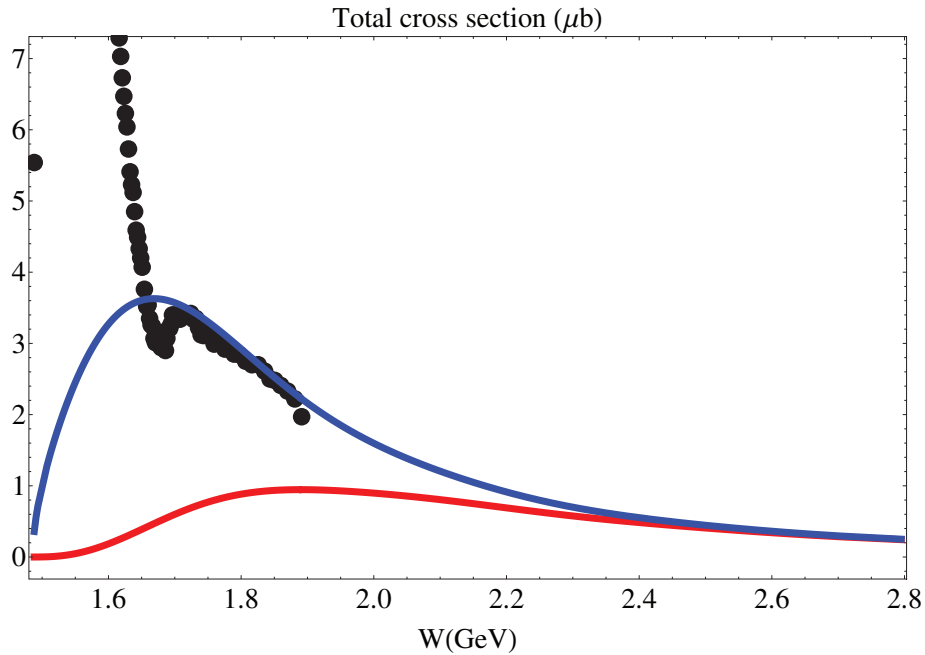


Figure 5.4: Regge contributions into the total cross section. Blue line shows normal Regge contributions, red line shows contributions with  $\text{Regge} \times DF$ .

As one can see this method effectively deals with large contributions and solves the duality problem.

## 5.2 Other partial wave analysis models

In addition to the described above MAID model one should list alternative partial wave analysis approaches. They are: Bonn-Gatchina (BnGa), Jülich-Bonn (JüBo) and SAID models. Since the main goal of this work is not related to the comparison of the approaches only brief introduction of the models based on a common paper which is done by MAID, SAID, JüBo and BnGa members [65] is listed.

### 5.2.1 Bonn-Gatchina approach

The BnGa approach relies on a fully relativistically invariant operator expansion method. The advantage of the model is in direct imposing analyticity and unitarity constraints as well as the



simultaneous analysis of many (more than 100) reactions. The scattering amplitude includes in itself the decay of baryon resonances and some  $t$  and  $u$ -channel exchange diagrams.

In order to impose the listed above properties a so-called  $N/D$ -method is applied to the description of the resonance spectrum. In a simplified version this method uses  $K$ -matrix approach with real parts of the two-body loop diagrams taken into account. For three-body final states, only the imaginary part is taken into account, which is calculated as the three-body integral.

At high energies the  $t$ -channel meson exchanges are taken into account. The contributions from  $\pi, \rho, \omega, K$  or  $K^*$  mesons are written in terms of Regge amplitudes.

### 5.2.2 Jülich-Bonn approach

Strictly speaking JüBo is not a partial wave analysis but rather a dynamical coupled-channel approach. This approach allows us to extract the baryon spectrum and simultaneously analyze pion- and photon-induced reactions.

Its advantage is that the theoretical constraints like analyticity and unitarity are manifestly implemented. The formalism allows us to determine the resonance states in terms of poles in the complex energy plane of the scattering matrix together with corresponding residues and helicity couplings. However this approach has its own disadvantages. For example the long fitting time and high computational efforts which is the consequence of the highly complex equations that leads from theory.

### 5.2.3 SAID approach

The recent SAID parametrization is based on a Chew-Mandelstam  $K$ -matrix. The hadronic  $T$  matrix is described

$$T_{\alpha\beta} = [1 - \bar{K}C]_{\alpha\sigma}^{-1} \bar{K}_{\sigma\beta} \quad (5.46)$$

where  $C$  is the Chew-Mandelstam function. The formalism differs from all described before in the way that resonance properties except  $\Delta(1232) 3/2^+$  are deduced. This resonance is explicitly introduced as  $K$ -matrix pole, all other resonances are calculated from the factor  $[1 - \bar{K}C]^{-1}$  which is common for  $\pi N$  scattering and  $\gamma N$  reactions. And also the resonance poles are not added by hand but are generated in the data analysis procedure. Thus only those are necessary are produced.



## Chapter 6

---

### Fixed- $t$ dispersion relation approach. Previous results

---

This section is devoted to the method of fixed- $t$  dispersion relations. First, mathematical aspect is described. Then, previous applications of this method are discussed. The main attention is put on the work written by Aznauryan on photo- and electroproduction of  $\eta$  meson [66]. Finally the model, used for the present data analysis is considered and the comparison with work of Aznauryan is done.

#### 6.1 Dispersion relations, mathematical formulation

Dispersion relations should be first formulated mathematically. Imagine that we have any complex function  $f(z)$  that is analytic in the upper half-plane and satisfies the following condition:  $Imf(z) \rightarrow 0, z \rightarrow \infty$ . Therefore we can write the following relation:

$$f(z) = \frac{1}{2\pi i} \oint \frac{f(z')}{z' - z} dz' = \frac{1}{2\pi i} \left( \mathcal{P} \int_{-\infty}^{+\infty} \frac{f(z')}{z' - z} dz' + i\pi f(z) \right) \quad (6.1)$$

Here  $\mathcal{P}$  is a notation for principle value integral,  $z'$  is a running integrating variable.

By simplification of this formula one can obtain the well-known relations for real and imaginary parts of  $f(z)$ :

For real part one gets:

$$Ref(z) = \frac{1}{\pi} \mathcal{P} \int_{-\infty}^{+\infty} \frac{Imf(z')}{z' - z} dz' \quad (6.2)$$

For imaginary part one gets:

$$Imf(z) = -\frac{1}{\pi} \mathcal{P} \int_{-\infty}^{+\infty} \frac{Ref(z')}{z' - z} dz' \quad (6.3)$$

For the complex even functions  $f(-z) = f^*(z)$  one gets the following relations for real and imaginary parts:

$$Ref(z) = \frac{2}{\pi} \mathcal{P} \int_0^{+\infty} \frac{z Imf(z')}{z'^2 - z^2} dz' \quad (6.4)$$

$$Imf(z) = -\frac{2}{\pi} \mathcal{P} \int_0^{+\infty} \frac{z' Ref(z')}{z'^2 - z^2} dz' \quad (6.5)$$

For the odd functions  $f(-z) = -f^*(z)$ , real and imaginary parts are calculated as shown below:

$$Ref(z) = \frac{2}{\pi} \mathcal{P} \int_0^{+\infty} \frac{z' Imf(z')}{z'^2 - z^2} dz' \quad (6.6)$$

$$Imf(z) = -\frac{2}{\pi} \mathcal{P} \int_0^{+\infty} \frac{z Ref(z')}{z'^2 - z^2} dz' \quad (6.7)$$

## 6.2 Data analysis using the fixed- $t$ dispersion relations approach

In data analysis different kinds of dispersion relations may be used and the one we are interested in is the method of fixed- $t$  dispersion relations for invariant amplitudes, which was successfully applied in the data analysis in the resonance region [19–29].

For example one can see the application of it in the works of Chew and Ball [39, 67], and also find the extensions pion electroproduction from Devenish and Dennery [68, 69].

Since 1990's the method was successfully applied to analyze the pion production data from the new generation of electron accelerators. In 2000's it was applied to  $\eta$  production and used in the analysis of the data on  $\eta$  photo- and electroproduction [66, 70].

Since our goal is to analyze the  $\eta$  photoproduction data we are interested in a work of Aznauryan [66] where the data existing at that time on  $\gamma p \rightarrow \eta p$  reaction [48, 71–74] were analyzed using fixed- $t$  dispersion relations approach. We consider in details the approach from this work.

### 6.2.1 Data analysis using fixed- $t$ dispersion relations in work of Aznauryan

The data set contained only three experimental observables:  $d\sigma/d\Omega$ ,  $T$ ,  $\Sigma$ . Below one can find the table which shows the energy range for the fitted data used in the analysis.

$\gamma p \rightarrow \eta p$	Observable	Energy range $W$ (MeV)
[73]TAPS	$d\sigma/d\Omega$	1491-1537
[71]GRAAL	$d\sigma/d\Omega$	1490-1716
[72]CLAS	$d\sigma/d\Omega$	1528-2012
[74] ELSA	$T$	1492-1719
[48] GRAAL	$\Sigma$	1506-1688

Table 6.1: Database used in the analysis in the work [66]

These data were analyzed with the set of 13 resonances:

Table 6.2: Resonances used for the data analysis in work [66].

Resonance	$\ell$
$N(1440)$	$1/2^+$ 1
$N(1520)$	$3/2^-$ 2
$N(1535)$	$1/2^-$ 0
$N(1650)$	$1/2^-$ 0
$N(1675)$	$5/2^-$ 2
$N(1680)$	$5/2^+$ 3
$N(1700)$	$3/2^-$ 2
$N(1710)$	$1/2^+$ 1
$N(1720)$	$3/2^+$ 1
$N(1900)$	$3/2^+$ 1
$N(1990)$	$7/2^+$ 3
$N(2000)$	$5/2^+$ 3
$N(2150)$	$3/2^-$ 2

As a result the contributions of first eight resonances from Tab. 6.2 were found and the model dependence of the resonance parameters was studied. In order to estimate this dependence the isobar model approach was used for the analysis of the same data.

Let us consider the formalism used in this work, taking into account that formulas were written originally for case  $\gamma^*N \rightarrow \eta N$ , and in this work are simplified for  $\gamma p \rightarrow \eta p$ .

The fixed- $t$  dispersion relations were performed for a set of four invariant amplitudes:

$$B_1(s, t)[GeV^{-2}], B_2(s, t)[GeV^{-2}], B_6(s, t)[GeV^{-3}], B_8(s, t)[GeV^{-3}]. \quad (6.8)$$

These amplitudes were chosen as an independent set out of eight ones [38], that describe the electromagnetic current. The dimensions of the amplitudes are given in quadratic brackets.

At fixed value of  $t$  the dispersion relations were performed according to the the formula below

$$\begin{aligned} Re B_i(s, t) &= eg_{\eta NN} R_i^p \left( \frac{1}{s - m_p^2} + \frac{\eta_i}{u - m_p^2} \right) \\ &+ \frac{\mathcal{P}}{\pi} \int_{s_{cut}}^{\infty} Im B_i(s', t) \left( \frac{1}{s' - s} + \frac{\eta_i}{s' - u} \right) ds', \end{aligned} \quad (6.9)$$

where  $m_p$  denotes the proton mass,  $s$ ,  $t$  and  $u$  are the Mandelstam variables,  $s_{cut} = (m_p + m_\pi)^2$  is the lowest limit for integration,  $e^2/4\pi = 1/137$ ,  $g_{\eta NN}$  is the  $\eta NN$  pseudoscalar coupling constant.

The factors  $\eta_i$  in the dispersion relations define the crossing symmetry properties of the invariant amplitudes, they are equal to  $\eta_1 = \eta_2 = \eta_6 = 1, \eta_8 = -1$ .  $R_i^p$  correspond to the residues in the nucleon poles and are recalculated through the nucleon proton Pauli form factors  $F_1^p = 1$ ,  $F_2^p = \kappa_p/2m_p$  with  $\kappa_p = 1.79$ . Thus the residues have the following form:

$$\begin{aligned} R_1^p &= F_1^p + 2m_p F_2^p, \\ R_2^p &= -F_1^p, \\ R_6^p &= 2F_2^p, \\ R_8^p &= F_2^p. \end{aligned} \quad (6.10)$$

The integrating path at a fixed- $t$  lies in both physical and unphysical regions. In the unphysical region from  $s_{cut} = (m_p + m_\pi)^2$  up to  $s = (m_p + m_\eta)^2$  the contributions only from  $N(1440) 1/2^+$ ,  $N(1535) 1/2^-$  and  $N(1650) 1/2^-$  resonances are taken into account for  $Im B_i(s, t)$ .

In the physical region contributions from all resonances are taken into account and constructed from the Breit-Wigner parameterizations.

The resonance contributions to the multipole amplitudes for all resonances except Roper are parameterized with a slightly different original MAID isobar model described in [9]. And therefore very similar to parametrization given Eqs. (5.3 - 5.5) with some small and insignificant changes. The energy dependent widths are as well very similar to what is written in a set of formulas given in Eqs. (5.6)

For  $N(1440) 1/2^+$ , however parametrization differs from the one that we use. Roper is a broad resonance and, despite lying below threshold, is expected to have also an influence on the production mechanism above threshold.

For such a case Aznauryan starts from an effective Lagrangian for the nucleon to Roper excitation and for the invariant amplitudes  $B_i^R(s, t)$  for both physical and unphysical regions we obtain:

$$B_i^{Rop}(s, t) = eg_{\eta NR} R_i^{Rop} \frac{1}{s - M_{Rop}^2 + iM_{Rop}\Gamma_{tot}}, \quad (6.11)$$

where:

$$\begin{aligned} R_1^{Rop} &= (m_p + M_{Rop})F_2^{Rop}, \\ R_2^{Rop} &= 0, \\ R_6^{Rop} &= 2F_2^{Rop}, \\ R_8^{Rop} &= F_2^{Rop}. \end{aligned}$$

The mass and the width of  $N(1440) 1/2^+$  were set to  $M_{Rop} = 1440$  MeV,  $\Gamma = 350$  MeV respectively. The branching ratio into the  $\pi N$  channel was taken to  $\beta_{\pi N} = 60\%$ . Values for  $A_{1/2}$  were taken from the Particle Data Group and then calculate the form factor  $F_2^{Rop}$ :

$$A_{1/2} = e \left( \pi k_R \frac{M_{Rop}}{m_p} \right)^{1/2} F_2^{Rop}. \quad (6.12)$$

$$F_2^{Rop} \equiv \frac{\kappa_p^R}{2m_p}, \quad \kappa_p^R = -0.5. \quad (6.13)$$

The contributions from  $N(1535) 1/2^-$  and  $N(1650) 1/2^-$  resonances in the unphysical region were calculated using following expressions:

$$\begin{aligned} \mathcal{E}_{0+} &\equiv \frac{E_{0+}}{2W[(E_i + m_p)(E_f + m_p)]^{1/2}}, \\ B_1(s, t) &= \mathcal{E}_{0+}, \\ B_2(s, t) &= 0, \\ B_6(s, t) &= 2B_8(s, t) = -\frac{(W - m_p)(E_i + m_p)\mathcal{E}_{0+}}{Wk^2}. \end{aligned} \quad (6.14)$$

with  $E_i$  and  $E_f$  energies in the initial and the final state.

## 6.2.2 Data analysis using fixed- $t$ dispersion relations with EtaMAID

Since the previous work [66] was published a new and precise data on  $\eta$  photoproduction were taken. We want to analyze these data using fixed- $t$  dispersion relations procedure. Let us consider our parametrization and discuss the differences from [66].

The data with the preliminary analysis with Legendre polynomials have already been given in Chapter 4, the energy and the angular coverages of these data are shown on Tab. 4.1. An EtaMAID isobar model approach is described in Section 5.1.

In present data analysis the dispersion integrals are performed for  $A_i(\nu, t)$ ,  $i = 1, 2, 3, 4$  invariant amplitudes which we chosen alternatively to  $B_i(s, t)$ . These amplitudes are related to the amplitudes  $B_1, B_2, B_6, B_8$  by the following relations:

$$\begin{aligned} A_1(\nu, t)[GeV^{-2}] &= B_1(\nu, t) - m_p B_6(\nu, t), \\ A_2(\nu, t)[GeV^{-4}] &= \frac{2B_2(\nu, t)}{t - m_\eta^2}, \\ A_3(\nu, t)[GeV^{-3}] &= -B_8(\nu, t), \\ A_4(\nu, t)[GeV^{-3}] &= -\frac{1}{2}B_6(\nu, t). \end{aligned} \quad (6.15)$$

In our formalism the Mandelstam variable  $s$  is replaced with a crossing symmetrical variable  $\nu$ . The relations between them are given in Eqs. (3.11) and (3.12).

Let us first describe the construction of invariant amplitude below threshold as this is the most difficult part in the analysis.

Multipoles and CGLN amplitudes are functions in close connection to experimental observables. They are generally only defined above threshold, and for multipoles, the threshold behavior is given by  $E_{\ell_{\pm}}, M_{\ell_{\pm}} \propto q^{\ell}$ , see Eqs. (5.12 and 5.13). Taking this into account we can define:

$$\tilde{E}_{\ell_{\pm}} = E_{\ell_{\pm}}/q^{\ell}, \quad \tilde{M}_{\ell_{\pm}} = M_{\ell_{\pm}}/q^{\ell}. \quad (6.16)$$

Then by going into unphysical region we face the problem with the meson momenta  $q(W)$  which real part becomes zero at threshold and below threshold the momenta starts having only imaginary part. In our parametrization of the multipoles Eq. (5.12) and Eq. (5.13) we always use  $|q^2(W)|$  which is very convenient because this value can be easily defined in this area.

Then we have a problem with the scattering angle  $\theta$  which is undefined in the area outside  $\theta = 0$  and  $\theta = 180$  degrees. Cosine of the scattering angle  $\cos \theta$  is infinite at threshold, however the product of  $\cos \theta$ , and  $q$  remains finite and can be easily extrapolated into unphysical region for any  $t$  and  $s$  or  $\nu$ , and using Eq. (3.9):

$$q \cos \theta = \frac{t - m_{\eta}^2 + 2k\omega}{2k}. \quad (6.17)$$

Taking this into account we we construct modified CGLN amplitudes  $\tilde{F}_i$ :

$$\tilde{F}_1 = F_1, \quad \tilde{F}_2 = F_2/q, \quad \tilde{F}_3 = F_3/q, \quad \tilde{F}_4 = F_4/q^2. \quad (6.18)$$

At threshold these modified CGLN amplitudes retain contributions from any multipole. In our case we truncate our series at the maximal orbital angular momentum  $\ell_{max} = 3$ :

$$\begin{aligned} \tilde{F}_1 = & \tilde{E}_{0+} + 3(\tilde{M}_{1+} + \tilde{E}_{1+})q \cos \theta + (3\tilde{M}_{2-} + \tilde{E}_{2-})q^2 \\ & + (\tilde{E}_{2+} + 2\tilde{M}_{2+})(15(q \cos \theta)^2 - 3q^2)/2 \\ & + 3q^2(4\tilde{M}_{3-} + \tilde{E}_{3-})q \cos \theta, \end{aligned} \quad (6.19)$$

$$\begin{aligned} \tilde{F}_2 = & 2\tilde{M}_{1+} + \tilde{M}_{1-} + 3(3\tilde{M}_{2+} + 2\tilde{M}_{2-})q \cos \theta \\ & + 3\tilde{M}_{3-}(15(q \cos \theta)^2 - 3q^2)/2, \end{aligned} \quad (6.20)$$

$$\begin{aligned} \tilde{F}_3 = & 3(\tilde{E}_{1+} - \tilde{M}_{1+}) + 15(\tilde{E}_{2+} - \tilde{M}_{2+})q \cos \theta \\ & + 3(\tilde{E}_{3-} + \tilde{M}_{3-})q^2, \end{aligned} \quad (6.21)$$

$$\tilde{F}_4 = 3(\tilde{M}_{2+} - \tilde{E}_{2+} - \tilde{M}_{2-} - \tilde{E}_{2-}) - 15(\tilde{M}_{3-} + \tilde{E}_{3-})q \cos \theta. \quad (6.22)$$

The leading contributions are:

$$\tilde{F}_1 = \tilde{E}_{0+}, \quad (6.23)$$

$$\tilde{F}_2 = 2\tilde{M}_{1+} + \tilde{M}_{1-}, \quad (6.24)$$

$$\tilde{F}_3 = 3(\tilde{E}_{1+} - \tilde{M}_{1+}), \quad (6.25)$$

$$\tilde{F}_4 = 3(\tilde{M}_{2+} - \tilde{E}_{2+} - \tilde{M}_{2-} - \tilde{E}_{2-}). \quad (6.26)$$

Now we construct the invariant amplitudes:

$$\begin{aligned}
 A_1 &= \mathcal{N} \left\{ \frac{W + m_p}{W - m_p} \tilde{F}_1 - (E_f + m_p) \tilde{F}_2 + \frac{m_p(t - m_\eta^2)}{(W - m_p)^2} \tilde{F}_3 \right. \\
 &\quad \left. + \frac{m_p(E_f + m_p)(t - m_\eta^2)}{W^2 - m_p^2} \tilde{F}_4 \right\}, \\
 A_2 &= \frac{\mathcal{N}}{W - m_p} \left\{ \tilde{F}_3 - (E_f + m_p) \tilde{F}_4 \right\}, \\
 A_3 &= \frac{\mathcal{N}}{W - m_p} \left\{ \tilde{F}_1 + (E_f + m_p) \tilde{F}_2 + \left( W + m_p + \frac{t - m_\eta^2}{2(W - M_N)} \right) \tilde{F}_3 \right. \\
 &\quad \left. + \left( W - m_p + \frac{t - m_\eta^2}{2(W + m_p)} \right) (E_f + m_p) \tilde{F}_4 \right\}, \\
 A_4 &= \frac{\mathcal{N}}{W - m_p} \left\{ \tilde{F}_1 + (E_f + m_p) \tilde{F}_2 + \frac{t - m_\eta^2}{2(W - m_p)} \tilde{F}_3 + \frac{t - m_\eta^2}{2(W + m_p)} (E_f + m_p) \tilde{F}_4 \right\},
 \end{aligned} \tag{6.27}$$

where  $\mathcal{N} = 4\pi/\sqrt{(E_i + m_p)(E_f + m_p)}$ ,  $E_i$  and  $E_f$  are defined in Eq. (3.8).

With this procedure we get the imaginary parts of invariant amplitudes which remain finite down to  $\pi N$  threshold and containing contributions from all partial waves. This can be seen later in the text on Fig. 6.3

Finally after obtaining the imaginary parts of  $A_1(\nu, t)$ ,  $A_2(\nu, t)$ ,  $A_3(\nu, t)$ ,  $A_4(\nu, t)$  we can calculate the real parts via principle value integral:

$$\text{Re}A_i(\nu, t) = A_i^{pole}(\nu, t) + \frac{2}{\pi} \mathcal{P} \int_{\nu_{thr}(t)}^{\infty} d\nu' \frac{\nu' \text{Im}A_i(\nu', t)}{\nu'^2 - \nu^2}, \quad \text{for } i = 1, 2, 4 \tag{6.28}$$

$$\text{Re}A_i(\nu, t) = A_i^{pole}(\nu, t) + \frac{2\nu}{\pi} \mathcal{P} \int_{\nu_{thr}(t)}^{\infty} d\nu' \frac{\text{Im}A_i(\nu', t)}{\nu'^2 - \nu^2}, \quad \text{for } i = 3 \tag{6.29}$$

where  $\nu_{thr}(t)$  is a value corresponding to the  $\pi N$  production threshold, and calculated as

$$\nu_{thr}(t) = \frac{W_{thr}^2 - m_p^2}{2m_p} + \frac{t - m_\eta^2}{4m_p} \tag{6.30}$$

with  $W_{thr} = m_p + m_\pi$ ,  $A_i^{pole}(\nu, t)$  are the nucleon pole contributions coming from the Born terms.  $\text{Im}A_i(\nu', t)$  contain contributions from resonances and Regge contributions (when used in the analysis).

For the upper limit of the integration with resonances we choose  $\nu_{Res} = 2660$  MeV because at higher energies the contributions from the resonances might be neglected. In case when we use Regge background we choose  $\nu_{Regge} = 20$  GeV.



Thus at fixed- $t$  our path lies in the following regions: red, orange and green, see plot below.

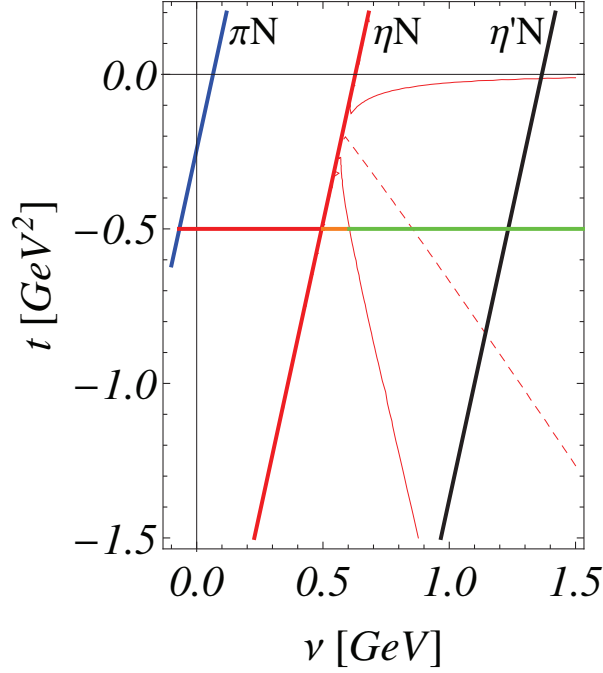


Figure 6.1: The Mandelstam plane for  $\gamma p \rightarrow \eta p$ . The red solid curves are the boundaries of the physical region from  $\theta = 0$  to  $\theta = 180^\circ$ . The red dashed line shows  $\theta = 90^\circ$ . The inclined vertical lines from left to right denote the thresholds for  $\pi N$ ,  $\eta N$ ,  $\eta' N$  production respectively. Horizontal line plotted at  $t = -0.5 \text{ GeV}^2$  with 3 colors: red, orange, green shows the energy regions for the integration at this value. The combination of red and orange regions cover energies from  $\nu_{thr}$  up to  $\nu_{\eta thr}$ . The green region covers energies from  $\nu_{\eta thr}$  up to  $\nu_{Res}$  and  $\nu_{Regge}$ .

Thus the relation for the real part can be written in simple form:

$$\text{Re}A_i(\nu, t) = \int_{\nu_{thr}(t)}^{\nu_{\eta thr}} \text{Im}A_i(Res) + \int_{\nu_{\eta thr}}^{\nu_{Res}} \text{Im}A_i(Res + Regge) + \int_{\nu_{Res}}^{\nu_{Regge}} \text{Im}A_i(Regge) \quad (6.31)$$

where  $\nu_{\eta thr}$  is calculated via

$$\nu_{\eta thr} = \frac{W_{\eta thr}^2 - m_p^2}{2m_p} + \frac{t - m_\eta^2}{4m_p}, \quad (6.32)$$

with  $W_{\eta thr} = m_p + m_\eta$ . A more clear way is to use the upper limits as a  $t$  dependent function, however this will change the results insignificantly.

After the real parts of invariant amplitudes are obtained we use the projection formulas written in the Appendix Eq. (A.7) in order to get the CGLN amplitudes which we then combine into helicity amplitudes Eq. (A.8) because of more compact formulas for the experimental observables.

### 6.2.3 Restrictions on the $t$ values for dispersion relations

It is also important to mention the difficulties with the data analysis using fixed- $t$  dispersion relations. They are related to the divergence of the dispersion relations at  $t = \text{const}$ . This problem was discussed in paper on pion photoproduction by Pasquini, Drechsel, Tiator [75].

In Eqs. (6.28, 6.29) we start integration from some  $\nu_{thr}(t)$  and go up to  $\nu_{Regge}$ , therefore part of our integral lies in the unphysical region. The way to construct the imaginary parts of invariant amplitudes in this area is to use the partial wave expansion of CGLN amplitudes Eq. (6.27) Where CGLN amplitudes are constructed according to already described procedure in Eq. (6.22).

But what about convergence of this expansion at large negative  $t$ -values? In present partial wave analysis we go up to  $t \approx -1.5 \text{ GeV}^2$  which is related to the last backward angle of  $\Sigma$  asymmetry [47]. Therefore we preform dispersion integrals for invariant amplitudes at this fixed value of  $t$ . According to [75] the convergence is based on the mathematical lemma: If a function  $f(z = x + iy)$  is analytic inside and on an ellipse  $C$  whose foci are at the points  $(x = \cos \theta = \pm 1, y = 0)$ , it can be expanded in a Legendre series. If we follow then the arguments from this paper we will have to solve the following equation.

$$\begin{aligned} & [s - (m_p + m_\eta)^2][s - (m_p - m_\eta)^2][u - (m_p + m_\eta)^2] \\ & \times [u - (m_p - m_\eta)^2] - (4m_p^2 - m_\eta^2)m_\eta^2 \\ & \times [2su - 2(m_p^2 - m_\eta^2)(s + u) + 2m_p^2 - m_\eta^4] = 0, \end{aligned} \quad (6.33)$$

for  $t = const$ , when  $s = u$  and

$$s + t + u = 2m_p^2 + m_\eta^2, \quad (6.34)$$

we get  $t = -4.83 \text{ GeV}^2$  therefore the the region where we are working have no kinematical boundaries.

In addition there is a work of Noelle [76] where the presented below box-diagram is discussed.

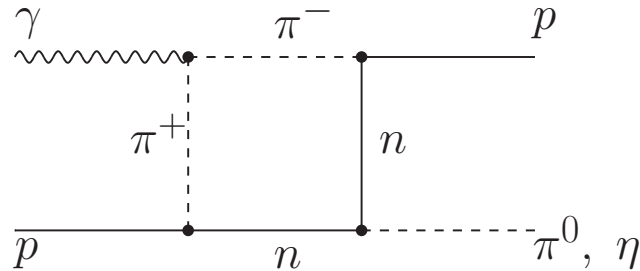


Figure 6.2: Diagram A from [76] for  $\gamma p \rightarrow \pi^0 p$  which gives the shape of  $su$  double spectral region.

This diagram also give corrections on our  $t$  values. However according to our analysis we can conclude that in our case the impact of this diagram should be small because we replace pion with an  $\eta$  that couples to the nucleon and the  $g_{\eta NN}$  coupling is small, therefore we can omit it.

## 6.2.4 Comparison of the approaches.

Taking into account information about these two approaches that were discussed in this chapter one can conclude that both of them are very similar to each other at some points. However there are differences between them. For the small differences we may put different multipole parametrization of the partial waves, less decay channels were taken into account by Aznauryan.

For the significant and most important differences we have that in our approach we take into account contributions from all resonances. Not only  $N(1440) 1/2^+$ ,  $N(1535) 1/2^-$  and

$N(1650) 1/2^-$ . This is especially important for  $N(1520) 3/2^-$  which contribution to the invariant amplitude is huge in comparison with other resonances despite very small branching ratio  $\beta_{\eta N} < 1\%$  and therefore must be taken into account. Such contribution you may see on figure below, where we compare invariant amplitudes from our initial solution with and without this resonance

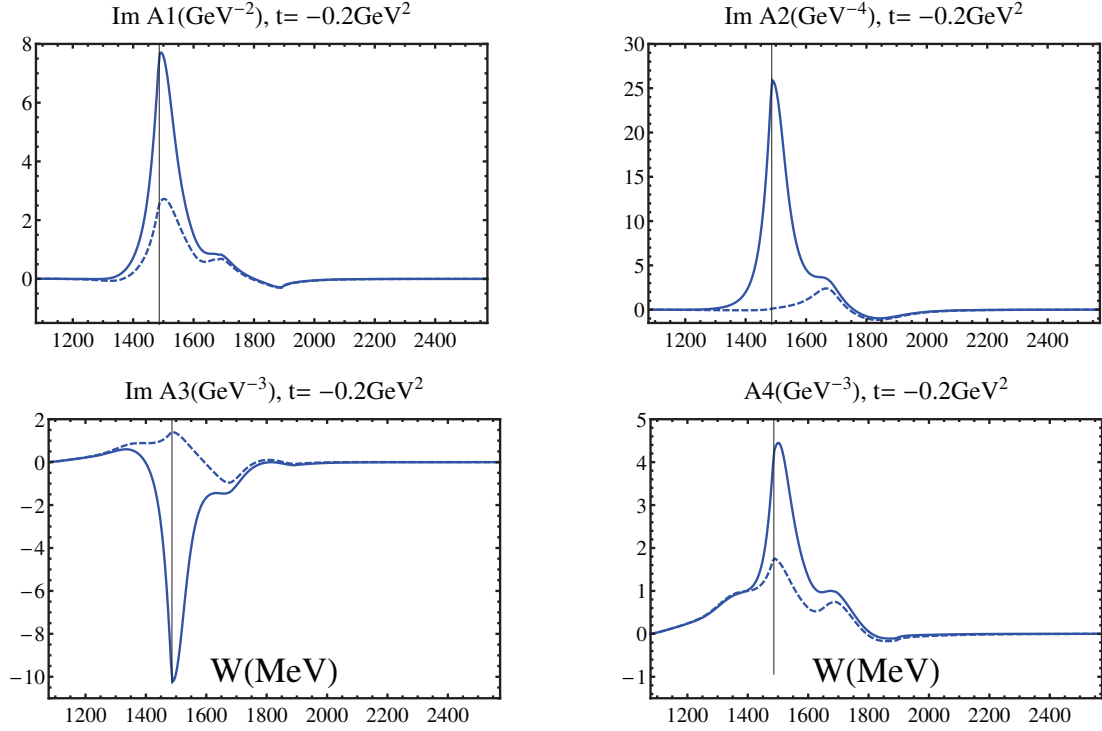


Figure 6.3: Invariant amplitudes for initial solution. Blue solid line shows imaginary parts of invariant amplitudes for a full set of resonances. Blue dashed line shows imaginary part of invariant amplitudes without  $N(1520) 3/2^-$ .

The second important difference is the resonance phase  $\Phi_j^\alpha$  which is introduced in our approach, as it will be shown in the chapter with the fit results it plays important role in the analysis.



# Chapter 7

---

## Fit results

---

This chapter is devoted to the description of the fit results obtained using isobar model (IB) and fixed- $t$  dispersion relations (DR) approaches. We pay a special attention to the comparison of results obtained with different methods. In our analysis we analyze the data presented in the table below.

Table 7.1: Data used in present work. In the first part of the table the fitted data is shown. In the second part of the table we show high energy data that was only described by our models.

$\gamma p \rightarrow \eta p$	Observable	Energy range (MeV)
[44] MAMI	$d\sigma/d\Omega$	1488-1851
[49] A2 MAMI	$T$	1495-1850
[49] A2 MAMI	$F$	1495-1850
[47] GRAAL	$\Sigma$	1490-1863
[50] CLAS	$E$	1525-1825
[77-80] DESY, Wilson, Daresbury, CEA	$d\sigma/dt$	2360-3987
[79] Daresbury	$\Sigma$	2360-2551
[81] Daresbury	$T$	2896

In our analysis we used the set of 14 resonances that were shown on the Tab. 3.1.

In our analysis we performed many fits where we tested the influence of resonant terms, Born terms and  $t$ -channel exchanges on the description the data. We obtained seven illustrative solutions with which we can show the evolution of our results. These 7 solutions are:

- Solution 1: With resonances only
- Solution 2: With resonances and Born terms
- Solution 3: With resonances Regge trajectories ( $s$ ) and Regge cuts ( $s$ )

Then we added unitarity phases  $\Phi_j^\alpha$  for  $j : 3/2^-, 3/2^+, 5/2^-$  states as a fitting parameters.

- Solution 4: With resonances  $\times e^{i\Phi_j^\alpha}$  and Born terms
- Solution 5: With resonances  $\times e^{i\Phi_j^\alpha}$ , Regge trajectories ( $s$ ) and Regge cuts ( $s$ )
- Solution 6: With resonances  $\times e^{i\Phi_j^\alpha}$  and Regge trajectories ( $\nu$ )

As a final step we added unitarity  $\Phi_j^\alpha$  for all resonances except  $N(1440) 1/2^+$ .

- Solution 7: With resonances  $\times e^{i\Phi_j^\alpha}$  for all resonances except  $N(1440) 1/2^+$ , and Regge trajectories ( $\nu$ )

We decided not to add the unitarity phase for Roper since we wanted to fit only the coupling constant of this resonance which describes the decay of  $N(1440) 1/2^+ \rightarrow \eta N$ .

Thus we get two groups of solutions. Group 1 where solutions are obtained without phases (Solutions 1-3). Group 2 where solutions are obtained using additional fitting parameters ( $\Phi_j^\alpha$ )(Solutions 4-7). Solutions from the first group have larger  $\chi^2$  values than solutions from the second one. Solutions 6 and 7 we consider as the final ones.

For each solution we show description of the observables. After we discuss solutions of group 1 and compare invariant amplitudes for them. Then we discuss solutions of group 2 and show comparison of invariant amplitudes as well. We show multipoles only for the last solution, however one can find plots of multipoles for all solutions in the Appendix. Resonances parameters, including unitarity phases, are discussed in the end.

## 7.1 Starting solution

Based on general considerations the starting solution has to be a *good one*, in order to get a reliable results during the minimization procedure. This means that resonance parameters should be more or less in agreement with, for example, PDG estimations and they should not vary too much from reliable physical values. Following these ideas and using the set of resonances from Tab. 3.1 we were able to obtain starting solution with a  $\chi^2/N_{dof} = 2.33$ .

The same resonance parameters are used as a starting parameters for the analysis using fixed- $t$  dispersion relations. The  $\chi^2$  value is much higher in this case:  $\chi^2/N_{dof} = 130$ . To get a good and reliable result one we use method of series, i.e we first obtain solution 1 (DR), then we use it as a starting solution for solution 2 (DR), then solution 2 (DR) is used as a starting one for solution 3 (DR) etc.

Below the description of the data with all obtained solutions is shown.

## 7.2 Solution 1. Fit results with resonances only

As a first step the fit was done with resonances only. The table below shows  $\chi^2$  values for the fitted data sets:

Table 7.2:  $\chi^2$  values for solution 1

Data	Observable	$\chi_{IB}^2$	$\chi_{DR}^2$	Number of points ( $N_{pt}$ )
[44] MAMI	$d\sigma/d\Omega$	4054	6889	2544
[49] A2 MAMI	$T$	523	1353	144
[49] A2 MAMI	$F$	509	975	144
[47] GRAAL	$\Sigma$	822	947	130
[50] CLAS	$E$	42	52	42
		$\chi_{IB}^2/N_{dof} = 2.07$	$\chi_{DR}^2/N_{dof} = 3.4$	

### 7.2.1 Description of the $d\sigma/d\Omega$ and the total cross section

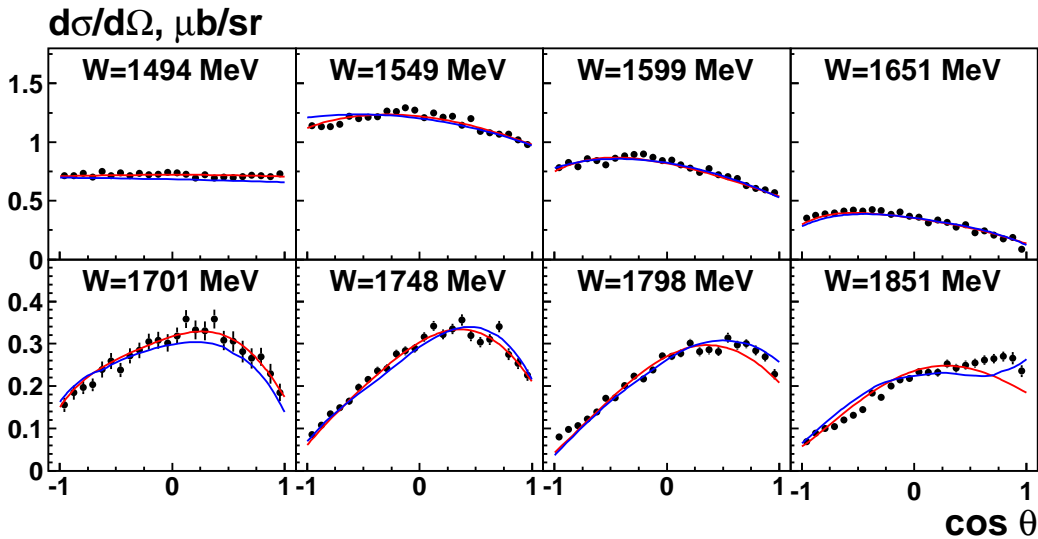


Figure 7.1: IB (red) and DR (blue) fit results for  $d\sigma/d\Omega$  [44]. Data are plotted from the threshold up to the last measured energy with the  $W$  step  $\sim 50$  MeV. For the IB fit  $\chi^2/N_{pt} = 4054/2544$ , for the DR fit  $\chi^2/N_{pt} = 6889/2544$ .

It is clearly seen that the data are described within the errors by both approaches. In most cases the differences between two curves are small. The descriptions are mainly overlapping with each other. Therefore the  $\chi^2$  difference is due to the small data errors. There is the problem with the description of the data at highest energies. The reason is that at these energies the contributions of  $t$ -channel exchanges should be taken into account. Fig. 7.2 shows the description of the total cross section. These data were not used in the analysis but it is useful to show the description of this observable because it indirectly shows the quality of the fit of the differential cross section. In addition the figure mainly shows the description of the cusp effect observed in the data which can be explained by the decay of  $N(1650) 1/2^-$  into  $K\Sigma$  channel.

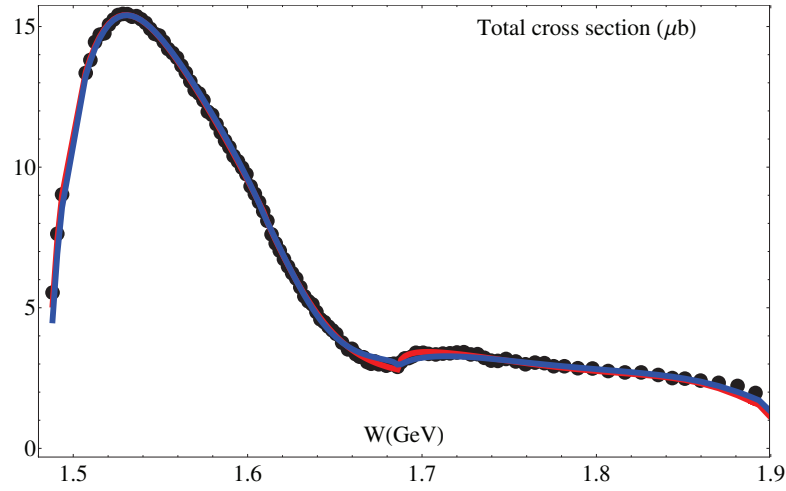


Figure 7.2: IB (red) and DR (blue) fit results for the total cross section, for solution 1. Results for all other solutions are very similar. Therefore we do not show similar figure for other solutions.

One can conclude that the data are perfectly described by both approaches and the cusp effect is reproduced.

### 7.2.2 Description of $T$ and $F$ asymmetries

The descriptions of polarization observables  $T$  and  $F$  are shown below on Figs. 7.3 and 7.4.

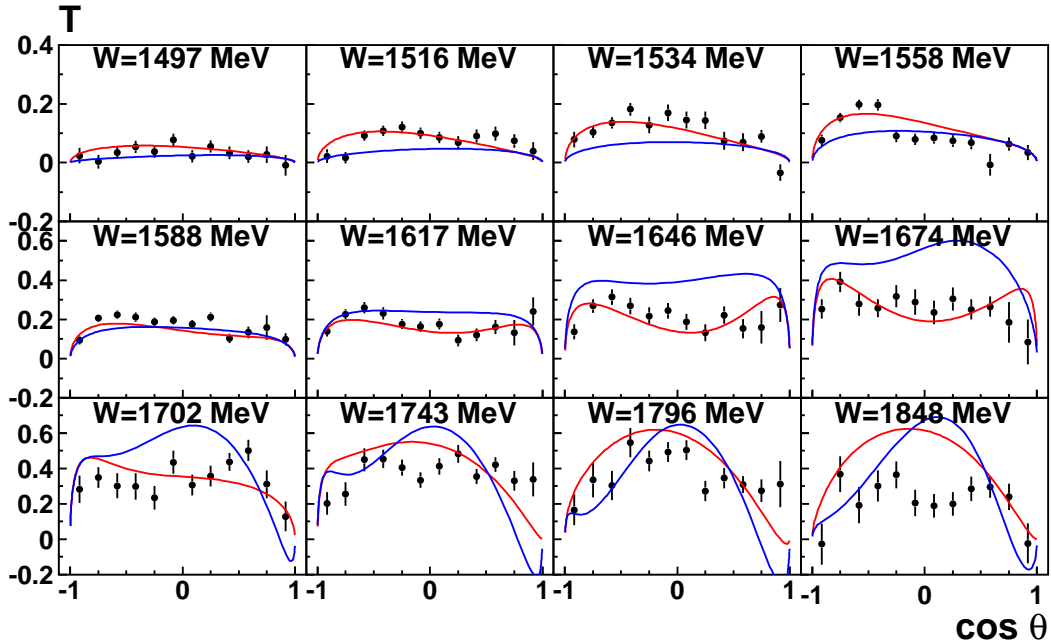


Figure 7.3: IB (red) and DR (blue) fit results for  $T$  [49]. For the IB fit  $\chi^2/N_{pt} = 523/144$ , for the DR fit  $\chi^2/N_{pt} = 1353/144$ .



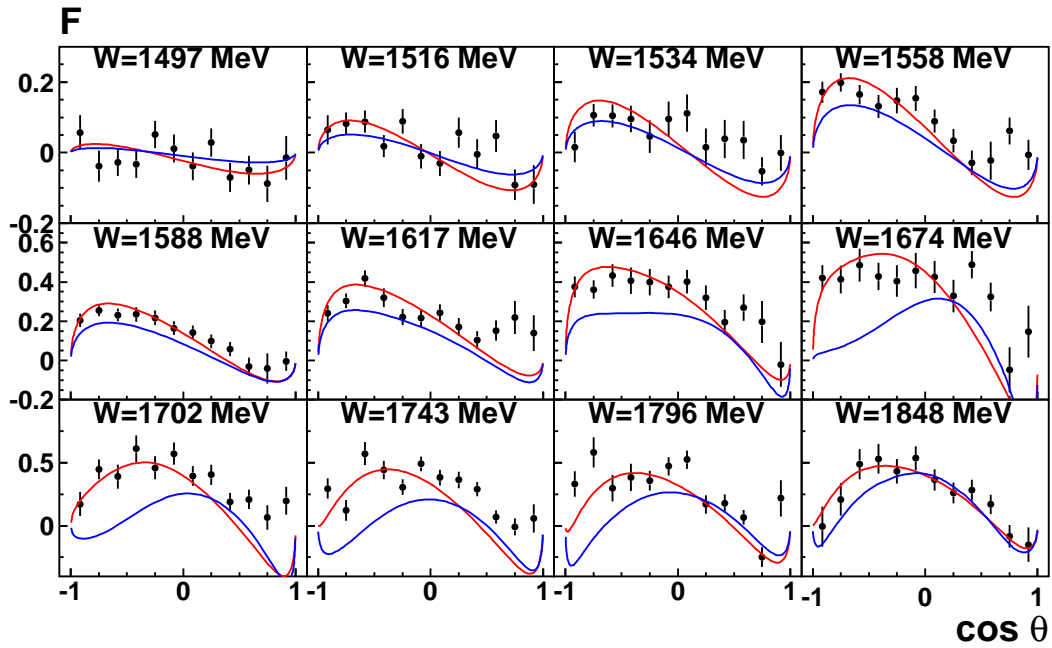


Figure 7.4: IB (red) and DR (blue) fit results for  $F$  [49]. For the IB fit  $\chi^2/N_{pt} = 509/144$ , for the DR fit  $\chi^2/N_{pt} = 975/144$ .

Unlike the case of differential cross section, the differences between IB and DR fits are bigger. In case of  $F$  red and blue curves are closer one to another than in case of  $T$ , where the red curves mostly lie within the errors but the blue ones are mainly off.

### 7.2.3 Description of $\Sigma$ and $E$ asymmetries

The descriptions of polarization observables  $\Sigma$  and  $E$  are shown below on Figs. 7.5 and 7.6.

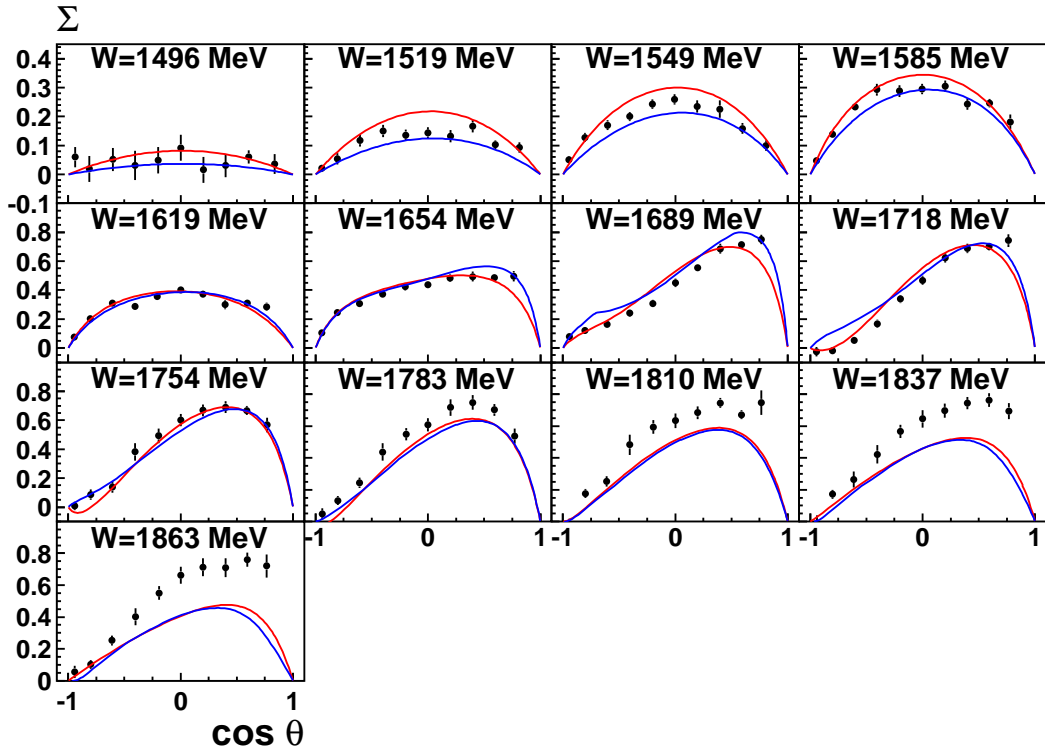


Figure 7.5: IB (red) and DR (blue) fit results for  $\Sigma$  [47]. For the IB fit  $\chi^2/N_{pt} = 822/130$ , for the DR fit  $\chi^2/N_{pt} = 947/130$

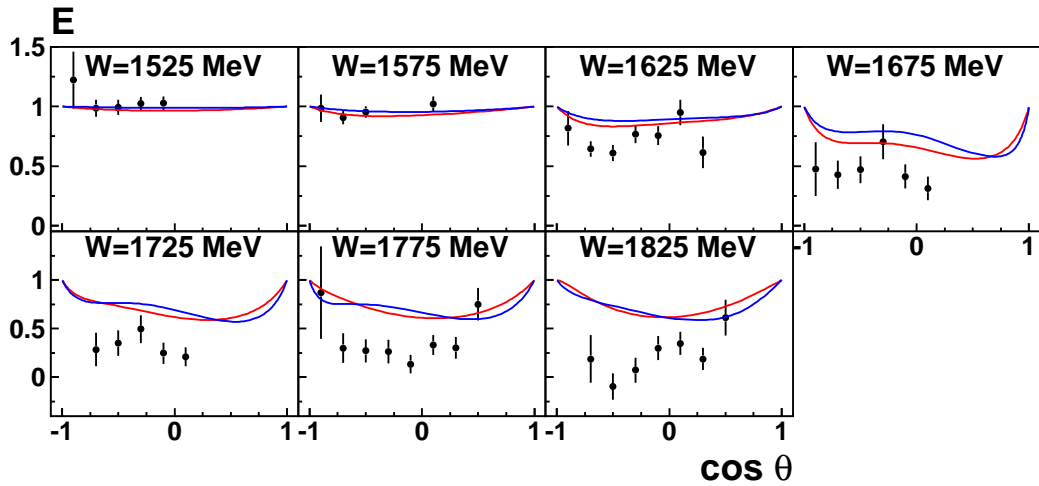


Figure 7.6: IB (red) and DR (blue) fit results for  $E$  [50]. For the IB fit  $\chi^2/N_{pt} = 42/42$ , for the DR fit  $\chi^2/N_{pt} = 52/42$

As one can see from Figs. 7.5 and 7.6 the results of both approaches are in a good agreement. Nevertheless the description is inconsistent with the data in case of  $\Sigma$  observable for energies above  $W = 1754$  MeV and with the data on  $E$  observable for energies above  $W = 1625$  MeV.

### 7.2.4 Solution 1 summary

This solution provides a good description of the data only for the differential and the total cross section. However the polarization data are only described with isobar model approach. Such a simple case where we have only resonances shows that one needs to improve our model in order to get good results.

### 7.3 Solution 2. Fit results with resonances and Born terms

In the next step Born terms were taken into account and Solution 2 was obtained. Unlike the case of pion photoproduction Born terms do not have a big impact to the scattering amplitude in  $\eta$  photoproduction. Nevertheless it is interesting to study the effect of such background.

The table of  $\chi^2$  values for the fitted data is presented below:

Table 7.3:  $\chi^2$  values for solution 2

Data	Observable	$\chi_{IB}^2$	$\chi_{DR}^2$	Number of points ( $N_{pt}$ )
[44] MAMI	$d\sigma/d\Omega$	3822	5170	2544
[49] A2 MAMI	$T$	605	1196	144
[49] A2 MAMI	$F$	443	711	144
[47] GRAAL	$\Sigma$	637	1111	130
[50] CLAS	$E$	29	37	42

$\chi_{IB}^2/N_{dof} = 1.88$      $\chi_{DR}^2/N_{dof} = 2.78$

#### 7.3.1 Description of the $d\sigma/d\Omega$

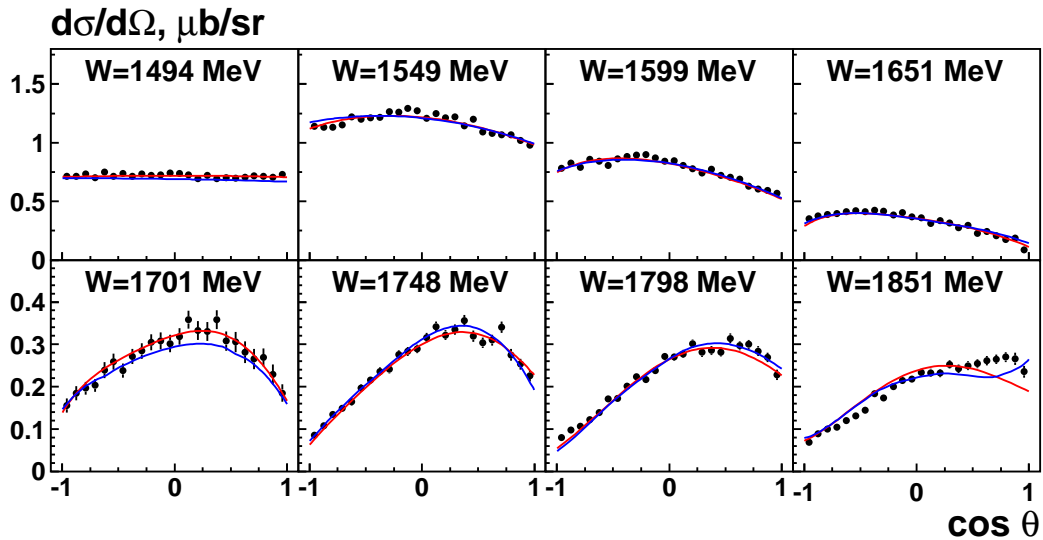


Figure 7.7: IB (red) and DR (blue) fit results for  $d\sigma/d\Omega$  [44]. Data are plotted from the threshold up to the last measured energy with the  $W$  step  $\sim 50$  MeV. For the IB fit  $\chi^2/N_{pt} = 3822/2544$ , for the DR fit  $\chi^2/N_{pt} = 5170/2544$ .

The description of this observable is similar to what was shown on Fig. 7.1

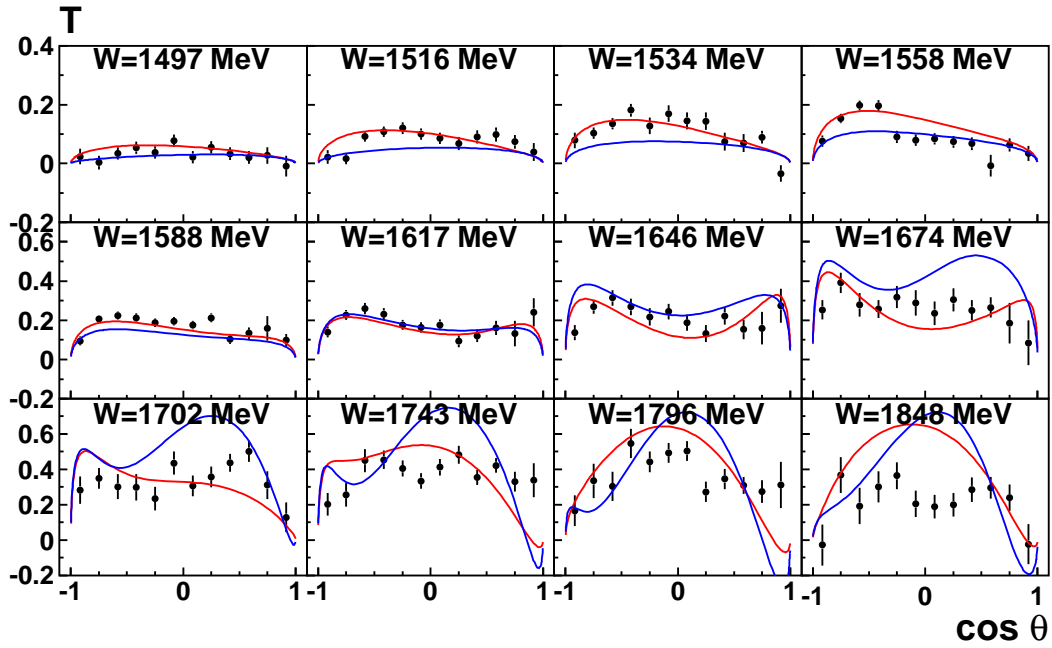
7.3.2 Description of  $T$  and  $F$  asymmetries

Figure 7.8: IB (red) and DR (blue) fit results for  $T$  [49]. For the IB fit  $\chi^2/N_{pt} = 605/144$ , for the DR fit  $\chi^2/N_{pt} = 1196/144$ .

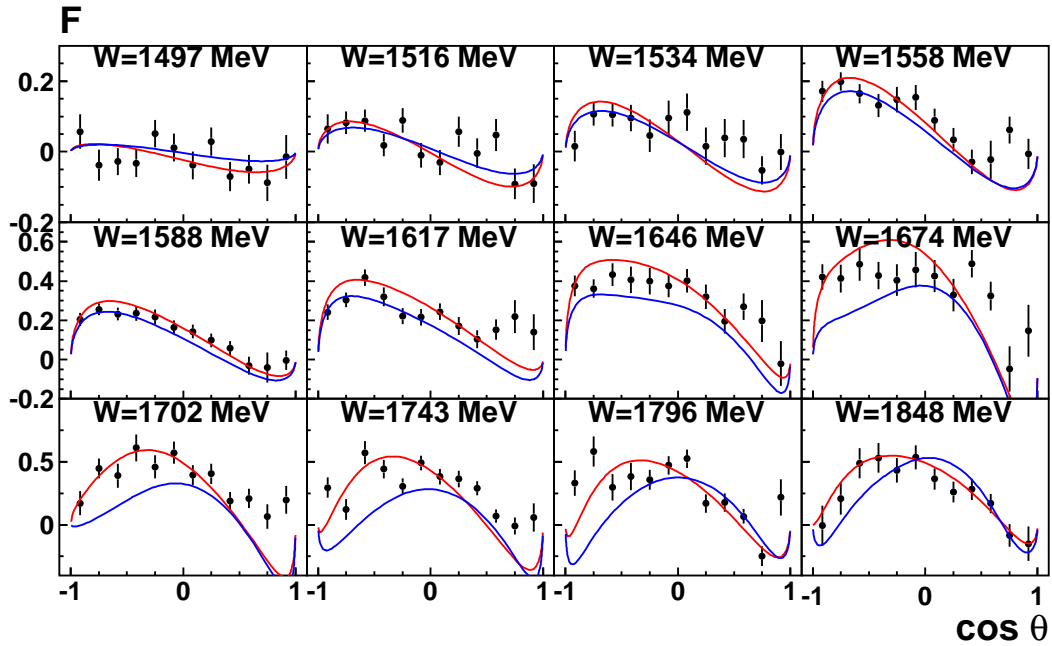


Figure 7.9: IB (red) and DR (blue) fit results for  $F$  [49]. For the IB fit  $\chi^2/N_{pt} = 443/144$ , for the DR fit  $\chi^2/N_{pt} = 711/144$ .

Figs. 7.8 and 7.9 show that the discrepancy between two curves, IB and DR, still remains.

### 7.3.3 Description of $\Sigma$ and $E$ asymmetries

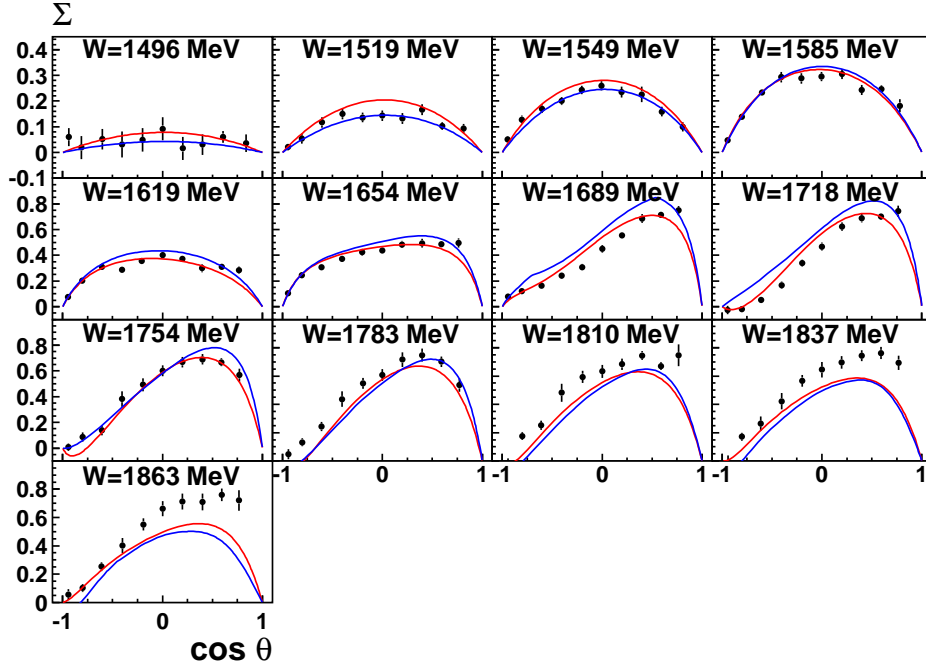


Figure 7.10: IB (red) and DR (blue) fit results for  $\Sigma$  [47]. For the IB fit  $\chi^2/N_{pt} = 637/130$ , for the DR fit  $\chi^2/N_{pt} = 1111/130$

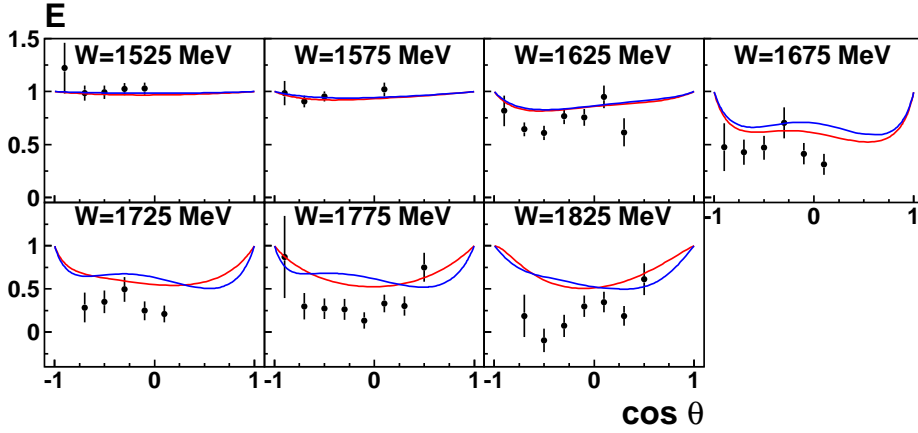


Figure 7.11: IB (red) and DR (blue) fit results for  $E$  [50]. For the IB fit  $\chi^2/N_{pt} = 29/42$ , for the DR fit  $\chi^2/N_{pt} = 37/42$ .

The results are very similar to what was shown on Figs. 7.5 and 7.6.

### 7.3.4 Solution 2 summary

Fit results in this case are almost identical to the previous ones. The introduction of the Born terms did not change the results significantly. The improvement in  $\chi^2$  comes mostly from the differential cross section. However one can see also an improvement in  $\chi^2$  for polarization data, but still the discrepancy between IB and DR results is still rather big. Obtained values for the coupling constant  $g_{\eta NN}^2/4\pi = 3.07 \times 10^{-3}$  in IB fit and  $g_{\eta NN}^2/4\pi = 3.34 \times 10^{-2}$  in DR fit.

## 7.4 Solution 3. Fit results with resonances and Regge contributions ( $s$ )

Up to now the background was purely real. With the introduction of Regge trajectories and Regge cuts one has to take into account their contributions to the imaginary part of the invariant amplitudes. In addition we apply the damping factor, see Eq. (5.44) in order to suppress the the Regge contributions in the resonance region and also in order to deal with duality problem. The constant  $\Lambda$  for the damping factor was set to  $\Lambda = 400$  MeV which comes from the result of the fit of high energy proton and neutron data with an isobar model.

The specific choice of the Regge expression was based on the results of [54].

Regge formulas are written in terms of Mandestam variable  $s$ , therefore they violate the dispersion relations, as it was explained before. But we expected that this violation has not a strong effect and the results at high energies should not be changed significantly.

The table of  $\chi^2$  values for the fitted data is presented below:

Table 7.4:  $\chi^2$  values for solution 3

Data	Observable	$\chi_{IB}^2$	$\chi_{DR}^2$	Number of points ( $N_{pt}$ )
[44]MAMI	$d\sigma/d\Omega$	5008	6361	2544
[49] A2 MAMI	$T$	453	1082	144
[49] A2 MAMI	$F$	425	809	144
[47] GRAAL	$\Sigma$	1117	1005	130
[50]CLAS	$E$	56	42	42
[77–80] DESY, Wilson, Daresbury, CEA	$d\sigma/dt$	33	108	52
[79]Daresbury	$\Sigma$	4	33	12
[81]Daresbury	$T$	3	31	3
		$\chi_{IB}^2/N_{dof} = 2.45$	$\chi_{DR}^2/N_{dof} = 3.11$	

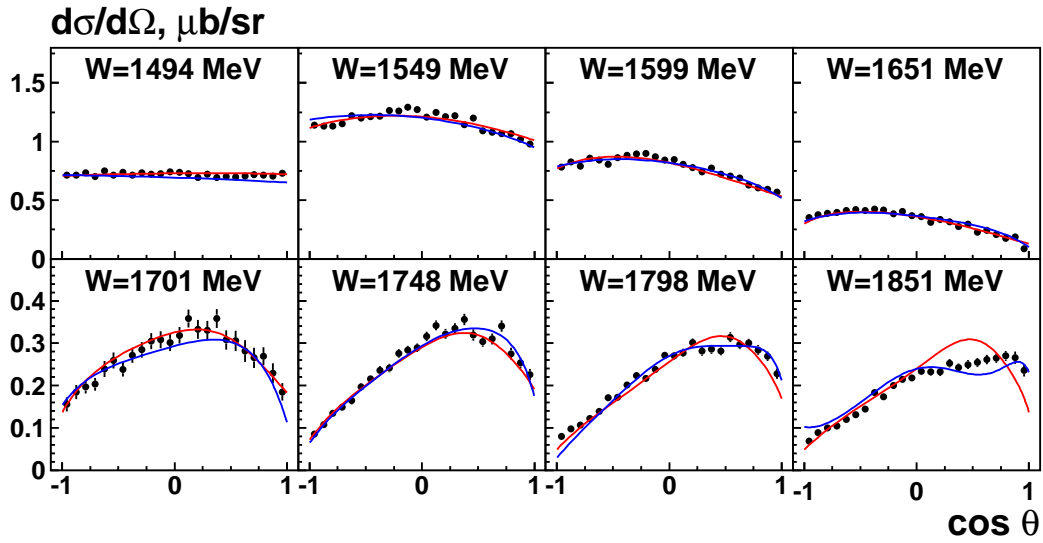
7.4.1 Description of the  $d\sigma/d\Omega$ 

Figure 7.12: IB (red) and DR (blue) fit results for  $d\sigma/d\Omega$  [44]. Data are plotted from the threshold up to the last measured energy with the  $W$  step  $\sim 50$  MeV. For the IB fit  $\chi^2/N_{pt} = 5008/2544$ , for the DR fit  $\chi^2/N_{pt} = 6361/2544$ .

The description of the differential and total cross section data is very similar to solutions 1 and 2.

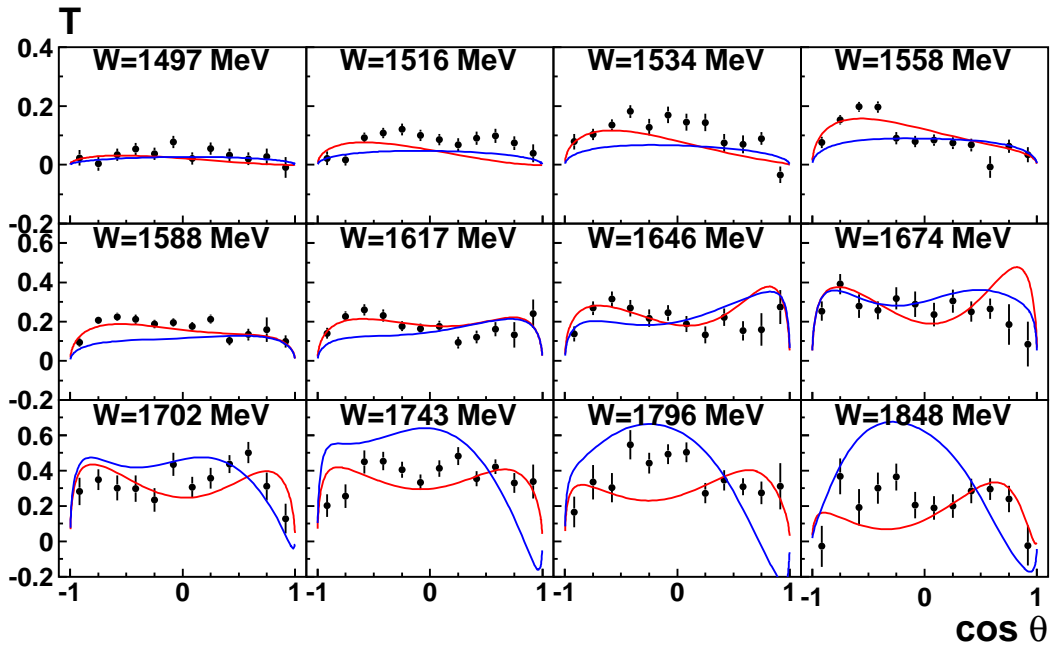
7.4.2 Description of  $T$  and  $F$  asymmetries

Figure 7.13: IB (red) and DR (blue) fit results for  $T$  [49]. For the IB fit  $\chi^2/N_{pt} = 453/144$ , for the DR fit  $\chi^2/N_{pt} = 1082/144$ .

Both approaches show the same inconsistency observed in solutions 1, 2.



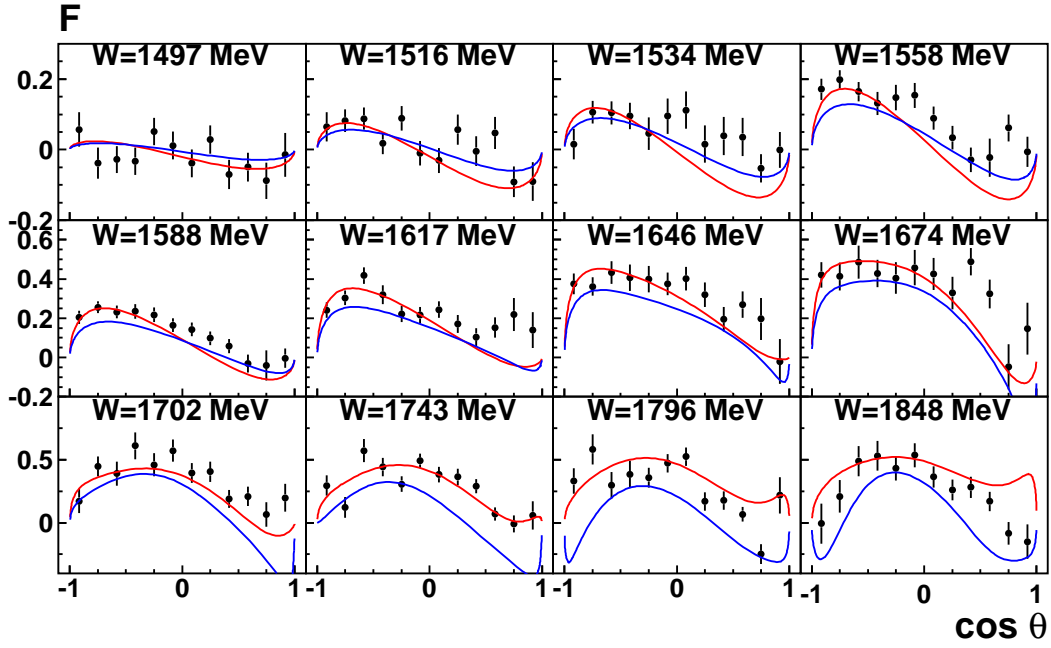


Figure 7.14: IB (red) and DR (blue) fit results for  $F$  [49]. For the IB fit  $\chi^2/N_{pt} = 425/144$ , for the DR fit  $\chi^2/N_{pt} = 809/144$ .

### 7.4.3 Description of $\Sigma$ and $E$ asymmetries

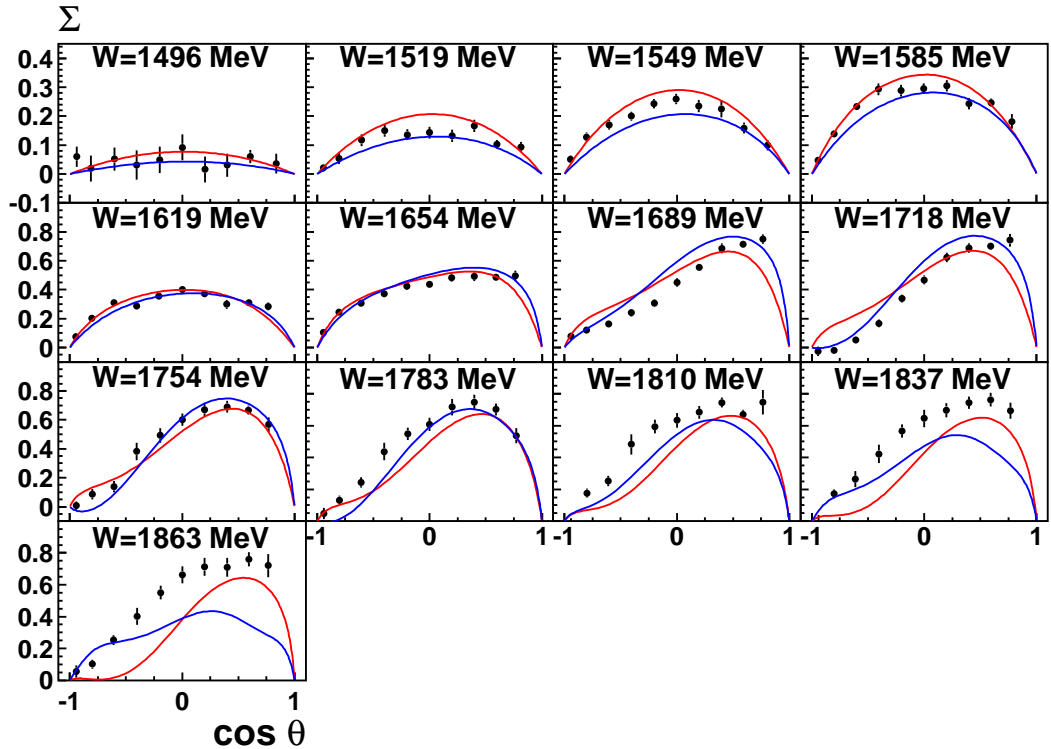


Figure 7.15: IB (red) and DR (blue) fit results for  $\Sigma$  [47]. For the IB fit  $\chi^2/N_{pt} = 1117/130$ , for the DR fit  $\chi^2/N_{pt} = 1005/130$ .

The description of  $\Sigma$  at energies above  $W = 1754 \text{ MeV}$  is similar to solutions 1, 2, but the

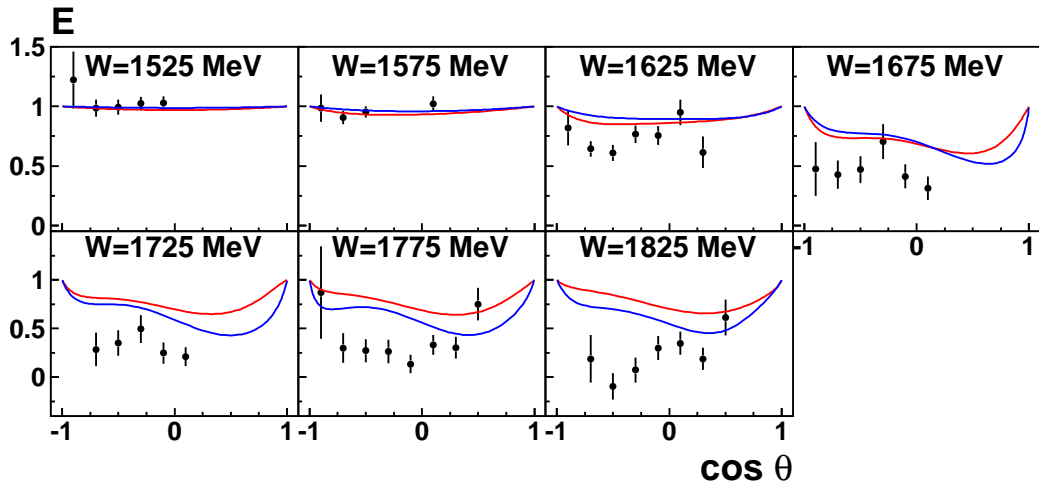


Figure 7.16: IB (red) and DR (blue) fit results for  $E$  [50]. For the IB fit  $\chi^2/N_{pt} = 56/42$ , for the DR fit  $\chi^2/N_{pt} = 42/42$ .

difference between IB and DR curves is bigger. The description of  $E$  did not change significantly.

#### 7.4.4 Description of $d\sigma/dt$ , $\Sigma$ , and $T$ at high energies

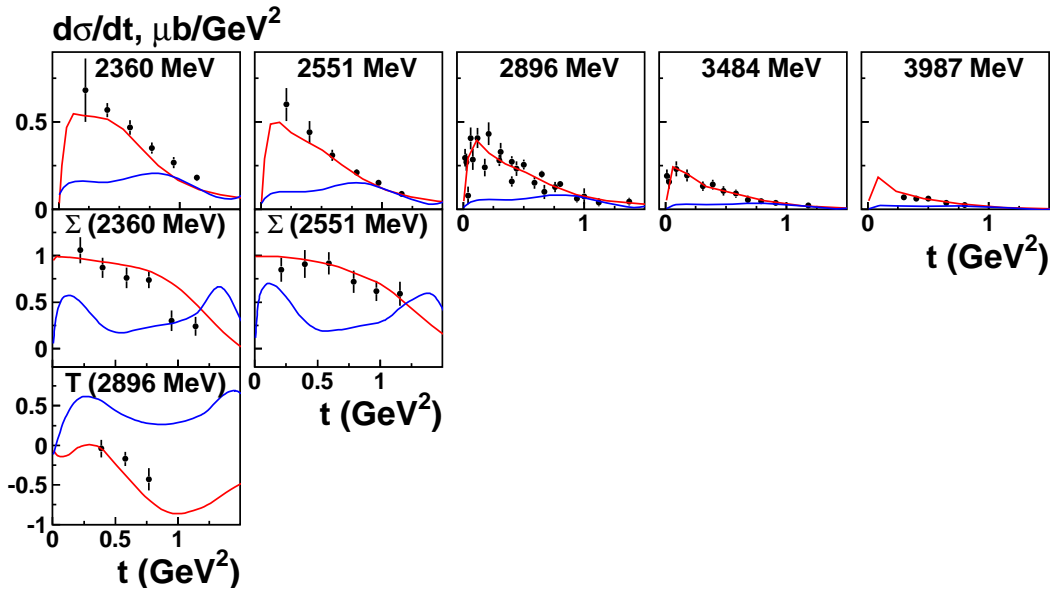


Figure 7.17: IB (red) and DR (blue) fit results for  $d\sigma/dt$ ,  $\Sigma$ ,  $T$  [77–80]. For the IB fit  $\chi^2/N_{pt} = 33/52$   $4/12$   $3/3$ , for the DR fit  $\chi^2/N_{pt} = 108/52$   $33/12$   $31/3$ .

Fig. 7.17 shows that the given form of Regge trajectories and Regge cuts strongly violates the fixed- $t$  dispersion relations which leads to the bad description of the data by DR fit.

### 7.4.5 Regge contributions to the invariant amplitudes at fixed $t$ -values

In this solution Regge contributions ( $W$ ) were taken into account. It is interesting to plot invariant amplitudes  $A_i$  in order to see how they change. Fig. 7.18 shows  $A_i(W)$  amplitudes at  $t = -0.2 \text{ GeV}^2$  with only Regge contributions taken into account.

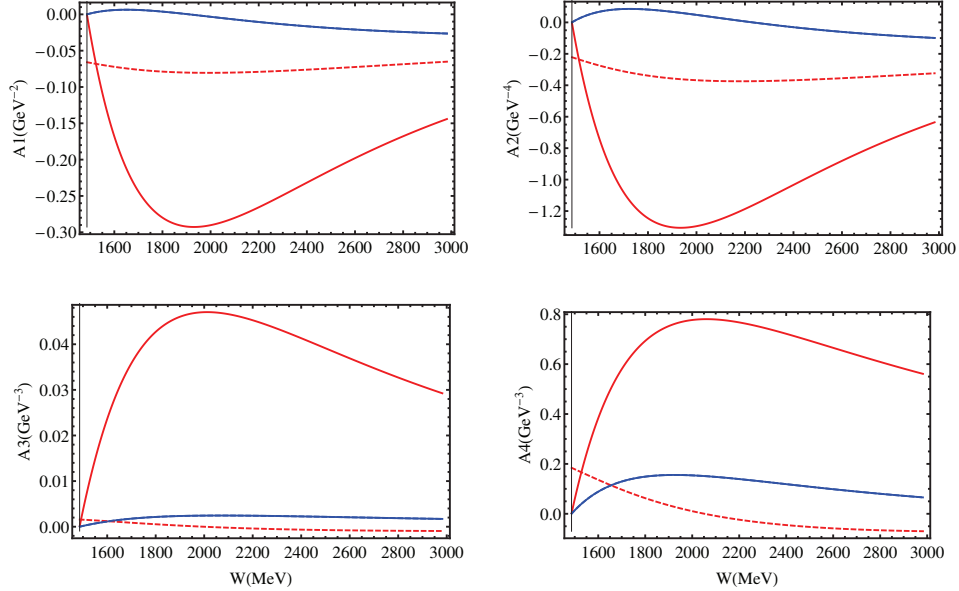


Figure 7.18: Regge contributions to the invariant amplitudes  $A_1, A_2, A_3, A_4$  for  $t = -0.2 \text{ GeV}^2$ . Solid red and blue lines denote real and imaginary parts obtained with an IB model. Red dashed lines denote real parts obtained using dispersion relations from the imaginary parts. Black vertical lines show the threshold of the physical region for a given  $t$ -value.

From Figs. 7.18 one can observe how big is the discrepancy between real parts in IB and DR approaches therefore the expected coincidence of the real parts at high energies is not observed.

### 7.4.6 Solution 3 summary

The fit results for the polarization observables did not change much. One can also observe that the Regge expressions in given form violate the fixed- $t$  dispersion relations significantly, thus high energy data are undescribed by such approach. In order to solve the problem with the description of high energy data it was concluded to use another form of Regge formulas, namely in terms of crossing symmetrical variable  $\nu$  which obeys the dispersion relations by definition.

## 7.5 Intermediate conclusion for solutions 1-3

The common feature of all presented fits is the inconsistency of the fit results of two different approaches for the  $T$  observable. The description of  $\Sigma$  and  $F$  with an IB fits usually gives the  $\chi^2$  value which is about two times better than the DR fit. The good agreement is only observed in the results for the differential and the total cross sections.

A good description of the differential cross section can be easily explained. If one has a look at the multipole decomposition of the observable using Legendre polynomials Eq. (4.6), one can see that the main contribution into this observable comes from the squares of the multipoles therefore the interference of them plays smaller role.

Also due to the dominance of  $N(1535) 1/2^-$  and  $N(1650) 1/2^-$  resonances which have the biggest branching ratios in  $\eta$  channel,  $\beta_\eta \approx 45\%$  and  $\beta_\eta \approx 20\%$  respectively, the total cross section is reproduced as well.

On Figs. 7.19 invariant amplitudes  $A_i$  for solutions 1-3 are presented.

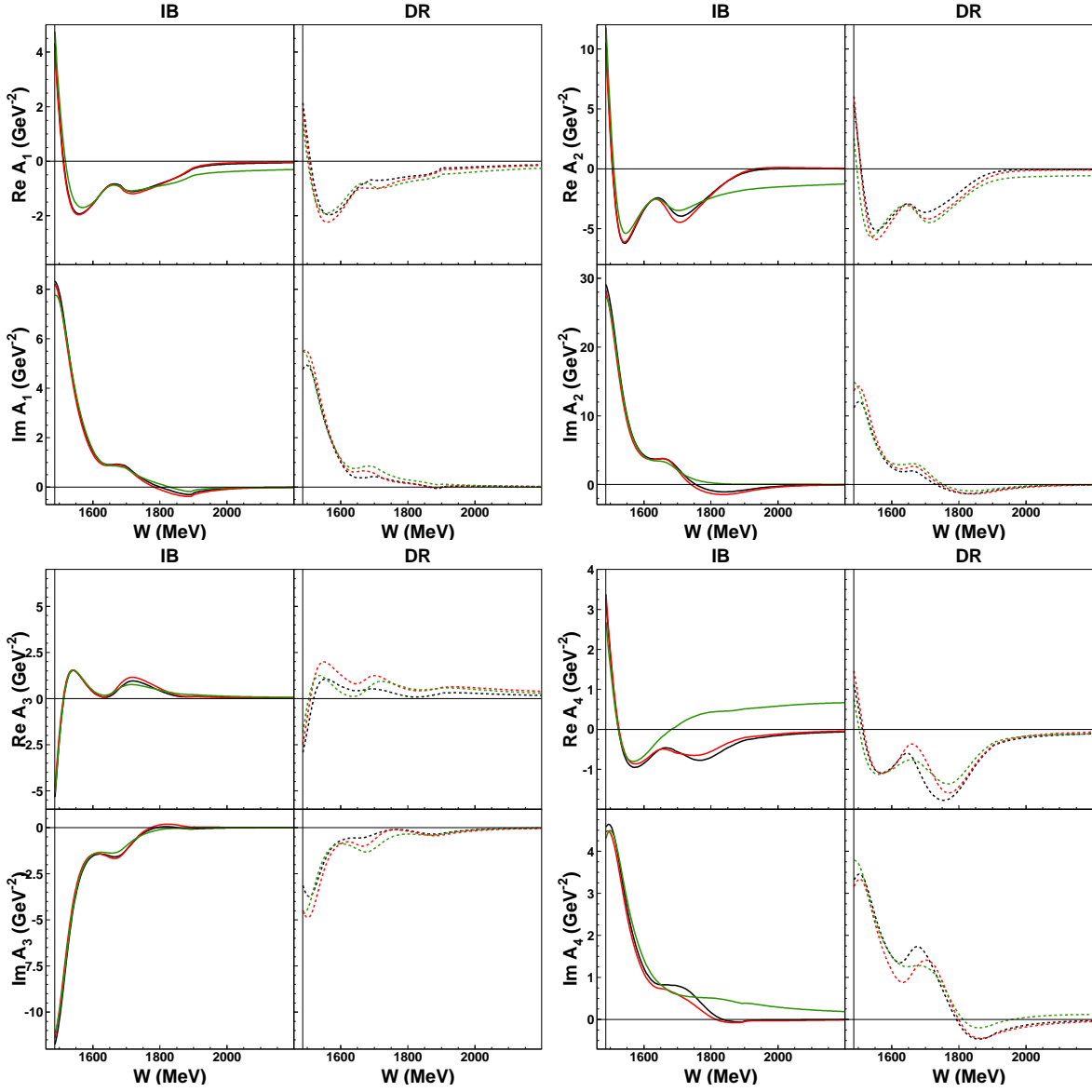


Figure 7.19: Invariant amplitudes  $A_i$  for solutions 1-3. Solution 1 is plotted in black, solution 2 in red, solution 3 in green. IB and DR results are drawn as solid and dashed curves respectively. Black vertical lines show the threshold of the physical region for a  $t = -0.2 \text{ GeV}^2$ .

In order to improve the description of the data, we have included the unitarity phases for  $J^P : 3/2^-, 3/2^+, 5/2^-$  intermediate states as a fitting parameters. As it has been described above in the Section 5.1. Such implementation significantly improved the results.

The reason why we have chosen these states is because the biggest description in the IB and DR results was observed in the  $T$  asymmetry. If we look on the partial wave contributions into this observable Eq. (A.30) we will see that the main impact comes from the interferences of  $E_{0+}$  with  $E_{1+}$ ,  $M_{1+}$ ,  $E_{2-}$ ,  $M_{2-}$ ,  $E_{2+}$ ,  $M_{2+}$  multipoles. The interferences of other partial waves may be neglected due to the dominance of  $E_{0+}$  multipole.

## 7.6 Solution 4. Fit results with resonances $\times e^{i\Phi_j^\alpha}$ for $j : 3/2^-, 3/2^+, 5/2^-$ states, and Born terms

Solution 4 is obtained by modifying the solution 2, where Born terms were used as a background. Here phases of  $N(1520) 3/2^-$ ,  $N(1675) 5/2^-$ ,  $N(1700) 3/2^-$ ,  $N(1720) 3/2^+$ ,  $N(1875) 3/2^-$ ,  $N(1900) 3/2^+$  were chosen as fitting parameters, the other ones were fixed to zero.

The table of  $\chi^2$  values for the fitted data is presented below:

Table 7.5:  $\chi^2$  values for solution 4

Data	Observable	$\chi_{IB}^2$	$\chi_{DR}^2$	Number of points ( $N_{pt}$ )
[44]MAMI	$d\sigma/d\Omega$	3427	3890	2544
[49]A2 MAMI	$T$	532	708	144
[49]A2 MAMI	$F$	316	534	144
[47] GRAAL	$\Sigma$	490	794	130
[50]CLAS	$E$	38	33	42
		$\chi_{IB}^2/N_{dof} = 1.68$	$\chi_{DR}^2/N_{dof} = 2.02$	

### 7.6.1 Description of the $d\sigma/d\Omega$

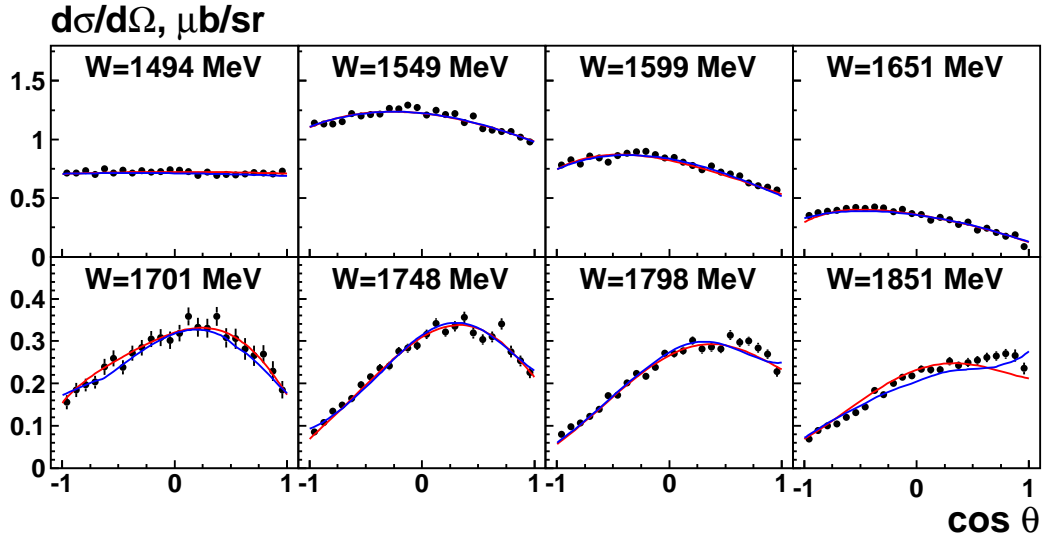


Figure 7.20: IB (red) and DR (blue) fit results for  $d\sigma/d\Omega$  [44]. Data are plotted from the threshold up to the last measured energy with the  $W$  step  $\sim 50$  MeV. For the IB fit  $\chi^2/N_{pt} = 3427/2544$ , for the DR fit  $\chi^2/N_{pt} = 3890/2544$ .

As in solutions 1-3 the description of these observables are good. The difference in  $\chi^2$  values became much smaller in comparison with solution 2.

### 7.6.2 Description of $T$ and $F$ asymmetries

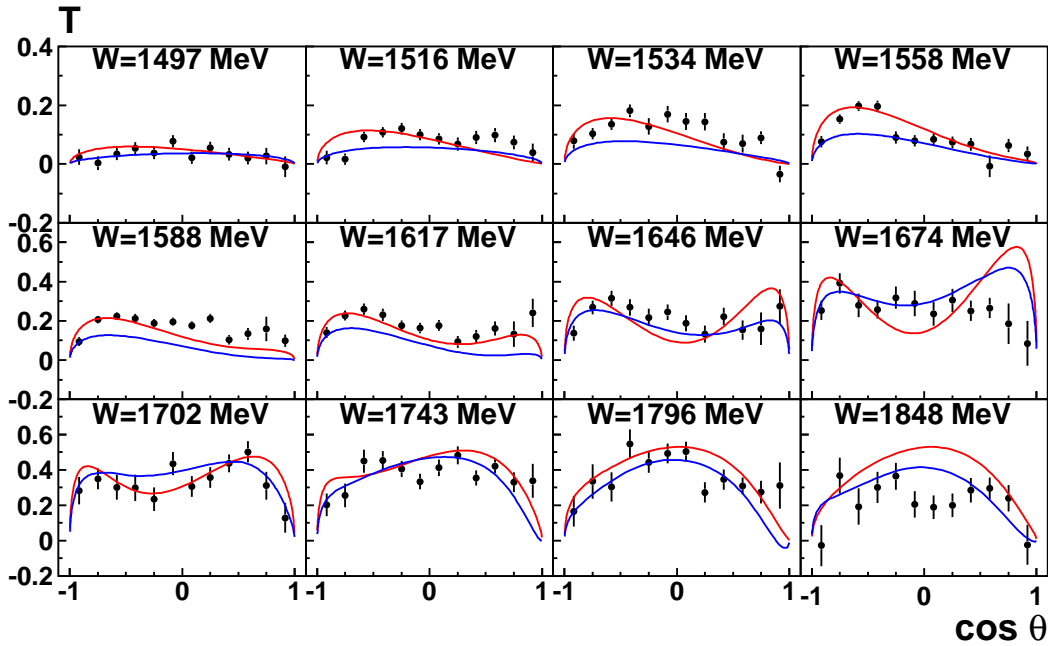


Figure 7.21: IB (red) and DR (blue) fit results for  $T$  [49].  $\chi^2/N_{pt} = 532/144$ , for the DR fit  $\chi^2/N_{pt} = 708/144$ .

Comparing the results on Fig. 7.8 and Fig. 7.21, one can see a big improvement in the description of  $T$  at energies above  $W = 1646$  MeV. The description of the data at energies  $W = 1588$  MeV and  $W = 1617$  MeV is now a bit worse than in solution 2.

The improvement in the description of  $F$  is observed at all energies.

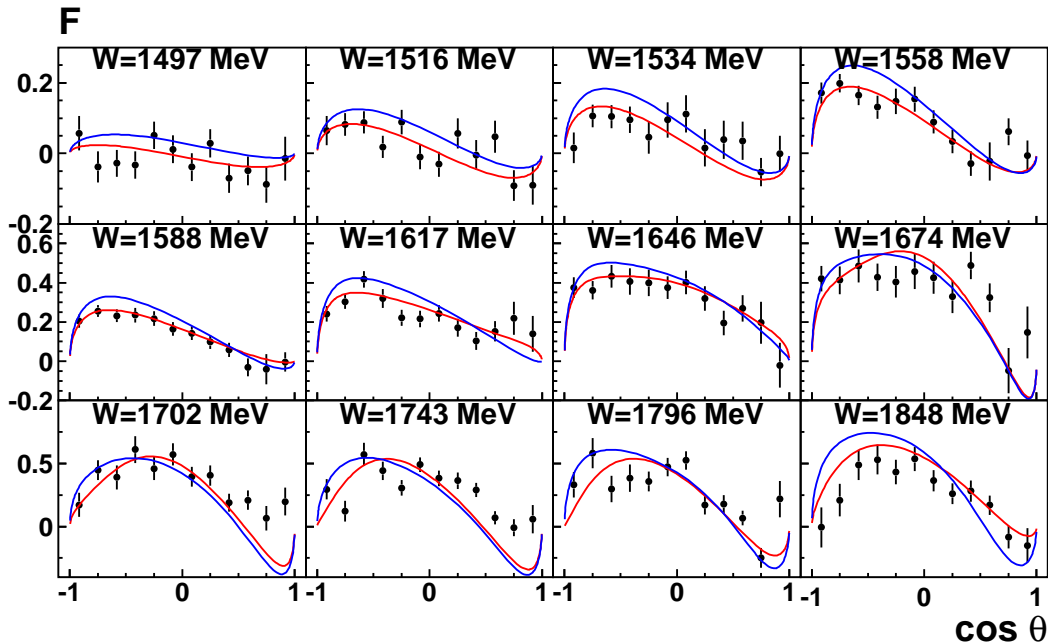


Figure 7.22: IB (red) and DR (blue) fit results for  $F$  [49]. For the IB fit  $\chi^2/N_{pt} = 316/144$ , for the DR fit  $\chi^2/N_{pt} = 534/144$ .

### 7.6.3 Description of $\Sigma$ and $E$ asymmetries

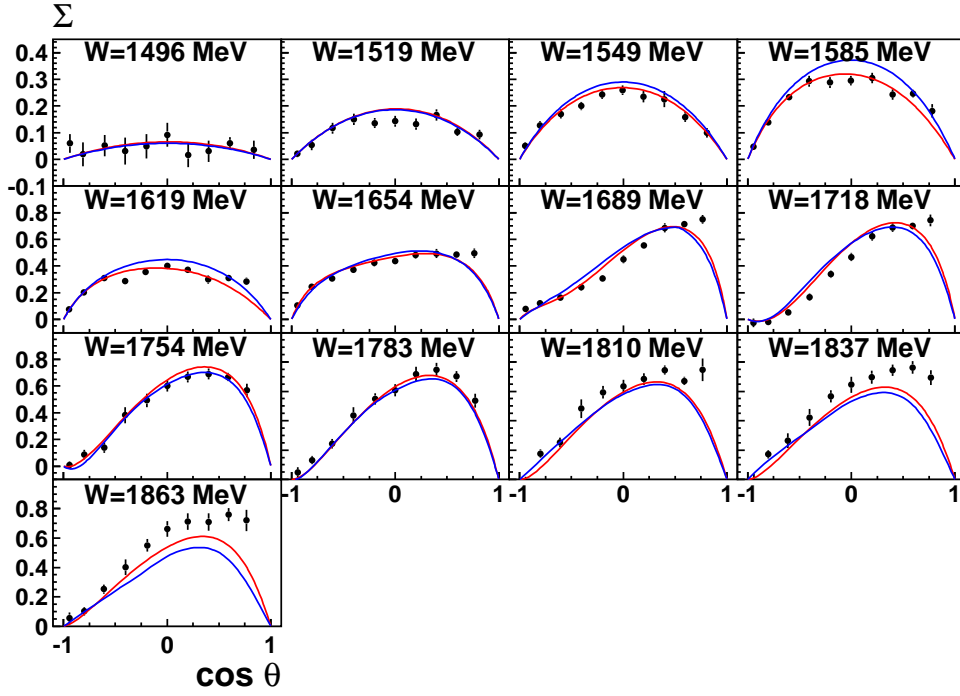


Figure 7.23: IB (red) and DR (blue) fit results for  $\Sigma$  [47]. For the IB fit  $\chi^2/N_{pt} = 490/130$ , for the DR fit  $\chi^2/N_{pt} = 794/130$

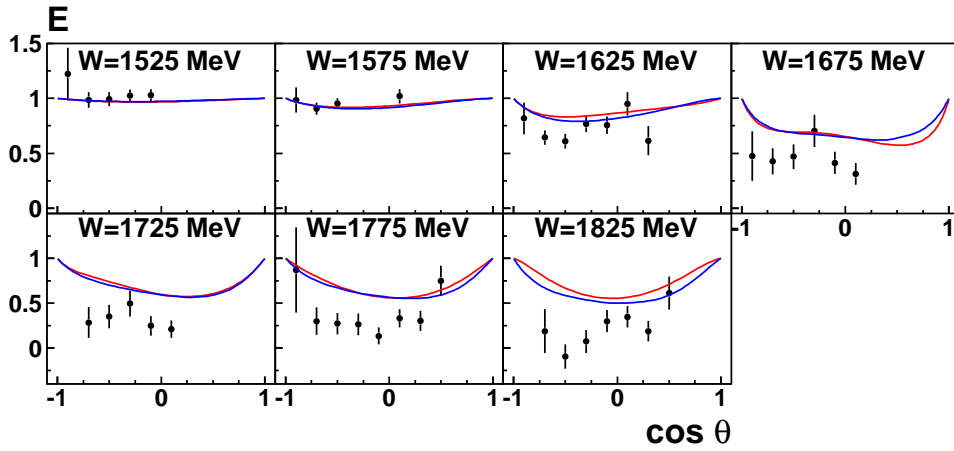


Figure 7.24: IB (red) and DR (blue) fit results for  $E$  [50]. For the IB fit  $\chi^2/N_{pt} = 38/42$ , for the DR fit  $\chi^2/N_{pt} = 33/42$

The  $\chi^2$  values became better. The consistency in the description remains.

### 7.6.4 Solution 4 summary

The introduction of the phases led to an improvement of the  $\chi^2$  values for all data, especially for the differential cross section. The description of other observables, especially  $T$ , also became better.

The value of the Born term coupling constant was obtained to be equal to  $g_{\eta NN}^2/4\pi = 10^{-6}$ . This means that contribution from the Born term is completely negligible.



7.6 Solution 4. Fit results with resonances  $\times e^{i\Phi_j^\alpha}$  for  $j : 3/2^-, 3/2^+, 5/2^-$  states, and Born terms

However one can see on Fig. 7.23 that data on  $\Sigma$  at energies  $W = 1837$  and  $W = 1863$  MeV are not described due to the very small impact from Born terms. This motivates us to use Regge background.

## 7.7 Solution 5. Fit results with resonances $\times e^{i\Phi_j^\alpha}$ for $j : 3/2^-, 3/2^+, 5/2^-$ states, and Regge contributions ( $s$ )

As we already seen the Regge contributions formulated in terms of  $W$  violate the fixed- $t$  dispersion relations. Nevertheless it is interesting to see the effect of the phases on the description of the data in the resonance region.

The table of  $\chi^2$  values for the fitted data is presented below:

Table 7.6:  $\chi^2$  values for solution 5

Data	Observable	$\chi_{IB}^2$	$\chi_{DR}^2$	Number of points ( $N_{pt}$ )
[44]MAMI	$d\sigma/d\Omega$	4729	3527	2544
[49] A2 MAMI	$T$	606	503	144
[49] A2 MAMI	$F$	316	581	144
[47] GRAAL	$\Sigma$	832	796	130
[50]CLAS	$E$	38	26	42
[77–80] DESY, Wilson, Daresbury, CEA	$d\sigma/dt$	34	102	52
[79]Daresbury	$\Sigma$	7	15	12
[81]Daresbury	$T$	3	19	3
		$\chi_{IB}^2/N_{dof} = 2.23$	$\chi_{DR}^2/N_{dof} = 1.86$	

### 7.7.1 Description of the $d\sigma/d\Omega$ and the total cross section

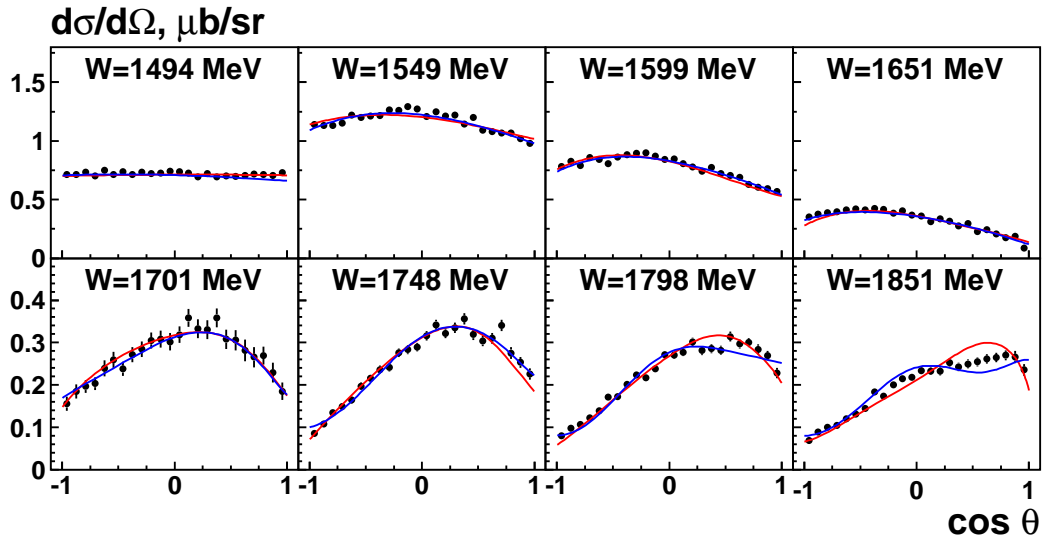


Figure 7.25: IB (red) and DR (blue) fit results for  $d\sigma/d\Omega$  [44]. Data are plotted from the threshold up to the last measured energy with the  $W$  step  $\sim 50$  MeV. For the IB fit  $\chi^2/N_{pt} = 4729/2544$ , for the DR fit  $\chi^2/N_{pt} = 3527/2544$ .

### 7.7.2 Description of $T$ and $F$ asymmetries

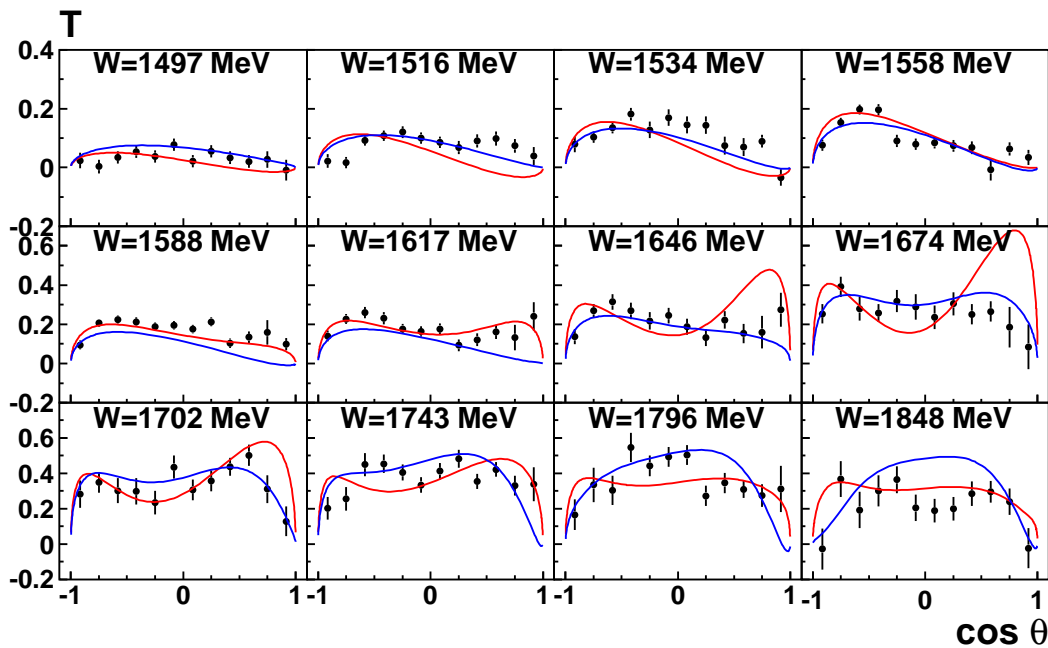


Figure 7.26: IB (red) and DR (blue) fit results for  $T$  [49]. For the IB fit  $\chi^2/N_{pt} = 606/144$ , for the DR fit  $\chi^2/N_{pt} = 503/144$ .

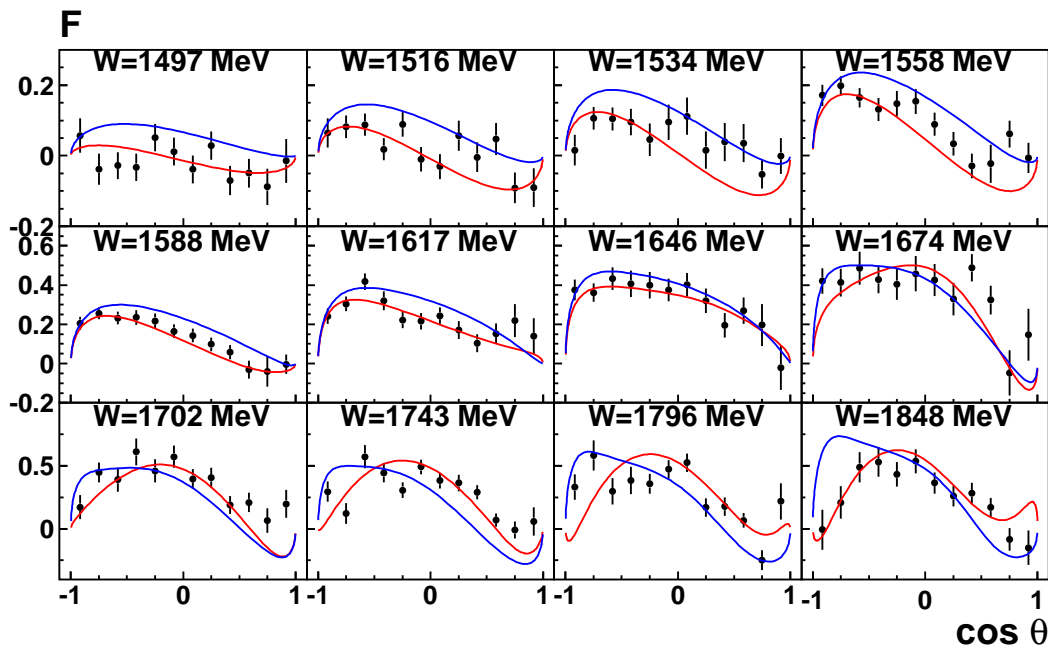


Figure 7.27: IB (red) and DR (blue) fit results for  $F$  [49]. For the IB fit  $\chi^2/N_{pt} = 316/144$ , for the DR fit  $\chi^2/N_{pt} = 581/144$ .

### 7.7.3 Description of $\Sigma$ and $E$ asymmetries

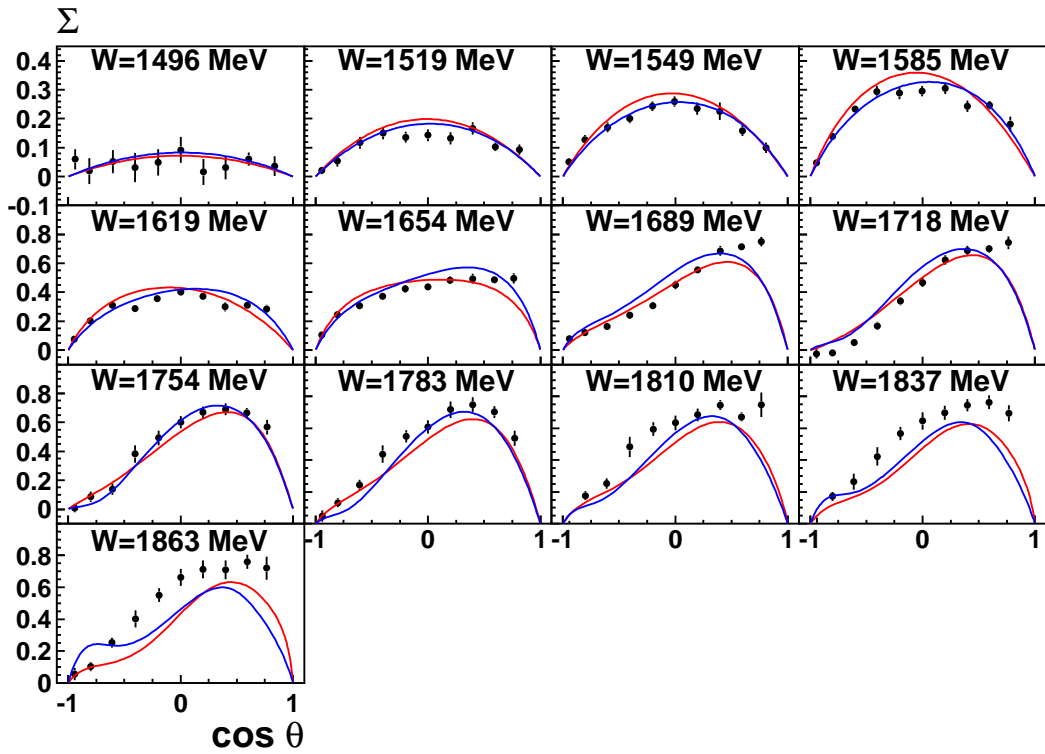


Figure 7.28: IB (red) and DR (blue) fit results for  $\Sigma$  [47]. For the IB fit  $\chi^2/N_{pt} = 832/130$ , for the DR fit  $\chi^2/N_{pt} = 796/130$

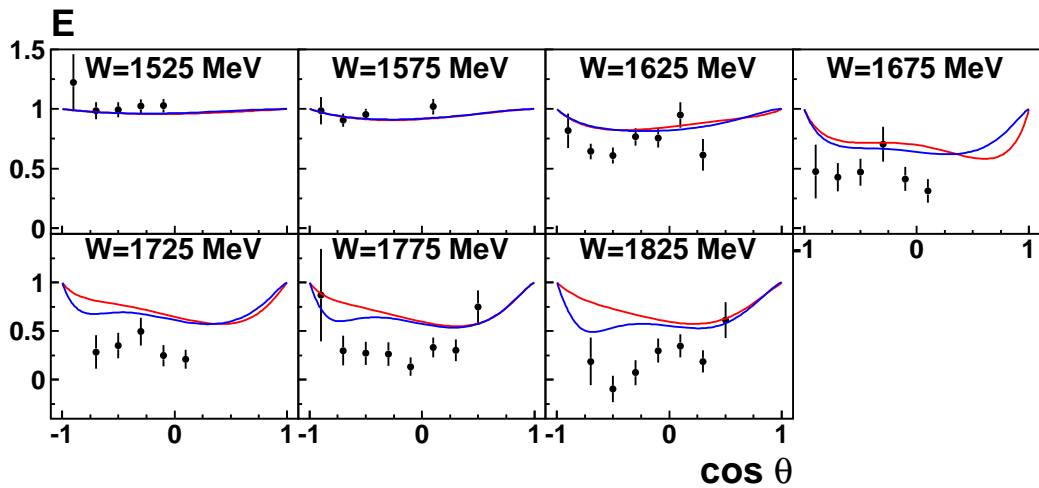


Figure 7.29: IB (red) and DR (blue) fit results for  $E$  [50]. For the IB fit  $\chi^2/N_{pt} = 45/42$ , for the DR fit  $\chi^2/N_{pt} = 33/42$

### 7.7.4 Description of $d\sigma/dt$ , $\Sigma$ , and $T$ at high energies

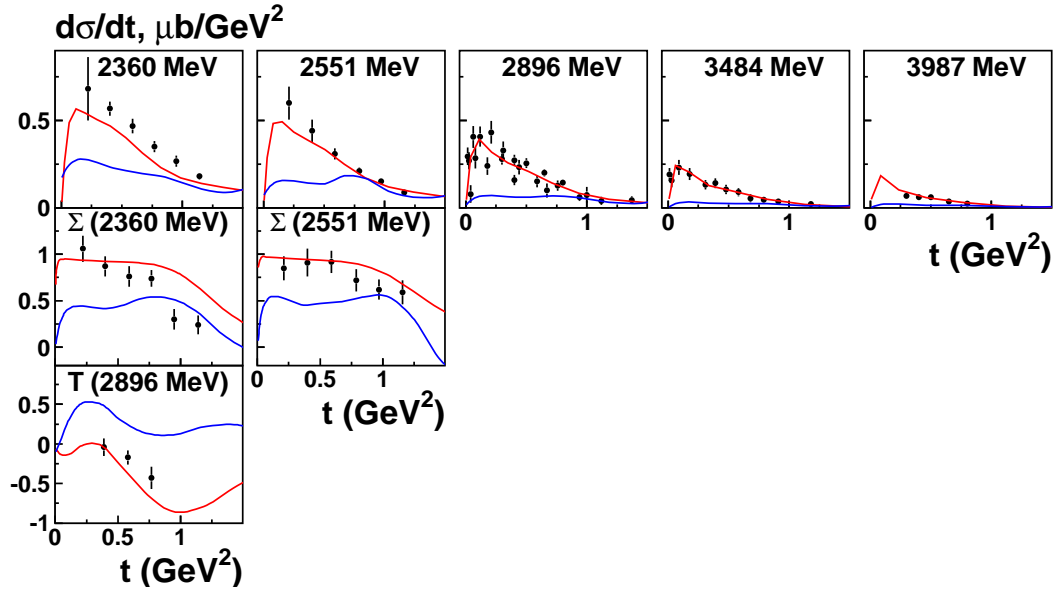


Figure 7.30: IB (red) and DR (blue) fit results for  $d\sigma/dt$ ,  $\Sigma$ ,  $T$  [77–80] as functions of  $t$ .  $d\sigma/dt$  is shown in  $\mu\text{b}/\text{GeV}^2$  units. For the IB fit  $\chi^2/N_{pt} = 34/52 \ 7/12 \ 3/3$ , for the DR fit  $\chi^2/N_{pt} = 102/52 \ 15/12 \ 19/3$

### 7.7.5 Solution summary

The results for the low energy data clearly show the improvement in the description of all fitted observables. Blue curves now lie closer to the red ones. Although the problem of the description of high-energy data by the DR fit still presents. The reason is that here for the Regge contributions non-crossing symmetrical expressions are still used.

## 7.8 Solution 6. Fit results with resonances $\times e^{i\Phi_j^\alpha}$ for $j : 3/2^-, 3/2^+, 5/2^-$ states, and Regge contributions ( $\nu$ )

In order to describe the high energy data another Regge formalism was used. As well as the previous one this formalism is also described in the paper of [54]. Now the Regge amplitudes are formulated in terms of crossing symmetrical variable  $\nu$  and fulfill the dispersion relations by definition.

The damping constant for the damping factor in Eq. (5.45) was set to  $\Lambda = 689$  MeV and was obtained from the analysis of high and low energy data with the isobar model approach.

The table of  $\chi^2$  values for the fitted data is presented below:

Table 7.7:  $\chi^2$  values for solution 6

Data	Observable	$\chi_{IB}^2$	$\chi_{DR}^2$	Number of points ( $N_{pt}$ )
[44]MAMI	$d\sigma/d\Omega$	3946	3641	2544
[49] A2 MAMI	$T$	536	519	144
[49] A2 MAMI	$F$	333	394	144
[47] GRAAL	$\Sigma$	377	437	130
[50]CLAS	$E$	53	36	42
[77–80] DESY, Wilson, Daresbury, CEA	$d\sigma/dt$	11	13	52
[79]Daresbury	$\Sigma$	7	7	12
[81]Daresbury	$T$	1	2	3
		$\chi_{IB}^2/N_{dof} = 1.84$	$\chi_{DR}^2/N_{dof} = 1.77$	

### 7.8.1 Description of the $d\sigma/d\Omega$

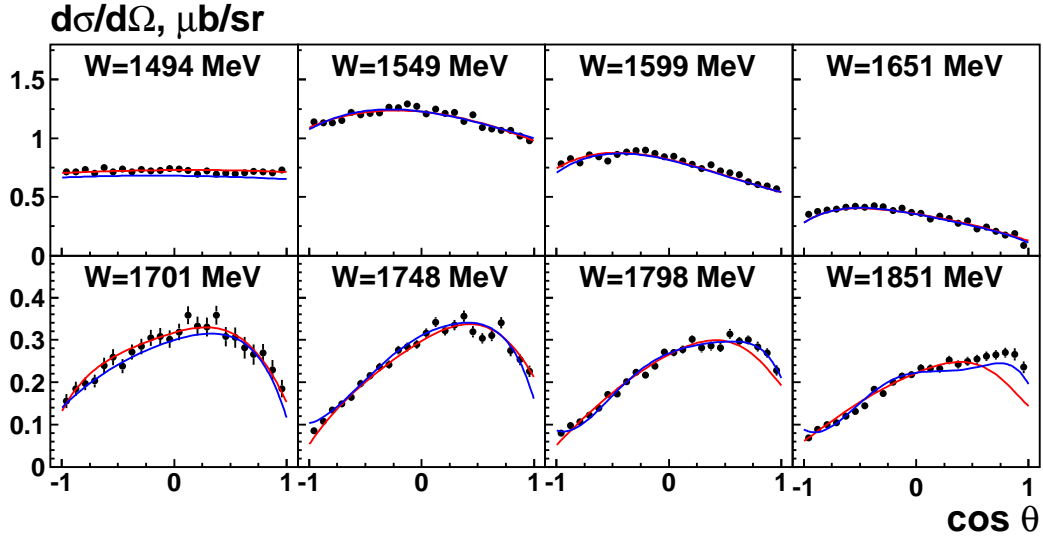


Figure 7.31: IB (red) and DR (blue) fit results for  $d\sigma/d\Omega$  [44]. Data are plotted from the threshold up to the last measured energy with the  $W$  step  $\sim 50$  MeV. For the IB fit  $\chi^2/N_{pt} = 3946/2544$ , for the DR fit  $\chi^2/N_{pt} = 3641/2544$ .

Fit results for this observable show the best agreement among all fits that were described here. DR fit now describes the data better than IB fit, especially the highest energy bins.

### 7.8.2 Description of $T$ and $F$ asymmetries

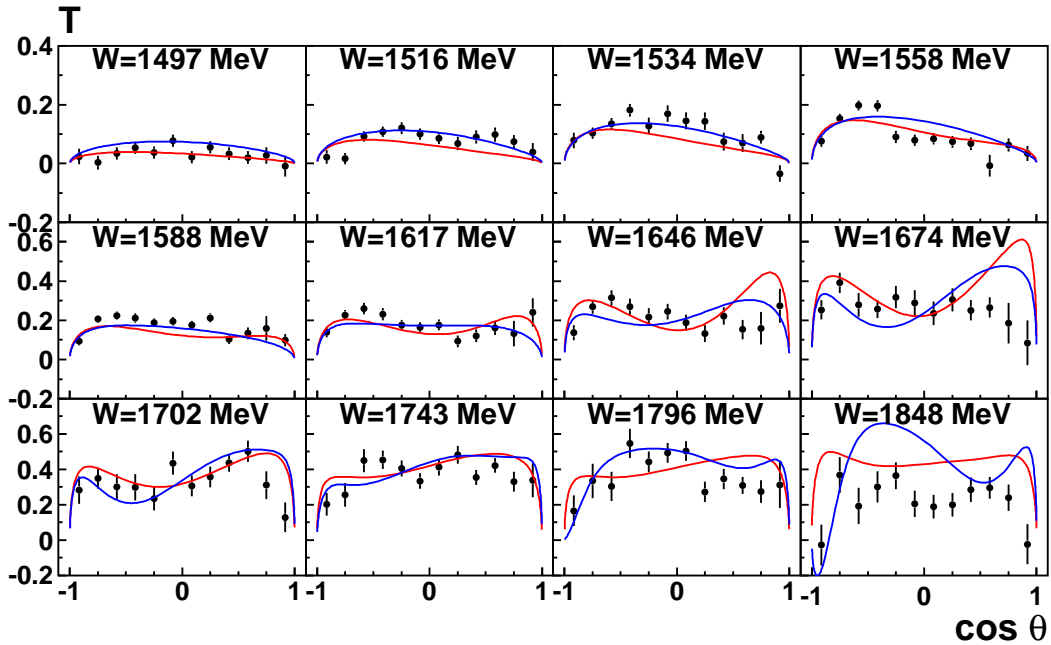


Figure 7.32: IB (red) and DR (blue) fit results for  $T$  [49]. For the IB fit  $\chi^2/N_{pt} = 536/144$ , for the DR fit  $\chi^2/N_{pt} = 519/144$ .

Both these observables are described with a close  $\chi^2$  and show the good agreement with the data.

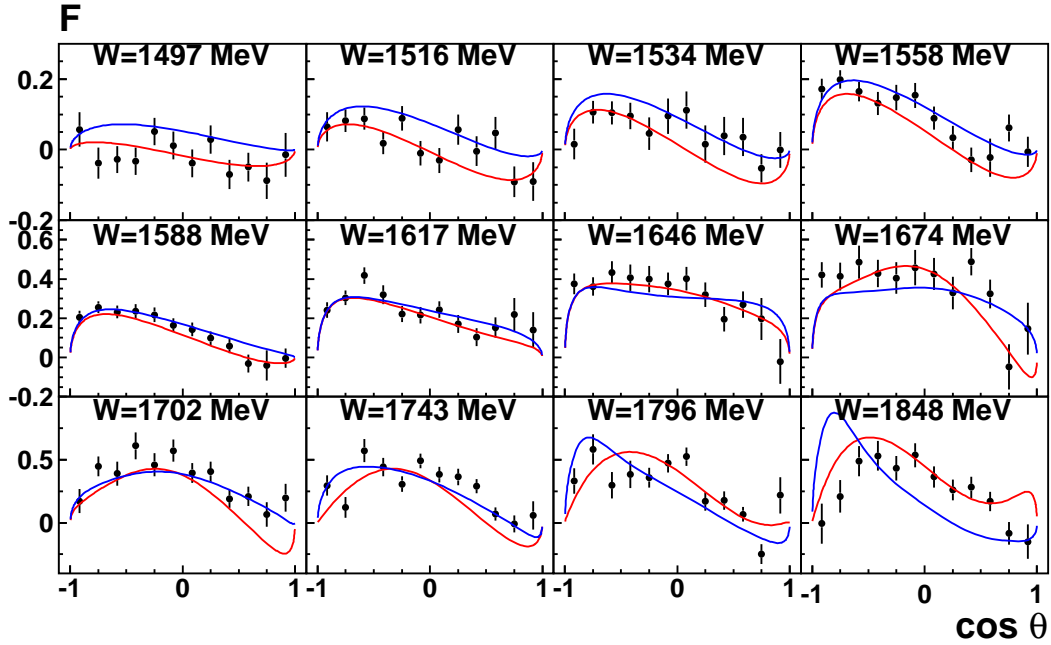


Figure 7.33: IB (red) and DR (blue) fit results for  $F$  [49]. For the IB fit  $\chi^2/N_{pt} = 333/144$ , for the DR fit  $\chi^2/N_{pt} = 394/144$ .

### 7.8.3 Description of $\Sigma$ and $E$ asymmetries

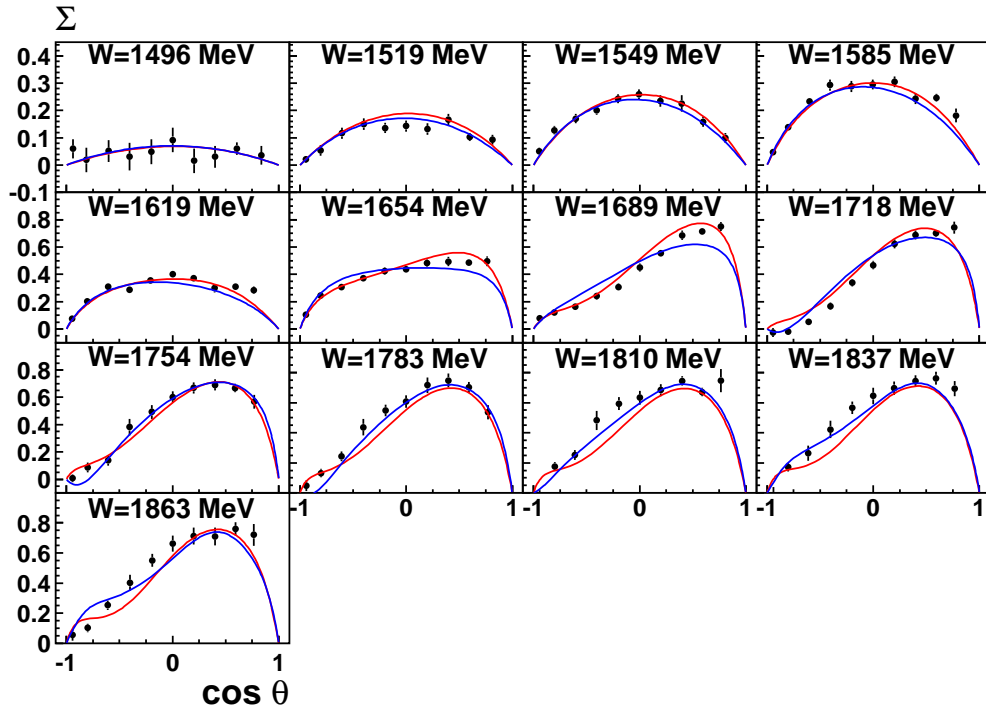


Figure 7.34: IB (red) and DR (blue) fit results for  $\Sigma$  [47]. For the IB fit  $\chi^2/N_{pt} = 377/130$ , for the DR fit  $\chi^2/N_{pt} = 437/130$

This fit has solved the problem with the description of  $\Sigma$  at energies above  $W = 1754$  MeV.



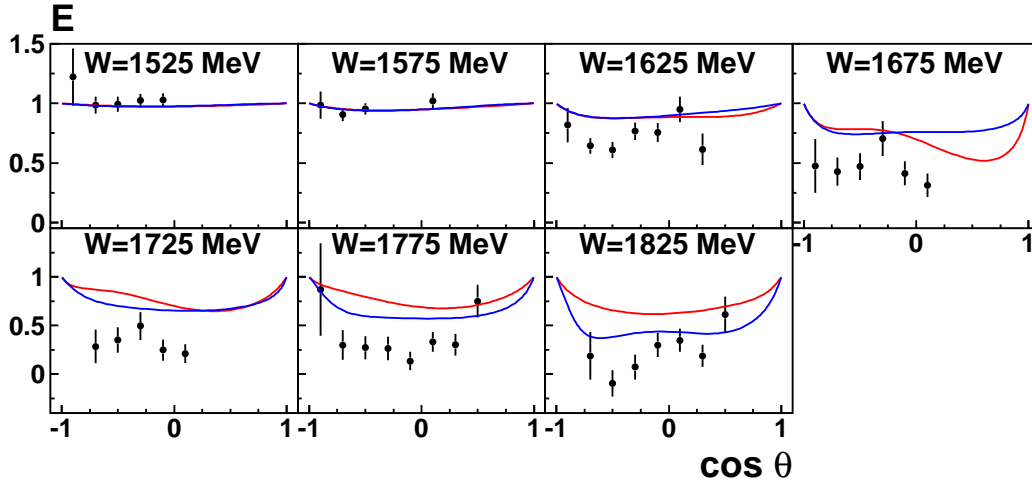


Figure 7.35: IB (red) and DR (blue) fit results for  $E$  [50]. For the IB fit  $\chi^2/N_{pt} = 53/42$ , for the DR fit  $\chi^2/N_{pt} = 36/42$

#### 7.8.4 Description of $d\sigma/dt$ , $\Sigma$ , and $T$ at high energies

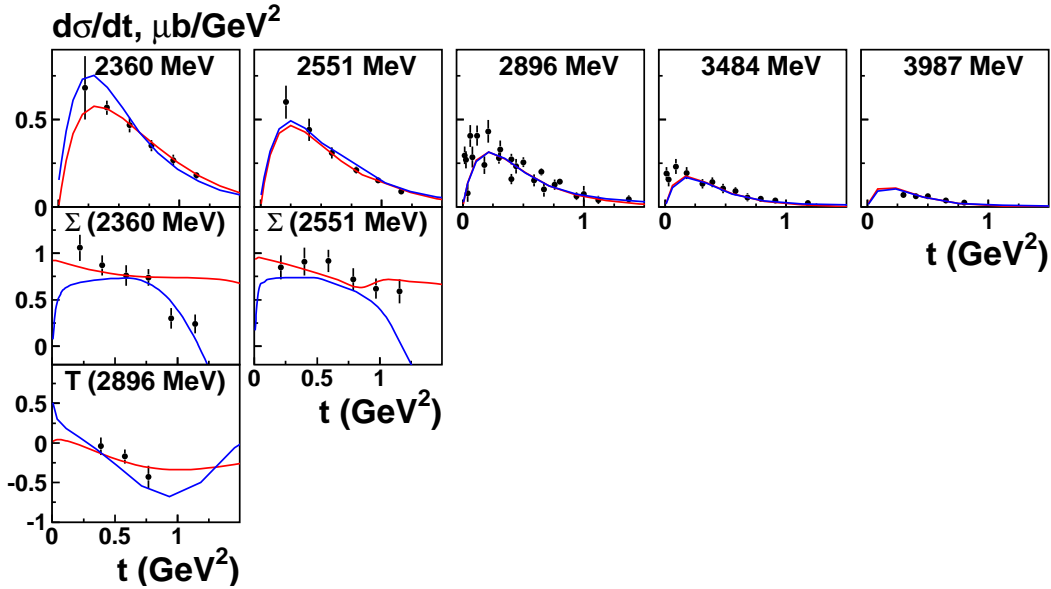


Figure 7.36: IB (red) and DR (blue) fit results for  $d\sigma/dt$ ,  $\Sigma$ ,  $T$  [77–80] as functions of  $t$ .  $d\sigma/dt$  is shown in  $\mu\text{b}/\text{GeV}^2$  units. For the IB fit  $\chi^2/N_{pt} = 11/52$   $7/12$   $1/3$ , for the DR fit  $\chi^2/N_{pt} = 13/52$   $7/12$   $2/3$ .

The high energy data for  $d\sigma/dt$  is now equally well described with both approaches. The descriptions of  $\Sigma$  and  $T$  are however does not coincide.

#### 7.8.5 Solution 6 summary

The description of the observables is now much better in comparison with the previous solutions. High energy data are now also described with the new Regge formalism. Next and the final step should be done by fitting the phases of all other resonances except of  $N(1440) 1/2^+$ .

## 7.9 Solution 7. Fit results with resonances $\times e^{i\Phi_j^\alpha}$ for all resonances, and Regge contributions $\nu$ )

Here the final solution is considered, where phases of all other resonances except of  $N(1440) 1/2^+$  are varied. The same parametrization of Regge contributions as in previous solution 6 is used, damping constant is fixed to  $\Lambda = 689$  MeV.

The table of  $\chi^2$  values for the fitted data is presented below:

Table 7.8:  $\chi^2$  values for solution 7

Data	Observable	$\chi_{IB}^2$	$\chi_{DR}^2$	Number of points ( $N_{pt}$ )
[44]MAMI	$d\sigma/d\Omega$	3448	3388	2544
[49] A2 MAMI	$T$	456	423	144
[49] A2 MAMI	$F$	318	426	144
[47] GRAAL	$\Sigma$	323	353	130
[50]CLAS	$E$	38	31	42
[77–80] DESY, Wilson, Daresbury, CEA	$d\sigma/dt$	11	13	52
[79]Daresbury	$\Sigma$	7	13	12
[81]Daresbury	$T$	1	2	3
		$\chi_{IB}^2/N_{dof} = 1.61$	$\chi_{DR}^2/N_{dof} = 1.61$	

### 7.9.1 Description of the $d\sigma/d\Omega$

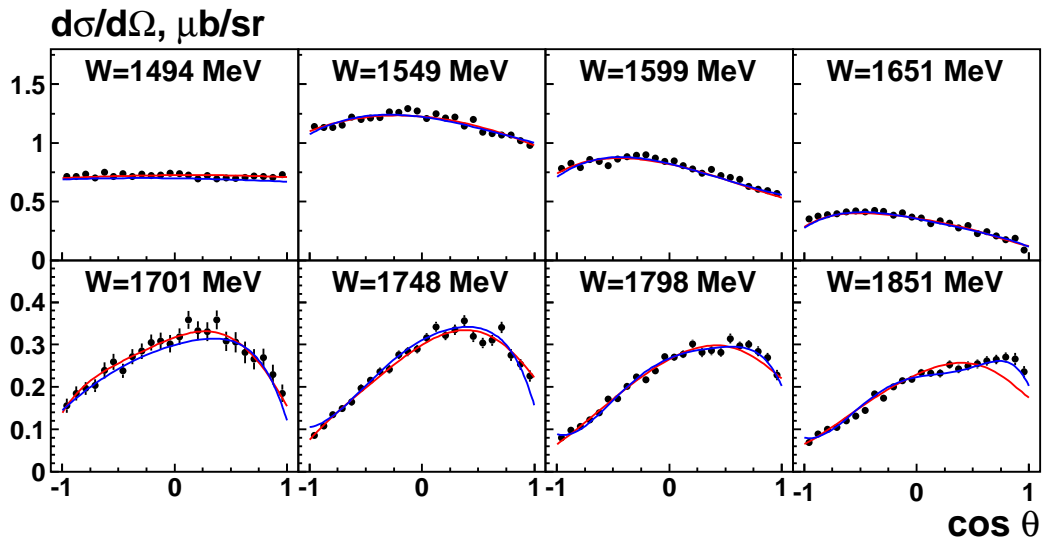


Figure 7.37: IB (red) and DR (blue) fit results for  $d\sigma/d\Omega$  [44]. Data are plotted from the threshold up to the last measured energy with the  $W$  step  $\sim 50$  MeV. For the IB fit  $\chi^2/N_{pt} = 3448/2544$ , for the DR fit  $\chi^2/N_{pt} = 3388/2544$ .

### 7.9.2 Description of $T$ and $F$ asymmetries

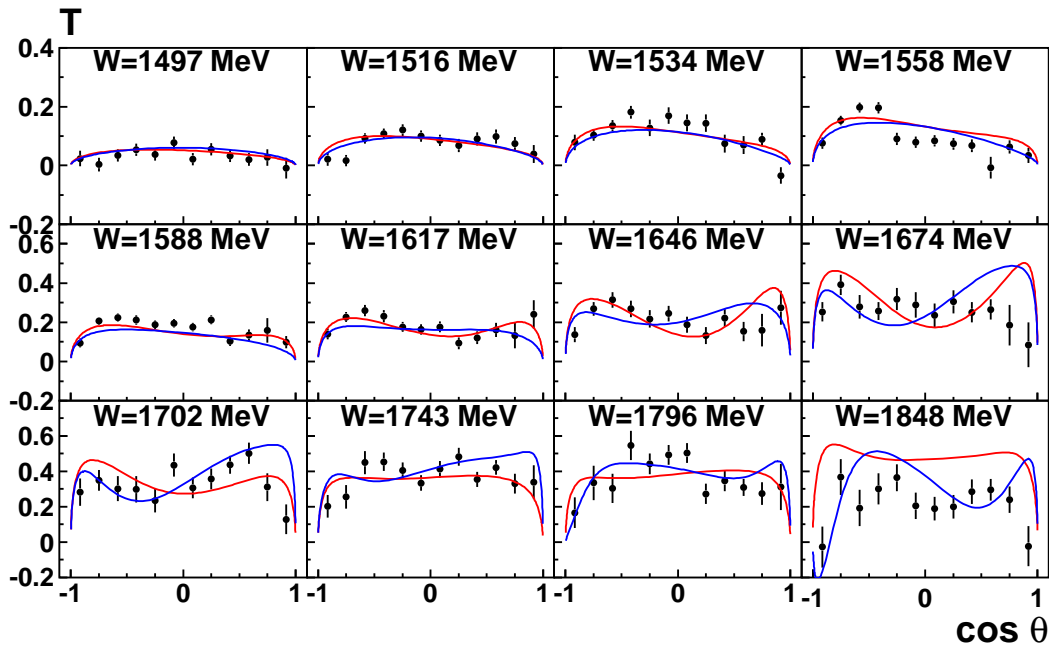


Figure 7.38: IB (red) and DR (blue) fit results for  $T$  [49]. For the IB fit  $\chi^2/N_{pt} = 456/144$ , for the DR fit  $\chi^2/N_{pt} = 423/144$ .

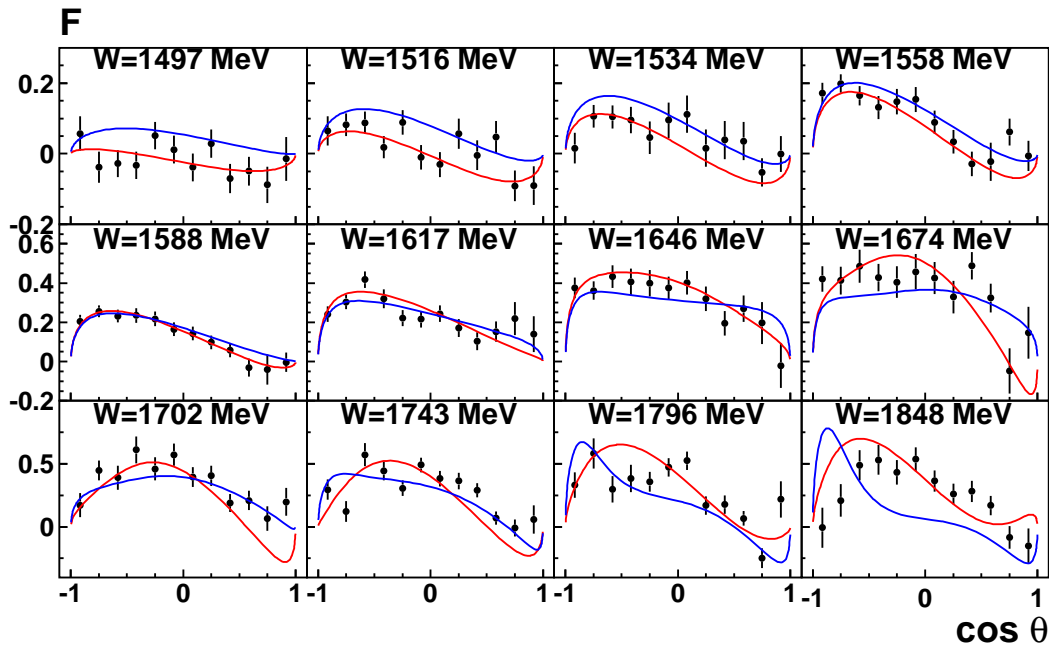


Figure 7.39: IB (red) and DR (blue) fit results for  $F$  [49]. For the IB fit  $\chi^2/N_{pt} = 318/144$ , for the DR fit  $\chi^2/N_{pt} = 426/144$ .

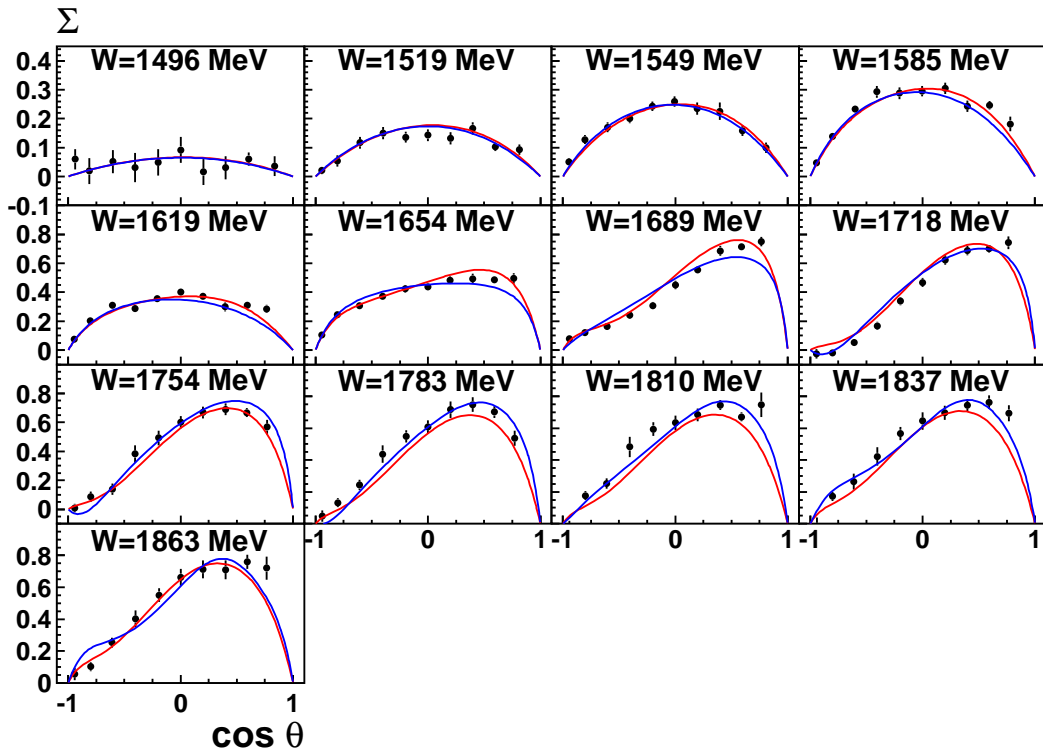
7.9.3 Description of  $\Sigma$  and  $E$  asymmetries

Figure 7.40: IB (red) and DR (blue) fit results for  $\Sigma$  [47]. For the IB fit  $\chi^2/N_{pt} = 323/130$ , for the DR fit  $\chi^2/N_{pt} = 353/130$

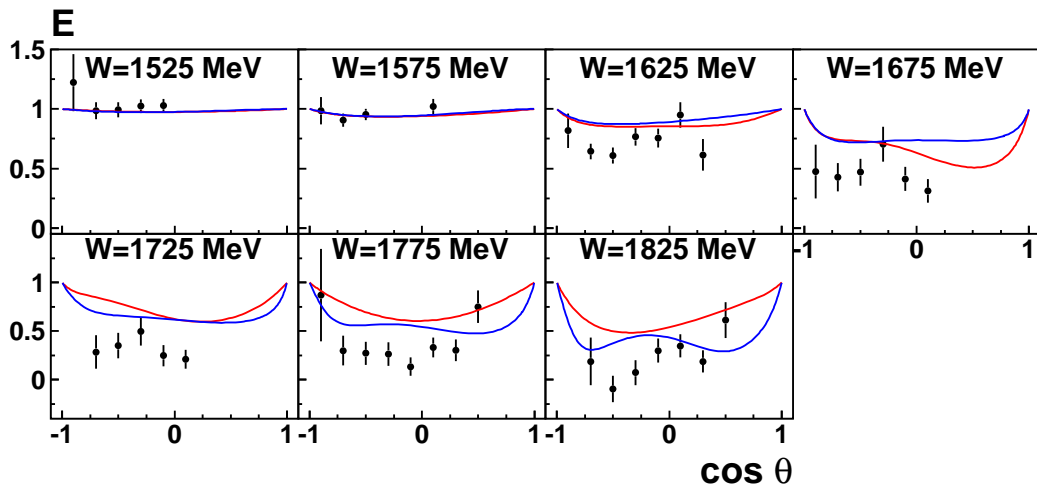


Figure 7.41: IB (red) and DR (blue) fit results for  $E$  [50]. For the IB fit  $\chi^2/N_{pt} = 38/42$ , for the DR fit  $\chi^2/N_{pt} = 31/42$

### 7.9.4 Description of $d\sigma/dt$ , $\Sigma$ , and $T$ at high energies

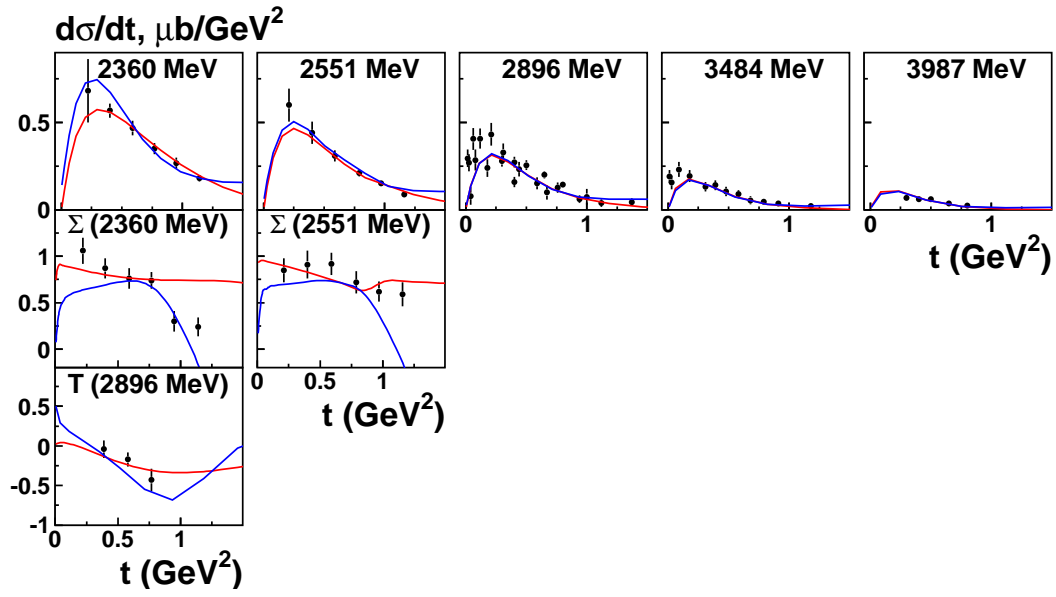


Figure 7.42: IB (red) and DR (blue) fit results for  $d\sigma/dt$ ,  $\Sigma$ ,  $T$  [77–80] as functions of  $t$ .  $d\sigma/dt$  is shown in  $\mu\text{b}/\text{GeV}^2$  units. For the IB fit  $\chi^2/N_{pt} = 11/52 \ 7/12 \ 1/3$ , for the DR fit  $\chi^2/N_{pt} = 13/52 \ 7/12 \ 2/3$

### 7.9.5 Regge contributions to the invariant amplitudes at fixed $t$ -values

In this solution Regge contributions ( $\nu$ ) were used. It is interesting to plot invariant amplitudes  $A_i$  in order to see how they change. Fig. 7.43 shows  $A_i(W)$  amplitudes at  $t = -0.2 \text{ GeV}^2$  with only Regge contributions taken into account. On Figs. 7.43 it is seen that at high energies now real parts in IB and DR approaches coincide.

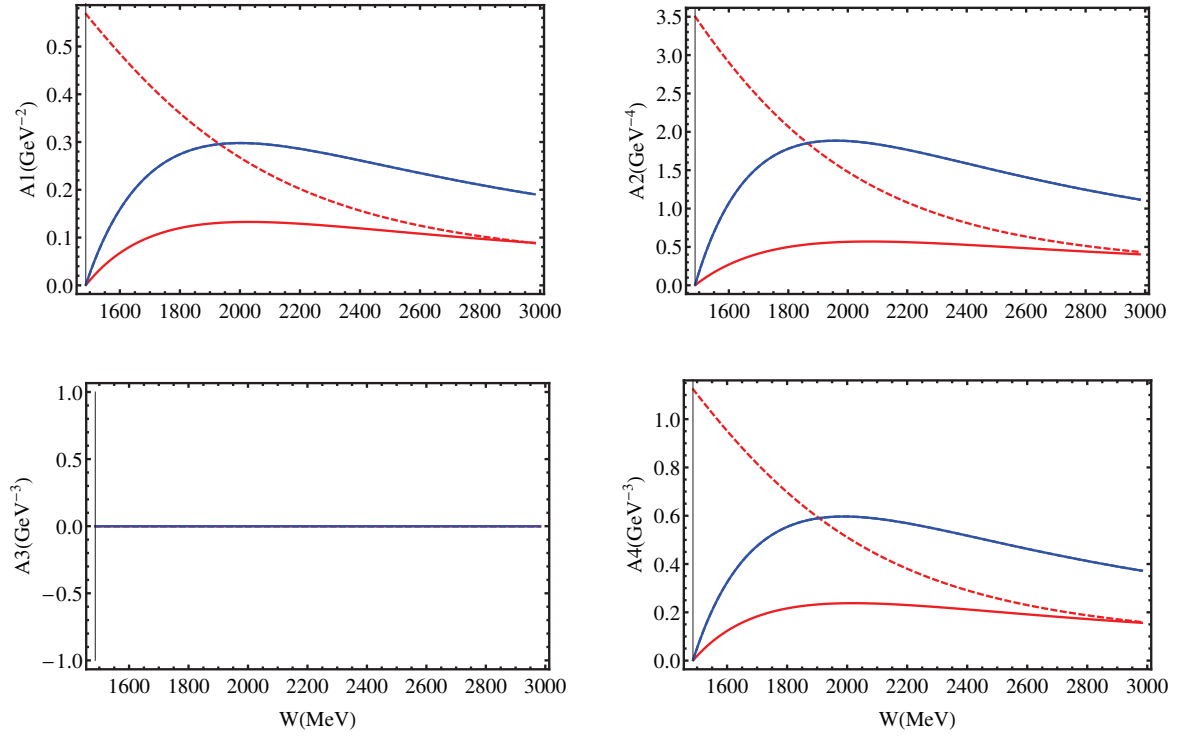


Figure 7.43: Regge contributions to the invariant amplitudes  $A_1, A_2, A_3, A_4$  for  $t = -0.2 \text{ GeV}^2$ . Solid red and blue lines denote real and imaginary parts obtained with an IB model. Red dashed lines denote real parts obtained using dispersion relations from the imaginary parts. Black vertical lines show the threshold of the physical region for a given  $t$ -value.

### 7.9.6 Multipoles

For this final solution we show the obtained electric and magnetic multipoles. For all other solutions the multipoles are presented in Appendix.

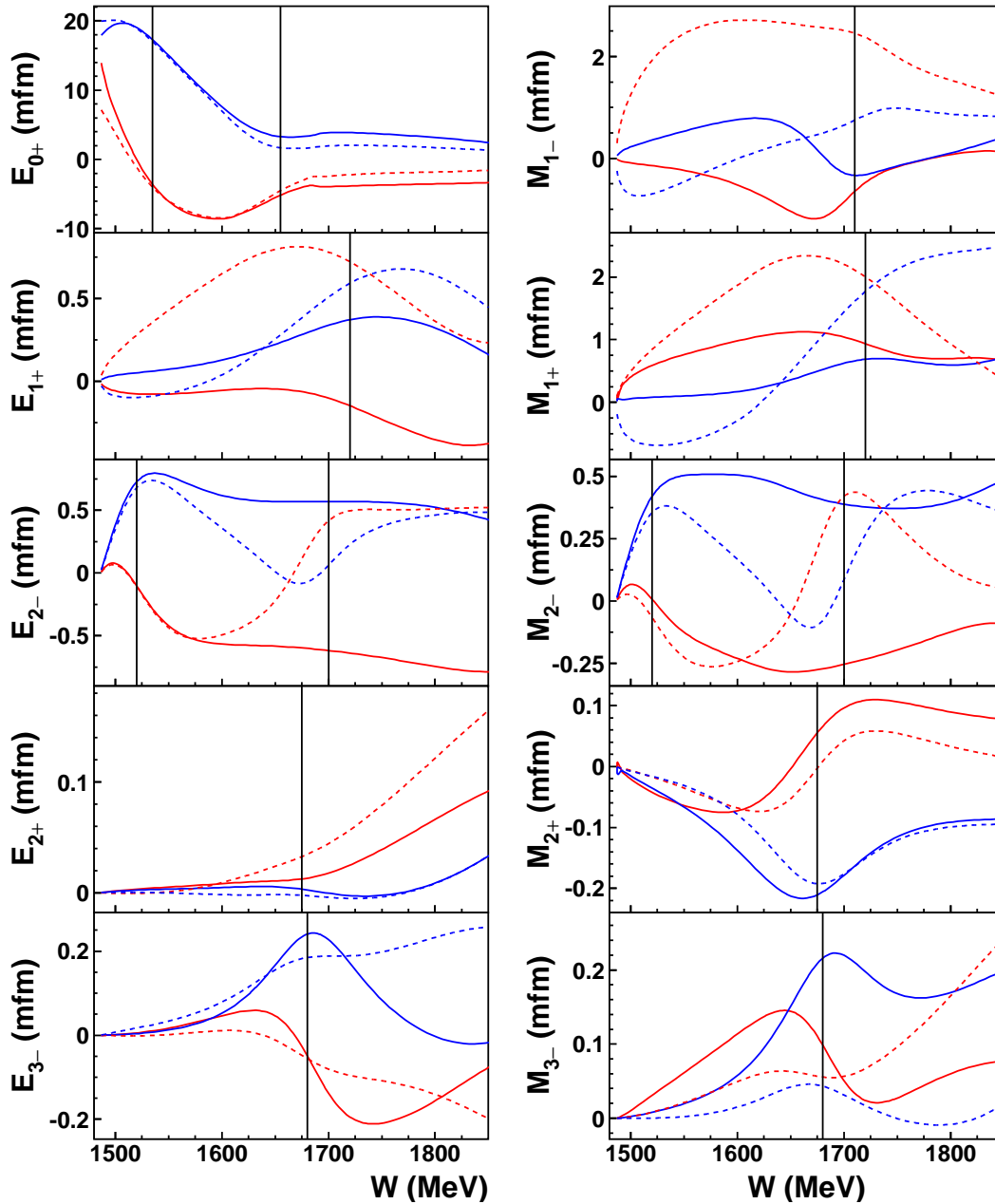


Figure 7.44: Multipoles for Solution 7. Here real parts of multipoles are drawn in red, imaginary parts in blue. IB results are drawn as solid curves, DR results as dashed curves. Vertical lines show the resonance positions.

An interesting observation is that despite the fact that solutions have very close  $\chi^2$  the multipoles look very different except for the  $E_{0+}$  which is the dominant one. This effect is known and the difference between multipoles is not so strong for  $\gamma p \rightarrow \pi N$  [65], where much more observables are measured. Therefore with the measuring of new polarization data for  $\gamma p \rightarrow \eta p$  one can also make the difference smaller.

### 7.9.7 Solution 7 summary

Descriptions of all analysed experimental data show good consistency with the data in both approaches. Observables are described with similar  $\chi^2$  values.

### 7.10 Intermediate conclusion for solutions 4-7

When we input phases for resonances and take into account Regge contributions in the proper form, we obtain a good description of the data. Our  $A_i$  amplitudes now obey dispersion relations equations.

On figs. 7.45 invariant amplitudes  $A_4$  for solutions 4-7 are presented.

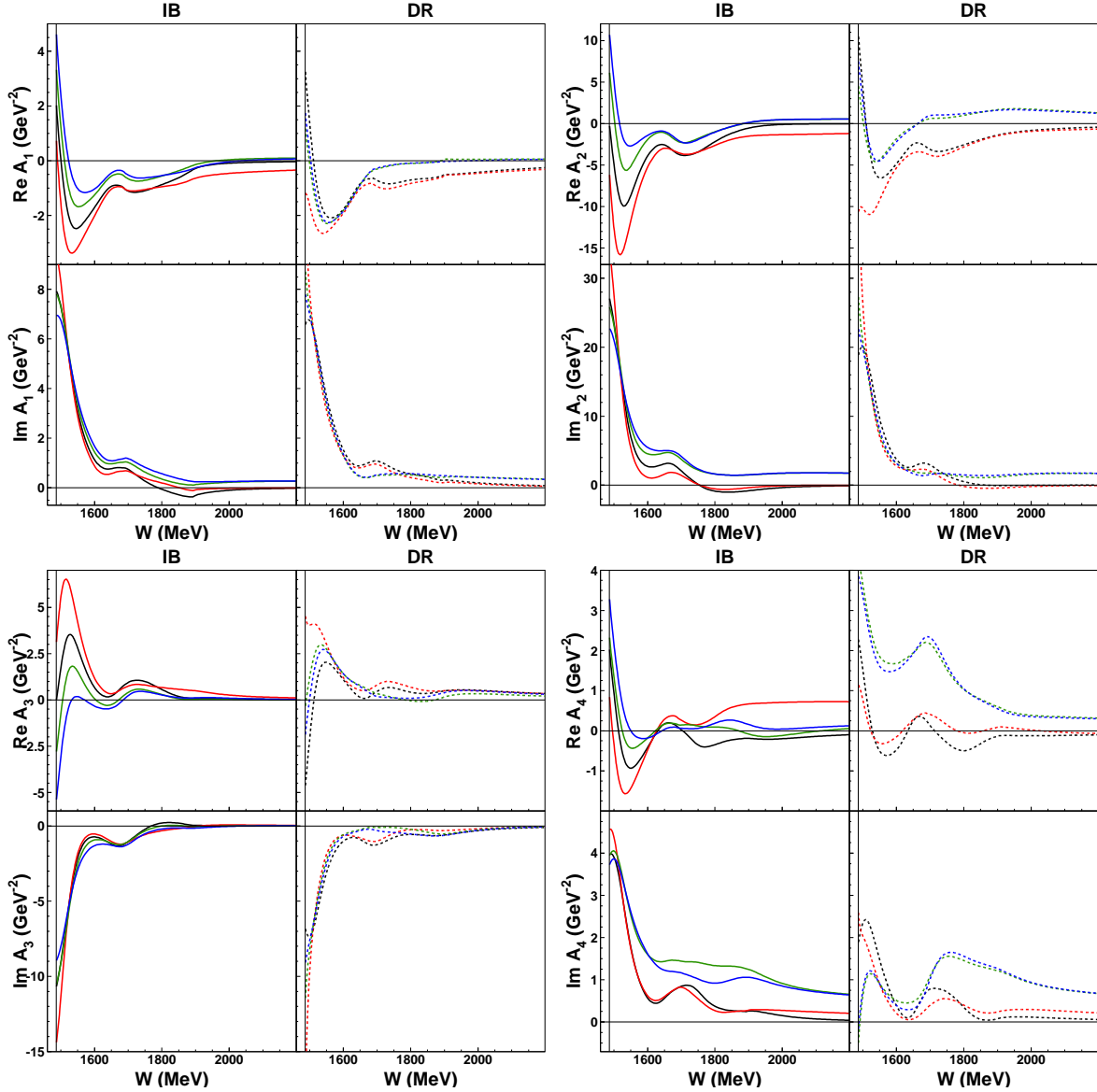


Figure 7.45: Invariant amplitudes  $A_i$  for solutions 4-7. Solution 4 is plotted in black, solution 5 in red, solution 6 in green and the final solution 7 in blue. IB and DR results are drawn as solid and dashed curves respectively. Black vertical lines show the threshold of the physical region for a  $t = -0.2 \text{ GeV}^2$



## 7.11 Final discussion of the resonance parameters

The partial wave analysis of  $\gamma p \rightarrow \eta p$  was done with two different approaches: using MAID isobar model and using fixed- $t$  dispersion relations.

Similar work was done in 2003 by Aznauryan [66] where fixed- $t$  dispersion relations approach was applied to analyze the existing experimental data at that time [48, 71–74].

The difference between present work and [66] is that

- 1) now modern and more precise data are used in the analysis,
- 2) in the DR case contributions of the unphysical region from all resonances are taken into account.

In the work [66] contributions below threshold were only taken into account from  $N(1440) 1/2^+$ ,  $N(1535) 1/2^-$ ,  $N(165) 1/2^-$ .

The initial task was to describe low-energy data and to determine the leading singularities of the scattering amplitude, *i.e.* the extraction of the resonance parameters. During the study, it was found that the use of  $t$ -channel exchanges and resonance phases provide a good description of the low energy data, and also the description of the high energy data. We did not attempt description of the high energy data in the beginning, but nevertheless the result gives space for further research.

Seven different solutions were investigated. Summary tables 7.9 and 7.10 show  $\chi^2$  values for all solutions together.

Table 7.9:  $\chi^2$  values. Red values are for IB fits, blue ones are for DR fits.

Sol.	$\chi_{d\sigma/d\Omega}^2$	$\chi_T^2$	$\chi_F^2$	$\chi_\Sigma^2$	$\chi_E^2$	$\chi_{d\sigma/dt}^2$	$\chi_\Sigma^2$	$\chi_T^2$	$\chi^2/N_{dof}$
1	4054 6889	523 1353	509 975	822 947	42 52				2.07 3.04
2	3822 5170	605 1196	443 711	637 1111	29 37				1.88 2.78
3	5008 6361	453 1082	425 809	1117 1005	56 42	33 108	4 33	3 31	2.45 3.11
4	3427 3890	532 708	316 534	490 794	38 33				1.68 2.02
5	4729 3527	606 503	316 581	832 796	38 26	34 102	7 15	3 19	2.23 1.86
6	3946 3641	536 519	333 394	377 437	53 36	11 13	7 7	1 2	1.84 1.77
7	3448 3388	456 423	318 426	323 353	38 31	11 13	7 13	1 2	1.61 1.61

Table 7.10:  $\chi^2/N_{pt}$  values. Red values are for IB fits, blue ones are for DR fits.

Sol.	$\chi_{d\sigma/d\Omega}^2$	$\chi_T^2$	$\chi_F^2$	$\chi_\Sigma^2$	$\chi_E^2$	$\chi_{d\sigma/dt}^2$	$\chi_\Sigma^2$	$\chi_T^2$
1	1.59 2.71	3.63 9.4	3.53 6.77	6.32 7.28	1 1.24			
2	1.5 2.03	4.2 8.3	3.07 4.93	4.9 8.55	0.69 0.88			
3	1.97 2.5	3.15 7.51	2.95 5.61	8.59 7.73	1.33 0.98	0.63 2.08	0.33 2.75	1 10.3
4	1.35 1.53	3.69 4.92	2.19 3.71	3.77 6.11	0.9 0.79			
5	1.86 1.39	4.21 3.49	2.19 4.03	6.4 6.12	0.9 0.62	0.65 1.96	0.58 1.25	1 6.33
6	1.55 1.43	3.72 3.6	2.31 2.74	2.9 3.36	1.26 0.86	0.21 0.25	0.58 0.58	0.33 0.66
7	1.36 1.33	3.17 2.94	2.21 2.96	2.48 2.72	0.9 0.74	0.21 0.25	0.58 1.08	0.33 0.66

Below the summary tables of resonance parameters for each resonance and all solutions are given. Red values are for IB fits and blue values are for DR fits. Values which were fixed in the fit are given in black bold type. The last line gives PDG values and star rating. Branching ratios are shown with the sign that is taken into account in the coupling constant  $g_{\eta N}$ .

- All given errors for masses, widths, photoexcitation helicity amplitudes and phases were taken from the fitting program (MIGRAD) and correspond to the values of the last (best) solution. The shown errors for the branching ratios are calculated out of errors of the coupling constants  $g_{\eta N}$ , which were used as a fitting parameters. For presented errors all correlations are taken into account by the MIGRAD package.
- For each resonance at least one of the photoexcitation helicity amplitudes ( $A_{1/2}$  or  $A_{3/2}$ ) must be fixed. These 2 parameters strongly correlate with each other, therefore we cannot fit both of them together. We decided to fix always  $A_{3/2}$  when both of them are present and fix  $A_{1/2}$  for  $1/2^+$  and  $1/2^-$  states. We fix these values either to the PDG estimations or to the results obtained in the latest EtaMAID analysis.

### $N(1440) 1/2^+$

At first let us discuss the fit parameters of  $N(1440) 1/2^+$ . This is four-star resonance which parameters are very well known. In all calculations mass, width, and  $A_{1/2}$  were fixed  $M = 1430$  MeV  $\Gamma = 350$  MeV  $A_{1/2} = -60 \times 10^{-3} \text{GeV}^{-1/2}$  respectively. Branching ratios into other channels  $\beta_{\pi N} = 65\%$ ,  $\beta_{K\Lambda} = \beta_{K\Sigma} = \beta_{\omega N} = \beta_{\eta' N} = 0\%$ ,  $\beta_{\pi\pi N} = 1 - \sum \beta_i$ . The only fitting parameter was coupling constant into  $\eta N$  channel. The values for  $g_{\eta N}$  are listed in the table below:

Table 7.11: Fit results for  $g_{\eta N}$  for  $N(1440) 1/2^+$ . Red values were obtained in the IB fit, blue ones in DR fit.

Solution	$g_{\eta N}$
1	17, 51
2	12, 22
3	13, 49
4	10, -11
5	3, -3
6	4, -27
7	18±94, -19±37

As one can see implementation of phases and additional physical constrains forced fit to pick a different sign of the coupling constant. The obtained errors are large because this is a sub-threshold resonance and only limited part of its energy dependent behavior is under control. However one can see that in the case of DR the error is about 2 times smaller because in this approach the real parts of the invariant amplitudes are obtained via the integration of the imaginary parts, therefore the sub-threshold behavior is taken into account.

$N(1520) 3/2^-$ 

Table 7.12: Resonance parameters for  $N(1520) 3/2^-$ . Red values were obtained in the IB fit, blue ones in DR fit. Fixed values are written in bold black. Branchings into other channels were fixed to  $\beta_{\pi N} = 61\%$ ,  $\beta_{K\Lambda} = \beta_{K\Sigma} = \beta_{\omega N} = \beta_{\eta' N} = 0\%$ ,  $\beta_{\pi\pi N} = 1 - \sum \beta_i$ . Stars show the overall PDG rating.

$N(1520) 3/2^-$	Solution	$M$	$\Gamma$	$\zeta_{\eta N} \beta_{\eta}(\%)$	$A_{1/2}$	$A_{3/2}$
Phase( $\Phi_j^\alpha$ )	1	1510, 1520	<b>115</b>	+0.09, +0.05	-25, -25	<b>140</b>
	2	1511, 1519	<b>115</b>	+0.08, +0.06	-25, -25	<b>140</b>
	3	1510, 1510	<b>115</b>	+0.08, +0.02	-25, -25	<b>140</b>
33, -18	4	1520, 1510	<b>115</b>	+0.13, +0.07	-25, -25	<b>140</b>
34, -25	5	1510, 1510	<b>115</b>	+0.12, +0.07	-25, -25	<b>140</b>
21, -37	6	1520, 1510	<b>115</b>	+0.1, +0.09	-25, -25	<b>140</b>
-2±73, -31±18	7	1510±10, 1514±6	<b>115</b>	+0.05±1, +0.1±1	-25±6, -25±6	<b>140</b>
****	PDG	1515 ± 5	115 <sup>+10</sup> <sub>-15</sub>	0 ± 1	-20 ± 5	140 ± 10

According to the PDG star rating  $N(1520)3/2^-$  is well studied resonance. Results of our analysis show consistency with the PDG estimations for this resonance. The  $A_{1/2}$  values however are at the top border of the interval in which we vary the values for this parameter.

We also fixed the width of this resonance. In the research we have observed that this parameter always got stuck in the unphysical value of  $\approx 50$  MeV.

We can conclude that the values obtained with both approaches are in a good agreement with each other and with PDG.

 $N(1535) 1/2^-$ 

Table 7.13: Resonance parameters for  $N(1535) 1/2^-$ . Red values were obtained in the IB fit, blue ones in DR fit. Fixed values are written in bold black. Branchings into other channels were fixed to  $\beta_{\pi N} = 52\%$ ,  $\beta_{K\Lambda} = \beta_{K\Sigma} = \beta_{\omega N} = \beta_{\eta' N} = 0\%$ ,  $\beta_{\pi\pi N} = 1 - \sum \beta_i$ . Stars show the overall PDG rating.

$N(1535) 1/2^-$	Solution	$M$	$\Gamma$	$\zeta_{\eta N} \beta_{\eta}(\%)$	$A_{1/2}$	$A_{3/2}$
Phase( $\Phi_j^\alpha$ )	1	1525, 1525	156, 168	+40, +40	<b>115</b>	-
	2	1525, 1525	155, 174	+40, +41	<b>115</b>	-
	3	1537, 1525	174, 175	+45, +41	<b>115</b>	-
0	4	1525, 1525	157, 175	+40, +44	<b>115</b>	-
0	5	1525, 1525	148, 175	+38, +43	<b>115</b>	-
0	6	1525, 1531	160, 175	+39, +41	<b>115</b>	-
-4 ± 31, 10 ± 27	7	1525±17, 1530±13	158±37, 175±47	+40±15, +40±13	<b>115</b>	-
****	PDG	1535 ± 10	150 ± 25	42 ± 10	115 ± 15	-

$N(1535) 1/2^-$  is also a well determined resonance with a big branching ratio into  $\eta N$  channel. Results of the analysis show a very good agreement with the PDG values. Both IB and DR approaches give close results. The obtained errors are qualitatively similar to the ones given by PDG.

$N(1650) 1/2^-$ 

Table 7.14: Resonance parameters for  $N(1650) 1/2^-$ . Red values were obtained in the IB fit, blue ones in DR fit. Fixed values are written in bold black. Branchings into other channels were fixed to  $\beta_{\pi N} = 51\%$ ,  $\beta_{K\Lambda} = 10\%$ ,  $\beta_{\omega N} = \beta_{\eta' N} = 0\%$ ,  $\beta_{\pi\pi N} = 1 - \sum \beta_i$ . Stars show the overall PDG rating.

$N(1650) 1/2^-$	Solution	$M$	$\Gamma$	$\zeta_{\eta N} \beta_{\eta}(\%)$	$A_{1/2}$	$A_{3/2}$
	1	1641, 1642	137, 117	-22, -16	<b>45</b>	-
	2	1640, 1640	135, 130	-22, -16	<b>45</b>	-
Phase( $\Phi_j^\alpha$ )	3	1640, 1640	125, 120	-20, -12	<b>45</b>	-
<b>0</b>	4	1640, 1643	135, 123	-21, -16	<b>45</b>	-
<b>0</b>	5	1640, 1640	135, 114	-23, -15	<b>45</b>	-
<b>0</b>	6	1645, 1650	137, 119	-22, -26	<b>45</b>	-
$4 \pm 27, -18 \pm 22$	7	1653 $\pm$ 21, 1640 $\pm$ 27	137 $\pm$ 29, 122 $\pm$ 28	-23 $\pm$ 16, -25 $\pm$ 14	<b>45</b>	-
****	PDG	1655 $^{+15}_{-10}$	140 $\pm$ 30	1 $\pm$ 2, 18 $\pm$ 4	45 $\pm$ 10	-

Another four star resonance is  $N(1650) 1/2^-$ . As well as  $N(1535) 1/2^-$  it has a big branching ratio into  $\eta N$  channel. The result for all parameters is a good agreement with the PDG values. The branching ratio into  $\eta N$  channel coincides with the results of Bonn-Gatchina analysis (18  $\pm$  4%). Both IB and DR approaches give similar results.

In addition in order to describe the decay of  $N(1650) 1/2^-$  into  $K\Sigma$  channel, coupling constant  $g_{K\Sigma}$  was used. Using this constant we were able to describe the cusp effect in the total cross section, see Fig. 7.2. Table below shows  $g_{K\Sigma}$  values for all solutions.

Table 7.15: Fit results for  $g_{K\Sigma}$  for  $N(1650) 1/2^-$

Solution	$g_{K\Sigma}$
1	94, 100
2	92, 89
3	99, 91
4	95, 97
5	100, 78
6	81, 35
7	68 $\pm$ 83, 43 $\pm$ 67

Values for the coupling constant coincide within the errors in both approaches. One can also see that in the DR case the error is smaller, the previous explanation for the case of Roper is valid for this constant also.

$N(1675) 5/2^-$ 

Table 7.16: Resonance parameters for  $N(1675) 5/2^-$ . Red values were obtained in the IB fit, blue ones in DR fit. Fixed values are written in bold black. Branchings into other channels were fixed to  $\beta_{\pi N} = 41\%$ ,  $\beta_{K\Lambda} = 1\%$ ,  $\beta_{K\Sigma} = \beta_{\omega N} = \beta_{\eta' N} = 0\%$ ,  $\beta_{\pi\pi N} = 1 - \sum \beta_i$ . Stars show the overall PDG rating.

$N(1675) 5/2^-$	Solution	$M$	$\Gamma$	$\zeta_{\eta N} \beta_{\eta}(\%)$	$A_{1/2}$	$A_{3/2}$
Phase( $\Phi_j^\alpha$ )	1	1670, 1670	165, 147	-1, -0.06	11, 11	20
	2	1670, 1670	165, 135	-1, -0.15	11, 13	20
	3	1670, 1670	165, 135	-1.7, -0.06	11, 26	20
60, 30	4	1670, 1680	165, 135	-1.2, -0.7	26, 26	20
-60, -6	5	1680, 1670	162, 157	0.2, -2	14, 27	20
43, -10	6	1680, 1678	165, 159	-1.4, -1.7	11, 11	20
22±91, -2±16	7	1680±10, 1677±8	165±19, 135±15	-2±1, -1.2±1	11±16, 12±8	20
****	PDG	1675 ± 5	150 <sup>+15</sup> <sub>-20</sub>	0 ± 1	19 ± 8	20 ± 5

$N(1675) 5/2^-$  is a four star resonance which parameters were well studied in pion photoproduction due to a high branching ratio,  $\approx 45\%$ , into this channel. However in  $\eta$  photoproduction the branching ratio is small. The value  $\beta_{\eta N} = 0 \pm 1$  is the only result which is given in PDG above the line. The results of different analysis below the line coincide with this estimation within the errors. Both approaches in our analysis are matched with PDG estimations. Obtained phases can not be precisely determined. But one can observe that DR errors are much smaller than the ones obtained with an IB.

 $N(1680) 5/2^+$ 

Table 7.17: Resonance parameters for  $N(1680) 5/2^+$ . Red values were obtained in the IB fit, blue ones in DR fit. Fixed values are written in bold black. Branchings into other channels were fixed to  $\beta_{\pi N} = 62\%$ ,  $\beta_{K\Lambda} = \beta_{K\Sigma} = \beta_{\omega N} = \beta_{\eta' N} = 0\%$ ,  $\beta_{\pi\pi N} = 1 - \sum \beta_i$ . Stars show the overall PDG rating.

$N(1680) 5/2^+$	Solution	$M$	$\Gamma$	$\zeta_{\eta N} \beta_{\eta}(\%)$	$A_{1/2}$	$A_{3/2}$
Phase( $\Phi_j^\alpha$ )	1	1684, 1675	120, 122	+0.22, +0.14	-21, -21	133
	2	1680, 1675	120, 120	+0.3, +0.24	21, -21	133
	3	1675, 1689	120, 120	+0.1, +0.2	-9, -21	133
0	4	1679, 1695	120, 120	+0.22, +0.12	-21, -9	133
0	5	1675, 1695	120, 120	+0.13, +0.1	-19, -10	133
0	6	1680, 1675	120, 129	+0.16, +0.05	-21, -9	133
3±83, 2±4	7	1691±18, 1675±10	120±20, 138±12	+0.16±1, +0.02±1	-21±10, -19±8	133
****	PDG	1685 ± 5	130 ± 10	0 ± 1	-15 ± 6	133 ± 12

Another four star resonance with a small branching ratio to the  $\eta N$  channel is  $N(1680) 5/2^+$ . The masses and widths of all solutions are in a good agreement with PDG values. The results for  $A_{1/2}$  are close to PDG mean values as well.

$N(1700) 3/2^-$ 

Table 7.18: Resonance parameters for  $N(1700) 3/2^-$ . Red values were obtained in the IB fit, blue ones in DR fit. Fixed values are written in bold black. Branchings into other channels were fixed to  $\beta_{\pi N} = 15\%$ ,  $\beta_{K\Lambda} = 3\%$ ,  $\beta_{K\Sigma} = \beta_{\omega N} = \beta_{\eta' N} = 0\%$ ,  $\beta_{\pi\pi N} = 1 - \sum \beta_i$ . Stars show the overall PDG rating.

$N(1700) 3/2^-$	Solution	$M$	$\Gamma$	$\zeta_{\eta N} \beta_{\eta}(\%)$	$A_{1/2}$	$A_{3/2}$
	1	1726, 1650	100, 100	-0.01, +0.3	20, 24	-37
	2	1750, 1650	146, 100	+0.09, +0.6	80, 20	-37
Phase( $\Phi_j^\alpha$ )	3	1750, 1650	223, 250	+0.2, -0.2	80, 80	-37
55, 49	4	1750, 1665	100, 115	-0.5, +1.1	20, 20	-37
-60, 60	5	1694, 1686	100, 100	-0.43, +0.15	20, 20	-37
20, 25	6	1650, 1685	250, 100	-0.4, +2	80, 20	-37
$30 \pm 86$ , $27 \pm 40$	7	$1650 \pm 56$ , $1686 \pm 39$	$250 \pm 117$ , $100 \pm 81$	$-0.3 \pm 1$ , $+2.7 \pm 1$	$80 \pm 56$ , $20 \pm 57$	-37
***	PDG	$1700 \pm 50$	$150_{-50}^{+100}$	No average	$41 \pm 17$	$-37 \pm 14$

Obtained masses and widths of  $N(1700) 3/2^-$  are in agreement with the PDG estimations. However the latest BnGa analysis [82] gives values for them  $\approx 1800$  and  $\approx 400$  MeV respectively, which is higher than the results from our IB and DR fits. Also the boundary values for the width were preferred by both fits.

There are no estimations for the branching ratio that are above the line from PDG. The values that were not used for averaging varies from 1% (old result) to 14% (latest result). In our analysis a big branching ratio is not observed.

The allowed boundary values for  $A_{1/2}$  were preferred in all solutions except DR fit for the first solution.

 $N(1710) 1/2^+$ 

Table 7.19: Resonance parameters for  $N(1710) 1/2^+$ . Red values were obtained in the IB fit, blue ones in DR fit. Fixed values are written in bold black. Branchings into other channels were fixed to  $\beta_{\pi N} = 5\%$ ,  $\beta_{K\Lambda} = 23\%$ ,  $\beta_{K\Sigma} = \beta_{\omega N} = \beta_{\eta' N} = 0\%$ ,  $\beta_{\pi\pi N} = 1 - \sum \beta_i$ . Stars show the overall PDG rating.

$N(1710) 1/2^+$	Solution	$M$	$\Gamma$	$\zeta_{\eta N} \beta_{\eta}(\%)$	$A_{1/2}$	$A_{3/2}$
	1	1701, 1680	100	+1.1, -1.7	50	-
	2	1701, 1740	100	+1.5, -1.1	50	-
Phase( $\Phi_j^\alpha$ )	3	1694, 1702	100	+0.8, +0.4	50	-
0	4	1700, 1724	100	-1, +0.8	50	-
0	5	1695, 1706	100	+0.2, +1.4	50	-
0	6	1710, 1740	100	+1.6, -0.3	50	-
$-35 \pm 107$ , $-43 \pm 111$	7	$1699 \pm 48$ , $1732 \pm 32$	100	$+0.96 \pm 4$ , $-0.19 \pm 5$	50	-
****	PDG	$1710 \pm 30$	$100_{-50}^{+150}$	10 - 50	$50 \pm 10$	-

The mass of  $N(1710) 1/2^+$  was determined with an agreement with the PDG values. The width was fixed for the same reasons as for the  $N(1520) 3/2^-$ . With the open ranges this parameter always got stuck in the unphysical value of  $\approx 50$  MeV. However the branching ratio obtained in our analysis is much smaller in comparison with the results of other groups.

$N(1720) 3/2^+$ 

Table 7.20: Resonance parameters for  $N(1720) 3/2^+$ . Red values were obtained in the IB fit, blue ones in DR fit. Fixed values are written in bold black. Branchings into other channels were fixed to  $\beta_{\pi N} = 11\%$ ,  $\beta_{K\Lambda} = 8\%$ ,  $\beta_{K\Sigma} = \beta_{\omega N} = \beta_{\eta' N} = 0\%$ ,  $\beta_{\pi\pi N} = 1 - \sum \beta_i$ . Stars show the overall PDG rating.

$N(1720) 3/2^+$	Solution	$M$	$\Gamma$	$\zeta_{\eta N} \beta_{\eta}(\%)$	$A_{1/2}$	$A_{3/2}$
Phase( $\Phi_j^\alpha$ )	1	1750, 1731	190, 213	+0.6, +1.7	96, 127	80
	2	1750, 1734	195, 171	+0.7, +1.4	93, 130	80
	3	1750, 1750	397, 168	+0.9, +1.2	80, 82	80
-6, -40	4	1750, 1747	228, 326	+1.2, +2.7	80, 80	80
-17, -44	5	1750, 1750	400, 370	+1, +6	80, 80	80
10, -39	6	1750, 1750	231, 344	+1, +7	80, 115	80
12±92, -40±7	7	1750±49, 1750±31	211±173, 323±191	+0.64±3, +9.2±2	80±50, 92±27	80
***	PDG	1720 <sup>+30</sup> <sub>-20</sub>	250 <sup>+150</sup> <sub>-100</sub>	0 ± 1, 3 ± 2	100 ± 20	135 ± 40 48 ± 2

The mass and the width of  $N(1720) 3/2^+$  are in agreement within the errors with the PDG estimations and results of other analysis. A clear tendency of choosing the bordered values for the mass of the resonance is observed. It is also seen that the uncertainties for the width obtained with both approaches are large. The obtained branching ratio into  $\eta N$  channel is compatible with other results. For  $A_{3/2}$  different two values above the line a given in PDG. In our case we fixed this value to 80.

 $N(1860) 5/2^+$ 

Table 7.21: Resonance parameters for  $N(1860) 5/2^+$ . Red values were obtained in the IB fit, blue ones in DR fit. Fixed values are written in bold black. Branchings into other channels were fixed to  $\beta_{\pi N} = 20\%$ ,  $\beta_{K\Lambda} = \beta_{K\Sigma} = \beta_{\omega N} = 0$ ,  $\beta_{\pi\pi N} = 1 - \sum \beta_i$ ,  $g_{\eta' N} = 0$ . Stars show the overall PDG rating.

$N(1860) 5/2^+$	Solution	$M$	$\Gamma$	$\zeta_{\eta N} \beta_{\eta}(\%)$	$A_{1/2}$	$A_{3/2}$
Phase( $\Phi_j^\alpha$ )	1	1860	270	-5, -2.5	1, -22	29, 49
	2	1860	270	-5.6, -3.9	-5, -31	36, 44
	3	1860	270	-3.5, -1.2	16, -5	8, 54
0	4	1860	270	-5.1, -0.4	2, -37	24, 9
0	5	1860	270	-3.4, -4.9	5, -7	21, 8
0	6	1860	270	-1.1, -6.3	59, -12	22, 11
3 ± 90, 0 ± 1	7	1860	270	-0.6±7, -6.9±8	54±123, -18±15	38±111, 1±18
**	PDG	1860 <sup>+100</sup> <sub>-40</sub>	270 <sup>+140</sup> <sub>-50</sub>	No average	No average	No average

$N(1860) 5/2^+$  is a poorly studied resonance with no given PDG estimations for the branching ratio and for  $A_{1/2}$ ,  $A_{3/2}$  photoexcitation helicity amplitudes. The results that we obtained with isobar model and with a fixed- $t$  dispersion relations are scattered. The errors of  $A_{1/2}$ ,  $A_{3/2}$  obtained with an IB fit are very large, however with an implementation of dispersion relations they are much smaller. One can conclude that even if the parameters are strongly correlated an additional physical constraint helps us to decrease the error.

- Until this point all resonances had masses that lay within the analyzed data interval. However we also included resonances with higher masses and large widths. We reduced the number of fitted parameters for these resonances because our analyzed data are not sufficient for the correct determination of their values.
- For  $N(1875) 3/2^-$  we fit only coupling constant,  $A_{1/2}$  helicity amplitude and phase.
- For the resonances with higher masses we fit only coupling constants and phases. Other parameters were fixed to the results obtained in the latest EtaMAID analysis or to the PDG estimations.

 $N(1875) 3/2^-$ 

Table 7.22: Resonance parameters for  $N(1875) 3/2^-$ . Red values were obtained in the IB fit, blue ones in DR fit. Fixed values are written in bold black. Branchings into other channels were fixed to  $\beta_{\pi N} = 4\%$ ,  $\beta_{K\Lambda} = 4\%$ ,  $\beta_{K\Sigma} = 15\%$ ,  $\beta_{\omega N} = 20\%$ ,  $\beta_{\pi\pi N} = 1 - \sum \beta_i$ ,  $g_{\eta' N} = 0$ . Stars show the overall PDG rating.

$N(1875) 3/2^-$	Solution	$M$	$\Gamma$	$\zeta_{\eta N} \beta_{\eta} (\%)$	$A_{1/2}$	$A_{3/2}$
	1	<b>1875</b>	<b>250</b>	+27, +20	11, 30	-7
	2	<b>1875</b>	<b>250</b>	+29, +23	10, 30	-7
Phase( $\Phi_j^\alpha$ )	3	<b>1875</b>	<b>250</b>	-0.6, +25	30, 30	-7
60, -27	4	<b>1875</b>	<b>250</b>	+1, +17	29, 24	-7
60, -16	5	<b>1875</b>	<b>250</b>	+20, +34	25, 12	-7
60, -34	6	<b>1875</b>	<b>250</b>	+0.7, +6	30, 25	-7
$60 \pm 84, -32 \pm 21$	7	<b>1875</b>	<b>250</b>	$+2.2 \pm 10, +5.5 \pm 8$	$30 \pm 19, 30 \pm 17$	-7
***	PDG	$1875_{-55}^{+45}$	$250 \pm 70$	$0 \pm 1$	$18 \pm 10$	$-7 \pm 4$

In case of  $N(1875) 3/2^-$  due to a limited data range the obtained results have large uncertainties.



$N(1880) 1/2^+$ ,  $N(1895) 1/2^-$ ,  $N(1900) 3/2^+$

Table 7.23: Resonance parameters for  $N(1880) 1/2^+$ . Red values were obtained in the IB fit, blue ones in DR fit. Fixed values are written in bold black. Branchings into other channels were fixed to  $\beta_{\pi N} = 6\%$ ,  $\beta_{K\Lambda} = 2\%$ ,  $\beta_{K\Sigma} = 17\%$ ,  $\beta_{\omega N} = 0\%$ ,  $\beta_{\pi\pi N} = 1 - \sum \beta_i$ ,  $g_{\eta N} = 0$ . Stars show the overall PDG rating.

$N(1880) 1/2^+$	Solution	$M$	$\Gamma$	$\zeta_{\eta N}\beta_{\eta}(\%)$	$A_{1/2}$	$A_{3/2}$
Phase( $\Phi_j^\alpha$ )	1	<b>1880</b>	<b>230</b>	-4, +6.7	<b>21</b>	-
	2	<b>1880</b>	<b>230</b>	-20, +1.6	<b>21</b>	-
	3	<b>1880</b>	<b>230</b>	+0.05, +5.5	<b>21</b>	-
<b>0</b>	4	<b>1880</b>	<b>230</b>	-19, +8.5	<b>21</b>	-
<b>0</b>	5	<b>1880</b>	<b>230</b>	-0.7, +4.3	<b>21</b>	-
<b>0</b>	6	<b>1880</b>	<b>230</b>	-19, -2.7	<b>21</b>	-
$-60 \pm 118$ , $-31 \pm 72$	7	<b>1880</b>	<b>230</b>	$-19 \pm 15$ , $-9.8 \pm 10$	<b>21</b>	-
**	PDG	$1875 \pm 40$	$230 \pm 50$	$25^{+30}_{-20}$	No average	

Table 7.24: Resonance parameters for  $N(1895) 1/2^-$ . Red values were obtained in the IB fit, blue ones in DR fit. Fixed values are written in bold black. Branchings into other channels were fixed to  $\beta_{\pi N} = 2.5\%$ ,  $\beta_{K\Lambda} = 18\%$ ,  $\beta_{K\Sigma} = 13\%$ ,  $\beta_{\omega N} = 0\%$ ,  $\beta_{\pi\pi N} = 1 - \sum \beta_i$ ,  $g_{\eta N} = -71$ . Stars show the overall PDG rating.

$N(1895) 1/2^-$	Solution	$M$	$\Gamma$	$\zeta_{\eta N}\beta_{\eta}(\%)$	$A_{1/2}$	$A_{3/2}$
Phase( $\Phi_j^\alpha$ )	1	<b>1896</b>	<b>130</b>	+27, +24	<b>-36</b>	-
	2	<b>1896</b>	<b>130</b>	+21, +15	<b>-36</b>	-
	3	<b>1896</b>	<b>130</b>	+18, +5	<b>-36</b>	-
<b>0</b>	4	<b>1896</b>	<b>130</b>	+21, +7	<b>-36</b>	-
<b>0</b>	5	<b>1896</b>	<b>130</b>	+6, +11	<b>-36</b>	-
<b>0</b>	6	<b>1896</b>	<b>130</b>	+3.5, +2.5	<b>-36</b>	-
$-35 \pm 107$ , $56 \pm 63$	7	<b>1896</b>	<b>130</b>	$+1.1 \pm 4$ , $+0.2 \pm 8$	<b>-36</b>	-
**	PDG	$1905 \pm 12$	$100^{+30}_{-10}$	$21 \pm 6$	$-16 \pm 6$	-

Table 7.25: Resonance parameters for  $N(1900) 3/2^+$ . Red values were obtained in the IB fit, blue ones in DR fit. Fixed values are written in bold black. Branchings into other channels were fixed to  $\beta_{\pi N} = 4\%$ ,  $\beta_{K\Lambda} = 12\%$ ,  $\beta_{K\Sigma} = 5\%$ ,  $\beta_{\omega N} = 13\%$ ,  $\beta_{\pi\pi N} = 1 - \sum \beta_i$ ,  $g_{\eta N} = -12$ . Stars show the overall PDG rating.

$N(1900) 3/2^+$	Solution	$M$	$\Gamma$	$\zeta_{\eta N}\beta_{\eta}(\%)$	$A_{1/2}$	$A_{3/2}$
Phase( $\Phi_j^\alpha$ )	1	<b>1900</b>	<b>200</b>	-1.5, -0.9	<b>19</b>	<b>-67</b>
	2	<b>1900</b>	<b>200</b>	-2, -2.1	<b>19</b>	<b>-67</b>
	3	<b>1900</b>	<b>200</b>	-0.07, 1.2	<b>19</b>	<b>-67</b>
$-28$ , $-49$	4	<b>1900</b>	<b>200</b>	-1.9, -1.4	<b>19</b>	<b>-67</b>
<b>60</b> , $-60$	5	<b>1900</b>	<b>200</b>	-0.6, -1	<b>19</b>	<b>-67</b>
$-11$ , $-18$	6	<b>1900</b>	<b>200</b>	-3, -6	<b>19</b>	<b>-67</b>
$-15 \pm 81$ , $-13 \pm 46$	7	<b>1900</b>	<b>200</b>	$-3.2 \pm 10$ , $-4.1 \pm 8$	<b>19</b>	<b>-67</b>
***	PDG	$1900 \pm 30$	$200 \pm 50$	$2 \pm 2$ , $10 \pm 4$	$24 \pm 14$	$-67 \pm 30$

For  $N(1880) 1/2^+$ ,  $N(1895) 1/2^-$  and  $N(1900) 3/2^+$  resonances the obtained values for the fitted parameters have large errors.

### Damping parameters

Finally we present the phenomenological parameters  $X$  and  $X_\gamma$  that are used in the parametrization  $f_{\gamma N}(W)$  and  $\tilde{f}_{\eta N}(W)$  Eqs. (5.5 and 5.13). These factors play a minor role in the parametrization therefore we give them without errors.

Table 7.26: Fit results for damping parameters  $X$  and  $X_\gamma$  for all resonances. IB results are written in red, DR results are written in blue.

Solution	$X$	$X_\gamma$
1	209, 318	0, 0
2	190, 278	204, 500
3	220, 250	500, 0
4	221, 375	350, 177
5	319, 83	500, 319
6	235, 100	500, 227
7	219, 123	194, 260

In addition to the presented above parameters we also use damping factors  $X_\gamma$  for selected resonances. They are shown below.

Table 7.27: Fit results for damping parameters  $X_\gamma$  for selected resonances.

Solution	$X_\gamma(N(1520) 3/2^-)$	$X_\gamma(N(1535) 1/2^-)$	$X_\gamma(N(1650) 1/2^-)$	$X_\gamma(N(1895) 1/2^-)$
1	500, 500	462, 177	292, 0	288, 0
2	500, 500	285, 145	324, 9	35, 0
3	500, 440	156, 173	328, 0	248, 0
4	500, 71	304, 462	347, 25	73, 490
5	0, 17	292, 321	0, 0	500, 1
6	9, 32	359, 5	500, 500	500, 13
7	428, 44	338, 342	0, 500	10, 132

### 7.11.1 Conclusion for the resonance parameters and error discussion

Below the final table of parameters from solution 7 is presented for the convenience. All the errors discussed above are presented as well.

Table 7.28: Parameters for the resonances used in the analysis. Red values correspond to the IB results from solution 7, blue values to the DR results from solution 7. Fixed values are written in bold black. The presented errors correspond to the errors from solution 7 as well.

Resonance	Phase( $\Phi_j^\alpha$ )	$M$	$\Gamma$	$\zeta_{\eta N} \beta_\eta (\%)$	$A_{1/2}$	$A_{3/2}$
$N(1520) 3/2^-$	$-2 \pm 73$	$1510 \pm 10$	<b>115</b>	$+0.05 \pm 1$	$-25 \pm 6$	<b>140</b>
	$-31 \pm 18$	$1514 \pm 6$	<b>115</b>	$+0.1 \pm 1$	$-25 \pm 6$	<b>140</b>
$N(1535) 1/2^-$	$-4 \pm 31$	$1525 \pm 17$	$158 \pm 37$	$+40 \pm 15$	<b>115</b>	
	$10 \pm 27$	$1530 \pm 13$	$175 \pm 47$	$+40 \pm 13$	<b>115</b>	
$N(1650) 1/2^-$	$4 \pm 27$	$1653 \pm 21$	$137 \pm 29$	$-23 \pm 16$	<b>45</b>	
	$-18 \pm 22$	$1640 \pm 27$	$122 \pm 28$	$-25 \pm 14$	<b>45</b>	
$N(1675) 5/2^-$	$22 \pm 91$	$1680 \pm 10$	$165 \pm 19$	$-2 \pm 1$	$11 \pm 16$	<b>20</b>
	$-2 \pm 16$	$1677 \pm 8$	$135 \pm 15$	$-1.2 \pm 1$	$12 \pm 8$	<b>20</b>
$N(1680) 5/2^+$	$3 \pm 83$	$1691 \pm 18$	$120 \pm 20$	$+0.16 \pm 1$	$-21 \pm 10$	<b>133</b>
	$2 \pm 4$	$1675 \pm 10$	$138 \pm 12$	$+0.02 \pm 1$	$-19 \pm 8$	<b>133</b>
$N(1700) 3/2^-$	$30 \pm 86$	$1650 \pm 56$	$250 \pm 117$	$-0.3 \pm 1$	$80 \pm 56$	<b>-37</b>
	$27 \pm 40$	$1686 \pm 39$	$100 \pm 81$	$+2.7 \pm 1$	$20 \pm 57$	<b>-37</b>
$N(1710) 1/2^+$	$-35 \pm 107$	$1699 \pm 48$	<b>100</b>	$+0.96 \pm 4$	<b>50</b>	
	$-43 \pm 111$	$1732 \pm 32$	<b>100</b>	$-0.19 \pm 5$	<b>50</b>	
$N(1720) 3/2^+$	$12 \pm 92$	$1750 \pm 49$	$211 \pm 173$	$+0.64 \pm 3$	$80 \pm 50$	<b>80</b>
	$-40 \pm 7$	$1750 \pm 31$	$323 \pm 191$	$+9.2 \pm 2$	$92 \pm 27$	<b>80</b>
$N(1860) 5/2^+$	$3 \pm 90$	<b>1860</b>	<b>270</b>	$-0.6 \pm 7$	$54 \pm 123$	$38 \pm 111$
	$0 \pm 1$	<b>1860</b>	<b>270</b>	$-6.9 \pm 8$	$-18 \pm 15$	$1 \pm 18$
$N(1875) 3/2^-$	$60 \pm 84$	<b>1875</b>	<b>250</b>	$+2.2 \pm 10$	$30 \pm 19$	<b>-7</b>
	$-32 \pm 21$	<b>1875</b>	<b>250</b>	$+5.5 \pm 8$	$30 \pm 17$	<b>-7</b>
$N(1880) 1/2^+$	$-60 \pm 118$	<b>1880</b>	<b>230</b>	$-1.9 \pm 15$	<b>21</b>	
	$-31 \pm 72$	<b>1880</b>	<b>230</b>	$-9.8 \pm 10$	<b>21</b>	
$N(1895) 1/2^-$	$-35 \pm 107$	<b>1896</b>	<b>130</b>	$+1.1 \pm 4$	<b>-36</b>	
	$56 \pm 63$	<b>1896</b>	<b>130</b>	$-0.2 \pm 8$	<b>-36</b>	
$N(1900) 3/2^+$	$-15 \pm 81$	<b>1900</b>	<b>200</b>	$-3.2 \pm 10$	<b>19</b>	<b>-67</b>
	$-13 \pm 46$	<b>1900</b>	<b>200</b>	$-4.1 \pm 8$	<b>19</b>	<b>-67</b>

As one can see from our analysis the resonance parameters obtained with 2 approaches in general coincide with the results of other groups. With both approaches the data are described similarly good, however we prefer the DR results over the IB ones because they were obtained with an additional physical constraints.

What is also very important are the obtained uncertainties. A general picture is that the errors obtained with the fixed- $t$  dispersion relations procedure are smaller or even much smaller than the ones obtained with the isobar model approach. The best example of this observation are the errors for the unitarity phases or the coupling constants for the  $N(1440) 1/2^+$  and  $N(1650) 1/2^-$ .

The results for the resonances with masses higher that  $M_R \geq 1860$  MeV have large errors because we are not able to precisely determine them with the limited data set.



# Chapter 8

---

## Summary and conclusion

---

In this work a partial wave analysis of  $\eta$  photoproduction data was performed in two approaches: isobar model approach (IB) and approach with fixed- $t$  dispersion relations for invariant amplitudes (DR). For both types of the approaches we used the EtaMAID model. In this model the scattering amplitude is parameterized with two parts the resonant part and non-resonant part. For a resonant part we took into account a set of 14 nucleon resonances. For the non-resonant part we considered two different types of background: Born terms in  $s$  and  $u$  channels, and  $t$ -channel exchanges. As a result we obtained 7 illustrative solutions that show different aspects of our parametrization and progression in the description of the data. The maximum energy and the largest negative  $t$ -value that were analyzed in the resonance region are  $W_{max} = 1863$  MeV and  $t_{max} = -1.5$  GeV<sup>2</sup> respectively. The maximum energy and the largest negative  $t$ -value that were taken into account for high energy data are  $W_{max} = 3987$  MeV and  $t_{max} = -1.37$  GeV<sup>2</sup>.

The  $t$ -channel exchanges were parameterized with Regge ansatz that typically works only at high energies whereas and at low energies it has large contributions. However we were able to smoothly damp this behavior at low energies which gave us a possibility to use Regge in the resonance region. On order to do this we multiplied Regge amplitudes with a damping factor function (DF), See Eqs. (5.44 and 5.45).

In our analysis we considered two types of Regge formalism and tested the behavior of them under the dispersion relations. In the first one the Regge ansatz was formulated in terms of Mandelstam variable  $s$  and contained Regge trajectories and Regge cuts. It was found that it strongly violates the dispersion relations. In the second one the Regge formalism was written in terms of crossing symmetrical variable  $\nu$  which fulfills the dispersion relations by definition.

For the resonance part we found that unitarity resonance phase  $\Phi_j^\alpha$  plays a very important role. The approach with phases was used in a MAID analysis for pion photoproduction [8], however it was never used for  $\eta$  photoproduction. We found that it significantly improved the results for the DR approach, however for the IB one the improvement is not so big.

We also compared our analysis with the one that was done in 2003 by Aznauryan [66] and found significant improvements in our case. For example in the unphysical region we took into account contributions from all resonances and not only  $N(1440) 1/2^+$ ,  $N(1535) 1/2^-$ , and  $N(1650) 1/2^-$ . We found out that  $N(1520) 3/2^-$  despite very small branching ration into  $\eta N$  channel produces the largest contribution into invariant amplitudes and should be taken into account.

We presented 7 illustrative solutions that describe our data with different  $\chi^2$ . However only solutions 6 and 7 should be considered as a *good ones*, if we follow the  $\chi^2$  criteria. The overall  $\chi_{Sol6}^2$  (IB/DR) = 1.84/1.77 and  $\chi_{Sol7}^2$  (IB/DR) = 1.61/1.61.

Nevertheless other solutions are informative as well. We show that Born terms play a small role in the  $\eta$  photoproduction and sometimes even negligible but they can still improve the results. In solutions 2 and 4 we obtained the values for  $g_{\eta NN}^2/4\pi$  coupling constant. In solution 2 we got  $g_{\eta NN}^2/4\pi = 3.07 \times 10^{-3}$  and  $g_{\eta NN}^2/4\pi = 3.34 \times 10^{-2}$  for IB and DR fit respectively. In solution 4 in both cases value were in the order of  $g_{\eta NN}^2/4\pi \approx 10^{-6}$

As a final result of our analysis we obtained resonance parameters in an improved a less model dependent way that takes into account such important properties as analyticity and crossing symmetry.

For example for the dominant resonance  $N(1535) 1/2^-$  we got the results that coincide with the results of other analysis and PDG estimations:

Table 8.1: Resonance parameters for  $N(1535) 1/2^-$ . Obtained with solutions 6 and 7. IB results are written in red, DR results are written in blue, fixed parameters are written in black. We omit here the obtained errors since we discussed them in the thesis before.

$N(1535) 1/2^-$	Solution	$M$	$\Gamma$	$\zeta_{\eta N} \beta_{\eta}(\%)$	$A_{1/2}$	$A_{3/2}$
	6	1525, 1531	160, 175	+39, +41	115	-
	7	1525, 1530	158, 175	+40, +40	115	-
****	PDG	$1535 \pm 10$	$150 \pm 25$	$42 \pm 10$	$115 \pm 15$	-

In principle all  $1/2^-$  states give very stable results that are in agreement with with the results of other analysis and PDG estimations

One can also mention the example of  $N(1700) 3/2^-$ . For this resonance it appeared that DR choose opposite sign for the factor  $\zeta_{\eta N}$ . The values for the  $A_{1/2}$  amplitude are different as well.

Table 8.2: Resonance parameters for  $N(1700) 3/2^-$ . Obtained with solutions 6 and 7. IB results are written in red, DR results are written in blue, fixed parameters are written in black. We omit here the obtained errors sicse we discussed them in the thesis before.

$N(1700) 3/2^-$	Solution	$M$	$\Gamma$	$\zeta_{\eta N} \beta_{\eta}(\%)$	$A_{1/2}$	$A_{3/2}$
	6	1650, 1685	250, 100	-0.4, +2	80, 20	-37
	7	1650, 1686	250, 100	-0.3, +2.7	80, 20	-37
***	PDG	$1700 \pm 50$	$150^{+100}_{-50}$	No average	$41 \pm 17$	$-37 \pm 14$

We also discussed the errors for the resonance parameters that were obtained using subroutine MINOS in the MINUIT package. One can observe in case of fixed- $t$  dispersion relations approach the errors are considerably smaller than in case of an isobar model approach. This means that the dispersion relations approach is not only more fundamental but also more accurate.

For further improvement one can also perform a combined fit of pion and  $\eta$  photoproduction data. This will give us additional constraints and allow us to determine the resonance parameters more precisely.

However in PDG pole positions are preferred over the Breit-Wigner parameters. In order to obtain them we collaborate with Tuzla and Zagreb (MTZ collaboration) where people developed the so-called L+P method (Laurant + Pietarinen) [83–86] with which these parameters can be obtained. This can be considered as a proposal for further improvement of the results.

Despite that both solutions 6 and 7 have very close  $\chi^2$  if we plot predictions for the unmeasured observables, for example  $P$  and  $H$ , we will get different results, see figures below.

For  $P$  we have:

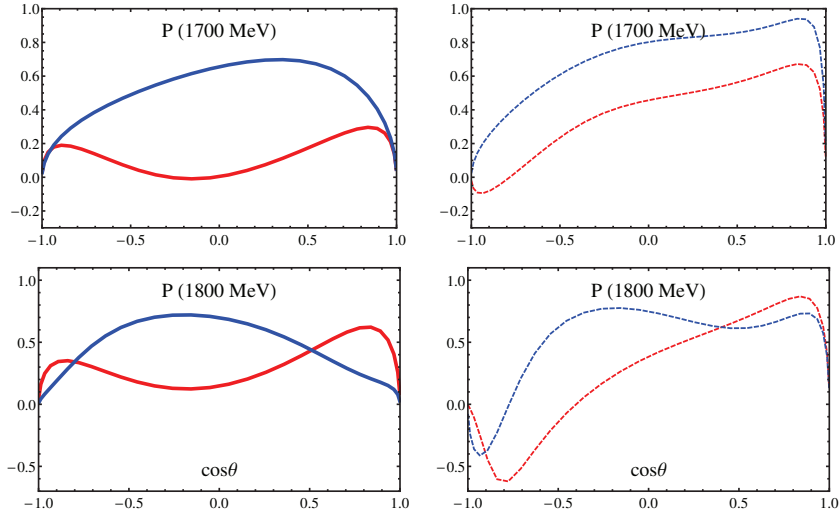


Figure 8.1: Predictions from solutions 6 and 7 for  $P$  observable at energies 1700 MeV and 1800 MeV. Solution 6 is plotted in blue (blue solid - IB, blue dashed - DR). Solution 7 is plotted in red (red solid - IB, red dashed - DR)

For  $H$  we have:

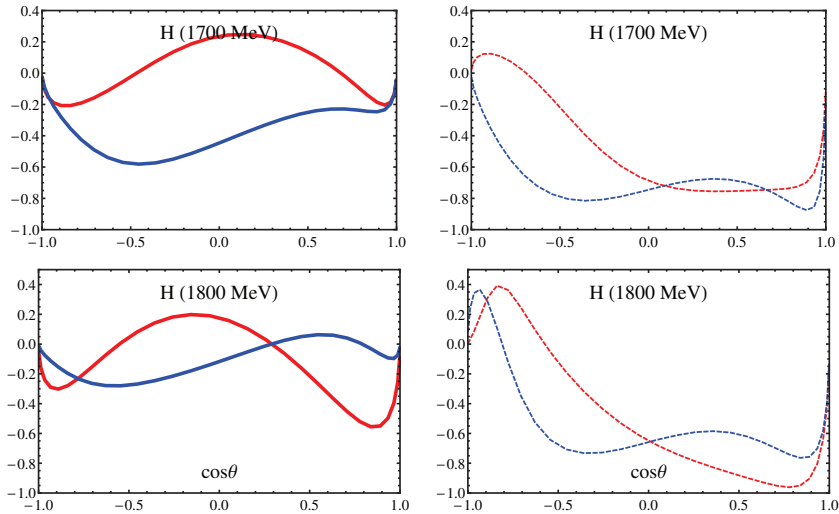


Figure 8.2: Predictions from solutions 6 and 7 for  $H$  observable at energies 1700 MeV and 1800 MeV. Solution 6 is plotted in blue (blue solid - IB, blue dashed - DR). Solution 7 is plotted in red (red solid - IB, red dashed - DR)

In order to solve this problem one has to perform a PWA including new polarization data. This can be considered as a proposal for further experimental improvement.





# Chapter A

---

## Formalism

---

### A.1 Reduced multipoles in terms of photo decay amplitudes $A_{1/2}$ and $A_{3/2}$

$$\bar{M}_{\ell+} = -\frac{1}{\ell+1} \left( A_{1/2}^{\ell+} + \sqrt{\frac{\ell+2}{\ell}} A_{3/2}^{\ell+} \right), \quad (\text{A.1})$$

$$\bar{E}_{\ell+} = -\frac{1}{\ell+1} \left( A_{1/2}^{\ell+} - \sqrt{\frac{\ell}{\ell+2}} A_{3/2}^{\ell+} \right), \quad (\text{A.2})$$

$$\bar{M}_{\ell+1,-} = +\frac{1}{\ell+1} \left( A_{1/2}^{\ell+1,-} - \sqrt{\frac{\ell}{\ell+2}} A_{3/2}^{\ell+1,-} \right), \quad (\text{A.3})$$

$$\bar{E}_{\ell+1,-} = -\frac{1}{\ell+1} \left( A_{1/2}^{\ell+1,-} + \sqrt{\frac{\ell+2}{\ell}} A_{3/2}^{\ell+1,-} \right). \quad (\text{A.4})$$

$J^P$	$\bar{E}$	$\bar{M}$
$1/2^-$	$-A_{1/2}$	—
$1/2^+$	—	$A_{1/2}$
$3/2^+$	$\frac{1}{2}(\frac{1}{\sqrt{3}}A_{3/2} - A_{1/2})$	$-\frac{1}{2}(\sqrt{3}A_{3/2} + A_{1/2})$
$3/2^-$	$-\frac{1}{2}(\sqrt{3}A_{3/2} + A_{1/2})$	$-\frac{1}{2}(\frac{1}{\sqrt{3}}A_{3/2} - A_{1/2})$
$5/2^-$	$\frac{1}{3}(\frac{1}{\sqrt{2}}A_{3/2} - A_{1/2})$	$-\frac{1}{3}(\sqrt{2}A_{3/2} + A_{1/2})$
$5/2^+$	$-\frac{1}{3}(\sqrt{2}A_{3/2} + A_{1/2})$	$-\frac{1}{3}(\frac{1}{\sqrt{2}}A_{3/2} - A_{1/2})$

Table A.1: The reduced multipoles  $\bar{M}_\alpha$  in terms of the photon decay amplitudes  $A_\lambda$ .

### A.2 Helicity amplitudes in terms of CGLN amplitudes

The helicity amplitudes are related to the CGLN amplitudes in the following way:

$$H_1 = -\frac{1}{2} \sqrt{(1-x^2)(1+x)} (F_3 + F_4) \quad (\text{A.5})$$

$$H_2 = \sqrt{1+x} [F_2 - F_1 + \frac{1-x}{2} (F_3 - F_4)] \quad (\text{A.6})$$

$$H_3 = \frac{1}{2} \sqrt{(1-x^2)(1-x)} (F_3 - F_4) \quad (\text{A.7})$$

$$H_4 = \sqrt{1-x} [F_1 + F_2 + \frac{1+x}{2} (F_3 + F_4)] \quad (\text{A.8})$$

with  $x = \cos \theta$ .

### A.3 Expansion of $B_i$ invariant amplitudes in terms of CGLN amplitudes

Amplitudes  $B_i$  can be expressed by the CGLN amplitudes  $F_i$  accordingly:

$$\begin{aligned}
 B_1 &= \mathcal{N} \left\{ F_1 - \frac{W + m_p}{W - m_p} (E_f + m_p) \frac{F_2}{q} \right\}, \\
 B_2 &= \frac{\mathcal{N}}{2(W - m_p)} (t - m_\eta^2) \left\{ \frac{F_3}{q} - (E_f + m_p) \frac{F_4}{q^2} \right\}, \\
 B_6 &= \frac{-2\mathcal{N}}{W - m_p} \left\{ F_1 + (E_f + m_p) \frac{F_2}{q} + \frac{t - m_\eta^2}{2(W - m_p)} \frac{F_3}{q} + \frac{t - m_\eta^2}{2(W + m_p)} (E_f + m_p) \frac{F_4}{q^2} \right\}, \\
 B_8 &= \frac{-\mathcal{N}}{W - m_p} \left\{ F_1 + (E_f + m_p) \frac{F_2}{q} + \left( W + m_p + \frac{t - m_\eta^2}{2(W - m_p)} \right) \frac{F_3}{q} \right. \\
 &\quad \left. + \left( W - m_p + \frac{t - m_\eta^2}{2(W + m_p)} \right) (E_f + m_p) \frac{F_4}{q^2} \right\}.
 \end{aligned} \tag{A.9}$$

where  $\mathcal{N} = 4\pi / \sqrt{(E_i + m_p)(E_f + m_p)}$ .

### A.4 Expansion of CGLN amplitudes in terms of $A_i$ and $B_i$ invariant amplitudes

The CGLN amplitudes are obtained from the invariant amplitudes  $A_i$  by the following equations

$$\begin{aligned}
 F_1 &= \frac{W - m_p}{8\pi W} \sqrt{(E_i + m_p)(E_f + m_p)} (A_1 + (W - m_p) A_4 - \frac{2m_p\nu_B}{W - m_p} (A_3 - A_4)), \\
 F_2 &= \frac{W + m_p}{8\pi W} q \sqrt{\frac{E_i - m_p}{E_f + m_p}} \left( -A_1 + (W + m_p) A_4 - \frac{2m_p\nu_B}{W + m_p} (A_3 - A_4) \right), \\
 F_3 &= \frac{W + m_p}{8\pi W} q \sqrt{(E_i - m_p)(E_f + m_p)} ((W - m_p) A_2 + A_3 - A_4), \\
 F_4 &= \frac{W - m_p}{8\pi W} q^2 \sqrt{\frac{E_i + m_p}{E_f + m_p}} \left( -(W + m_p) A_2 + A_3 - A_4 \right),
 \end{aligned} \tag{A.10}$$

with  $\nu_B = (t - m_\eta^2)/(4m_p)$ .

The CGLN amplitudes are obtained from the invariant amplitudes  $B_i$  by the following equations

$$\begin{aligned}
 F_1 &= \frac{W - m_p}{8\pi W} \sqrt{(E_i + m_p)(E_f + m_p)} \left( B_1 - \frac{1}{2}(W + m_p) B_6 - \frac{2m_p\nu_B}{W - m_p} \left( \frac{1}{2}B_6 - B_8 \right) \right), \\
 F_2 &= \frac{W + m_p}{8\pi W} q \sqrt{\frac{E_i - m_p}{E_f + m_p}} \left( -(B_1 + \frac{1}{2}(W - m_p) B_6) - \frac{2m_p\nu_B}{W + m_p} \left( \frac{1}{2}B_6 - B_8 \right) \right), \\
 F_3 &= \frac{W + m_p}{8\pi W} q \sqrt{(E_i - m_p)(E_f + m_p)} \left( \frac{W - m_p}{2m_p\nu_B} B_2 + \frac{1}{2}B_6 - B_8 \right), \\
 F_4 &= \frac{W - m_p}{8\pi W} q^2 \sqrt{\frac{E_i + m_p}{E_f + m_p}} \left( -\frac{W + M_N}{2m_p\nu_B} B_2 + \frac{1}{2}B_6 - B_8 \right).
 \end{aligned} \tag{A.11}$$

with  $\nu_B = (t - m_\eta^2)/(4m_p)$ .

## A.5 Observables expressed in CGLN amplitudes

$$\sigma_0 = \text{Re} \{ F_1^* F_1 + F_2^* F_2 + (1 - x^2) (F_3^* F_3 / 2 + F_4^* F_4 / 2 + F_2^* F_3 + F_1^* F_4 + x F_3^* F_4) - 2x F_1^* F_2 \} \rho \quad (\text{A.12})$$

$$\hat{\Sigma} = -(1 - x^2) \text{Re} \{ (F_3^* F_3 + F_4^* F_4) / 2 + F_2^* F_3 + F_1^* F_4 + x F_3^* F_4 \} \rho \quad (\text{A.13})$$

$$\hat{T} = \sqrt{1 - x^2} \text{Im} \{ F_1^* F_3 - F_2^* F_4 + x (F_1^* F_4 - F_2^* F_3) - (1 - x^2) F_3^* F_4 \} \rho \quad (\text{A.14})$$

$$\hat{P} = -\sqrt{1 - x^2} \text{Im} \{ 2F_1^* F_2 + F_1^* F_3 - F_2^* F_4 - x (F_2^* F_3 - F_1^* F_4) \} \rho \quad (\text{A.15})$$

$$-(1 - x^2) F_3^* F_4 \} \rho \quad (\text{A.16})$$

$$\hat{E} = \text{Re} \{ F_1^* F_1 + F_2^* F_2 - 2x F_1^* F_2 + (1 - x^2) (F_2^* F_3 + F_1^* F_4) \} \rho \quad (\text{A.17})$$

$$\hat{F} = \sqrt{1 - x^2} \text{Re} \{ F_1^* F_3 - F_2^* F_4 - x (F_2^* F_3 - F_1^* F_4) \} \rho \quad (\text{A.18})$$

$$\hat{G} = (1 - x^2) \text{Im} \{ F_2^* F_3 + F_1^* F_4 \} \rho \quad (\text{A.19})$$

$$\hat{H} = \sqrt{1 - x^2} \text{Im} \{ 2F_1^* F_2 + F_1^* F_3 - F_2^* F_4 + x (F_1^* F_4 - F_2^* F_3) \} \rho \quad (\text{A.20})$$

$$\hat{C}_{x'} = \sqrt{1 - x^2} \text{Re} \{ F_1^* F_1 - F_2^* F_2 - F_2^* F_3 + F_1^* F_4 - x (F_2^* F_4 - F_1^* F_3) \} \rho \quad (\text{A.21})$$

$$\hat{C}_{z'} = \text{Re} \{ 2F_1^* F_2 - x (F_1^* F_1 + F_2^* F_2) + (1 - x^2) (F_1^* F_3 + F_2^* F_4) \} \rho \quad (\text{A.22})$$

$$\hat{O}_{x'} = \sqrt{1 - x^2} \text{Im} \{ F_2^* F_3 - F_1^* F_4 + x (F_2^* F_4 - F_1^* F_3) \} \rho \quad (\text{A.23})$$

$$\hat{O}_{z'} = -(1 - x^2) \text{Im} \{ F_1^* F_3 + F_2^* F_4 \} \rho \quad (\text{A.24})$$

$$\hat{L}_{x'} = -\sqrt{1 - x^2} \text{Re} \{ F_1^* F_1 - F_2^* F_2 - F_2^* F_3 + F_1^* F_4 + (1 - x^2) (F_4^* F_4 - F_3^* F_3) / 2 + x (F_1^* F_3 - F_2^* F_4) \} \rho \quad (\text{A.25})$$

$$\hat{L}_{z'} = \text{Re} \{ 2F_1^* F_2 - x (F_1^* F_1 + F_2^* F_2) + (1 - x^2) (F_1^* F_3 + F_2^* F_4 + F_3^* F_4) + x(1 - x^2) (F_3^* F_3 + F_4^* F_4) / 2 \} \rho \quad (\text{A.26})$$

$$\hat{T}_{x'} = -(1 - x^2) \text{Re} \{ F_1^* F_3 + F_2^* F_4 + F_3^* F_4 + x (F_3^* F_3 + F_4^* F_4) / 2 \} \rho \quad (\text{A.27})$$

$$\hat{T}_{z'} = \sqrt{1 - x^2} \text{Re} \{ F_1^* F_4 - F_2^* F_3 + x (F_1^* F_3 - F_2^* F_4) + (1 - x^2) (F_4^* F_4 - F_3^* F_3) / 2 \} \rho \quad (\text{A.28})$$

$$\text{with } \hat{\Sigma} = \Sigma \sigma_0 \text{ etc. and } \rho = q/k. \quad (\text{A.29})$$

## A.6 $T$ asymmetry expressed in terms of multipoles from the set of resonances used in the analysis

$$\begin{aligned}
 \frac{\hat{T}}{1-x^2} &= \frac{3}{2} \text{Im} \left[ 2E_{0+}^*(E_{1+} - M_{1+}) + E_{3-}^*(-2E_{0+} + 4E_{2-} + 9E_{2+}) \right. \\
 &- M_{3-}^*(2E_{0+} + 5E_{2-} + 9M_{2-} - 9M_{2+}) + E_{1+}^*(4E_{2-} + 9E_{2+}) \\
 &+ 2M_{1-}^*(E_{2-} + E_{2+} + M_{2-} - M_{2+}) + M_{1+}^*(-5E_{2+} + 4M_{2-} - 4M_{2+}) \left. \right] \\
 &- x \frac{3}{2} \text{Im} \left[ 2E_{0+}^*(E_{2-} - 4E_{2+} + M_{2-} + 4M_{2+}) - E_{1+}^*(30E_{3-} + 2M_{1-} - 8M_{1+} + 3M_{3-}) \right. \\
 &+ E_{2-}^*(25E_{2+} + 8M_{2-} + 2M_{2+}) + 3E_{2p}^*(M_{2-} - 6M_{2+}) + 3E_{3-}^*(4M_{1-} - M_{1+} - 9M_{3-}) \\
 &- 2M_{1-}^*(M_{1+} + 4M_{3-} - 25M_{3-}M_{1+}^* + 30M_{2+}M_{2-}^*) \left. \right] \\
 &+ x^2 \frac{1}{2} \text{Im} \left[ -30E_{0+}^*(E_{3-} + M_{3-}) + 9E_{1+}^*(-4E_{2-} + E_{2+} - 10M_{2+}) + E_{2-}^*(6E_{3-} - 75M_{3-}) \right. \\
 &+ E_{2+}^*(486E_{3-} + 30M_{1-} - 75M_{1+}) - 90M_{2-}E_{3-}^* + 30M_{2+}M_{1-}^* + 6M_{1+}^*(M_{2+} - 6M_{2-}) \\
 &+ 9M_{3-}(M_{2-}^* + 54M_{2+}^*) \left. \right] \\
 &- x^3 \frac{45}{2} \text{Im} \left[ E_{1+}(4E_{3-} + M_{3-}) - 3E_{2+}E_{2-}^* - E_{2+}^*(M_{2-} - 6M_{2+}) \right. \\
 &+ 6M_{3-}E_{3-}^* + 3M_{3-}M_{1+} - 4M_{2+}M_{2-} \left. \right] \\
 &- x^4 \frac{675}{2} \text{Im} \left[ E_{3-}E_{2+}^* + M_{3-}M_{2+}^* \right] \tag{A.30}
 \end{aligned}$$

## A.7 Projection formulas for multipoles out of CGLN amplitudes

$$M_{\ell+} = \frac{1}{2(\ell+1)} \int_{-1}^{+1} dx \left( F_1 P_\ell(x) - F_2 P_{\ell+1}(x) - F_3 \frac{P_{\ell-1}(x) - P_{\ell+1}(x)}{2\ell+1} \right) \tag{A.31}$$

$$\begin{aligned}
 E_{\ell+} &= \frac{1}{2(\ell+1)} \int_{-1}^{+1} dx \left( F_1 P_\ell(x) - F_2 P_{\ell+1}(x) + \ell F_3 \frac{P_{\ell-1}(x) - P_{\ell+1}(x)}{2\ell+1} \right. \\
 &\quad \left. + (\ell+1) F_4 \frac{P_\ell(x) - P_{\ell+2}(x)}{2\ell+3} \right) \tag{A.32}
 \end{aligned}$$

$$M_{\ell-} = \frac{1}{2\ell} \int_{-1}^{+1} dx \left( -F_1 P_\ell(x) + F_2 P_{\ell-1}(x) + F_3 \frac{P_{\ell-1}(x) - P_{\ell+1}(x)}{2\ell+1} \right) \tag{A.33}$$

$$\begin{aligned}
 E_{\ell-} &= \frac{1}{2\ell} \int_{-1}^{+1} dx \left( F_1 P_\ell(x) - F_2 P_{\ell+1}(x) - \ell F_3 \frac{P_{\ell-1}(x) - P_{\ell+1}(x)}{2\ell+1} \right. \\
 &\quad \left. + \ell F_4 \frac{P_{\ell-2}(x) - P_\ell(x)}{2\ell-1} \right) \tag{A.34}
 \end{aligned}$$

# Chapter B

## Plots of the fit results

### B.1 Plots for Solution 1

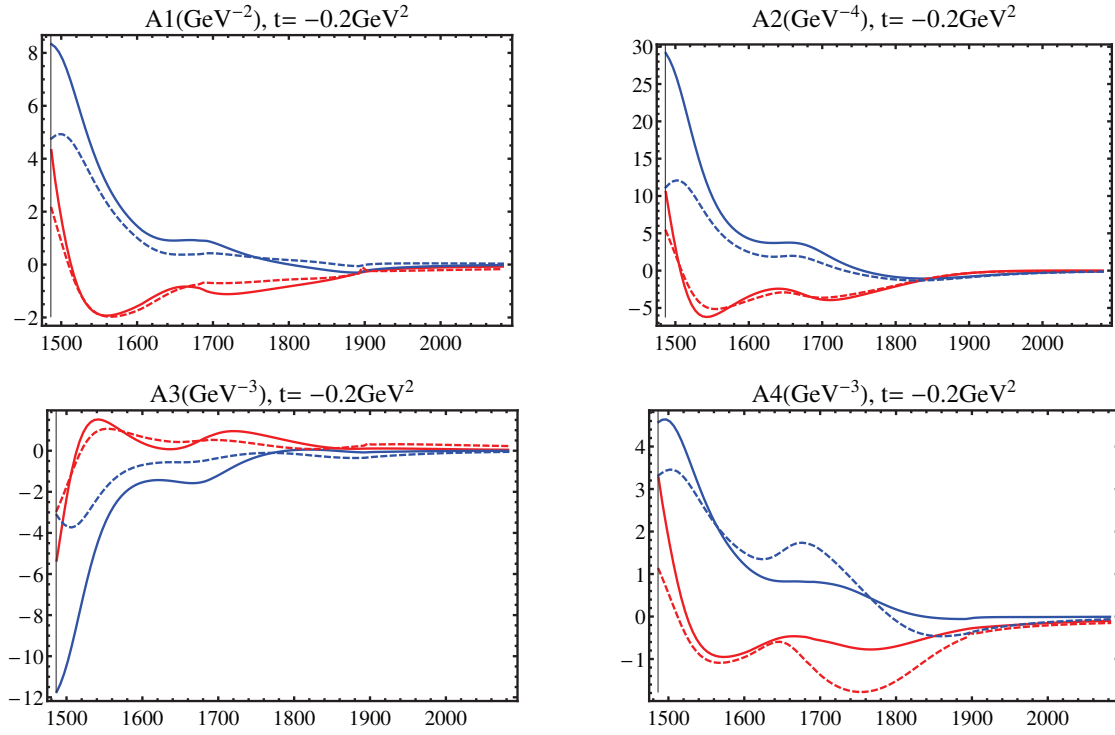


Figure B.1: Invariant amplitudes for Solution 1. Real parts of amplitudes are drawn in red, imaginary parts in blue. IB results are drawn as solid curves, DR results as dashed curves. Vertical black line denote the physical threshold for a given  $t$  value.

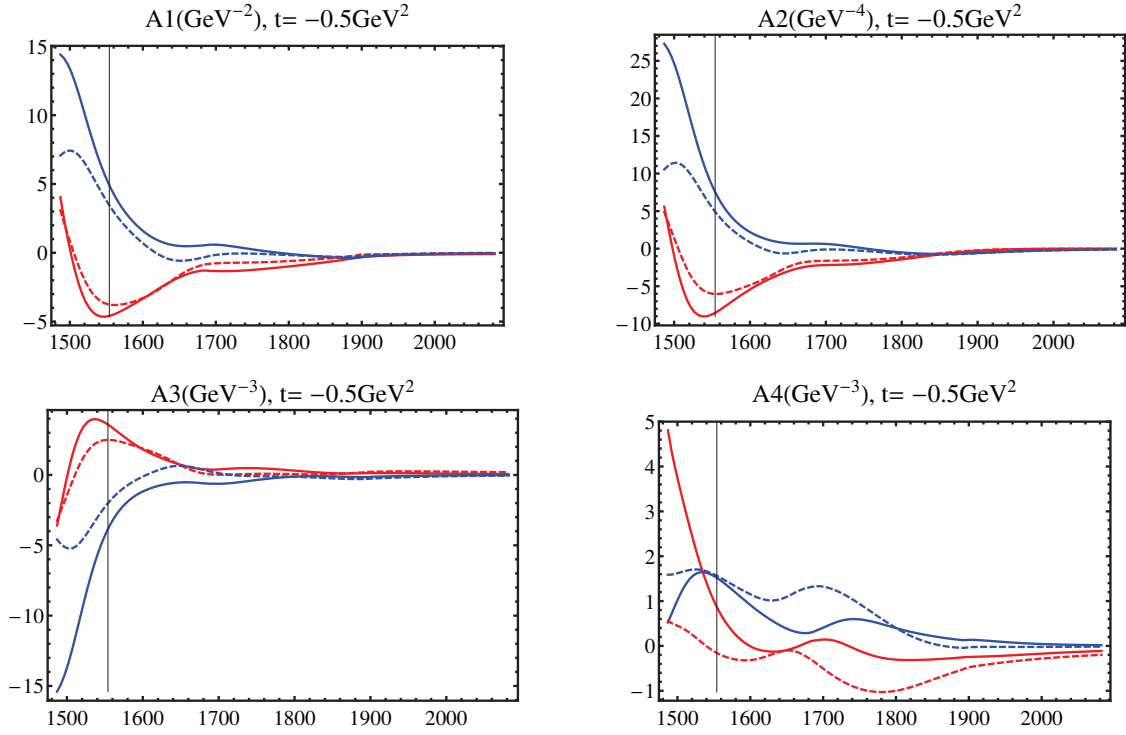


Figure B.2: Invariant amplitudes for Solution 1. Real parts of amplitudes are drawn in red, imaginary parts in blue. IB results are drawn as solid curves, DR results as dashed curves. Vertical black line denote the physical threshold for a given  $t$  value.

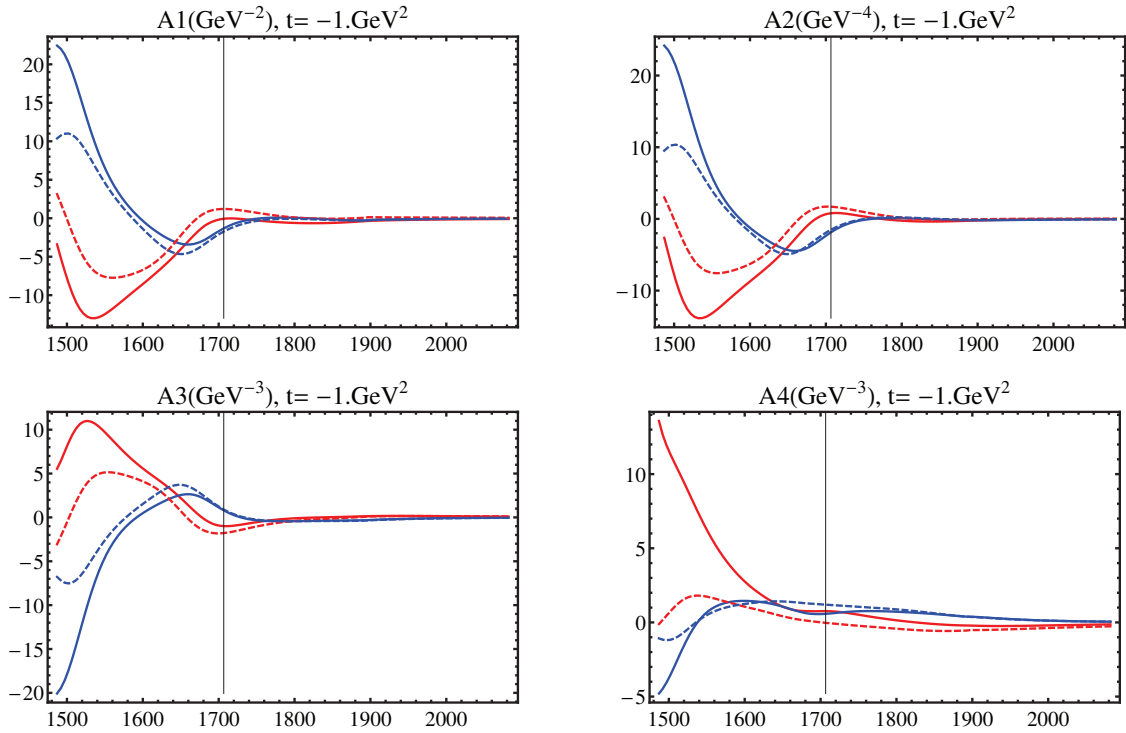


Figure B.3: Invariant amplitudes for Solution 1. Real parts of amplitudes are drawn in red, imaginary parts in blue. IB results are drawn as solid curves, DR results as dashed curves. Vertical black line denote the physical threshold for a given  $t$  value.

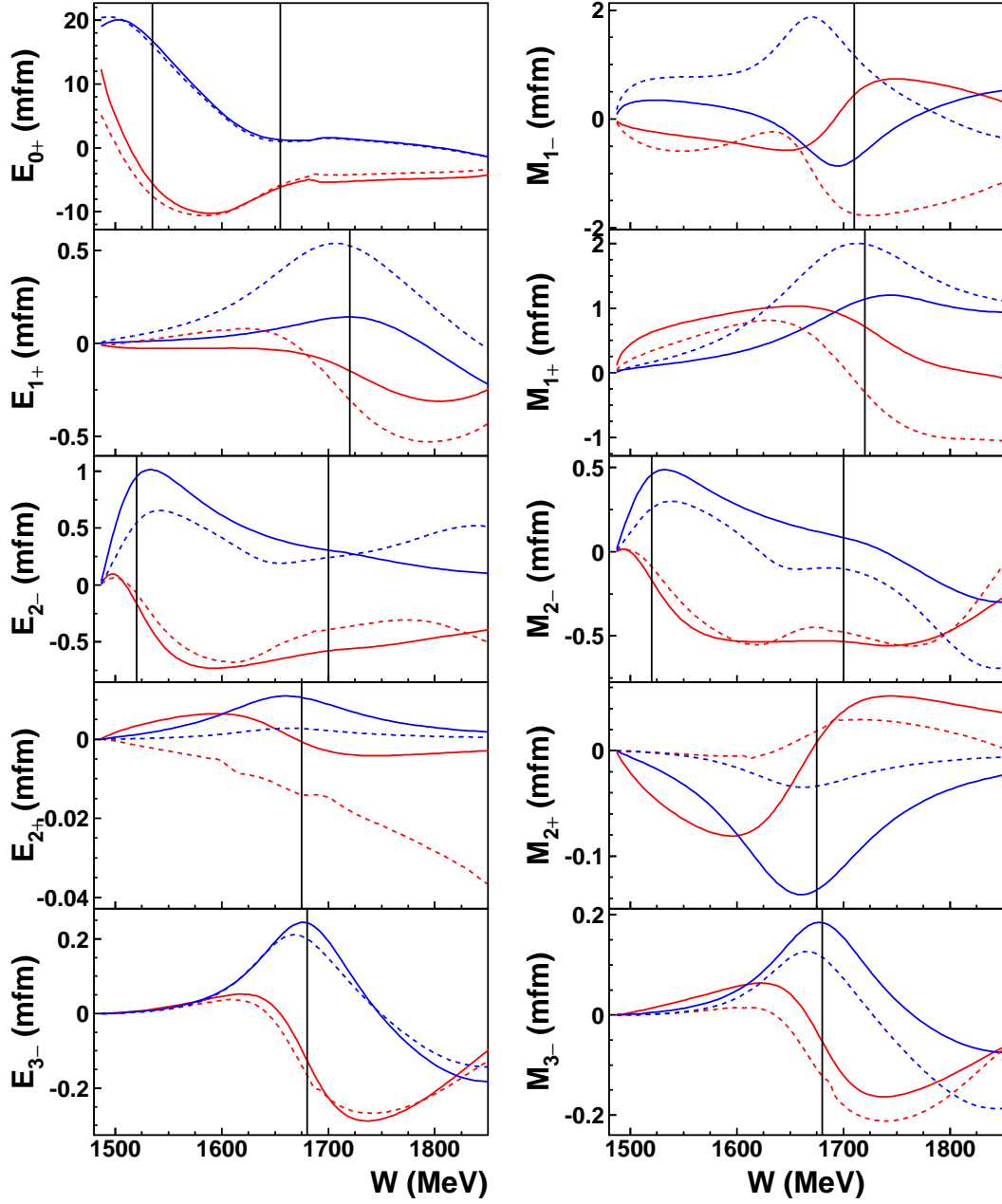


Figure B.4: Multipoles for Solution 1. Real parts of multipoles are drawn in red, imaginary parts in blue. IB results are drawn as solid curves, DR results as dashed curves.

## B.2 Plots for Solution 2

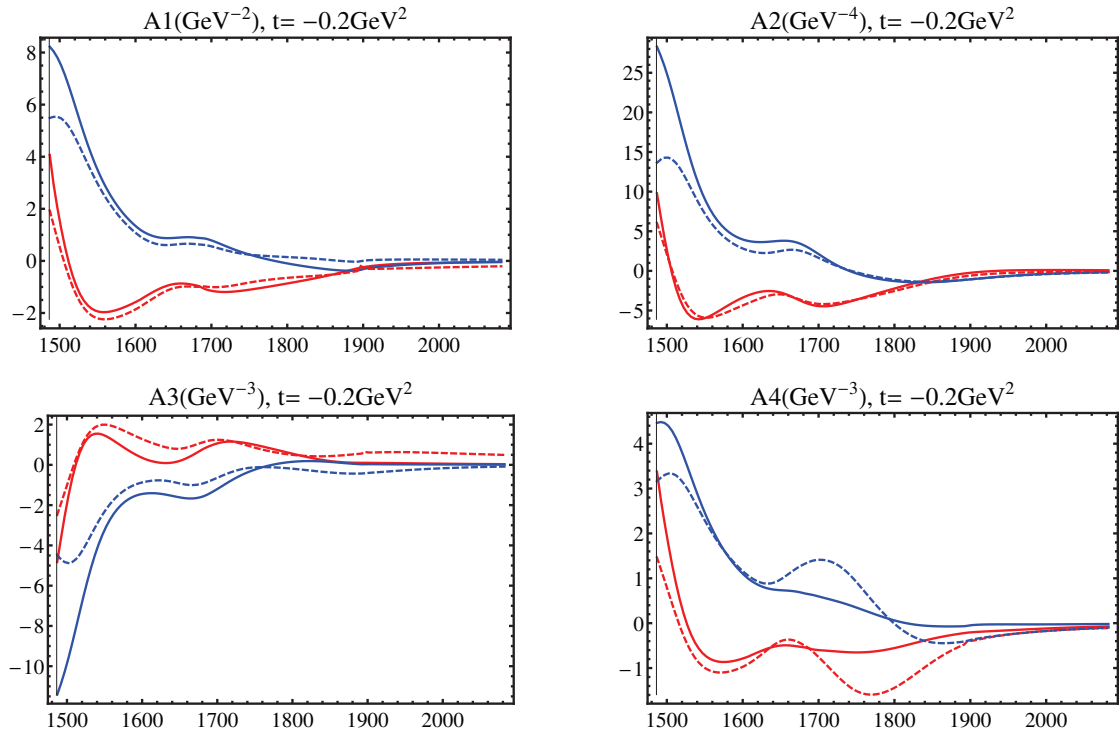


Figure B.5: Invariant amplitudes for Solution 2. Real parts of amplitudes are drawn in red, imaginary parts in blue. IB results are drawn as solid curves, DR results as dashed curves. Vertical black line denote the physical threshold for a given  $t$  value.



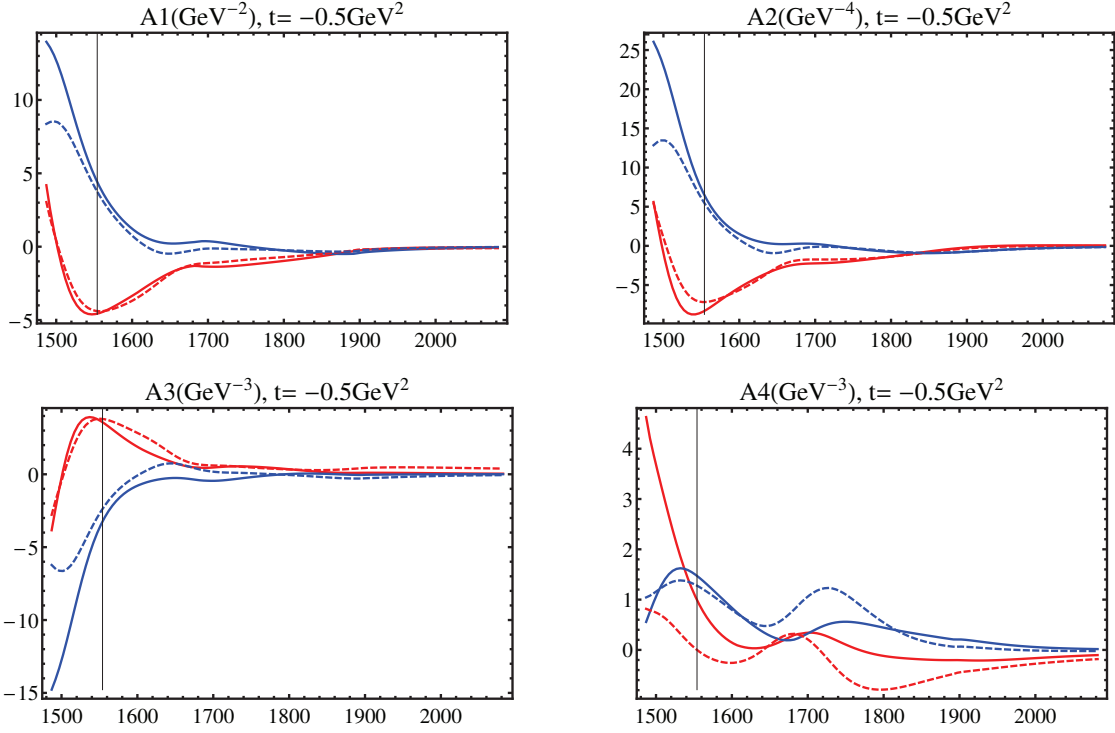


Figure B.6: Invariant amplitudes for Solution 2. Real parts of amplitudes are drawn in red, imaginary parts in blue. IB results are drawn as solid curves, DR results as dashed curves. Vertical black line denote the physical threshold for a given  $t$  value.

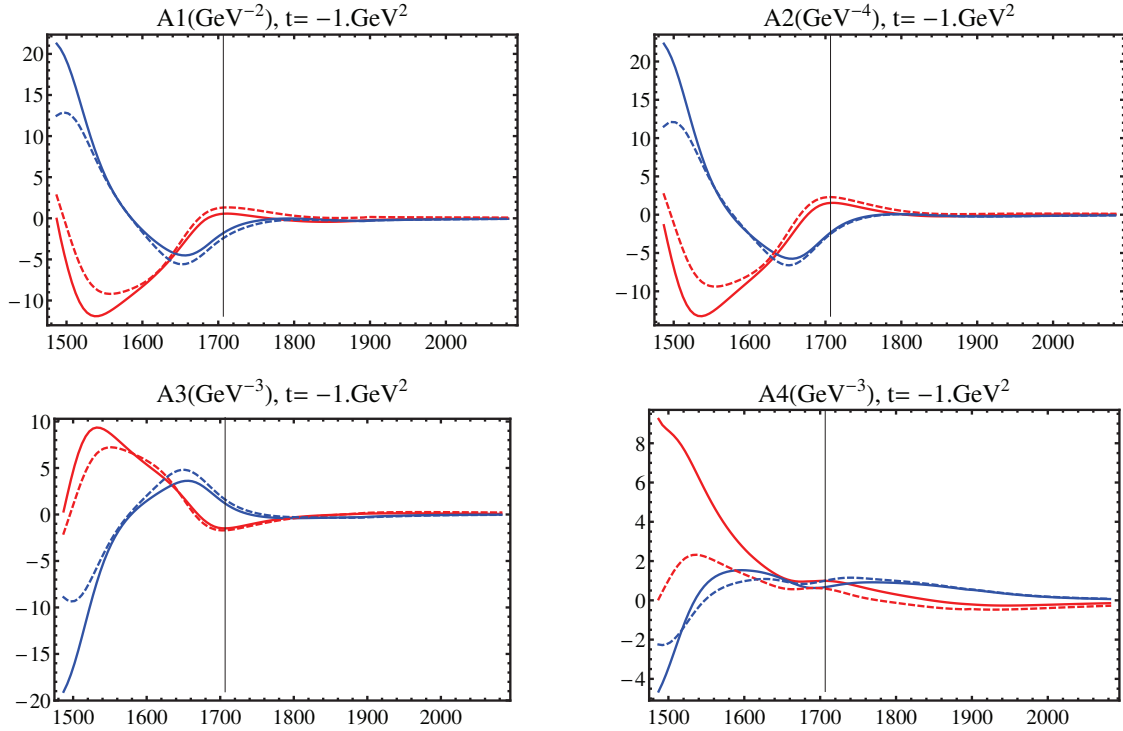


Figure B.7: Invariant amplitudes for Solution 2. Real parts of amplitudes are drawn in red, imaginary parts in blue. IB results are drawn as solid curves, DR results as dashed curves. Vertical black line denote the physical threshold for a given  $t$  value.

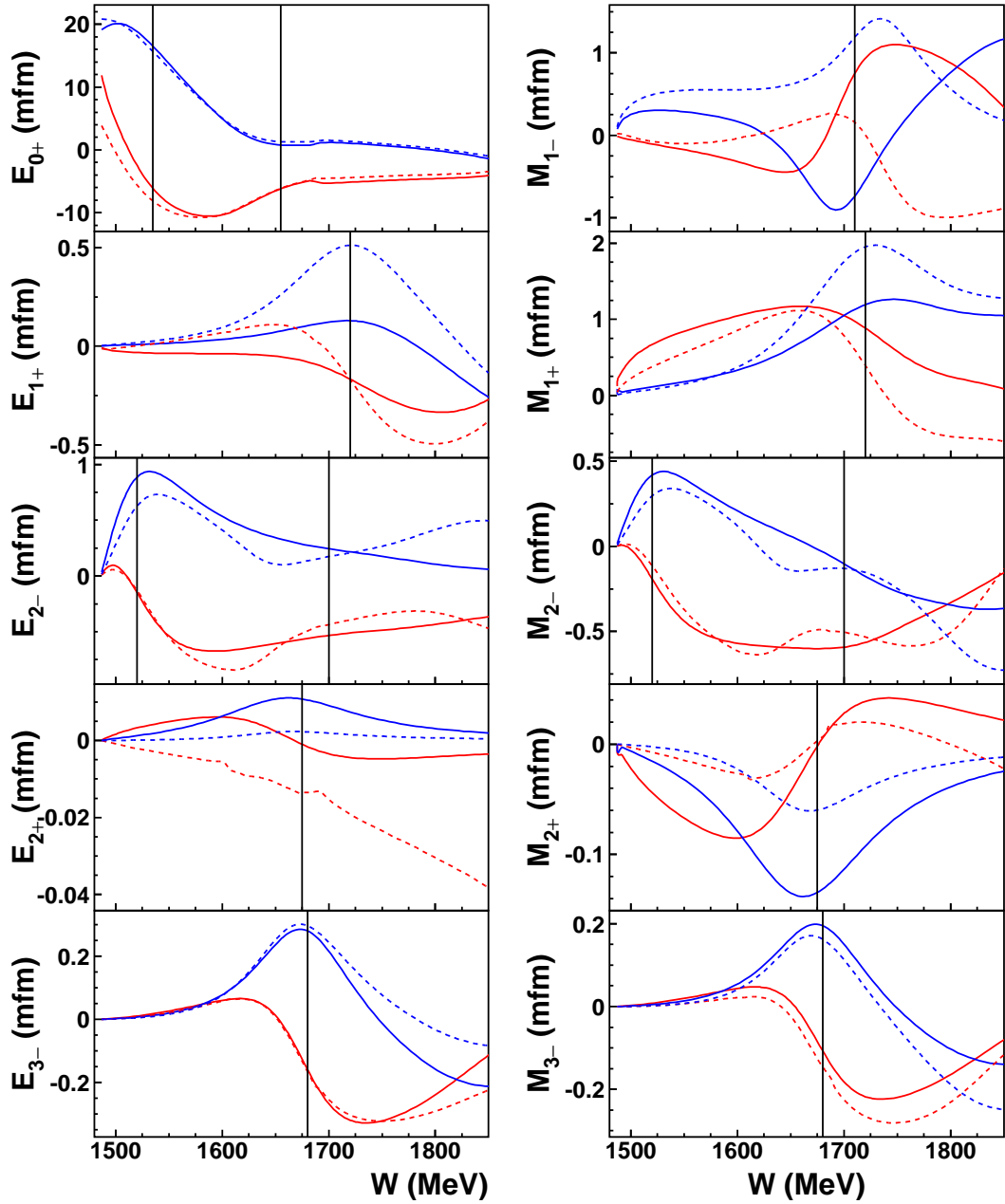


Figure B.8: Multipoles for Solution 2. Real parts of multipoles are drawn in red, imaginary parts in blue. IB results are drawn as solid curves, DR results as dashed curves.

### B.3 Plots for Solution 3

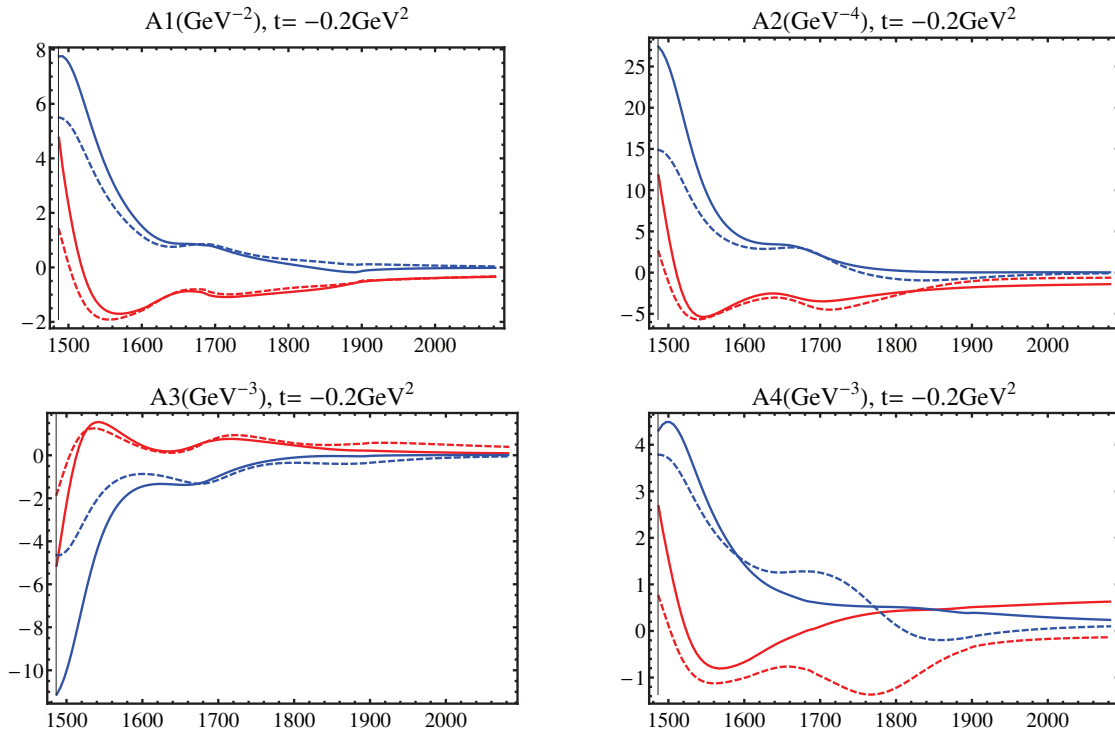


Figure B.9: Invariant amplitudes for Solution 3. Real parts of amplitudes are drawn in red, imaginary parts in blue. IB results are drawn as solid curves, DR results as dashed curves. Vertical black line denote the physical threshold for a given  $t$  value.

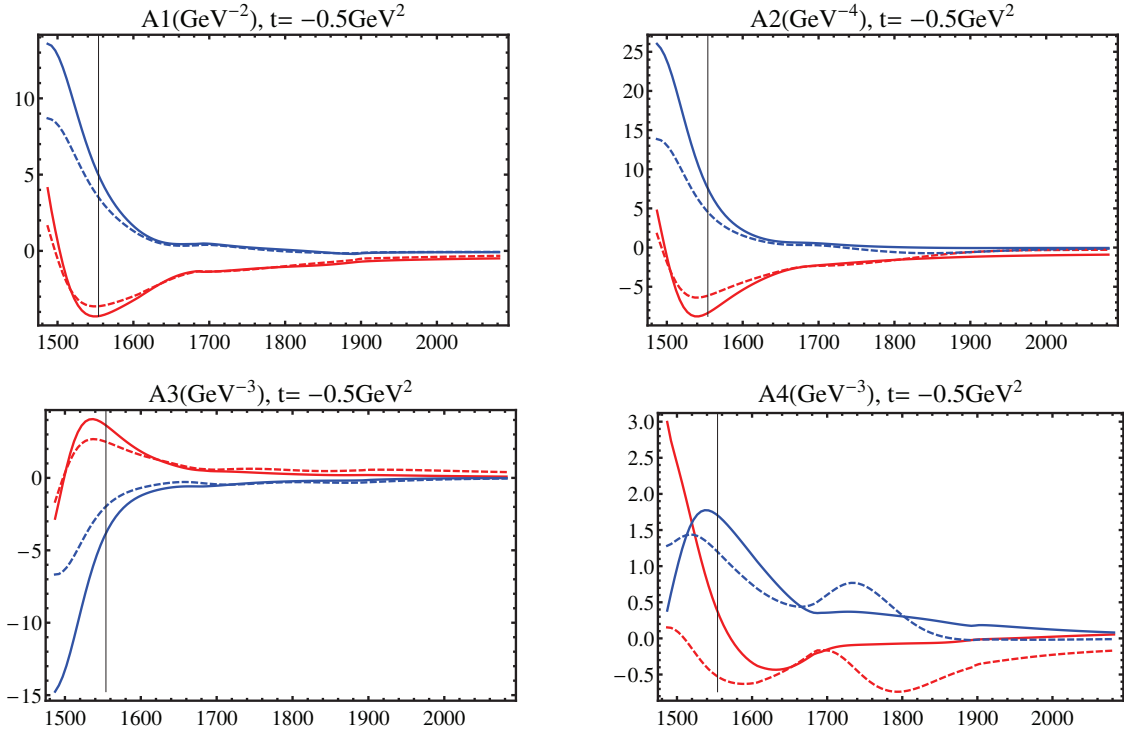


Figure B.10: Invariant amplitudes for Solution 3. Real parts of amplitudes are drawn in red, imaginary parts in blue. IB results are drawn as solid curves, DR results as dashed curves. Vertical black line denote the physical threshold for a given  $t$  value.

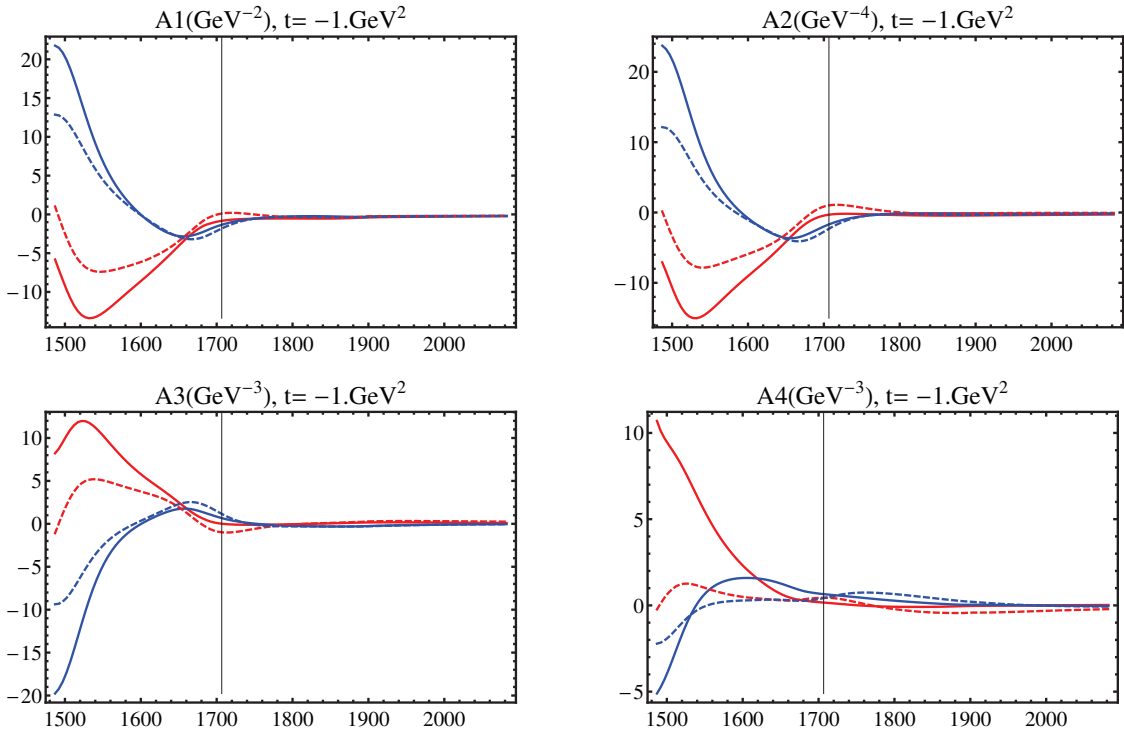


Figure B.11: Invariant amplitudes for Solution 3. Real parts of amplitudes are drawn in red, imaginary parts in blue. IB results are drawn as solid curves, DR results as dashed curves. Vertical black line denote the physical threshold for a given  $t$  value.

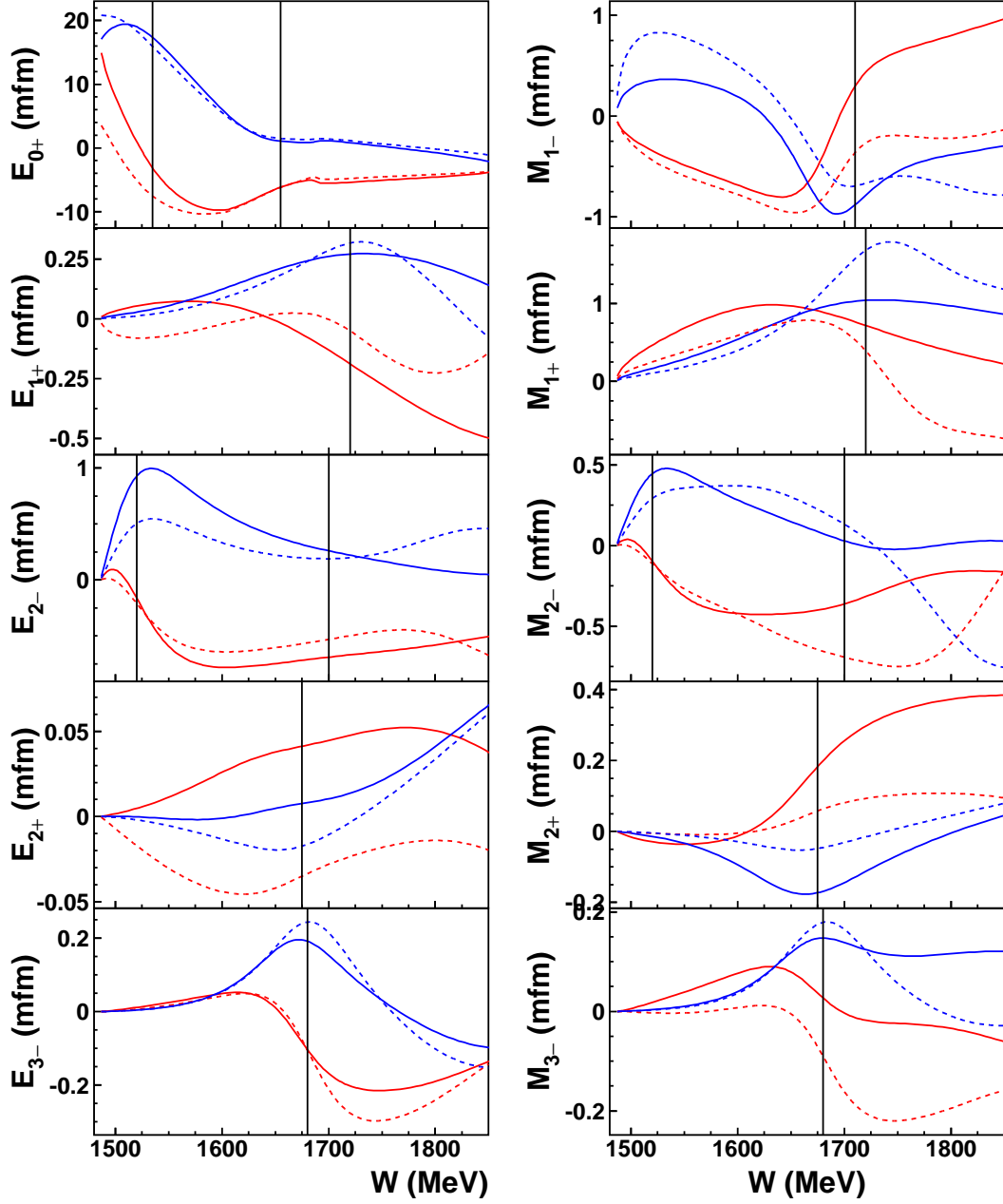


Figure B.12: Multipoles for Solution 3. Real parts of multipoles are drawn in red, imaginary parts in blue. IB results are drawn as solid curves, DR results as dashed curves.

### B.4 Plots for Solution 4

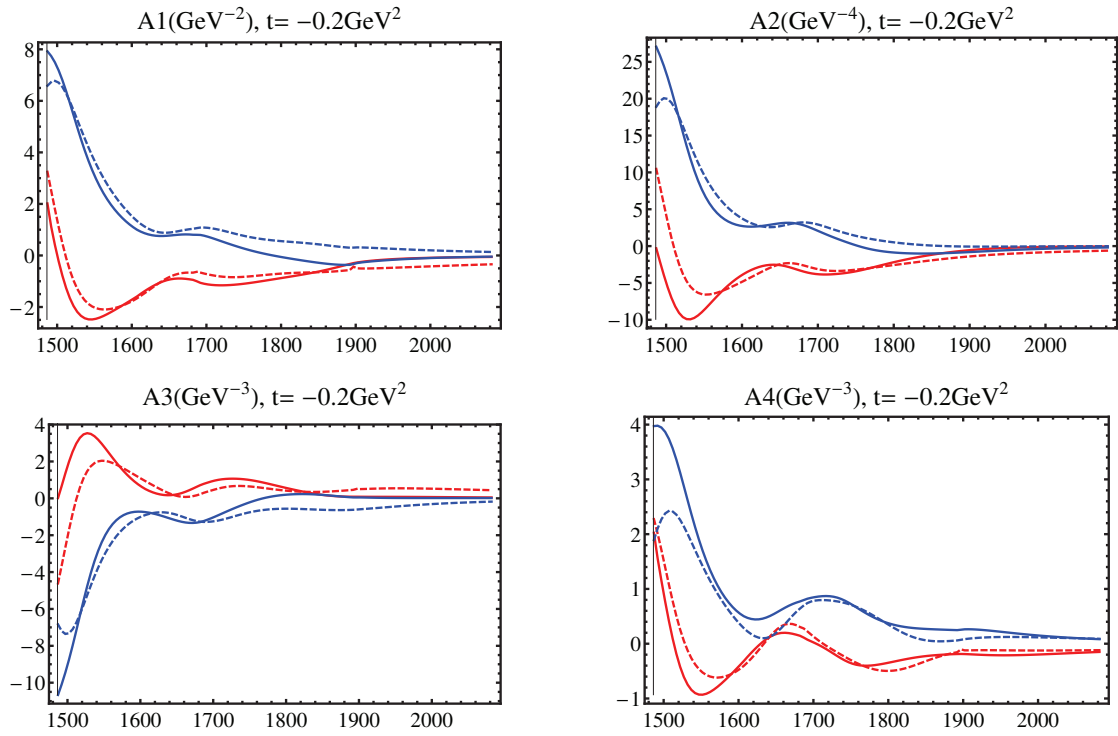


Figure B.13: Invariant amplitudes for Solution 4. Real parts of amplitudes are drawn in red, imaginary parts in blue. IB results are drawn as solid curves, DR results as dashed curves. Vertical black line denote the physical threshold for a given  $t$  value.

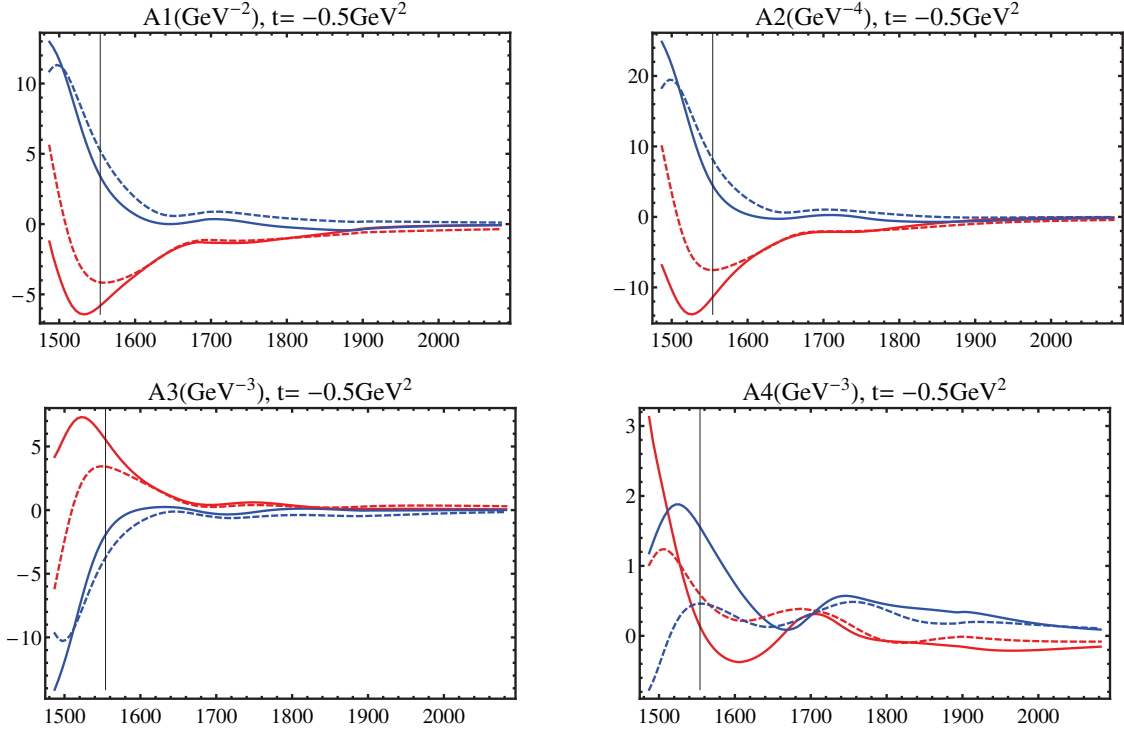


Figure B.14: Invariant amplitudes for Solution 4. Real parts of amplitudes are drawn in red, imaginary parts in blue. IB results are drawn as solid curves, DR results as dashed curves. Vertical black line denote the physical threshold for a given  $t$  value.

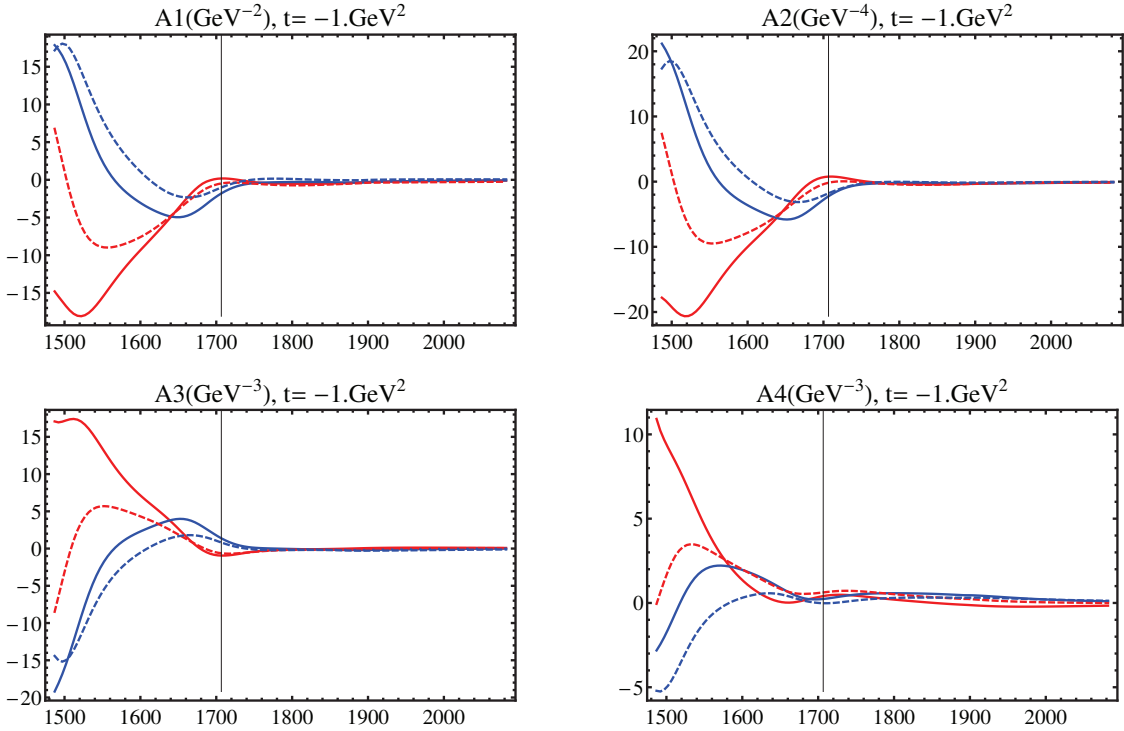


Figure B.15: Invariant amplitudes for Solution 4. Real parts of amplitudes are drawn in red, imaginary parts in blue. IB results are drawn as solid curves, DR results as dashed curves. Vertical black line denote the physical threshold for a given  $t$  value.

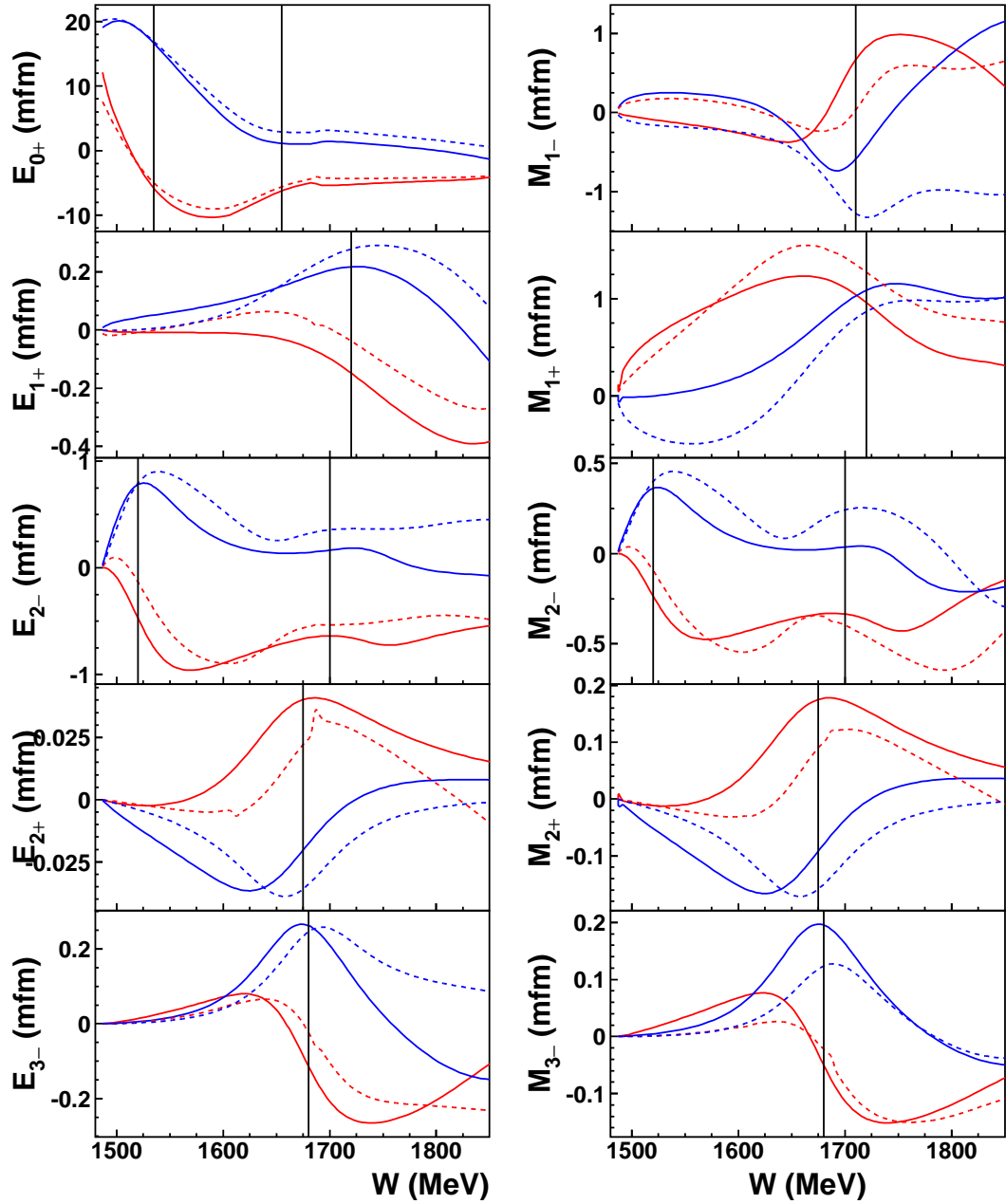


Figure B.16: Multipoles for Solution 4. Real parts of multipoles are drawn in red, imaginary parts in blue. IB results are drawn as solid curves, DR results as dashed curves.



### B.5 Plots for Solution 5

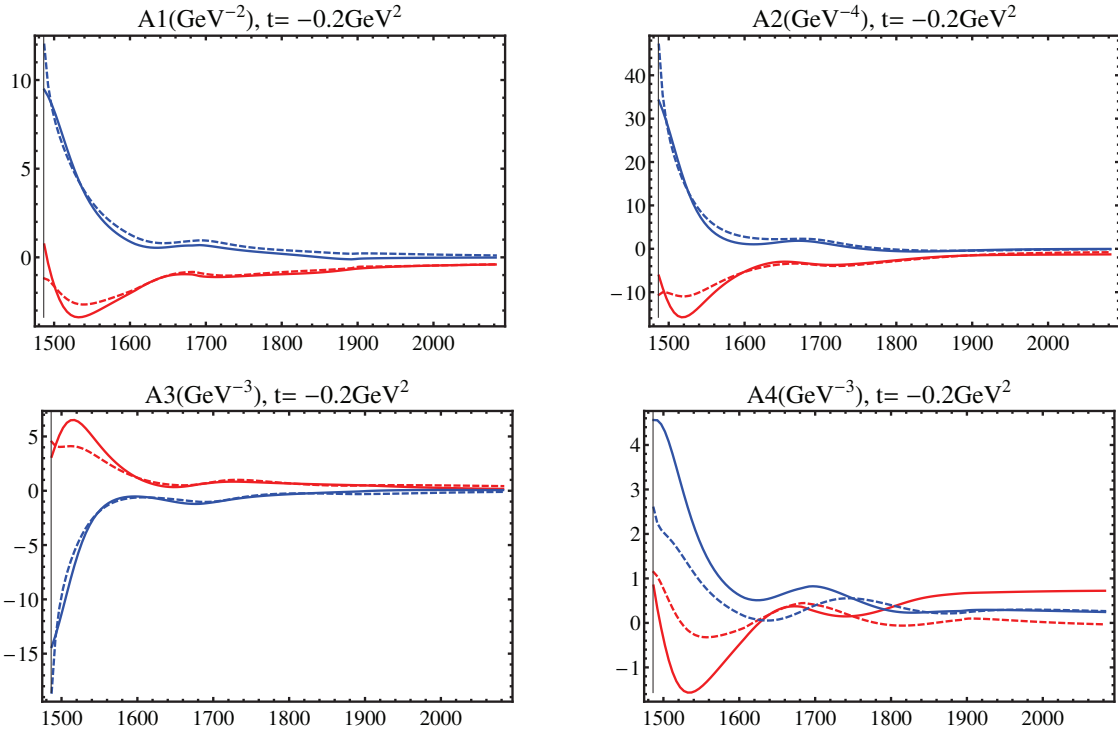


Figure B.17: Invariant amplitudes for Solution 5. Real parts of amplitudes are drawn in red, imaginary parts in blue. IB results are drawn as solid curves, DR results as dashed curves. Vertical black line denote the physical threshold for a given  $t$  value.

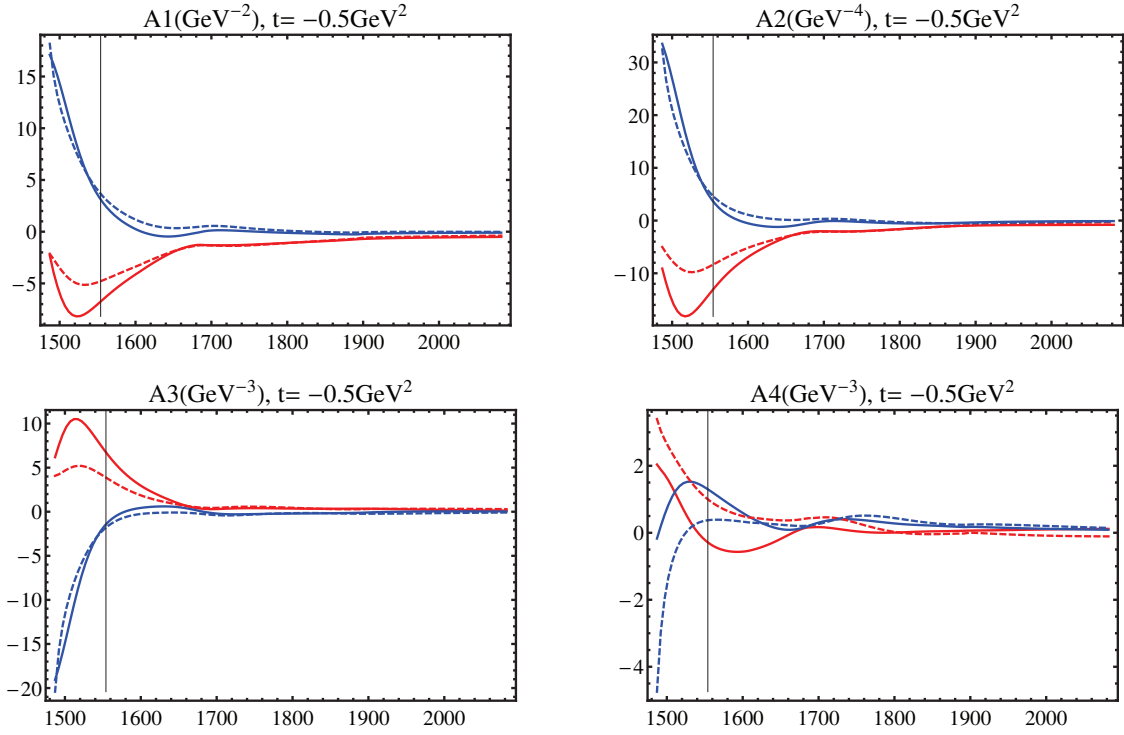


Figure B.18: Invariant amplitudes for Solution 5. Real parts of amplitudes are drawn in red, imaginary parts in blue. IB results are drawn as solid curves, DR results as dashed curves. Vertical black line denote the physical threshold for a given  $t$  value.

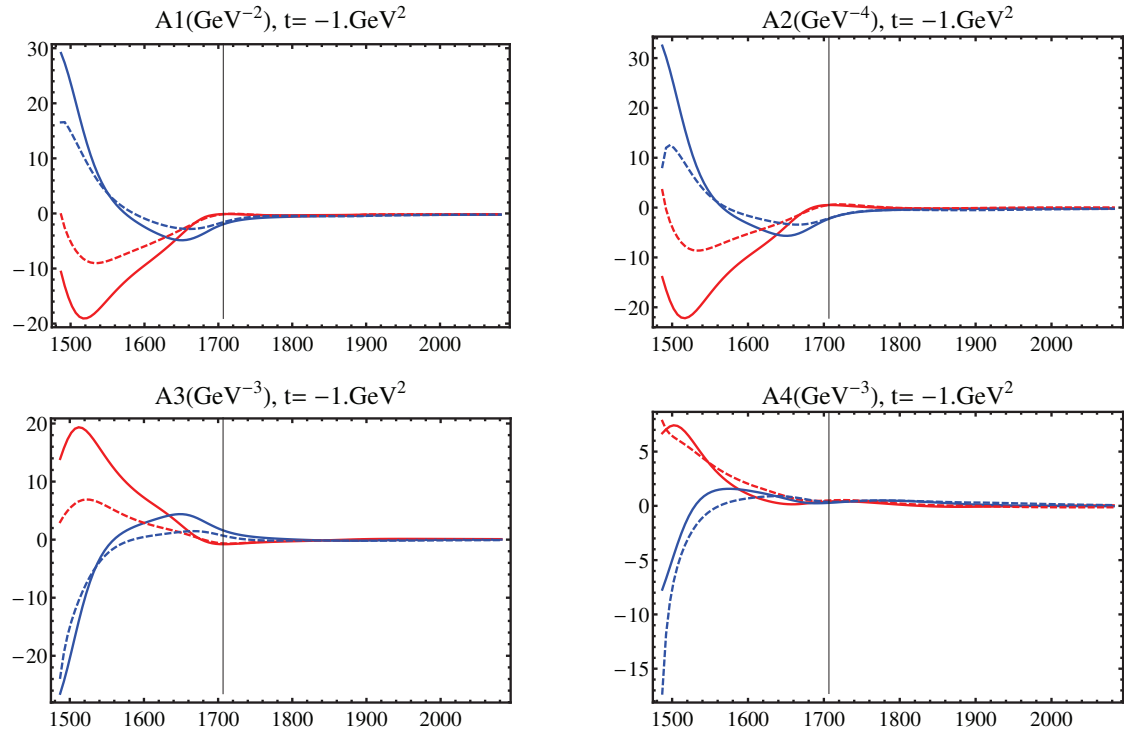


Figure B.19: Invariant amplitudes for Solution 5. Real parts of amplitudes are drawn in red, imaginary parts in blue. IB results are drawn as solid curves, DR results as dashed curves. Vertical black line denote the physical threshold for a given  $t$  value.

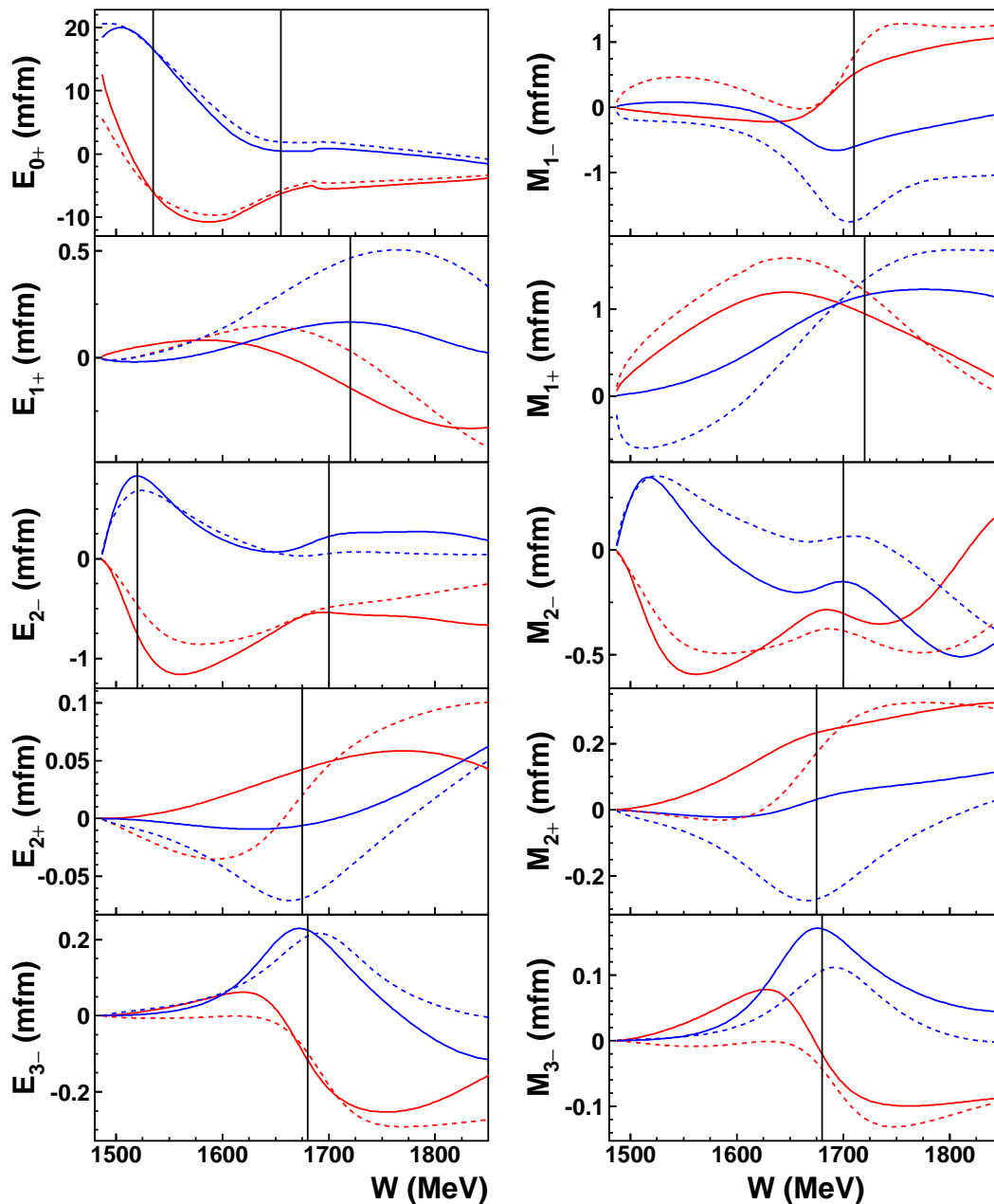


Figure B.20: Multipoles for Solution 5. Real parts of multipoles are drawn in red, imaginary parts in blue. IB results are drawn as solid curves, DR results as dashed curves.

## B.6 Plots for Solution 6

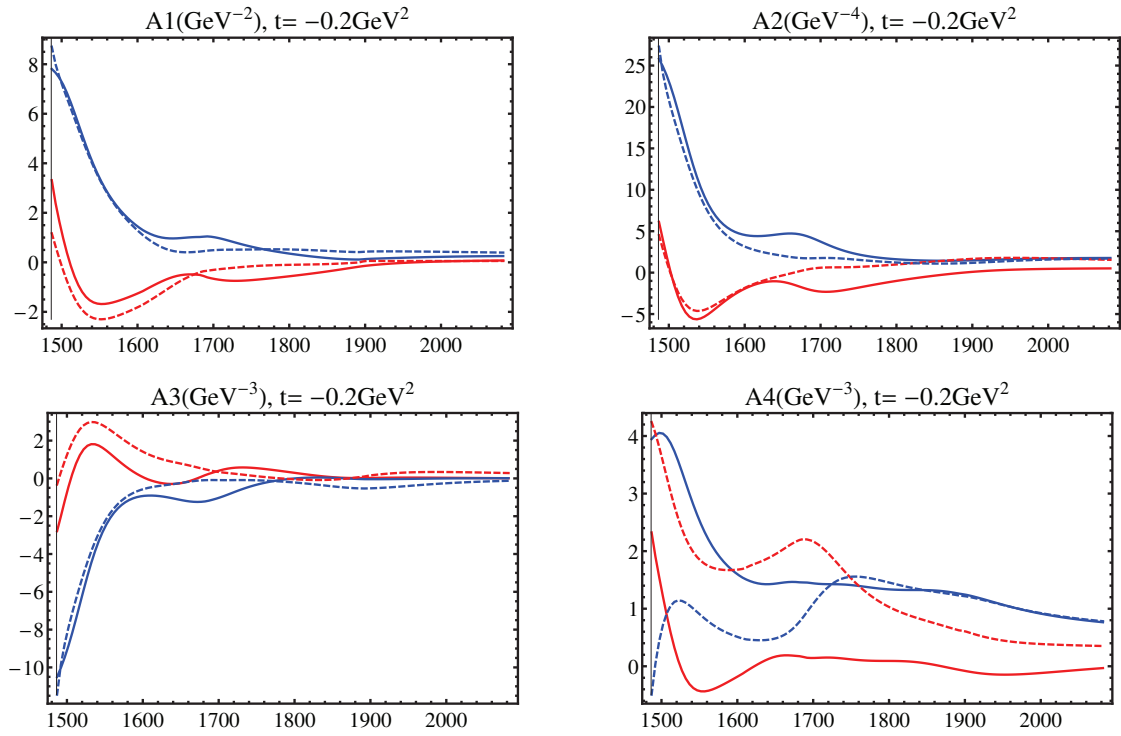


Figure B.21: Invariant amplitudes for Solution 6. Real parts of amplitudes are drawn in red, imaginary parts in blue. IB results are drawn as solid curves, DR results as dashed curves. Vertical black line denote the physical threshold for a given  $t$  value.

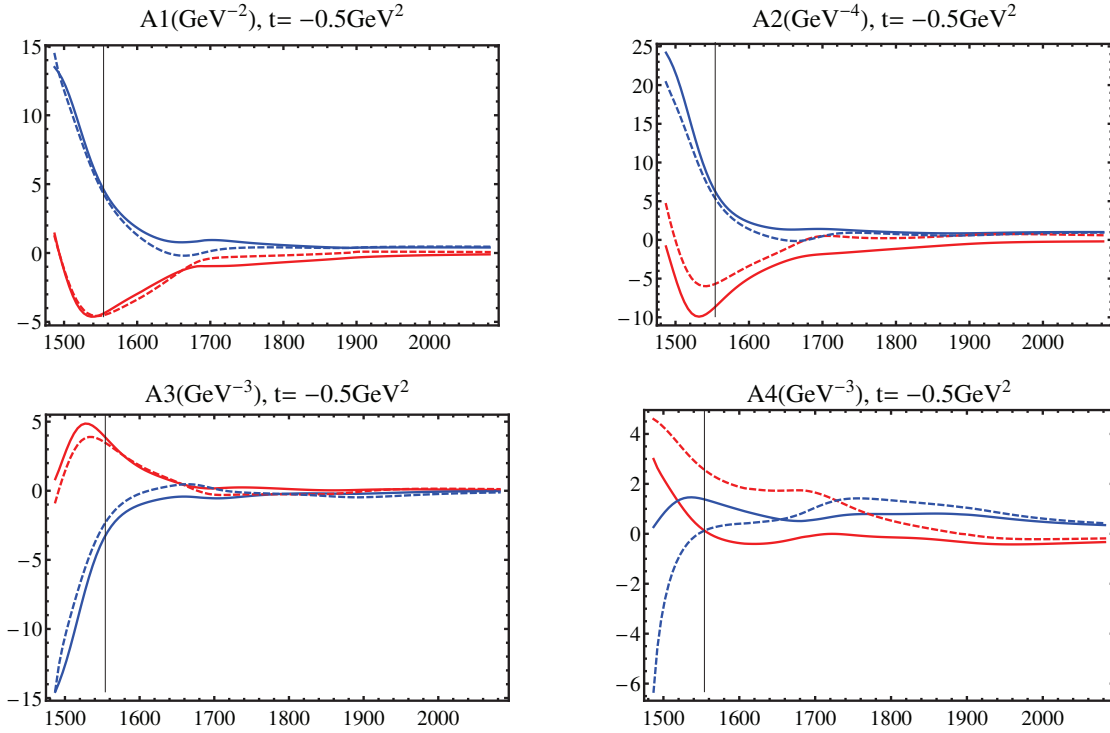


Figure B.22: Invariant amplitudes for Solution 6. Real parts of amplitudes are drawn in red, imaginary parts in blue. IB results are drawn as solid curves, DR results as dashed curves. Vertical black line denote the physical threshold for a given  $t$  value.

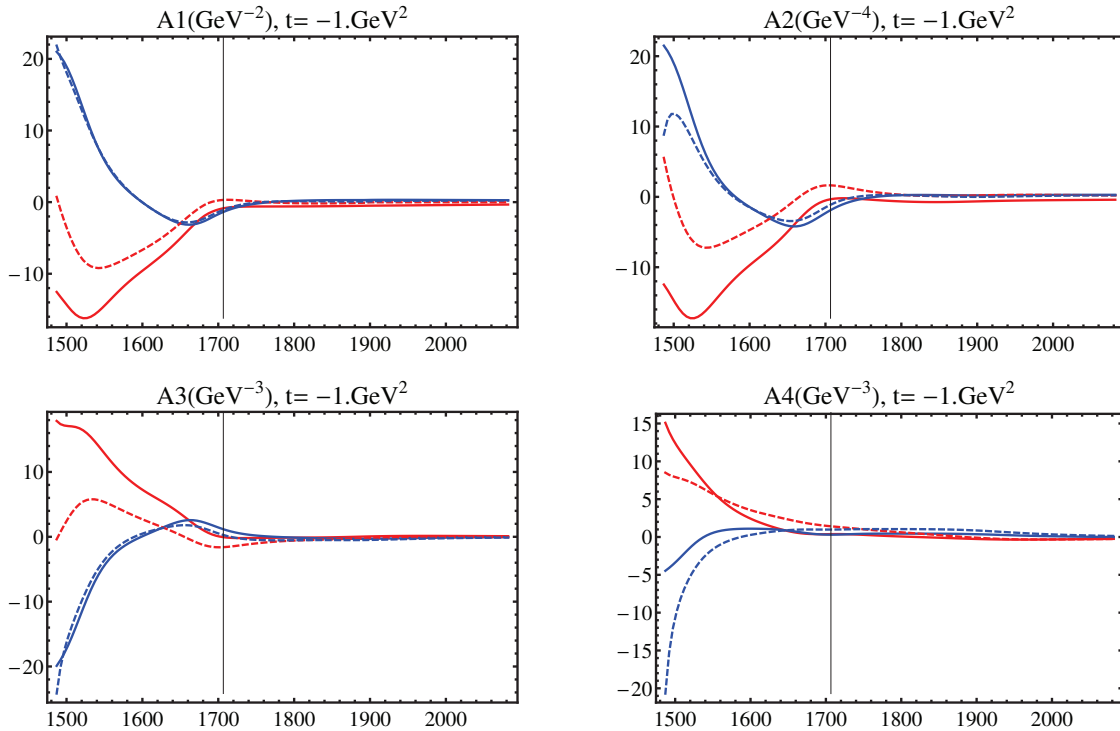


Figure B.23: Invariant amplitudes for Solution 6. Real parts of amplitudes are drawn in red, imaginary parts in blue. IB results are drawn as solid curves, DR results as dashed curves. Vertical black line denote the physical threshold for a given  $t$  value.

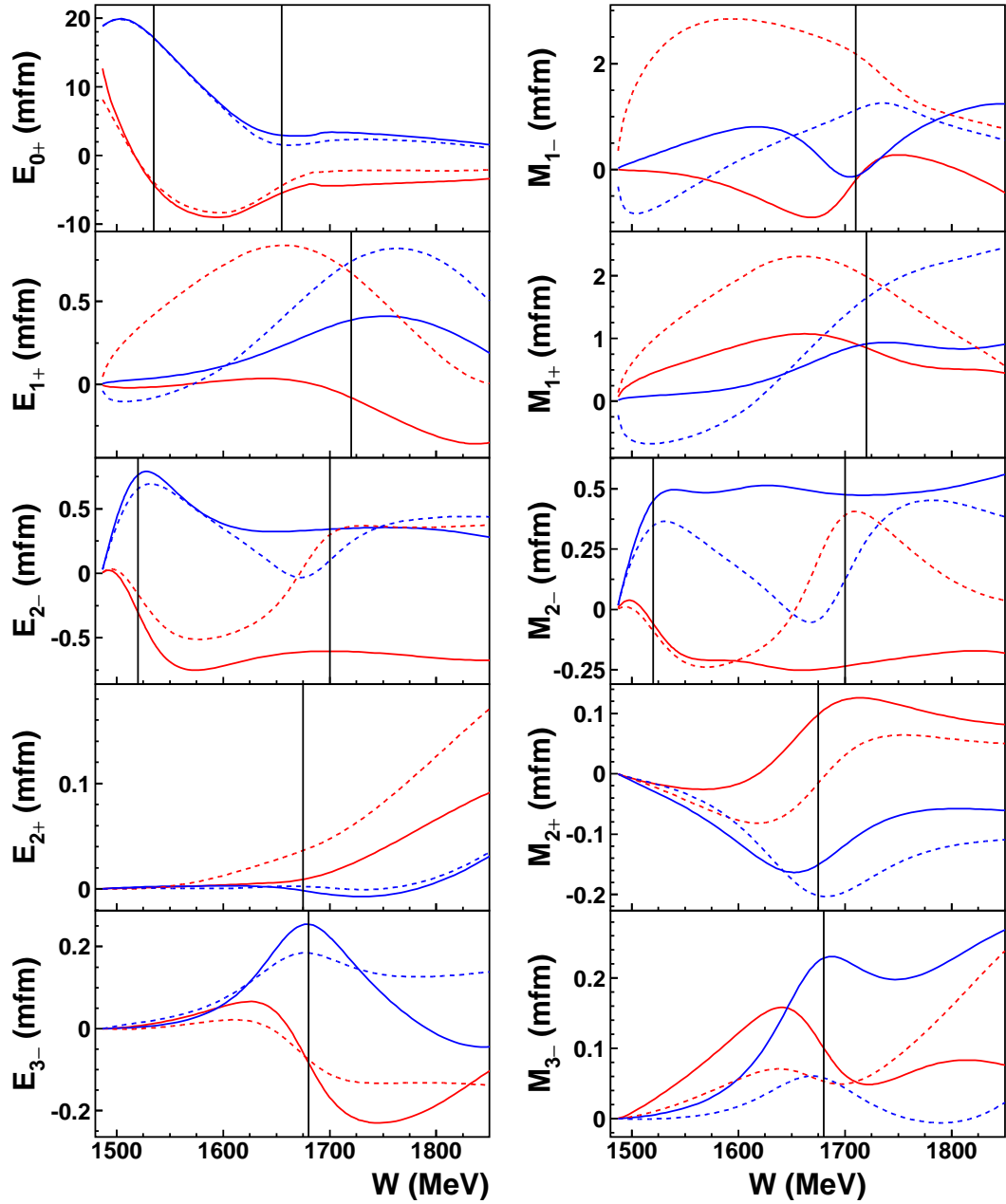


Figure B.24: Multipoles for Solution 6. Real parts of multipoles are drawn in red, imaginary parts in blue. IB results are drawn as solid curves, DR results as dashed curves.

### B.7 Plots for Solution 7

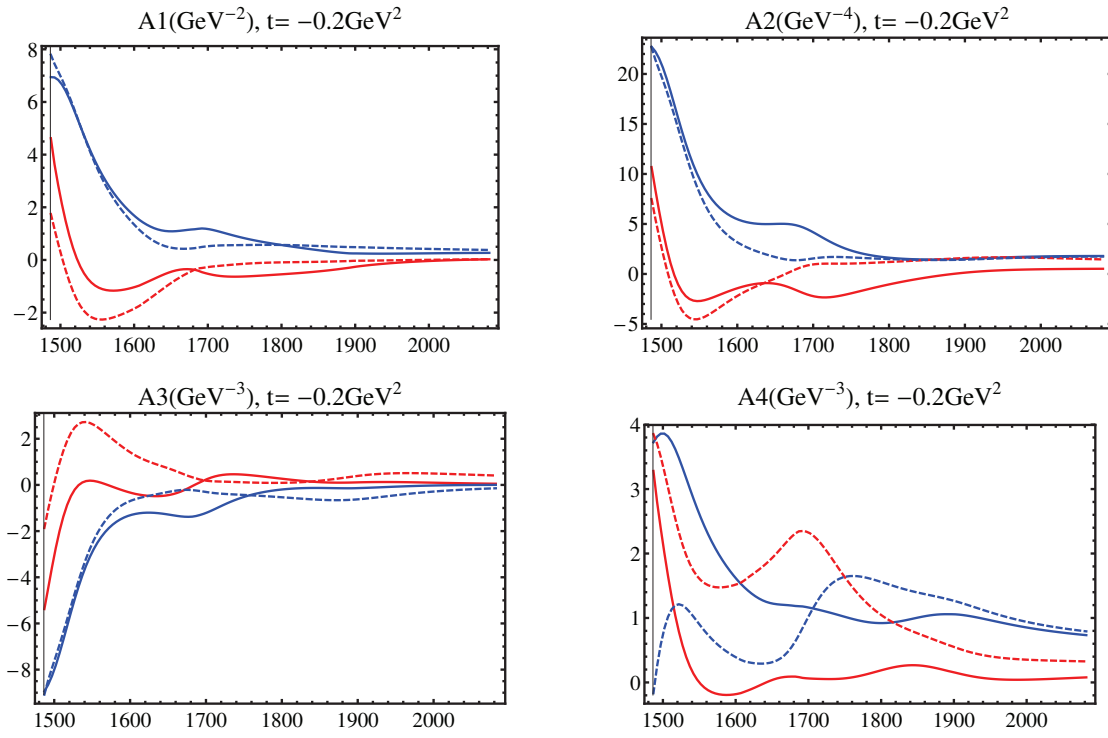


Figure B.25: Invariant amplitudes for Solution 7. Real parts of amplitudes are drawn in red, imaginary parts in blue. IB results are drawn as solid curves, DR results as dashed curves. Vertical black line denote the physical threshold for a given  $t$  value.

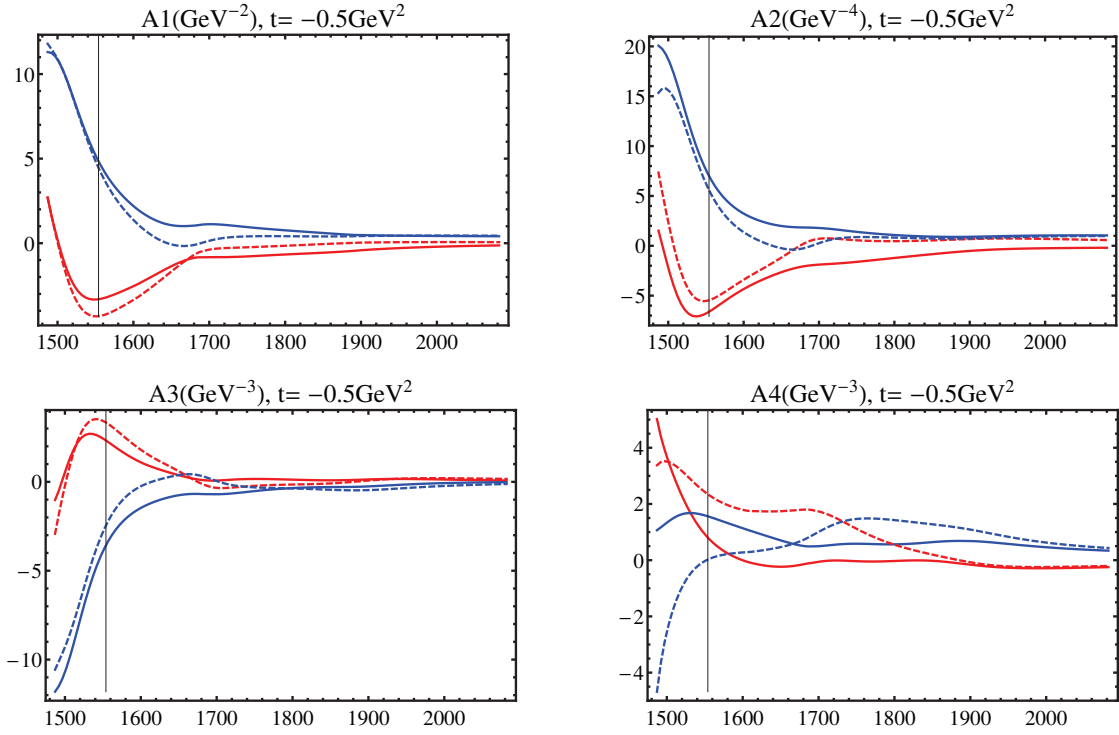


Figure B.26: Invariant amplitudes for Solution 7. Real parts of amplitudes are drawn in red, imaginary parts in blue. IB results are drawn as solid curves, DR results as dashed curves. Vertical black line denote the physical threshold for a given  $t$  value.

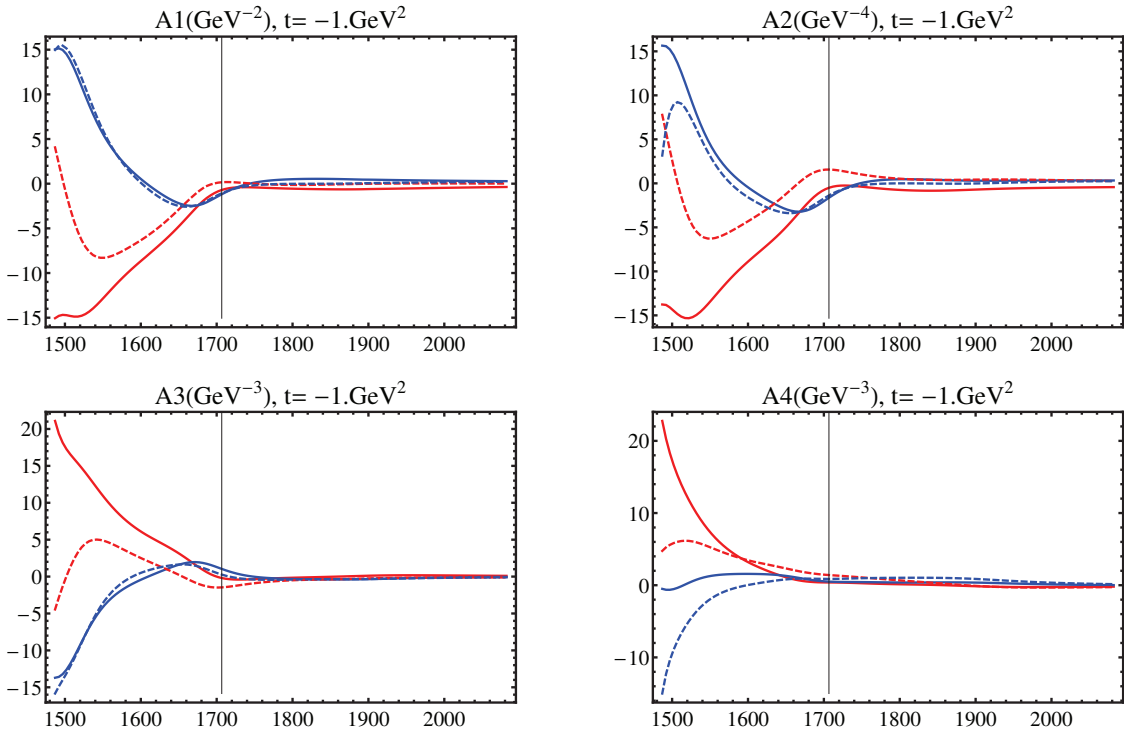


Figure B.27: Invariant amplitudes for Solution 7. Real parts of amplitudes are drawn in red, imaginary parts in blue. IB results are drawn as solid curves, DR results as dashed curves. Vertical black line denote the physical threshold for a given  $t$  value.



---

## Acknowledgements

---

I would like to acknowledge the continuous support of my supervisor, Michael Ostrick. First of all, I am thankful for giving me the opportunity to carry out the cutting-edge research in his group, for valuable advices and patience. I am grateful for the stimulation of the progress when I was stuck with difficulties. I thank my supervisor for encouraging and supporting my participations at different workshops and conferences.

Undoubtedly, it is worth to mention other members of our group in the Institute of Nuclear Physics, Mainz, Germany. Besides very useful and rich discussions about physics and mathematics, these people gave me a lot of friendly support, pleasant moments and life experience. I am thankful to Lothar Tiator, Viktor Kashevarov, Mikhail Gorchtein, Oleksandr Tomalak, Vahe Sokhoyan. I would like also to thank my English native speaker colleagues: Cristina Collicot and Philippe Martel for checking my spelling.

I am also thankful to the members of our Mainz-Tuzla-Zagreb collaboration: Jugoslav Stahov, Hedim Osmanovic, Mirza Hadzimehmedovic, Alfred Svarc and Rifat Omerovic.

My special thanks go to my parents, to my wife and to the whole family. I am very thankful for their support that keeps me believing in myself.

Furthermore, I would like to thank Mikhail Gorchtein for his useful advices and suggested changes that improved the EtaMAID model. In addition I would like to thank Vincent Mathieu for our useful e-mail exchanges.

I appreciate the collaboration with Inna Aznauryan for a useful exchange of computer codes.



## **Kirill Nikonov**

Research associate, PhD student  
Johannes Gutenberg University Mainz  
Institute of Nuclear Physics

e-mail: nikonov@uni-mainz.de  
kvnikonov@gmail.com

**born** July 30, 1989 in *Leningrad, USSR*

**nationality** Russia

**married since** 04.09.2015

**current address:** Richard-Schirrmann Str. 12, 55122 Mainz, Germany

### **EDUCATION**

- 07.2012- 09.2013** Postgraduate Student, Petersburg Nuclear Physics Institute
- 09.2010 - 06.2012** Master of Physics, Quantum Mechanics Department, Physical Faculty, Saint-Petersburg State University
- 09.2006 - 06.2010** Bachelor of Physics, Quantum Mechanics Department, Physical Faculty, Saint-Petersburg State University
- 06.2006** graduated from Secondary School

### **EMPLOYMENT HISTORY**

- 10.2013 - presently** Research associate, PhD student, Johannes Gutenberg University, Mainz
- 07.2012- 09.2013** Postgraduate Student, Petersburg Nuclear Physics Institute, Gatchina

### **RESEARCH INTERESTS**

My first research was made in 2009, it was entitled: "Decomposition of the scattering cross section by angular moments, data preparation for partial-wave analysis".

In 2010 I've graduated as bachelor with the thesis entitled: "Calculation of dispersion corrections for the particles with an arbitrary spin into two scalar or pseudoscalar mesons".

In 2011 I started learning  $K$ -matrix and  $D$ -matrix approaches in partial wave analysis. The comparison of them has been analyzed in my Magister thesis entitled: "The analysis of the meson-meson data in the framework of the dispersion  $D$ -matrix method".

All the time of my education in the University I was working with Russian members of Bonn-Gatchina Partial Wave Analysis (PWA) group. I was involved in the checking of analytic properties and gauge invariance of the scattering amplitude.

In 2013 I started my work in Mainz learning studies about complete experiment and working on applying analytical constraints in single energy PWA.

In 2015 I started to work on my PhD thesis entitled: "Partial wave analysis of eta meson photoproduction using fixed-t dispersion relations".

## LIST OF PUBLICATIONS

A.V. Anisovich, V.V. Anisovich, M.A. Matveev, K.V. Nikonov, V.A. Nikonov, J. Nyiri, A.V. Sarantsev, T.O. Vulfs. Analysis of the meson-meson data in the framework of the dispersion  $D$ -matrix method. Phys.Rev. **D84**, 076001, (2011).

V.V. Anisovich, K.V. Nikonov, V.A. Nikonov. Proton-proton diffractive collisions at ultrahigh energies. Phys.Rev.D88 (2013) no. 1, 014039

V.V. Anisovich, K.V. Nikonov, V.A. Nikonov, J. Nyiri. Proton-proton, pion-proton and pion-pion diffractive collisions at ultrahigh energies. Int.J.Mod.Phys.A29 (2014) 1450096.

Bled Workshops in Physics, Vol. 16, No. 1, page 40. Proceedings of the Mini-Workshop: "Exploring Hadron Resonances", Bled, Slovenia, July 5-11, 2015.

Single energy partial wave analyses on eta photoproduction – experimental data. Bled Workshops Phys. 18 (2017) no.1, 35-38.

Single energy partial wave analyses on eta photoproduction – pseudo data. Bled Workshops Phys. 18 (2017) no.1, 17-21.

Fixed- $t$  analyticity as a constraint in single-energy partial-wave analyses of meson photoproduction reactions. Phys.Rev. C97 (2018) no.1, 015207.

# Versicherung

für das Gesuch um Zulassung zur Promotion am Fachbereich 08

Hiermit versichere ich gemäß § 12 Abs. 3e der Promotionsordnung des Fachbereichs 08, Physik, Mathematik und Informatik der Johannes Gutenberg-Universität Mainz vom 02.12.2013:

- a) Ich habe die jetzt als Dissertation vorgelegte Arbeit selbständig verfasst. Es wurden ausschließlich die angegebenen Quellen und Hilfsmittel verwendet. Von der Ordnung zur Sicherung guter wissenschaftlicher Praxis in Forschung und Lehre und vom Verfahren zum Umgang mit wissenschaftlichem Fehlverhalten habe ich Kenntnis genommen.
- b) Ich habe oder hatte die jetzt als Dissertation vorgelegte Arbeit nicht schon als Prüfungsarbeit für eine andere Prüfung eingereicht \*)

Ich hatte die jetzt als Dissertation vorgelegte Arbeit als Prüfungsarbeit für folgende Prüfung eingereicht: \*)

\_\_\_\_\_  
(Bezeichnung der Prüfung)

\_\_\_\_\_  
(Bezeichnung und Ort der Prüfungsstelle)

- c) Ich hatte weder die jetzt als Dissertation vorgelegte Arbeit noch Teile davon an einer anderen Stelle als Dissertation eingereicht \*)


Ich hatte die folgende Abhandlung mit anstehendem Ergebnis als Dissertation eingereicht \*)

\_\_\_\_\_  
(Titel der Abhandlung)

\_\_\_\_\_  
(Fakultät bzw. Fachbereich und Hochschule)

\_\_\_\_\_  
(Ergebnis bzw. Beurteilung)

18.05.18  
(Datum)

  
(Unterschrift)

\*) Nichtzutreffendes bitte streichen

18.03.2014/mm



---

## Bibliography

---

- [1] A. Esposito, A. Pilloni and A. D. Polosa, Phys. Rept. **668**, 1 (2016).
- [2] D. Diakonov, V. Petrov and M. V. Polyakov, Z. Phys. A **359**, 305 (1997).
- [3] P. A. M. Guichon, Phys. Lett. B **200**, 235 (1988).
- [4] N. Isgur, R. Kokoski and J. Paton, Phys. Rev. Lett. **54**, 869 (1985).
- [5] V. V. Anisovich, M. A. Matveev, J. Nyiri and A. V. Sarantsev, Phys. Atom. Nucl. **69**, 520 (2006).
- [6] M. Gell-Mann, Phys. Lett. **8**, 214 (1964).
- [7] G. Zweig, Developments in the Quark Theory of Hadrons, Volume 1. Edited by D. Lieberberg and S. Rosen. pp. 22-101
- [8] D. Drechsel, O. Hanstein, S. S. Kamalov and L. Tiator, Nucl. Phys. A **645**, 145 (1999).
- [9] W. T. Chiang, S. N. Yang, L. Tiator and D. Drechsel, Nucl. Phys. A **700**, 429 (2002).
- [10] A. V. Anisovich, E. Klempt, V. A. Nikonov, A. V. Sarantsev and U. Thoma, Eur. Phys. J. A **47**, 153 (2011).
- [11] E. Gutz *et al.* [CBELSA/TAPS Collaboration], Eur. Phys. J. A **50**, 74 (2014).
- [12] D. Ronchen *et al.*, Eur. Phys. J. A **49**, 44 (2013).
- [13] D. Ronchen *et al.*, Eur. Phys. J. A **50**, no. 6, 101 (2014) Erratum: [Eur. Phys. J. A **51**, no. 5, 63 (2015)].
- [14] R. A. Arndt, W. J. Briscoe, I. I. Strakovsky and R. L. Workman, Phys. Rev. C **74**, 045205 (2006).
- [15] <https://maid.kph.uni-mainz.de/>
- [16] <https://pwa.hiskp.uni-bonn.de/>
- [17] <http://collaborations.fz-juelich.de/ikp/meson-baryon/main>
- [18] <http://gwdac.phys.gwu.edu/>
- [19] R. C. E. Devenish and D. H. Lyth, Nucl. Phys. B **43**, 228 (1972).
- [20] R. C. E. Devenish and D. H. Lyth, Nucl. Phys. B **93**, 109 (1975).
- [21] R. L. Crawford, Nucl. Phys. B **97**, 125 (1975).
- [22] I. M. Barbour and R. L. Crawford, Nucl. Phys. B **111**, 358 (1976).

- [23] F. A. Berends and A. Donnachie, Nucl. Phys. B **136**, 317 (1978).
- [24] I. M. Barbour, R. L. Crawford and N. H. Parsons, Nucl. Phys. B **141**, 253 (1978).
- [25] I. Arai and H. Fujii, Nucl. Phys. B **194**, 251 (1982).
- [26] R. L. Crawford and W. T. Morton, Nucl. Phys. B **211**, 1 (1983).
- [27] I. G. Aznauryan, V. D. Burkert, H. Egiyan, K. Joo, R. Minehart and L. C. Smith, Phys. Rev. C **71**, 015201 (2005).
- [28] I. G. Aznauryan *et al.* [CLAS Collaboration], Phys. Rev. C **78**, 045209 (2008).
- [29] I. G. Aznauryan *et al.* [CLAS Collaboration], Phys. Rev. C **80**, 055203 (2009).
- [30] N. Isgur, nucl-th/0007008.
- [31] C. Patrignani *et al.* [Particle Data Group], Chin. Phys. C **40**, no. 10, 100001 (2016)
- [32] V. V. Anisovich, M. A. Matveev, V. A. Nikonov, J. Nyiri and A. V. Sarantsev, Hackensack, USA: World Scientific (2008) 580 p
- [33] D. B. Leinweber, T. Draper and R. M. Woloshyn, Phys. Rev. D **48**, 2230 (1993).
- [34] R. G. Edwards, J. J. Dudek, D. G. Richards and S. J. Wallace, Phys. Rev. D **84**, 074508 (2011).
- [35] H. Osmanovic *et al.*, Phys. Rev. C **97**, no. 1, 015207 (2018).
- [36] S. Mandelstam, Phys. Rev. **115**, 1741 (1959).
- [37] S. Mandelstam, Phys. Rev. **112**, 1344 (1958).
- [38] F. A. Berends, A. Donnachie and D. L. Weaver, Nucl. Phys. B **4**, 1 (1967).
- [39] G. F. Chew, M. L. Goldberger, F. E. Low and Y. Nambu, Phys. Rev. **106**, 1345 (1957).
- [40] J.D. Bjorken and S.D. Drell, "Relativistic quantum fields", (McGraw-Hill, New York, 1965).
- [41] C. G. Fasano, F. Tabakin and B. Saghai, Phys. Rev. C **46**, 2430 (1992).
- [42] Vol 4 - Landau, Lifshitz - Quantum Electrodynamics (2ed., Pergamon, 1982)
- [43] E. F. McNicoll *et al.* [Crystal Ball at MAMI Collaboration], Phys. Rev. C **82**, 035208 (2010), Erratum: [Phys. Rev. C **84**, 029901 (2011)].
- [44] V. L. Kashevarov *et al.* [A2 Collaboration], Phys. Rev. Lett. **118**, no. 21, 212001 (2017).
- [45] V. Crede *et al.* [CBELSA/TAPS Collaboration], Phys. Rev. C **80**, 055202 (2009).
- [46] M. Williams *et al.* [CLAS Collaboration], Phys. Rev. C **80**, 045213 (2009).
- [47] O. Bartalini *et al.* [GRAAL Collaboration], Eur. Phys. J. A **33**, 169 (2007).
- [48] J. Ajaka *et al.*, Phys. Rev. Lett. **81**, 1797 (1998).
- [49] C. S. Akondi *et al.* [A2 at MAMI Collaboration], Phys. Rev. Lett. **113**, no. 10, 102001 (2014).



- [50] I. Senderovich *et al.* [CLAS Collaboration], Phys. Lett. B **755**, 64 (2016).
- [51] W. T. Chiang, S. N. Yang, L. Tiator, M. Vanderhaeghen and D. Drechsel, Phys. Rev. C **68**, 045202 (2003).
- [52] V. L. Kashevarov, L. Tiator and M. Ostrick, Bled Workshops Phys. **16**, 9 (2015).
- [53] V. L. Kashevarov *et al.* [A2 Collaboration], JPS Conf. Proc. **13**, 020029 (2017).
- [54] V. L. Kashevarov, M. Ostrick and L. Tiator, Phys. Rev. C **96**, no. 3, 035207 (2017).
- [55] L. Tiator, C. Bennhold and S. S. Kamalov, Nucl. Phys. A **580**, 455 (1994).
- [56] A. C. Irving and R. P. Worden, Phys. Rept. **34**, 117 (1977).
- [57] G. R. Goldstein and J. F. Owens, Phys. Rev. D **7**, 865 (1973).
- [58] I. S. Barker and J. K. Storrow, Nucl. Phys. B **137**, 413 (1978).
- [59] P. V. Landshoff and J. C. Polkinghorne, Phys. Rept. **5**, 1 (1972).
- [60] A. Donnachie and Y. S. Kalashnikova, Phys. Rev. C **93**, no. 2, 025203 (2016).
- [61] G. F. Chew and S. C. Frautschi, Phys. Rev. Lett. **8**, 41 (1962).
- [62] A. V. Anisovich, V. V. Anisovich and A. V. Sarantsev, Phys. Rev. D **62**, 051502 (2000).
- [63] P. D. B. Collins, "An Introduction to Regge Theory and High-Energy Physics,"
- [64] J. Nys *et al.* [JPAC Collaboration], Phys. Rev. D **95**, no. 3, 034014 (2017).
- [65] A. V. Anisovich *et al.*, Eur. Phys. J. A **52**, no. 9, 284 (2016).
- [66] I. G. Aznauryan, Phys. Rev. C **68**, 065204 (2003).
- [67] J. S. Ball, Phys. Rev. **124**, 2014 (1961).
- [68] R. C. E. Devenish and D. H. Lyth, Phys. Rev. D **5**, 47 (1972) Erratum: [Phys. Rev. D **6**, 2067 (1972)].
- [69] P. Dennery, Phys. Rev. **124**, 2000 (1961).
- [70] I. G. Aznaurian, Phys. Rev. D **57**, 2727 (1998).
- [71] F. Renard *et al.* [GRAAL Collaboration], Phys. Lett. B **528**, 215 (2002).
- [72] M. Dugger *et al.* [CLAS Collaboration], Phys. Rev. Lett. **89**, 222002 (2002).
- [73] B. Krusche *et al.*, Phys. Rev. Lett. **74**, 3736 (1995).
- [74] A. Bock *et al.*, Phys. Rev. Lett. **81**, 534 (1998).
- [75] B. Pasquini, D. Drechsel and L. Tiator, Eur. Phys. J. A **27**, 231 (2006).
- [76] P. Noelle, Prog. Theor. Phys. **60**, 778 (1978).
- [77] W. Braunschweig, W. Erlewein, H. Frese, K. Luebelsmeyer, H. Meyer-Wachsmuth, D. Schmitz, A. Schultz Von Dratzig and G. Wessels, Phys. Lett. **33B**, 236 (1970).

- [78] J. Dewire, B. Gittelman, R. Loe, E. C. Loh, D. J. Ritchie and R. A. Lewis, Phys. Lett. **37B**, 326 (1971).
- [79] P. J. Bussey *et al.*, Phys. Lett. **61B**, 479 (1976).
- [80] D. Bellenger, S. Deutsch, D. Luckey, L. S. Osborne and R. Schwitters, Phys. Rev. Lett. **21**, 1205 (1968).
- [81] P. J. Bussey *et al.*, Nucl. Phys. B **185**, 269 (1981).
- [82] V. Sokhoyan *et al.* [CBELSA/TAPS Collaboration], Eur. Phys. J. A **51**, no. 8, 95 (2015)  
Erratum: [Eur. Phys. J. A **51**, no. 12, 187 (2015)].
- [83] A. Svarc, M. Hadzimehmedovic, H. Osmanovic, J. Stahov, L. Tiator and R. L. Workman, Phys. Rev. C **88**, no. 3, 035206 (2013).
- [84] A. Svarc, M. Hadzimehmedovic, R. Omerovic, H. Osmanovic and J. Stahov, Phys. Rev. C **89**, no. 4, 045205 (2014).
- [85] A. Svarc, M. Hadzimehmedovic, H. Osmanovic, J. Stahov, L. Tiator and R. L. Workman, Phys. Rev. C **89**, no. 6, 065208 (2014).
- [86] A. Svarc, PoS Hadron **2017**, 136 (2018).